Doctoral Thesis

MAXIMIZING THE ELECTROCATALYTIC ACTIVITIES OF NON-NOBLE TRANSITION METAL'S COMPOUNDS FOR WATER ELECTROLYSIS

Mohsin Ali Raza Anjum

Department of Chemical Engineering

Graduate School of UNIST

2018

MAXIMIZING THE ELECTROCATALYTIC ACTIVITIES OF NON-NOBLE TRANSITION METAL'S COMPOUNDS FOR WATER ELECTROLYSIS

Mohsin Ali Raza Anjum

Department of Chemical Engineering

Graduate School of UNIST

Maximizing the Electrocatalytic Activities of Non-Noble Transition Metal's Compounds for Water Electrolysis

A thesis/dissertation
submitted to the Graduate School of UNIST
in partial fulfillment of the
requirements for the degree of
Doctor of Philosophy

Mohsin Ali Raza Anjum

05. 28. 2018
Approved by

_____
Advisor
Jae Sung Lee

Maximizing the Electrocatalytic Activities of Non-Noble Transition Metal's Compounds for Water Electrolysis

Mohsin Ali Raza Anjum

This certifies that the thesis of Mohsin Ali Raza Anjum is approved.

05. 28. 2018

Signature

_____

Thesis Advisor: Prof. Jae Sung Lee

Signature

_____

Prof. Ja Hun Kwak: Thesis Committee Member #1

Signature

_____

Prof. Sang Hoon Joo: Thesis Committee Member #2

Signature

_____

Prof. Kwangjin An: Thesis Committee Member #3

Signature

_____

Prof. Ji-Wook Jang: Thesis Committee Member #4;

Abstract

The rapid growth in population and advancement in heavy industry, has badly influenced world economy due to sharp rise in cost of oil prices. Currently, about 80% of energy is produced from fossil fuels, which adds greenhouse gases (CO_2, SO_x & NO_x) to the environment by increasing global temperature and environmental pollution. Therefore, development of sustainable, environmentally friendly and alternatives energy sources to fossil fuels attracts much attentions in recent decades. Among the various alternative advanced clean energy technologies, the fuel cells, CO and CO_2 to liquid fuel conversions, water electrolysis, solar, wind, marine energy, electrochemical energy storage (EES) devices including various types of batteries and supercapacitors (SCs) have been attracted much attention in recent years. Although, many efforts have been exercised to improve these technologies but they are still facing many challenges like high cost, durability, reliability, efficiency and maintenance to commercialize at public sectors. The hydrogen (H_2) is the only alternative clean fuel which can mitigate energy and environmental related issues. Among the various alternative energy technologies, for example fuel cells, CO_2 conversions and water electrolysis uses hydrogen as the primary energy carrier. Currently, about 95% of total hydrogen is produced by using conventional technologies like steam methane reforming (SMR) and coal gasification (CG). Evidently, these methods are adding more greenhouse gases to the environment and the quality of hydrogen is also poor. The pure hydrogen is generated by water electrolysis which is usually conducted either photochemically and photoelectrochemically or electrochemically. Amongst all water electrolysis processes, the electrochemical water splitting is the only available greener, sustainable and rapid route of generating highly pure H_2 at commercial scale.

Transition metal compounds (TMCs) such as phosphides, carbides and chalcogenides have attracted massive attention as alternatives of noble metals (Pt, Ru or Ir) since last few years due to their superior electrical conductivity, mechanical strength, and chemical stability. In spite of the success, there are still many challenges like poor performance, stability in wide pH range, expensive and poisonous starting precursors, environmentally unsafe synthetic procedures, lack of in-depth mechanistic knowledge and so on which are creating hurdles for sustainable hydrogen production with both economic and environmental advantage. Here, simple, economical, ecofriendly and commercially adoptable synthesis procedures are developed to increase the number of active sites and intrinsic catalytic activity of transition metals carbides, phosphides and sulfides through heteroatom doping. Moreover, these nanostructures are grafted on conductive substrates (like doped-graphene, carbon cloth, nickel foam etc.) for electrochemical water splitting applications.

The electrochemical properties of molybdenum carbides are tuned either by encapsulating or imbedding them in boron (B) and nitrogen (N) co-doped carbon network (BCN) via a unique organometallic complex-assisted approach. Due to the synergic effect of BCN network, the molybdenum carbides show a remarkable electrocatalytic hydrogen evolution (HER), oxygen evolution (OER) and oxygen reduction (ORR) performances and excellent durability in both acidic and basic aqueous defeating the most of earlier reported molybdenum carbides based electrocatalyst in the literature. The mechanistic study for water electrolysis and the synergic effect BCN network at electrochemical performance of molybdenum carbides is also discussed in detail.

The intrinsic catalytic activity stability of molybdenum phosphides nanocrystallite (MoP) are modulated by dual-doping of S and N into its structure via a unique, inexpensive and environmental-friendly thiourea-phosphate-assisted rout. The number of active sites are also increased by controlling the shape of nanoparticles and loading them on S, N self-doped graphene. The obtained MoP/SNG catalysts displays extraordinary hydrogen evolution (HER) performance in both acidic and alkaline media. Similarly, the sulfur-doped CoP (S:CoP) and Co_2P (S:Co_2P) nanoparticles are also synthesized as a noble metal-free electrocatalyst via above indigenously developed thiourea-phosphate-assisted route. The S-doped Co-phosphide based electrode exhibits excellent activity and stability for overall water splitting defeating noble mental-based Pt/C, IrO_2, and reported non-noble metal-based electrocatalysts. Density functional theory calculations reveal that the excellent activity is attributable to the modified electronic structures of Co-phosphides which favor the overall water splitting at both S:CoP and S:Co_2P electrodes. The S-doping also increases the number of exposed active sites especially on the conductive substrates which works as the excellent alkaline electrolyzers for overall water splitting.

The electroctalytic hydrogen evolution reaction (HER) activity of MoS_2 increases when it possesses multifunctional active sites including strucural defects, Mo-exposed edges, S-vacancies, 1T-phase and expanded interlayer distances. Previous reports on MoS_2-based catalysts targeted only a single or few of these active sites, the all-in-one MoS_2 electrocatalyst synthesized herein contains all of the above chararcteristics by using a supramolecular structure of melamine-phosphomolybdate (MA-PMo_{12}) and a weakly reducing thiourea. During preparation, the *in-situ* produced NH_3 gas acts as interculants between MoS_2 sheets and makes expanded interlayers spacing ammoniated 1-T MoS_2 (A-MoS_2). After reduction of guest NH_3 into interlayer-expanded MoS_2 in hydrogen leads to form an MoS_2 with multiple active sites described above (R-MoS_2) which exhibits surprisingly high hydrogen evolution reaction (HER) activity in alkaline media outperforms to all earlier reported MoS_2-based electrocatalysts.

Table of Contents

List of Figures

List of Tables

Abbreviations

1. AFM: Atomic Force Microscopy
2. Ag/AgCl: Silver/silver chloride
3. A-MoS_2: Ammonia intercalated molybdenum sulfide
4. BCN: Boron and Nitrogen co-doped Carbon
5. BET: Brunauer–Emmett–Teller
6. BF-TEM: Bright-Field Transmission Electron Microscopy
7. CA: Chronoamperometry
8. CC: Carbon cloth
9. C_{dl}: Double layer capacitance
10. CE: Counter Electrode
11. CV: Cyclic Voltammetry
12. DOS: density of states
13. ECSA: Electrochemical Active Surface Area
14. EDS: Energy-Dispersive X-ray Spectroscopy
15. EIS: Electrochemical Impedance Spectroscopy
16. FE-SEM: Field-Emission Scanning Electron Microscope
17. FFT: Fast Fourier Transforms
18. GCE: Glassy Carbon Electrode
19. HAADF-STEM: High-angle annular dark-field scanning transmission electron microscopy
20. HER: Hydrogen Evolution Reaction
21. HRTEM: High Resolution Transmission Electron Microscope
22. ICP-OES: Inductively Coupled Plasma Optical Emission Spectroscopy
23. Im: Imidazole
24. J_0: Exchange current density
25. LSV: linear sweep voltammetry
26. MA-PMo_{12}: Melamine-phosphomolybdate
27. MIB: Molybdenum-Imidazole-Borate complex
28. NF: Nickel Foam
29. NG: Nitrogen-doped Graphene
30. NPs: Nanoparticles
31. OER: Oxygen Evolution Reaction
32. ORR: Oxygen Reduction Reaction
33. PDOS: Projected Density of States

34. Pt: Platinum
35. R_{ct}: Charge Transfer Resistances
36. R_d: Diffusion Resistance
37. RDE: Rotating Disc Electrode
38. RE: Reference Electrode
39. rGO: Reduced graphene oxide
40. RHE: Reversible Hydrogen Electrode
41. R-MoS_2: Reduced molybdenum sulfide
42. R_s: Series (or Solution) Resistance
43. SNG: Sulfur and Nitrogen dual-doped Graphene
44. STEM: Scanning Transmission Electron Microscopy
45. TEM: Transmission Electron Microscope
46. TGA: Thermosgravimetric Analysis
47. TOF: Turnover Frequency
48. TS: Tafel Slope
49. UV-Vis-NIR: Ultra-Violet Visible Near Infra-Red Spectroscopy
50. WE: Working Electrode
51. XPS: X-ray Photoelectron Spectroscopy
52. XRD: X-ray Diffraction
53. η: Overpotential
54. η_{10}: Overpotential at current density of 10 mA cm^{-2}
55. χ: Electronegativity

1. Introduction

The fast depletion of fossil fuels and increasing demand with rapid growth in population, heavy industry and defense technology, has influenced world economy badly due to sharp rise in cost of oil prices. According to the International Energy Agency (IEA), the world energy demand approached 18 TW in 2013 and it is projected to further enhance from 18 (2013) to 24-26 TW in 2040. About 80% of this energy is produced from fossil (coal, oil and gas) fuels, which will further increase the carbon dioxide (CO_2) emissions from 32 Gt/year in 2013 to 37-44 Gt/year in 2040.[1] Due to the drastic rise in global temperature and environmental pollution by emission of exhaust gases (CO_2, SO_x & NO_x) form overuse of fossil fuels (e.g. coal, petroleum products, natural gas) has enforced the researcher and scientists to develop other alternatives to fossil fuels, sustainable and environmentally friendly sources of energy in recent decades.[2-3] Among the various alternative advanced clean energy technologies, the fuel cells, CO and CO_2 to liquid fuel conversions, water electrolysis, solar, wind, marine energy, electrochemical energy storage (EES) devices including various types of batteries and supercapacitors (SCs) have been attracted much attention in recent past years.[3-7] Although, a lot of efforts have been made to improve these technologies but they are still facing many challenges like high cost, durability, reliability, efficiency and maintenance to commercialize at public sectors.[5, 8] However, the adoption and commercialization of these clean energy technologies has to be accelerated to eliminate the climate risks and maintain the economic growth in a timely manner. Although these innovative technologies will face many political and financial challenges relative to established technologies, but governments should make policies to enhance the use of economically viable environmental-friendly energy solutions.[8]

Now the world has realized that the hydrogen (H_2) is the only alternative clean fuel which can mitigate all of above energy and environmental related problems.[9-10] Among the various alternative energy technologies, for example fuel cells, CO_2 conversions and water electrolysis uses hydrogen as the primary energy carrier. The hydrogen is also being used in many industrial applications like oil reforming, hydrogenation of oils to fats (margarine), treating metals, processing foods, producing NH_3 for fertilizer and rocket fuel.[11-12] Therefore, an effective storage and production of cheaper hydrogen gas is a critical challenge to ensure a secure and clean energy future.[12] So for many kinds of materials including metal hydrides,[13-14] high surface area porous carbon materials,[15-16] metal organic frameworks (MOFs),[17-18] and covalent organic frameworks (COFs)[19] have been developed to store hydrogen as a compressed gas or as a cryogenic liquid.[12]

Currently, around 500 billion cubic meters per year (≈44.5 million tons) of hydrogen gas is produced by several pathways including steam methane reforming (SMR),[20-21] water electrolysis (WE),[11-12, 22]

photochemical or photoelectrochemical (PEC) water splitting,[23] coal gasification (CG),[12, 24] decomposition of hydrazine and formic acid.[12, 25] Now a days, more than 95% of total hydrogen is being generated by using already established technologies like steam methane reforming (SMR) and coal gasification (CG), while only 4% of the hydrogen is generated by water electrolysis.[12] Evidently, conventional hydrogen production (SMR & CG) methods are strongly reliant on the burning of fossil fuels (methane gas and coal) at high temperature, which are adding more greenhouse gases to the environment. Secondly, the hydrogen obtained from these methods contains CO_2 as an impurity, which reduces the durability, efficiency and poisons the noble metals (Pt, Ru, Pd) based electrocatalysts used in fuel cell technology. Therefore, we would not achieve our main objective "green energy and environment" if remain dependent on present conventional hydrogen production technologies. Hydrogen production by decomposition of alkali and alkaline reactive metal hydrides, borohydrides ($NaBH_4$, $LiBH_4$ etc.) or ammonia –boranes are other alternative rapid ways to generate H_2 in huge quantity or instant demand, but the toxicity and cost of these materials are big issues. Especially metal's hydride/borohydride producing via fine chemical industries cause the environmental pollution, therefore, these are not greener way to produce hydrogen gas at large scale.[26] The limitations of each H_2 production technology are summarized in **Table 1.1**.

Table 1.1. Main technologies for hydrogen production and their limitations

H_2 production Technology	Reactions	Limitations
Steam methane reforming (SMR)	1. $CH_4 + 2H_2O\ (steam) \xrightarrow{\Delta} 4H_{2\,(g)} + CO_{2\,(g)}$	• High temperature, • Impure H_2 gas • Greenhouse gases (CO_2, NO_x, SO_x, other particulates matters), • Environmental pollution & • Cost and depletion of natural sources
Coal gasification (CG)	1. $C + 2H_2O\ (steam) \xrightarrow{\Delta} 2H_{2\,(g)} + CO_{2\,(g)}$	
Metal (Alkali/Alkaline) hydride/borohydride (MH)	1. $MH_{(s)} + H_2O \xrightarrow{\Delta} H_{2\,(g)} + M(OH)_{(s)}$ 2. $MH_{2\,(s)} + H_2O \xrightarrow{\Delta} H_{2\,(g)} + M(OH_2)_{(s)}$	• Low mass energy density, • Low quantity of H_2 release (maximum 8%) • Very heavy and expensive • Storage tank is much larger than gasoline tank with same amount of energy contents • Only pure hydrogen can be stored in the storage tank
Solar-hydrogen conversion (SHC)	1. Photo-chemically 2. Photo-electrochemical	• System efficiency and durability • Immature technology (still at conceptual stage) • Limited photoactive materials • Commercial viability due to low H_2 production capacity
Other renewable energy sources	1. Biomass conversion 2. Thermolysis (using solar heat)	
Electrochemical water splitting (EC)	1. $2H_2O \xrightarrow{Electricity} 2H_{2\,(g)} + O_{2\,(g)}$	• Cost of electricity • Expensive noble metals (Pt, Ru or Ir) based electrocatalysts • Durability and system efficiency

Amongst above all hydrogen production processes, the water electrolysis is the best solution to overcome pollution problems and only possible way to generate hydrogen in a sustainable way, because

of abundancy of its feedstock "water". But this method is still facing many challenges like high cost of electricity and highly efficient noble metal-based (Pt, Ir or Ru) electrocatalysts. In fact, the electricity issue could be resolved by producing it via cost effective solar-, wind- or other renewable technologies, which are being popular in worldwide especially in Japan, Germany, District of Columbia, China, Europe and the United States (US).[27] Japan remained dominant in filing the cumulated energy related patents in past, but since last decade the US and China have published roughly 60% of renewable energy and 60% of all energy patents annually.[27] China and Germany have set their targets to generate 15 and 35% electricity through renewables by 2020, respectively. The developed nations will require to meet 75–100% of their energy needs with renewable sources by 2050. The United States (US), 29 states and the District of Columbia have already adopted these renewable energy portfolio standards which needs for installation of renewable energy.[27] This trend will be helpful in providing a strong foundation for water electrolysis to sustained hydrogen production. During the low energy demand timing such as at the night time or working hours, the energy produced by wind or solar could be stored in the form of hydrogen or can directly be used to split water for hydrogen and oxygen.[12]

Water electrolysis reaction is usually conducted by three common methods i) photochemical, ii) photoelectrochemical and electrochemical. Although, the hydrogen production by using direct solar energy based on photo- or photo-electrochemical is the greenest and sustainable way for water electrolysis. However, the quantity of hydrogen generated even after many days would still be much less than 100 mL in volume.[28-29] Secondly, the direct solar-to-hydrogen conversion is still at developing stage and could be opted for large scale H_2 production in future as the rapid advancement in this technology. Due to these limitations, currently, this approach also could not be adopted at commercial scale for hydrogen production, despite it is being ecofriendly. Amongst all water electrolysis processes, the electrochemical water splitting is the only available greener, sustainable and rapid route of generating highly pure H_2 at commercial scale. Towards this end, the researchers and scientists have already been explored the precious metal-free (Pt, Ir, Ru) hydrogen and oxygen evolution electrocatalysts in the last decade.[2-3, 12] Fortunately, a lot of earth abundant nanostructured electrocatalysts including transition metal's alloys, carbides, phosphides, chalcogenides (sulfides, selenides, tellurides), borides, nitrides, oxides and hydroxides have been developed especially with the help of advanced nanoscience and nanotechnology and most of them displayed noble metal like performances and stability in both acidic and basic electrolytes.[12, 30-34]

1.1 Electrochemistry of water electrolysis

As displayed in **Figure 1.1a**, the electrolyzer cell comprises on four parts, anode, cathode, electrolyte (H_2O) and gas separating membrane (diaphragm). The anode and cathode is coated with oxygen and hydrogen evolving electrocatalysts, respectively. When both electrodes are connected with external

voltage source (e.g. battery), the water electrolysis started without any delay by generating hydrogen bubbles at cathode and oxygen at anode. The ions conductive membrane prevents the mixing of both gases and allows the ions for continuous electrolysis. Both pure gases are collected and stored for further applications. The overall water splitting is divided into two half-cell reactions: the hydrogen evolution reaction (or water reduction reaction) and oxygen evolution reaction (water oxidation reaction) as shown in **Figure 1.1**. As water has poor proton conductivity, therefore, the water electrolysis is usually being conducted in aqueous acidic, alkaline or phosphate buffer solutions. According to electrolyte, the water electrolysis follow different mechanisms as explained in two half-cell reactions in **Figure 1.1b**. Whatever the electrolyte, the water splitting requires thermodynamic voltage of 1.23 V at 25 °C and 1 atm. However, practically more overvoltage is needed than theoretical value (1.23 V at STP) to start water electrolysis because of intrinsic activation barriers, solution and contact resistances offers to HER and OER. Potential requires more than 1.23 V is termed as overpotentials and denoted as eta (η). The hydrogen and oxygen evolution reaction thermodynamically requires 0.0 and 1.23 V in overall water splitting. The overpotential more than these values are calculated by subtracting 0.0V for HER (η_{HER} = E-0) and 1.23 V for OER (η_{OER} = E-1.23). Therefore, the practical operational voltage (E_{OP}) for water electrolysis could be calculated as in **Eq. 1.1**:[12]

$$E_{OP} = 1.23\ V + \eta_{HER} + \eta_{OER} + \eta_{others} \qquad (1.1)$$

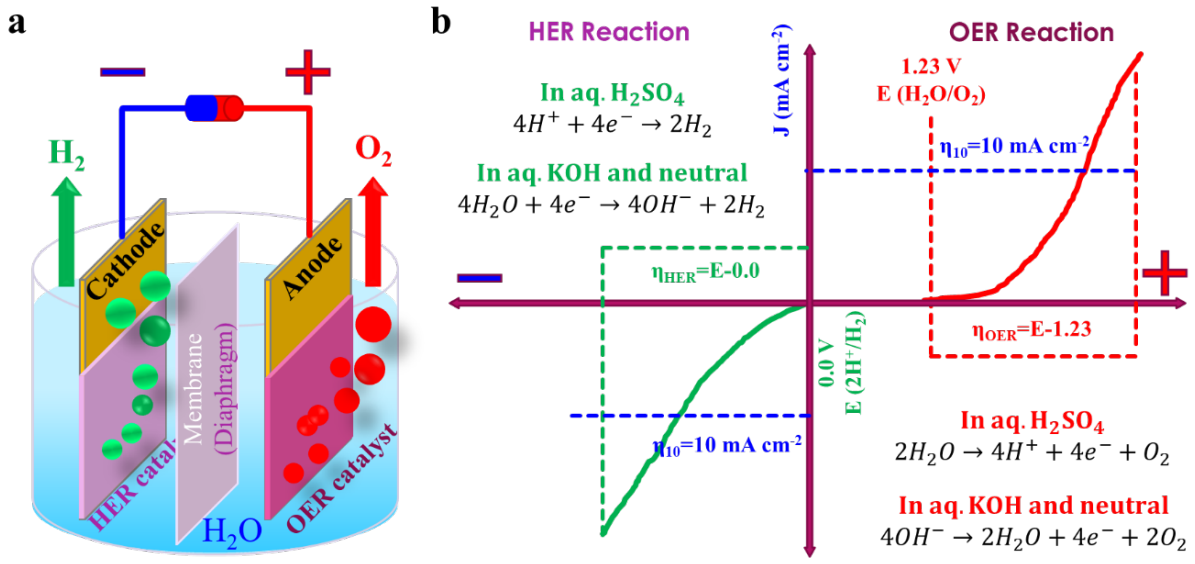

Figure 1.1. Schematic diagram of (a) a typical electrolyzer cell and (b) reaction mechanisms for two half-cell reactions: HER (left) and OER (right) in acidic, aqueous and neutral media.

From the **Eq. 1.1** it is clear that the operational voltage could be reduced by minimizing the internal cathodic (η_{HER}), anodic (η_{OER}) and other (η_{others}) energy barriers. The η_{others} can be reduced by optimizing the design of electrolyzer like reducing the distance between anode and cathode, by increasing the conductivity of electrolyte or increasing solution temperatures. However, the η_{HER} and η_{OER} could only

be minimized by developing efficient electrocatalysts for both hydrogen and oxygen evolution reactions. So for Pt and Ir/Ru based electrocatalysts are used as standards for HER and OER respectively. Therefore, developing other transition metal based electrocatalysts are necessary for economical water splitting for sustainable hydrogen energy.

1.1.1 Reaction mechanisms for hydrogen (HER) and oxygen evolution reaction (OER)

As discussed earlier, both HER and OER follow different paths in acidic and alkaline media. Generally, HER is a typical two electron transfer reaction which usually follow three common reaction steps in both electrolytes named as: i) Volmer (VS), ii) Heyrovsky (HS) and iii) Tafel (TS). The scientists are agreed on reaction mechanism in acid but there is still ambiguity on HER mechanism in alkaline media.[12] As displayed in **Figure 1.2**, the Volmer (VS) and Heyrovsky reaction steps (HS) differ in both media while the recombination of two adsorbed protons (H*) to form molecular hydrogen i.e. Tafel reaction is same. Proton (H+) first discharge at the catalyst surface by taking electron from it to become adsorbed proton (H*) as shown in **Figure 1.2a**. In second step it either react with aqueous proton through HS or combine with other adjacent H* via TS to form dihydrogen molecule. In alkaline, firstly water dissociate into aqueous hydroxyl anion (OH^-) and adsorbed proton (H*) in Volmer step, then it either take proton from water (HS) or follow the same Tafel step as in acid as displayed in **Figure 1.2b**.

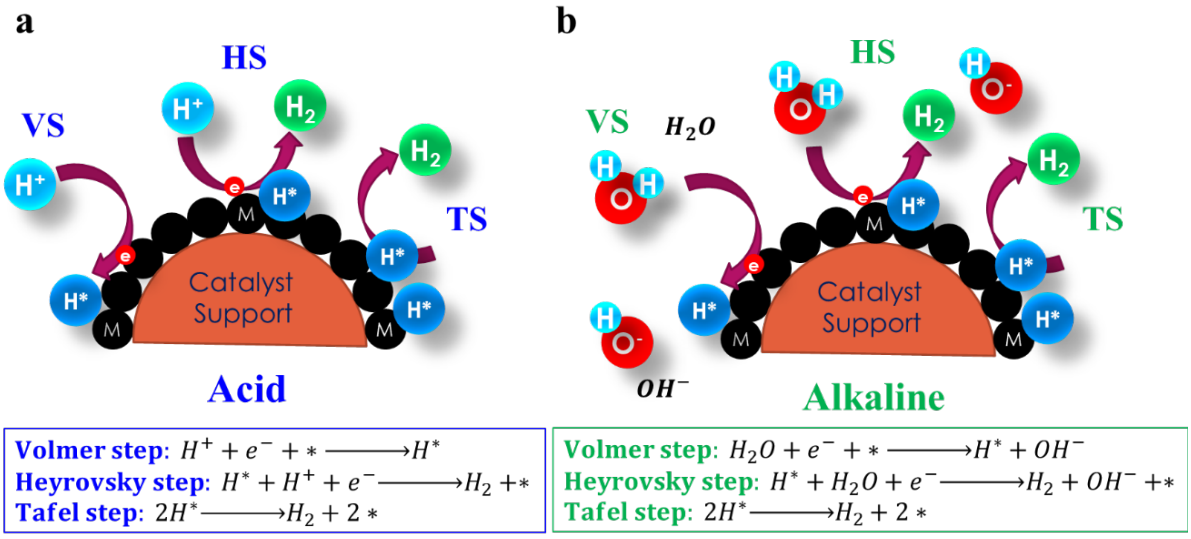

Figure 1.2. HER mechanism in (a) acidic and (b) alkaline or neutral media

From the above discussion, it is revealed that the rate of the overall reaction is greatly dependent on first hydrogen adsorption (Volmer) step. The free energy of hydrogen adsorption (ΔG_H) is the best descriptor of this Volmer step and is calculated by density functional theory (DFT). If ΔG_H is more positive, the hydrogen strongly adsorbed at the surface making the HS/TS difficult. Conversely, if it is more negative then hydrogen bounds to the surface too weakly and it will slow down the Volmer step that will limit the overall reaction rate (TOF). Therefore, the value of ΔG_H should be equal or near to

zero just like in Pt for any best performing non-Pt electrocatalysts, it should bound reaction intermediates neither too strongly nor too weakly.[12, 35]

There are many mechanisms for OER like John Harrison's oxide/electrochemical oxide,[36] Krasil'shchkov,[37] Wade and Hackerman's path,[38] Yeager,[26, 37] Bockris's path[37] in both acidic and alkaline solutions and still it is widely discussed in scientific community during last few decades. Among all of them, the oxide path and electrochemical oxide path proposed by John Harrison are the widely used in the electrochemical water splitting. The possible reaction mechanism of OER in both electrolytes are described in **Table 1.2**.

Table 1.2. Possible reaction mechanisms of the oxygen evolution reaction on metal oxides/hydroxides as reported in literature.[26, 37]

Oxide path	
Acidic solutions	Alkaline solutions
1. $S + H_2O \rightarrow H^+(aq.) + e^- + S-OH$ 2. $2S-OH \rightarrow S-O+S+H_2O$ 3. $2S-O \rightarrow 2S + O_2\,(g)$	1. $S + OH^-(aq.) \rightarrow e^- + S-OH$ 2. $2S-OH \rightarrow S-O+S+H_2O$ 3. $2S-O \rightarrow 2S + O_2\,(g)$
Electrochemical oxide path	
1. $S + H_2O \rightarrow H^+(aq.) + e^- + S-OH$ 2. $S-OH \rightarrow S-O+H^+(aq.)+e^-$ 3. $2S-O \rightarrow 2S + O_2\,(g)$	1. $S + OH^-(aq.) \rightarrow e^- + S-OH$ 2. $S-OH+OH^-(aq.) \rightarrow S-O+H_2O+e^-$ 3. $2S-O \rightarrow 2S + O_2\,(g)$
Krasil'shchkov path	
1. $S + H_2O \rightarrow H^+(aq.) + e^- + S-OH$ 2. $S-OH \rightarrow S-O^- + H^+(aq.)$ 3. $S-O^- \rightarrow S-O+e^-$ 4. $2S-O \rightarrow 2S + O_2\,(g)$	1. $S + OH^-(aq.) \rightarrow e^- + S-OH$ 2. $S-O^- \rightarrow S-O+e^-$ 3. $2S-O \rightarrow 2S + O_2\,(g)$
Wade and Hackerman's path (Acid only)	
1. $2S + H_2O \rightarrow H^+(aq.) + 2e^- + S-O+S-H_2O$ 2. $S-O+2S-OH^- \rightarrow 2S+S-H_2O+O_2\,(g)$	
Yeager's path (alkaline)	**Bockris path**
1. $S + OH^-(aq.) \rightarrow e^- + S-OH$ 2. $S^z-OH \rightarrow S^{z+1}-OH+S+e^-$ 3. $S^{z+1}-OH+2OH^-(aq.) \rightarrow 2S+H_2O+O_2\,(g)$	1. $S + OH^-(aq.) \rightarrow e^- + S-OH$ 2. $S-OH+OH^-(aq.) \rightarrow S-H_2O_2+e^-$ 3. $S-H_2O_2+OH^-(aq.) \rightarrow S-O_2H^-+H_2O$ 4. $S-H_2O_2+S-O_2H^- \rightarrow 2S+2OH^-(aq.)+O_2\,(g)$

1.2 Electrochemical characterization parameters for HER and OER

The catalytic HER/OER performances for a specific electrocatalyst are usually determined by some important and critical parameters those mainly include total electrode (anode/cathode) activity, Tafel analysis, a long-term durability, Faradic efficiency, electrochemical surface areas (ECSA), impedance analysis, the number of active sites as well as turnover frequency (TOF).

1.2.1 Electrode activity

The total electrode activity for both HER and OER is measured either by cyclic voltammetry (CV) or linear scan voltammetry (LSV). To avoid the addition large capacitive currents to a specific reaction, all measurements (CV/LSV) are generally conducted at low sweeping rates (usually 5 mVs^{-1}). The obtained currents then normalized either to geometric surface area or mass of the active material loaded on the electrode for a specific reaction. Generally, two potentials are considered, one at which HER/OER reaction starts and other where the cathodic/anodic currents are high enough to see the gas bubbles. The former is called "onset potential" and generally defined at current densities between 0.5-2 mA cm^{-2}. The second is "overpotential (η)" the extra/additional potential required to drive a HER/OER reaction in sustainable way than its reversible potential. The overpotential more than these values are calculated by subtracting 0.0V for HER (η_{HER} = E-0) and 1.23 V for OER (η_{OER} = E-1.23) as already described in **Figure 1.1b**. The overpotential (η_{10} & η_{100}) at current densities of 10 and 100 mA cm^{-2} is generally compared to specify the HER/OER activity for a given electrocatalysts.[12, 26] Mostly, these overpotentials are reported after iR_s compensation as in **Eq. 1.2** & **1.3**, here R_s is the series/solution resistance and generally determined by electrochemical impedance spectroscopy (EIS) analysis.

$$\eta_{HER}\ (iR_s\ compensated) = E_{HER} - 0.0\ V - iR_s \qquad (1.2)$$

$$\eta_{OER}\ (iR_s\ compensated) = E_{OER} - 1.23\ V - iR_s \qquad (1.3)$$

1.2.2 Tafel analysis

Tafel analysis is generally used to predict mechanism and kinetics of electrocatalytic reaction at the electrode-electrolytes interface. The two critical parameters i.e. Tafel slopes and exchange current densities (J_0) at zero overpotential are derived from the Tafel plot. The Tafel slope reveals the reaction path way while J_0 tells how the reaction kinetic is fast. The Tafel plot actually is a relationship between overpotential (η) and logarithmic values of the current density (J) and can be determined by famous Butler–Volmer equations for HER (**Eq. 1.4**) and OER (**1.5**) as follows.[26, 39]

$$\ln J_C = J_0 + \left(^{-\alpha_C nRF}/_{RT}\right)\eta \qquad (1.4)$$

$$\ln J_A = J_0 + \left(^{\alpha_A nRF}/_{RT}\right)\eta \qquad (1.5)$$

Generally, it is denoted with linear equation (y = b + mx), here "m" is Tafel slope and b is exchange currents can be calculated from y-intercept linear line between η and log (J). The Tafel slopes can also be determined by linear relationship between iR_s-corrected overpotential and of log ($1/R_{ct}$) determined are various overpotentials by EIS.[26, 33] If the Tafel slope is in between 30 to 40 mV dec^{-1}, the HER

reaction follow the Volmer-Tafel path if more than 40 then Volmer-Heyrovsky is the preferred mechanism.

1.2.3 Electrocatalyst stability

The durability of any catalysts for any electrochemical reaction is and critical parameters for commercialization of water electrolysis system. The stability for HER/OER is usually determined by accelerated voltammetry cycles (more than 5000 cycles) or constant voltage (chronoamperometry, CA) or constant current (chronopotentiometry, CP) at least for 10 hours. Generally, I/E *vs* t measurements are conducted at higher current densities. A current density of 10 mA cm^{-2} is frequently selected in such electrolysis, because this value is considered as standard in both HER, OER and solar fuel synthesis.[33]

1.2.4 Hydrogen bonding energy

The standard Gibbs free energy of hydrogen bonding (ΔG_H) is always calculated through density functional theory (DFT) and it should be close to zero for any best HER electrocatalyst. Sabatier Volcano plot of exchange current density vs. ΔG_H is generally used to determine the HER/OER activity of a catalysts. Any electrocatalyst having the value closer to plateau of Sabatier Volcano plot displays better performances for HER, OER or other electrochemical reactions.[30, 33, 35]

1.2.5 Faradic efficiency

It describes the efficiency with how many of the provided electrons by external circuits are driving desired HER/OER reaction in an electrochemical water splitting. The Faradic efficiency of any desired reaction is the ratio between the experimentally generated H_2/O_2 amount to the theoretical determined H_2/O_2 amount. The theoretical produced H_2 value can be estimated by integration of galvanostatic or potentiostatic electrolysis while the practical hydrogen generated can be determined by gas chromatography (GC) or a water–gas displacing method.[12, 33]

1.2.6 Number of active sites and turnover frequency (TOF)

TOF of an electrocatalyst for any electrochemical process is another critical and kinetic parameter which reveal that how many number of active sites of a catalysts are taking part in catalyzing the desired electrochemical reaction per unit time. However, in heterogeneous catalysis, it is hard to find the actual number of active sites and TOF. The **Eq. 1.6** is generally used to determine the turnover frequency for both HER and OER.[26]

$$TOF = J \times {}^{N_A}/_{n} \times F \times \Gamma \qquad (1.6)$$

Here, *J* is cathodic/anodic current density (A cm^{-2}), N_A is the Avogadro number, the factor $1/n$ is the number of electrons consumed to produce a molecule of gas (in case of H_2: $1/2$ and for O_2, it is $1/4$), *F* is the Faraday constant (96,485 C) and Γ stands for number active sites or participating atoms in electrolysis. In case of HER, some researchers used all atoms of the material as active sites which is totally inaccurate approach because all atoms are not accessible to drive the HER reaction.[12, 26] However, some people find the active sites by CO-stripping, hydrogen under potential deposition (H-UPD), metals-UPD (e.g. Ag, Cu) or peroxide oxidation, etc. Unfortunately, all these methods have their own limitations or applicable to noble metal (Pt, Ru, Ir etc.) based electrocatalysts only. In case of OER, the redox features of transition metals (Co, Ni etc.) could be useful to determine surface concentrations of atoms which are driving the OER reaction.[26]

1.2.7 Electrochemical active surface area (ECSA)

It is actually exposed area of an electrocatalytic material at the electrode-electrolyte interface and generally determined from the double layer capacitance (C_{dl}) of the electrocatalysts. The C_{dl} is measured by performing the CV cycles at various scan rates in the non-Faradaic region. The difference of both anodic and cathodic currents ($\Delta J = J_a - J_c$) is plotted verses scan rates, the slope of this line gives the double layer capacitance. The specific capacitance for a flat surface is generally found to be in the range of 20-60 µF cm^{-2}. The **Eq. 1.7** is being used for ECSA by generally assuming 40 µF cm^{-2}. Specific capacitance for a flat electrode.

$$A_{ECSA}^{Catalyst} = \frac{C_{dl}^{Catalysts}\ (mF.cm^{-2})}{40\mu F.cm^{-2}\ per\ cm_{ECSA}^{2}} = Value^{Catalyst}\ cm_{ECSA}^{2} \qquad (1.7)$$

1.2.8 Electrochemical impedance spectroscopy (EIS) analysis

Electrochemical Impedance Spectroscopy (EIS) is useful tool to determine charge transfer and transport processes occurring at electrocatalysts-electrolyte interface or inside the material. As displayed in Figure 1.3, the EIS Nyquist plots used to determine series resistance for iR_s compensation, the diffusion or Warburg resistance (R_d) offered to ions and finally charge transfer resistance (R_{ct}) at the interface. The first time constant at high frequency is related to the surface porosity (R_d) of the materials and second one at low frequency corresponds to the charge transfer process (R_{ct}) at electrode.

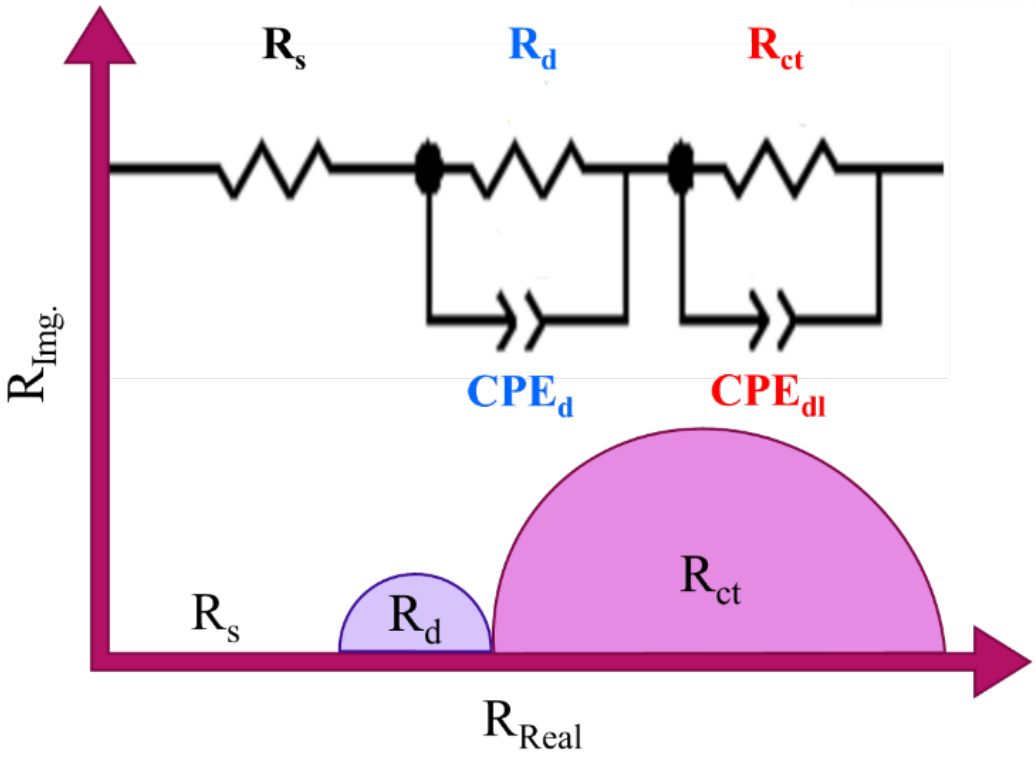

Figure 1.3. EIS Nyquist plot to determine the series (R_s), diffusion (R_d) and charge transfer (R_{CT}) resistances and their equivalent circuit model.

1.3 Electrocatalysts development strategies

The electrolysis of water to generate hydrogen and oxygen in a sustainable way is one of the "holy desire" but remains deceptive target in electrocatalysis and renewable energy technology.[2, 5, 40] This elusive goal has been unachieved so for mainly because of unavailability of more efficient non-precious metals to replace the most common incumbent noble-metal-based materials (Pt and Ir/Ru) for the hydrogen evolution reaction (HER) and oxygen evolution reaction (OER) in electrochemical water slitting.[12, 34-35, 41] The field of electrocatalysis has observed much advancements since last few decades, as affirmed by rapidly increase in number of research articles on this topic. To improve the water slitting efficiency by reducing the overpotentials of two half-reactions, a lot of cheaper earth-abundant materials have been explored for HER[2, 11-12, 30] and OER.[2, 31-32, 42] The transition metals including Mo, W, Ti, Co, Ni, Fe, Cu and their compounds with nonmetals e.g. C, N, B, O, P, S, Se and Te have been extensively investigated to replace noble metal based (Pt, Pd, Ir, Ru) electrocatalysts for both HER and OER. Among them Mo, Co, Ni and Fe compounds like phosphides, carbides, sulfides and oxides got much attraction in field of water electrolysis due to their noble metal like electrochemical properties.[3, 12, 31-32]

It is very important to consider the abundance and cost factor while designing or developing a non-noble metal HER/OER electrocatalyst for a sustainable and economically viable water electrolysis.

methods of preparation. Additionally, the selected material and its synthesis method should be low-cost, environmentally friendly and based on highly scalable procedures. Furthermore, one could avoid the additional recycling process for the economically and ecofriendly electrocatalysts at the end of their lifetime, as is commonly required for precious noble metals containing electrocatalysts. Similarly, the selection of electrocatalyst supports is also very important, it must be cheapest and able to enhance the electrochemical performances through maximizing the conductivity, electrochemical surface area (ECSA) and effective mass/charge transport during electrolysis. Uniform grafting of nanomaterials onto highly conductive and cheaper substrates like graphite (graphene, CNTs), carbon (porous carbon, carbon paper or carbon cloth) or metallic foams (such as Ni, Co or Cu foam) would be better choice to reduce large overpotentials and enhance stabilities of the electrocatalysts.[30]

By increasing the number of active sites of a desired electrocatalyst is also another effective strategy to enhance overall water splitting system efficiency and to control the cost. This could be achieved by coupling of active material with conductive supports (GO, CNTs etc.), making the 0D,1D, 2-D or 3D nanostructures (like, quantum dots, nanowires, nanosheets, nanoparticles, or mesoporous structure), controlling shape (cubic, octahedral, trigonal etc.) of the nanoparticles or high-loading of the catalyst amount to expose the more surface active sites per unit mass or area.[35] The other possible way is to increase the intrinsic catalytic activity of the material through making nano-alloys, core-shell structures, structural defects, polymorph, heteroatom doping or intercalations. By maximizing intrinsic activity, we can decrease the loading of the catalysts which also mitigate the mass transport problems coming from high mass loadings which also leads to direct decrease in cost and enhance the electrode activity more than 10 times of magnitude. However, high-loading of catalyst could only give 1 to 3 times higher performances as compared to low mass loading.[35]

1.4 Objectives and motivations

The challenge in electrochemical water splitting is to replace the noble metals (Pt, Ru or Ir) with inexpensive non-precious metal electrocatalysts. Transition metal compounds (TMCs) such as phosphides, carbides and chalcogenides have attracted massive attention since last few years due to their superior electrical conductivity, mechanical strength, and chemical stability. They have been proven to be high performance electrocatalysts with good activity, high stability, and nearly ≈100% Faradic efficiency in acidic, alkaline and neutral media for HER and OER. In spite of the success of TMCs as good electrocatalysts for water slitting, there are still many challenges like poor performance, stability in wide pH range, expensive and poisonous starting precursors, environmentally unsafe synthetic procedures, lack of in-depth mechanistic knowledge and so on which are creating hurdles for sustainable hydrogen production with both economic and environmental advantage.

The main objective of this work is to increase the number of active sites and intrinsic activity of transition metals carbides, phosphides and sulfides through the knowledge of material chemistry, nanoscience and nanotechnology. Moreover, development and designing of simple, economical, ecofriendly and commercially viable synthesis procedures for preparation of transition metal phosphides, carbides, sulfides and their grafting on conductive substrates (like doped-graphene, carbon cloth, nickel foam etc.) for electrochemical water splitting.

1.5 Research theme and achievements

The **second chapter** is focused on the tuning of electrochemical properties of five different phases of molybdenum carbides by encapsulating carbides NPs with boron (B) and nitrogen (N) co-doped carbon shell (BCN) via a unique organometallic complex-assisted approach. The BCN network protected multiple phases of mesoporous molybdenum carbide displayed high electrochemical active surface area, reduced charge transfer resistances and improved wetting properties. Due to the synergic effect of BCN shell, all phases of molybdenum carbides showed a remarkable electrocatalytic HER performance and durability in both acidic and basic aqueous defeating the most of earlier reported molybdenum carbides based electrocatalyst in the literature. The mechanistic study for HER over BCN encapsulated molybdenum carbides is also being discussed in detail.

In **third Chapter**, the electronic structure of most stable and active β-Mo_2C was modulated by boron and nitrogen co-doping. The dramatic increment in the HER, OER and ORR performances were observed especially in alkaline media. The B and nitrogen co-doped β-Mo_2C also displayed exceptional stability for HER and OER in aqueous 1.0M KOH. The mechanism of overall water splitting at B, N: Mo_2C@BCN is also described in alkaline media.

The novel and ecofriendly general synthesis procedure for transition metal phosphides is first time presented in **Chapter 4**. The intrinsic catalytic activity stability of molybdenum phosphides nanocrystallite (MoP) are tuned by dual-doping of S and N into its structure via a unique, inexpensive and environmental-friendly (thio)urea-phosphate-assisted rout. The number of active sites are also increased by controlling the shape of nanoparticles and loading them on S, N self-doped graphene. The obtained MoP/SNG catalysts displayed extraordinary hydrogen evolution performance in both acidic and alkaline media.

Mono cobalt phosphide (CoP) and di-cobalt phosphide nanoparticles are also prepared by adopting the above eco-friendly synthetic approach. The intrinsic electrocatalytic HER and OER performance of CoP is enhanced by doping of sulfur (S) into its structure and is being discussed in **Chapter 5**. Similarly, the electrochemical properties of metallic cobalt phosphides (Co_2P) are also modulated by same approach as in CoP. The mechanism of overall water spitting at S-doped Co_2P and change in its

electronic structure after S-doping is also investigated by experimental and theoretical methods in **Chapter 6**.

Theoretical and experimental studies reveal that the Mo ($10\bar{1}0$) edge of molybdenum sulfide (MoS_2) is most active site with about 50% hydrogen coverage and low hydrogen binding energy ($\Delta G_H \approx 0.08$ eV) closer to ideal value of 0 eV for HER. But its basal plane shows poor performance due to possessing high hydrogen binding energy i.e. 1.92 eV.[35] To this end, ample efforts have been devoted to improve the catalytic activity of MoS_2 by converting 2H to 1T phase through chemical exfoliation,[43] increasing the number of active sites through engineering its nanostructure such as vertically aligned nanofilms[44] and double-gyroid mesoporous films[45], creating sulfur vacancies and defects through thermal treatment,[46-49] introducing various chemical compositions such as amorphous MoS_x films,[50-51] dimeric $[Mo_3S_{13}]^{2-}$ clusters,[52] and metal-doped MoS_3,[53] compounding with conductive substrates (e.g. carbon nanotubes, Au, graphene, etc.)[54-57] and expanding the interlayer spacing through microwave-assisted solvothermal reduction of $(NH_4)_2MoS_4$[58-60] or trapping of foreign species into the MoS_2 sheets.[60-61] However, all these efforts are exercised either by using expensive, corrosive and dangerous chemicals or following the environmentally unsafe synthetic procedures. Due to low output of active sites in MoS_2 and environmental concerns, the above method could not be opted for large scale applications.

A simple strategy is presented in **Chapter 7** to synthesize MoS_2 with multiple active sites such as defects, S-deficiency, Mo-exposed edge, and expanded interlayer spacing by hydrothermal reaction using supramolecular melamine-phosphomolybdate (MA-PMo_{12}) and thiourea as precursors. During the hydrothermal reaction, *in-situ* generated NH_3 molecules were intercalated into MoS_2 sheets with an interlayer spacing of 8.4 Å, and 1T phase MoS_2 (71%) was dominantly observed (A-MoS_2). The further defects and S-vacancies in A-MoS_2 (R-MoS_2) were generated by removing intercalated NH_3 and H_2S through thermal annealing in hydrogen gas at 500 °C. Edge-terminated and interlayer-expanded MoS_2 structures in R-MoS_2 after the thermal reduction remained, and the fraction of 1T phase was still considerable (33.7%). The hybrids of R-MoS_2 with reduced graphene oxide and nickel foam (R-MoS_2/NG and R-MoS_2/NF) displayed remarkable hydrogen evolution reaction (HER) in alkaline media. Being environmentally safe and cheaper precursors used in this approach, could be opted for commercial production of metallic (1T) or defective MoS_2 for electrochemical applications.

1.6 References

1. Teske, S.; Sawyer, S.; Schäfer, O.; Pregger, T.; Simon, S.; Naegler, T.; Schmid, S.; Özdemir, E. D.; Pagenkopf, J.; Kleiner, F., Energy [r] evolution-a sustainable world energy outlook 2015. **2015**.

2. Roger, I.; Shipman, M. A.; Symes, M. D., Earth-abundant catalysts for electrochemical and photoelectrochemical water splitting. *Nat. Rev. Chem.* **2017,** *1*, 0003.

3. Jiao, Y.; Zheng, Y.; Jaroniec, M.; Qiao, S. Z., Design of electrocatalysts for oxygen-and hydrogen-involving energy conversion reactions. *Chem. Soc. Rev.* **2015,** *44* (8), 2060-2086.

4. Arico, A. S.; Bruce, P.; Scrosati, B.; Tarascon, J.-M.; Van Schalkwijk, W., Nanostructured materials for advanced energy conversion and storage devices. *Nat. Mater.* **2005,** *4* (5), 366.

5. Chu, S.; Cui, Y.; Liu, N., The path towards sustainable energy. *Nat. Mater.* **2017,** *16* (1), 16-22.

6. Bashyam, R.; Zelenay, P., A class of non-precious metal composite catalysts for fuel cells. *Nature* **2006,** *443* (7107), 63-66.

7. Wang, Y.; Kong, B.; Zhao, D.; Wang, H.; Selomulya, C., Strategies for developing transition metal phosphides as heterogeneous electrocatalysts for water splitting. *Nano Today* **2017,** *15*, 26-55.

8. Chu, S.; Majumdar, A., Opportunities and challenges for a sustainable energy future. *Nature* **2012,** *488* (7411), 294.

9. Zeng, K.; Zhang, D., Recent progress in alkaline water electrolysis for hydrogen production and applications. *Prog. Energy Combust. Sci.* **2010,** *36* (3), 307-326.

10. Kirubakaran, A.; Jain, S.; Nema, R., A review on fuel cell technologies and power electronic interface. *Renew Sustain Energy Rev.* **2009,** *13* (9), 2430-2440.

11. Mahmood, N.; Yao, Y.; Zhang, J. W.; Pan, L.; Zhang, X.; Zou, J. J., Electrocatalysts for Hydrogen Evolution in Alkaline Electrolytes: Mechanisms, Challenges, and Prospective Solutions. *Adv. Sci.* **2018,** *5*, 1700464.

12. Zou, X.; Zhang, Y., Noble metal-free hydrogen evolution catalysts for water splitting. *Chem. Soc. Rev.* **2015,** *44* (15), 5148-5180.

13. Sakintuna, B.; Lamari-Darkrim, F.; Hirscher, M., Metal hydride materials for solid hydrogen storage: a review. *Int. J. Hydrog. Energy.* **2007,** *32* (9), 1121-1140.

14. Ngene, P.; Longo, A.; Mooij, L.; Bras, W.; Dam, B., Metal-hydrogen systems with an exceptionally large and tunable thermodynamic destabilization. *Nat. Commun.* **2017,** *8* (1), 1846.

15. Darkrim, F. L.; Malbrunot, P.; Tartaglia, G., Review of hydrogen storage by adsorption in carbon nanotubes. *Int. J. Hydrog. Energy.* **2002,** *27* (2), 193-202.

16. Sevilla, M.; Mokaya, R., Energy storage applications of activated carbons: supercapacitors and hydrogen storage. *Energy Environ. Sci.* **2014,** *7* (4), 1250-1280.

17. Murray, L. J.; Dincă, M.; Long, J. R., Hydrogen storage in metal–organic frameworks. *Chem. Soc. Rev.* **2009,** *38* (5), 1294-1314.

18. Suh, M. P.; Park, H. J.; Prasad, T. K.; Lim, D.-W., Hydrogen storage in metal–organic frameworks. *Chem. Rev.* **2011,** *112* (2), 782-835.

19. Ding, S.-Y.; Wang, W., Covalent organic frameworks (COFs): from design to applications. *Chem. Soc. Rev.* **2013,** *42* (2), 548-568.

20. Barelli, L.; Bidini, G.; Gallorini, F.; Servili, S., Hydrogen production through sorption-enhanced steam methane reforming and membrane technology: a review. *Energy* **2008,** *33* (4), 554-570.

21. Simpson, A. P.; Lutz, A. E., Exergy analysis of hydrogen production via steam methane reforming. *Int. J. Hydrog. Energy.* **2007,** *32* (18), 4811-4820.

22. Anjum, M. A. R.; Lee, J. S., Sulfur and Nitrogen Dual-Doped Molybdenum Phosphide Nanocrystallites as an Active and Stable Hydrogen Evolution Reaction Electrocatalyst in Acidic and Alkaline Media. *ACS Catal.* **2017,** *7* (4), 3030-3038.

23. Ding, Q.; Song, B.; Xu, P.; Jin, S., Efficient electrocatalytic and photoelectrochemical hydrogen generation using MoS_2 and related compounds. *Chem* **2016,** *1* (5), 699-726.

24. Turner, J. A., Sustainable hydrogen production. *Science* **2004,** *305* (5686), 972-974.

25. Tedsree, K.; Li, T.; Jones, S.; Chan, C. W. A.; Yu, K. M. K.; Bagot, P. A.; Marquis, E. A.; Smith, G. D.; Tsang, S. C. E., Hydrogen production from formic acid decomposition at room temperature using a Ag–Pd core–shell nanocatalyst. *Nature Nanotechnol.* **2011,** *6* (5), 302.

26. Anantharaj, S.; Ede, S.; Karthick, K.; Sankar, S. S.; Sangeetha, K.; Karthik, P.; Kundu, S., Precision and correctness in the evaluation of electrocatalytic water splitting: revisiting activity parameters with a critical assessment. *Energy Environ. Sci.* **2018**, DOI: 10.1039/c7ee03457a

27. Trancik, J. E., Renewable energy: Back the renewables boom. *Nature* **2014,** *507* (7492), 300-302.

28. Hisatomi, T.; Kubota, J.; Domen, K., Recent advances in semiconductors for photocatalytic and photoelectrochemical water splitting. *Chem. Soc. Rev.* **2014,** *43* (22), 7520-7535.

29. Fountaine, K. T.; Lewerenz, H. J.; Atwater, H. A., Efficiency limits for photoelectrochemical water-splitting. *Nature Commun.* **2016,** *7*, 13706.

30. Faber, M. S.; Jin, S., Earth-abundant inorganic electrocatalysts and their nanostructures for energy conversion applications. *Energy Environ. Sci.* **2014,** *7* (11), 3519-3542.

31. Anantharaj, S.; Ede, S. R.; Sakthikumar, K.; Karthick, K.; Mishra, S.; Kundu, S., Recent Trends and Perspectives in Electrochemical Water Splitting with an Emphasis on Sulfide, Selenide, and Phosphide Catalysts of Fe, Co, and Ni: A Review. *ACS Catal.* **2016,** *6* (12), 8069-8097.

32. Wang, J.; Cui, W.; Liu, Q.; Xing, Z.; Asiri, A. M.; Sun, X., Recent Progress in Cobalt-Based Heterogeneous Catalysts for Electrochemical Water Splitting. *Adv. Mater.* **2016,** *28* (2), 215-230.

33. Shi, Y.; Zhang, B., Recent advances in transition metal phosphide nanomaterials: synthesis and applications in hydrogen evolution reaction. *Chem. Soc. Rev.* **2016,** *45* (6), 1529-1541.

34. Suen, N. T.; Hung, S. F.; Quan, Q.; Zhang, N.; Xu, Y. J.; Chen, H. M., Electrocatalysis for the oxygen evolution reaction: recent development and future perspectives. *Chem. Soc. Rev.* **2017,** *46* (2), 337-365.

35. Seh, Z. W.; Kibsgaard, J.; Dickens, C. F.; Chorkendorff, I.; Nørskov, J. K.; Jaramillo, T. F., Combining theory and experiment in electrocatalysis: Insights into materials design. *Science* **2017,** *355* (6321), eaad4998.

36. Bockris, J. O. M., Kinetics of activation controlled consecutive electrochemical reactions: anodic evolution of oxygen. *J. Chem. Phy.* **1956,** *24* (4), 817-827.

37. Fabbri, E.; Habereder, A.; Waltar, K.; Kötz, R.; Schmidt, T. J., Developments and perspectives of oxide-based catalysts for the oxygen evolution reaction. *Catal. Sci. Technol.* **2014,** *4* (11), 3800-3821.

38. Wade, W. H.; Hackerman, N., Anodic phenomena at an iron electrode. *J. Chem. Soc. Faraday Tras.* **1957,** *53*, 1636-1647.

39. Bard, A. J.; Faulkner, L. R.; Leddy, J.; Zoski, C. G., *Electrochemical methods: fundamentals and applications*. Wiley New York: 1980; Vol. 2.

40. Anjum, M. A. R.; Jeong, H. Y.; Lee, M. H.; Shin, H. S.; Lee, J. S., Efficient Hydrogen Evolution Reaction Catalysis in Alkaline Media by All-in-One MoS2 with Multifunctional Active Sites. *Adv. Mater.* **2018**, 1707105.

41. Mahmood, J.; Li, F.; Jung, S.-M.; Okyay, M. S.; Ahmad, I.; Kim, S.-J.; Park, N.; Jeong, H. Y.; Baek, J.-B., An efficient and pH-universal ruthenium-based catalyst for the hydrogen evolution reaction. *Nature Nanotechnol.* **2017,** *12* (5), 441.

42. Xie, L.; Zhang, R.; Cui, L.; Liu, D.; Hao, S.; Ma, Y.; Du, G.; Asiri, A. M.; Sun, X., High-Performance Electrolytic Oxygen Evolution in Neutral Media Catalyzed by a Cobalt Phosphate Nanoarray. *Angew. Chem.* **2017,** *129* (4), 1084-1088.

43. Lukowski, M. A.; Daniel, A. S.; Meng, F.; Forticaux, A.; Li, L.; Jin, S., Enhanced hydrogen evolution catalysis from chemically exfoliated metallic MoS2 nanosheets. *J. Am. Chem. Soc.* **2013,** *135* (28), 10274-10277.

44. Wang, H.; Lu, Z.; Xu, S.; Kong, D.; Cha, J. J.; Zheng, G.; Hsu, P.-C.; Yan, K.; Bradshaw, D.; Prinz, F. B., Electrochemical tuning of vertically aligned MoS2 nanofilms and its application in improving hydrogen evolution reaction. *Proc. Natl. Acad. Sci.* **2013,** *110* (49), 19701-19706.

45. Kibsgaard, J.; Chen, Z.; Reinecke, B. N.; Jaramillo, T. F., Engineering the surface structure of MoS2 to preferentially expose active edge sites for electrocatalysis. *Nat. Mater.* **2012,** *11* (11), 963-969.

46. Wang, D.; Zhang, X.; Zhang, D.; Shen, Y.; Wu, Z., Influence of Mo/P Ratio on CoMoP nanoparticles as highly efficient HER catalysts. *Appl. Catal. A: General* **2016,** *511*, 11-15.

47. Ye, G.; Gong, Y.; Lin, J.; Li, B.; He, Y.; Pantelides, S. T.; Zhou, W.; Vajtai, R.; Ajayan, P. M., Defects Engineered Monolayer MoS2 for Improved Hydrogen Evolution Reaction. *Nano Lett.* **2016,** *16* (2), 1097-1103.

48. Xie, J.; Zhang, H.; Li, S.; Wang, R.; Sun, X.; Zhou, M.; Zhou, J.; Lou, X. W. D.; Xie, Y., Defect-rich MoS2 ultrathin nanosheets with additional active edge sites for enhanced electrocatalytic hydrogen evolution. *Adv. Mater.* **2013,** *25* (40), 5807-5813.

49. Yin, Y.; Han, J.; Zhang, Y.; Zhang, X.; Xu, P.; Yuan, Q.; Samad, L.; Wang, X.; Wang, Y.; Zhang, Z., Contributions of phase, sulfur vacancies, and edges to the hydrogen evolution reaction catalytic activity of porous molybdenum disulfide nanosheets. *J. Am. Chem. Soc.* **2016,** *138* (25), 7965-7972.

50. Tran, P. D.; Tran, T. V.; Orio, M.; Torelli, S.; Truong, Q. D.; Nayuki, K.; Sasaki, Y.; Chiam, S. Y.; Yi, R.; Honma, I., Coordination polymer structure and revisited hydrogen evolution catalytic mechanism for amorphous molybdenum sulfide. *Nat. Mater.* **2016,** *15* (6), 640

51. Morales-Guio, C. G.; Hu, X., Amorphous molybdenum sulfides as hydrogen evolution catalysts. *Acc. Chem. Res.* **2014,** *47* (8), 2671-2681.

52. Kibsgaard, J.; Jaramillo, T. F.; Besenbacher, F., Building an appropriate active-site motif into a hydrogen-evolution catalyst with thiomolybdate [Mo3S13] 2− clusters. *Nat. Chem.* **2014,** *6* (3), 248-253.

53. Merki, D.; Vrubel, H.; Rovelli, L.; Fierro, S.; Hu, X., Fe, Co, and Ni ions promote the catalytic activity of amorphous molybdenum sulfide films for hydrogen evolution. *Chem. Sci.* **2012,** *3* (8), 2515-2525.

54. Shi, J.; Ma, D.; Han, G.-F.; Zhang, Y.; Ji, Q.; Gao, T.; Sun, J.; Song, X.; Li, C.; Zhang, Y., Controllable growth and transfer of monolayer MoS2 on Au foils and its potential application in hydrogen evolution reaction. *ACS Nano* **2014,** *8* (10), 10196-10204.

55. Voiry, D.; Fullon, R.; Yang, J.; e Silva, C. d. C. C.; Kappera, R.; Bozkurt, I.; Kaplan, D.; Lagos, M. J.; Batson, P. E.; Gupta, G., The role of electronic coupling between substrate and 2D MoS2 nanosheets in electrocatalytic production of hydrogen. *Nat. Mater.* **2016,** *15* (9), 1003.

56. Li, Y.; Wang, H.; Xie, L.; Liang, Y.; Hong, G.; Dai, H., MoS2 nanoparticles grown on graphene: an advanced catalyst for the hydrogen evolution reaction. *J. Am. Chem. Soc.* **2011,** *133* (19), 7296-7299.

57. Vrubel, H.; Merki, D.; Hu, X., Hydrogen evolution catalyzed by MoS 3 and MoS 2 particles. *Energy Environ. Sci.* **2012,** *5* (3), 6136-6144.

58. Sun, Y.; Alimohammadi, F.; Zhang, D.; Guo, G., Enabling Colloidal Synthesis of Edge-Oriented MoS2 with Expanded Interlayer Spacing for Enhanced HER Catalysis. *Nano Lett.* **2017,** *17* (3), 1963-1969.

59. Gao, M.-R.; Chan, M. K.; Sun, Y., Edge-terminated molybdenum disulfide with a 9.4-A interlayer spacing for electrochemical hydrogen production. *Nat. Commun.* **2015,** *6*, 7493.

60. Rasamani, K. D.; Alimohammadi, F.; Sun, Y., Interlayer-expanded MoS 2. *Materials Today* **2017,** *20* (2), 83-91.

61. Tang, Y. J.; Wang, Y.; Wang, X. L.; Li, S. L.; Huang, W.; Dong, L. Z.; Liu, C. H.; Li, Y. F.; Lan, Y. Q., Molybdenum Disulfide/Nitrogen-Doped Reduced Graphene Oxide Nanocomposite with Enlarged Interlayer Spacing for Electrocatalytic Hydrogen Evolution. *Adv. Energy Mater.* **2016,** *6* (12), 1600116.

2. BCN-shell Encaged Multiple Phases of Molybdenum Carbide for Effective Hydrogen Evolution Reaction

2.1 Abstract

Various phases of molybdenum carbide protected by boron-carbon-nitrogen (BCN) shell are prepared by thermal decomposition of Mo-imidazole-borate organometallic complex with appropriate alteration in imidazole-borate ligand structure. All phases of molybdenum carbide are conformally protected by BCN network and effectively catalyze the hydrogen evolution reaction (HER) with enhanced stability in both acidic and basic media outperforming most of molybdenum carbides based electrocatalysts reported in the literature. Hexagonal β-Mo_2C@BCN gives consistently most stable performance in all conditions. The less active cubic α and hexagonal η phases also exhibit improved HER performance and stability due to the synergistic effect of BCN encapsulation. The dual electrophilic and nucleophilic nature of BCN shells provide protection to molybdenum carbides nanoparticles from chemical corrosion and aggregation, and enhance their catalytic HER activity by acting as an electron/proton transfer medium because of increased wetting properties.

2.2 Introduction

Due to noble metal-like characteristics, transition metal carbides (TMCs) have drawn great attention as active catalytic materials in the field of catalysis and electrocatalysis.[1-2] Especially their good thermal, mechanical and chemical stabilities in dilute aqueous acidic as well as alkaline media,[3-4] makes them emerging material as efficient catalysts for hydrogen evolution,[5-9] oxygen reduction/evolution,[10-11] water gas shift reactions,[12] lithium[13-14] or sodium ion batteries,[15] and supercapacitors.[16] The insertion of carbon atom into the lattice of transition metals (e.g. Mo, W) causes in the expansion of lattice parameters. In the result of hybridization between metal d-orbitals and s-/p-orbitals of carbon atoms, metal d-band width contracts and degree of electron filling increases,[12, 17-19] which provides more noble metal-like characteristics to TMCs compared to parent transition metals.

Alternatives of most active and expansive Pt based hydrogen evolution reaction (HER) catalysts such as non-precious transition metals or their carbides, sulfides, borides, nitrides, and phosphides have been extensively explored.[20-22] But the catalytic activity and stability of these electrocatalysts are still very low, in this regard, many attempts have been exercised to increase the catalytic performance by making porous structure,[6] nanowires[23] or doping with heteroatoms.[24] The heteroatom doping into the structure of these materials plays a critical role in tuning electrochemical properties and by providing synergistic coupling effect.[24-26] Molybdenum carbides also have been considered as efficient material for catalyzing

HER in both aqueous acidic and basic electrolytes,[6, 9, 21-22] and similar alteration in their structure have already been exercised to improve their catalytic behavior by doping with heteroatoms such as N,[9, 27] S[28][17] or N, S dual doping.[24] Another common effective approach is to make their hybrid composite with single or more elements doped carbon network, which can improve electron/mass transfer characteristics.

Herein, multiple phases of molybdenum carbides wrapped by a few layers of B and N co-doped carbon (BCN) nanostructure are prepared successfully, by carburizing Mo-imidazole-borate organometallic complex in inert atmosphere. The multiple phases such as hexagonal (β, η), orthorhombic (α, β) and cubic (α) molybdenum carbides are synthesized by simply altering the imidazole-borate ligand structure by taking advantage of this unique. These hybrid composites offer reduced charge transfer resistances and enhanced water adsorption properties due to the presence of boron and nitrogen species in carbon network. All phases of molybdenum carbide display an improved catalytic performance and stability in all values of pH defeating most of molybdenum carbides reported in the literature.

2.3 Experimental section

2.3.1 Synthesis of Mo-imidazole-borate organometallic complex

All chemicals were used as purchased without further purification. Imidazole-borate was synthesized by following the previously reported method with slight modification.[29-30] Typically, boric acid (1mmol, 61.83 mg, Sigma-Aldrich) was dissolved in glycerol (10 mL, Junsei) in 3-necked, round-bottom flask (250 mL) equipped with a reflux condenser, a magnetic stir bar, and a thermocouple. The reaction mixture was heated to a temperature of 100 ^{0}C until the clear solution was obtained and was maintained at this temperature for 2 h. After cooling down to 50 ^{0}C, a solution of imidazole (5 mmol, 340.4 mg) in ethanol (Sigma-Aldrich) was poured gradually. The reaction mixture was again heated slowly to remove excess water and ethanol, and then allowed to cool after the light yellow color appeared. For the synthesis of Mo based organometallic complex, the Mo(V) chloride (1 mmol, 273.2 mg, Sigma-Aldrich) was dissolved in equal volume (20 mL) of 3 % aqueous acetic acid and ethanol under continuous stirring for 1 h. Then, this freshly prepared solution was poured gradually into the above imidazole-borate monomeric solution by adjusting pH<4 with the 3 % acetic acid and heated slowly to 90 ^{0}C then 130 ^{0}C. After complete removal of water, the dark brown precipitates were collected by centrifugation and washed with ethanol until neutral pH. The obtained product Mo-Imidazole-borate complex was dried at 60 ^{0}C for one day before further experiments.

2.3.2 Preparation of BCN encaged different phases of molybdenum carbides

Different phases of molybdenum carbides were prepared by just modifying the imidazole-borate ligand structure. Detailed compositions can be found in Table 1. The as-prepared Mo-Imidazole-borate complex was calcined in a tube furnace under N_2 gas with a ramping rate of 5 ^{0}C min-1, kept at 900 ^{0}C for 5 h and then cooled down naturally. The resulting dark grey powders, denoted as Mo_2C@BCN (around 40 wt. % of initial precursors) was collected and sealed in a vial before further analysis and characterizations. For comparison, Mo_2C nanoparticles are also prepared without developing BCN network.

Table 2.1. Composition of starting materials for preparation of multiple phase of molybdenum carbides

Name	Imidazole	Boric acid	$MoCl_5$
o-β-Mo_2C	5 mmol	NIL	1 mmol
o-α-Mo_2C@BCN	5 mmol	1 mmol	1 mmol
h-η-MoC@BCN	5 mmol	2 mmol	1 mmol
h-β-Mo_2C@BCN	5 mmol	3 mmol	1 mmol
c-α-Mo_2C@BCN	5 mmol	4 mmol	1 mmol
o-β-Mo_2C@BCN	5 mmol	5 mmol	1 mmol

2.3.3 Characterizations

Crystallographic information of all powder samples were determined by powder X-ray diffraction (XRD, PANalytical pw 3040/60 X'pert) with Cu Kα radiations. The surface morphologies and structural information were examined with field-emission scanning electron microscope (FE-SEM, Hitachi, S-4800, 15 kV) and normal transmission electron microscope (TEM, JEOL, JEM-2100). The chemical compositions, elemental mapping and in-depth crystal information of samples were collected by high resolution transmission electron microscope (HRTEM, JEOL, JEM-2100F). X-ray photoelectron spectroscopy (XPS, ThermoFisher, K-alpha) was used to obtain the surface atomic composition and chemical states. Surface areas and pore size distribution of the catalysts were characterized by N2 adsorption-desorption isotherms by using Mirae Scientific Instruments, Nanoporosity-XQ at liquid-nitrogen temperature.

2.3.4 Electrochemical measurements

The catalyst ink was prepared by dispersing 10 mg of a catalyst in 1.0 mL mixture of deionized water and 2-propanol (7:3) and 20 µL of 5% Nafion solution. The mixture was sonicated for 1 h in a water bath. The working electrode was prepared by drop casting of 15 µL ink onto a glassy carbon electrode (0.7-0.8 mg cm^{-2} loading) followed by dropping 5 µL Nafion solution in order to fix the catalyst. The electrode was dried at room temperature for 1 h before electrochemical measurements. Electrochemical

HER activity and stability tests were carried out in a three electrode cell configuration using a rotating disc electrode (RDE, PAR Model 636 RDE) attached with a potentiostat (Ivium technologies). An Ag/AgCl (3.0M NaCl) electrode and a Pt wire were used as reference and counter electrodes, respectively. All potentials were referenced to the reversible hydrogen electrode (RHE) by converting with the equation $E_{RHE}=E_{(Ag/AgCl)} + 0.059pH + 0.209$.

Linear sweep voltammogram was measured in aqueous 0.5 M H_2SO_4 (pH 0.3) and 1.0 M KOH and NaOH (pH 14) at a scan rate of 5 mV s-1 with 1600 rpm after 20 cyclic voltammetry (CV) cycles in the range of 0.2 to -0.5 and -0.8 to -1.3 V vs. Ag/AgCl reference electrode for acid and basic solutions, respectively. The electrochemical stability tests were conducted by performing up to 3000 CV cycles in the above potential ranges. Electrochemical impedance spectroscopy (EIS) was conducted in the same setup in the frequency range of 100 kHz to 1 MHz with a modulation amplitude of 10 mV. The EIS spectra were fitted by the Z-view software. To evaluate the electrochemical active surface area (ECSA), CV was conducted from 0.0 to 0.3 V (in 0.5 M H_2SO_4) and -0.8 to -0.5 V (in 1.0 M KOH or NaOH) vs. Ag/AgCl with different sweep rates between 10 to 100 mV s^{-1}.

2.4 Results and Discussion

2.4.1 Organometallic complex-assisted synthesis and characterization of Mo-carbides

The generalized preparation procedure for B- and N-doped carbon (BCN) shell protected molybdenum carbides (named as Mo_2C@BCN) is described in **Figure 2.1a**, and discussed in detail under Experimental Section. Firstly, as-prepared different imidazole (Im)-borate (**Eqn. 2.1**) monomers (**Table 1.1**) were used as an organic linker to make an organometallic complex of Mo cation at 130 ^{0}C under nitrogen in glycerol and dilute aqueous acetic acid solution (**Eqn. 2.2**). The color change with synthesis time is also monitored as in **Figure 2.1b**.

$$n(Im) + H_3BO_4 \xrightarrow{\Delta} (Im)_nB(OH)_{3-n} + nH_2O \quad (Eq.2.1)$$

$$(Im)_nB(OH)_{3-n} + MoCl_5 \xrightarrow{aq.CH_3COOH,Gly} MIB - complex + HCl \quad (Eq.2.2)$$

The dark brown precipitate of Mo-Im-Borate complex (MIB) are collected which possess zeolitic-imidazolate framework-like (ZIF) topologies because of imidazole linkers can make Mo-Im-Mo bridge just like Si-O-Si in zeolite framworks.[31] The Powder X-ray diffraction (XRD) pattern of MIB complex did not show any significant peak due to its amorphous nature as shown in **Figure 2.2a**. Then, the as-obtained MIB complex was calcined at 900 ^{0}C in N_2 atmosphere to synthesize BCN network encapsulated dark grey Mo_2C nanoparticles (NPs). During the thermal decomposition at higher temperature, Mo reacts with the imidazole-borate linkers and converted to molybdenum carbides NPs

covered by the few layers of BCN. Five different phases (hexagonal β, η, orthorhombic α, β and cubic α) are successfully formed by just manipulating imidazole-borate ligand structures by varying the imidazole-to-boric acid ratio by keeping the all other conditions same (**Table 2.1**). Due to the different structure, the imidazole-borate ligands may have tendency to coordinate with Mo atoms making different spatial atomic arrangements in MIB to yield distinct phases of molybdenum carbide.

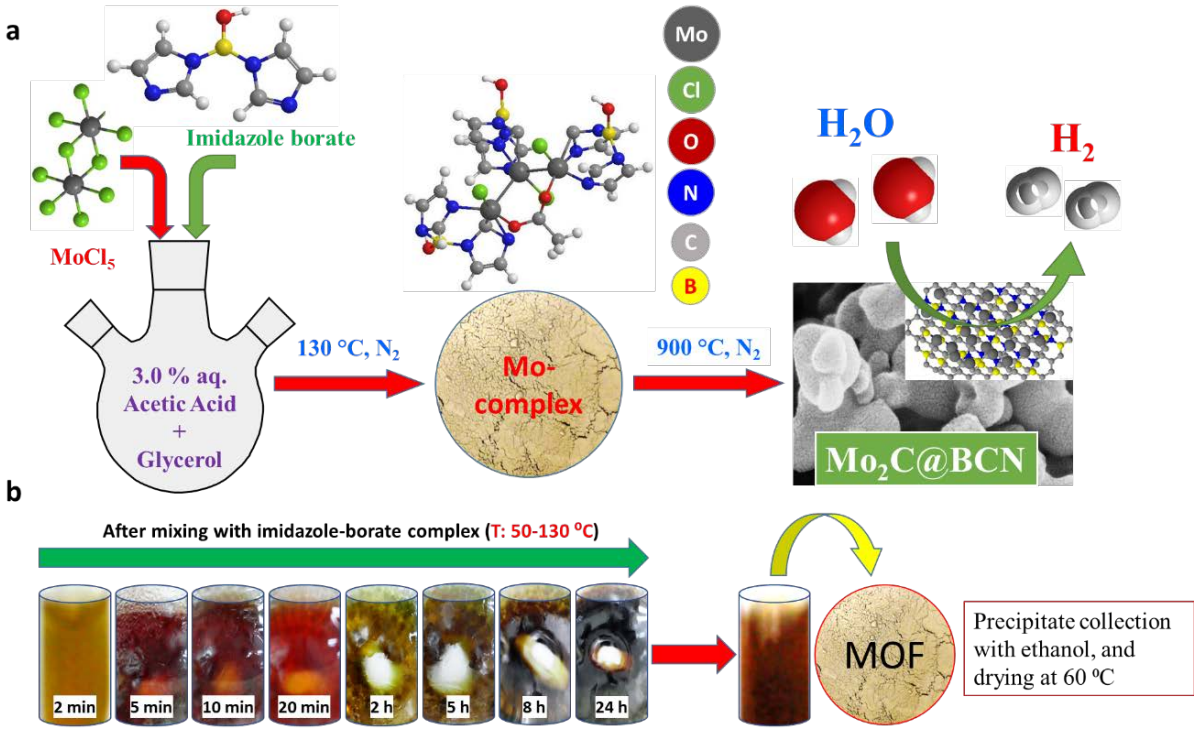

Figure 2.1. (a) Schematic illustration for preparation of BCN-encaged diffrent phases of molybdenum carbide and evolution of color during the synthesis of Mo-Im-Borate complex.

The formation of highly crystalline different phases like orthorhombic (α-Mo_2C, β-Mo_2C), hexagonal (β- Mo_2C, η-MoC) and cubic (α-MoC_{1-x}) molybdenum carbides are confirmed by XRD (**Figure 2.2b**) along with simulated XRD patterns of all phases. Surprising, the multiple phases are easily synthesized by just slight tuning imidazole-borate ligand structure at the same annealing temperature of 900^{0}C for 5 h in N_2. Additionally, the cubic α-MoC_{1-x} and hexagonal η-MoC phase could also be synthesized at 750 ^{0}C (**Figure 2.2c**) and 800 ^{0}C (**Figure 2.2d**), respectively, which are much lower temperature as for α-MoC_{1-x} (800 ^{0}C) and hexagonal η-MoC (1050 ^{0}C) by annealing a mixture of Mo salts and organic compounds[32]. Additional, for the preparation of η-MoC the other metallic impurities like NiI_2 and Cu was also required as guest atoms to make metal organic framework, the removal of such impurities is difficult to get the pure product.[32,6] The particle size calculated by applying Scherrer formula (**Figure 2.2e**), the average crystallite sizes of o-α-Mo_2C (14 nm), η-MoC (6.3 nm), h-β-Mo_2C (11.6 nm), α-MoC_{1-x} (4.2 nm) and o-β-Mo_2C (8.9 nm), which are smaller or comparable with previously reported in literature.[6, 21, 28] Mo-complex structure effectively prevent from agglomeration of NPs during the

confined carburization reaction. The irregular spherical particles of grain size 30-200 nm were observed by Field emission scanning electron microscopy (FESEM) as shown in **Figure 2.2f**.

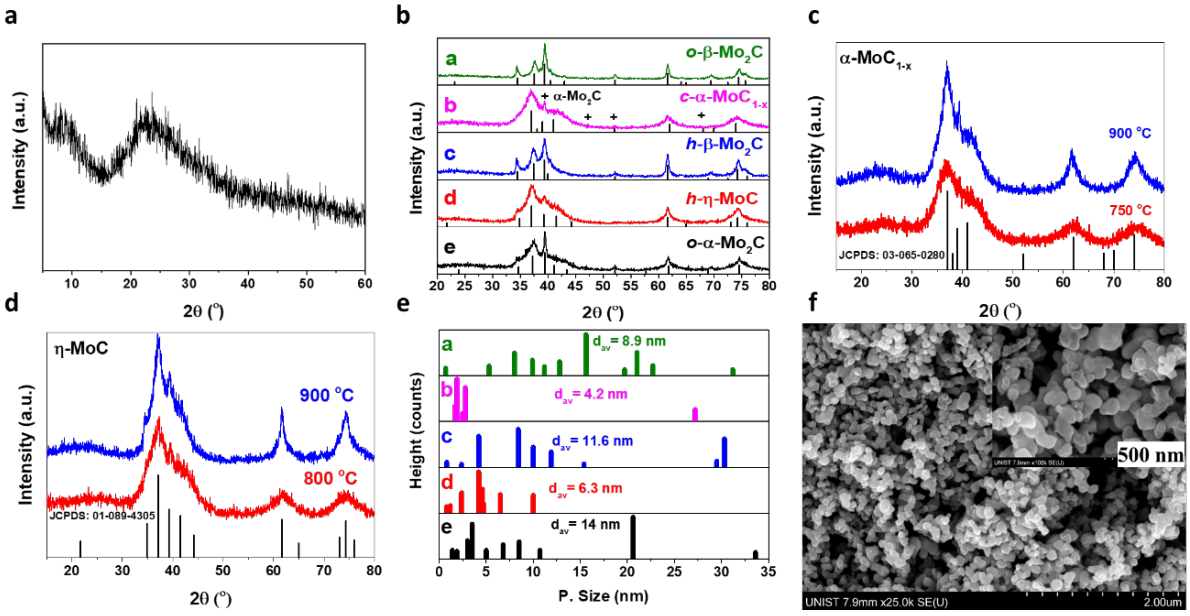

Figure 2.2. XRD pattern of (a) Mo-Im-borate complex, (b) as-synthesized multiple phase of molybdenum carbide at 900 ^{0}C, (c) cubic α-MoC_{1-x} at 750 to 900 ^{0}C, (d) hexagonal η-MoC at 800-900 ^{0}C, (e) particle size distribution obtained from XRD pattern in (b) by Scherrer equation and (f) SEM image sample annealed at 900 ^{0}C.

The transmission electron microscopy (TEM) image at low magnification (**Figure 2.3a**) display irregular shaped porous morphology as in SEM images. The small nanoparticles (5-14 nm) of molybdenum carbide are caged in BCN network as encircled by dots in good agreement with XRD. High resolution TEM images in **Figure 2.3b-d** confirm that molybdenum carbide NPs are well protected in uniform BCN shells of 3.0±0.5 nm thick having interplanar distances of 0.377 and 0.345 nm of (012) planes of boron carbide (JCPDS 01-086-1120) and (002) planes of graphitic carbon, respectively.[33] The lattice fringes **Figure 2.3b-f** of hexagonal η-MoC (0.243), hexagonal β-Mo_2C (0.229), orthogonal β-Mo_2C (0.28), orthogonal α-Mo_2C (0.246) and cubic α-MoC_{1-x} (0.24) nm are belonging to the (006), (101), (211), (002) and (111) crystal planes of each phase, respectively. EDX elemental maps (**Figure 2.3g-l**) confirms the uniform distribution of Mo, B, N and C atoms throughout the particle which is another evidence of successful encapsulation of molybdenum carbides NPs by BCN.

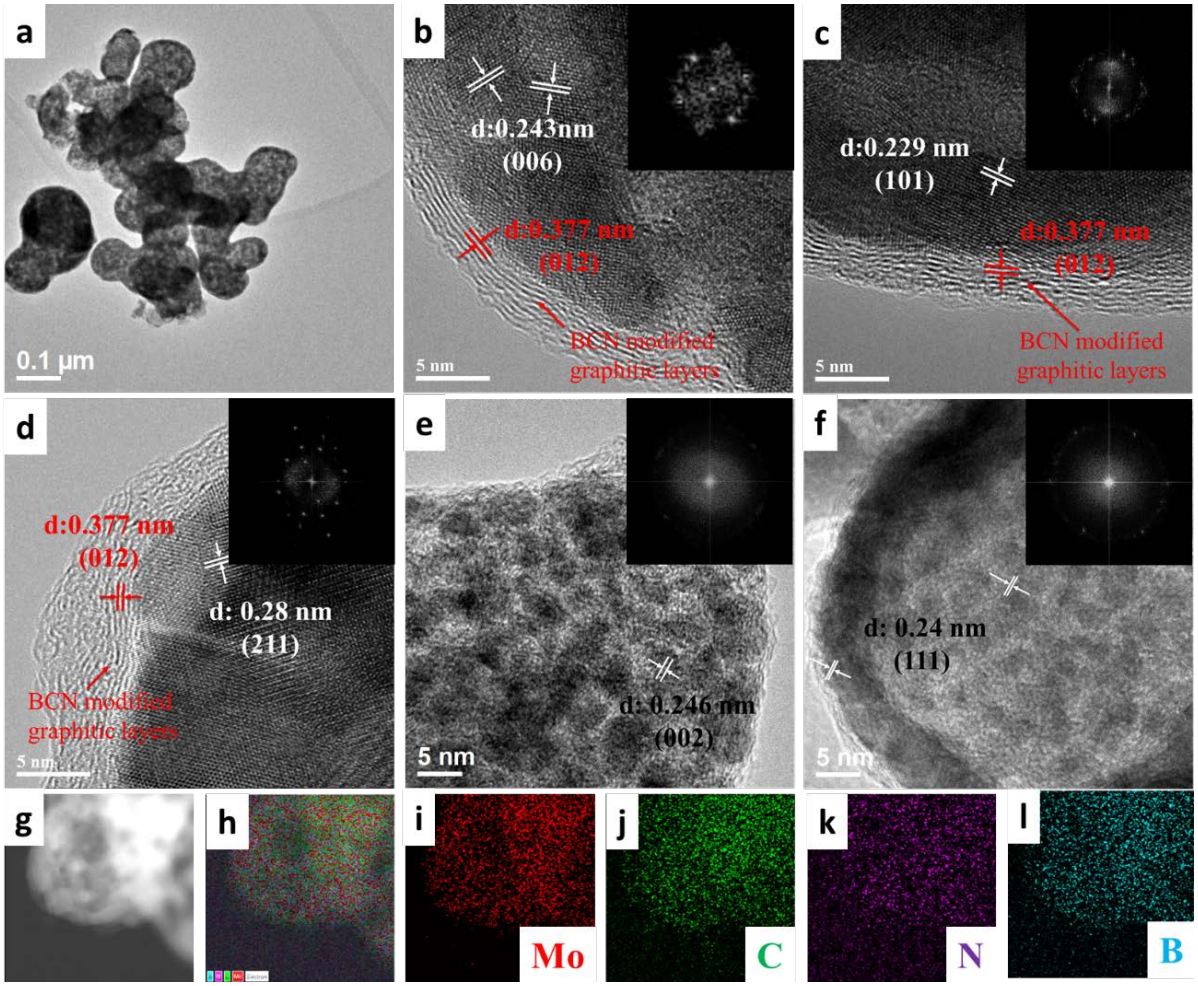

Figure 2.3. TEM image (a) at low magnification; scale bar: 100 nm, HR-TEM image of (b) hexagonal η-MoC, (c) hexagonal β-Mo_2C, (d) orthogonal β-Mo_2C, (e) orthogonal α-Mo_2C, (f) cubic α-MoC_{1-x} and corresponding fast Fourier transform (FFT) pattern (inset); scale bar: 5nm. (g-l) EDS-STEM elemental maps for Mo (red), C (green), N (purple) and B (light blue).

Three oxidation states for molybdenum Mo^{+2} (Mo-carbide), Mo^{+4} (MoO_2) and Mo^{+6} (MoO_3) are identified by X-ray photoelectron spectroscopy (XPS) of Mo 3d spectra as displayed in **Figure 2.4a**. The minor surface oxides are observed in XPS because of exposure of NPs in air,[22, 32] as confirmed by quantitative analysis of XPS in **Table 2.2**. Five peaks of B-C, B-N, B, B-O (B_2O_3) and MoB are identified in B1s spectra (**Figure 2.4b**). The signals at 398.2, 399 and 401 eV in N1s XPS (**Figure 2.4c**)can be assigned to pyridinic/B-N, pyrrolic and graphitic (N-C_3) nitrogen,[33-34] along with Mo-N and Mo-Mo peaks at 394.2 eV and 395.5 respectively.[32, 35] The C1s (**Figure 2.4d**) spectra display a Mo-C peak at 283 eV,[36] and near 284.5, 285.2 and 288 eV corresponds to C bonding with N, O, and B, accordingly.[33] The pore size in the range of 3-10 nm and BET surface areas 87.1 and 48.36 m^2/g are found to be for h-β-Mo_2C@BCN and c-α-MoC_{1-x}@BCN by N_2 adsorption−desorption isotherms as shown in Figure 1.4e-f.

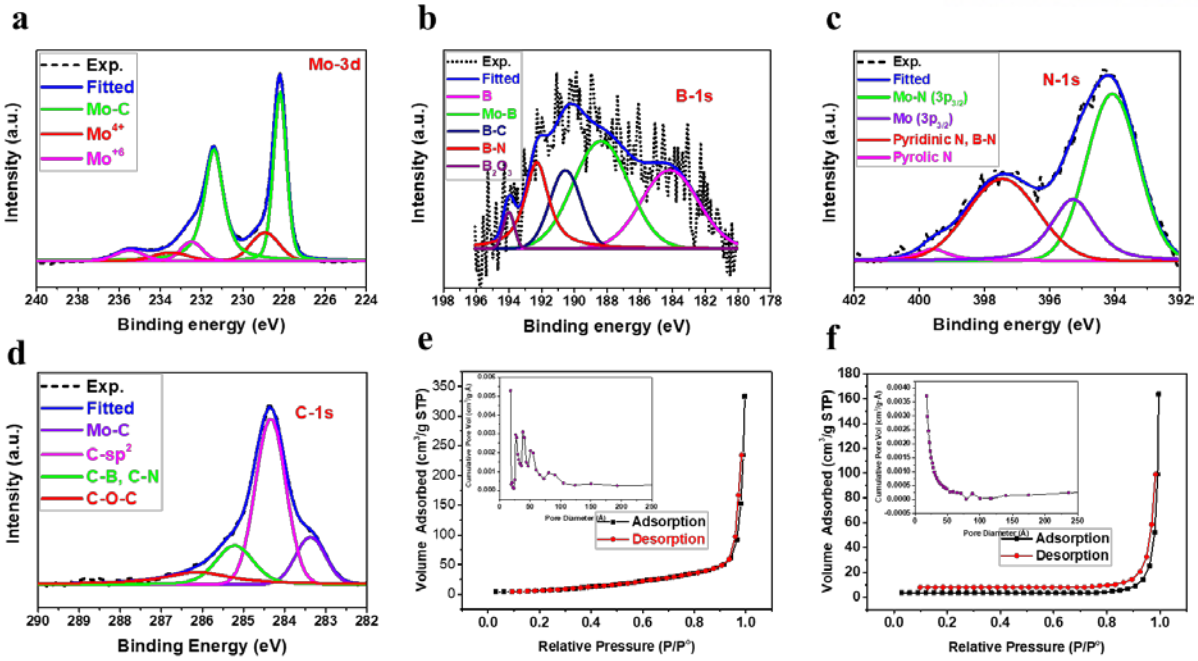

Figure 2.4. XPS spectra of (a) Mo 3d, (b) B 1s, (c) N 1s) and (d) C 1s. BET isotherms for (e) h-β-Mo_2C@BCN, (f) c-α-MoC_{1-x}@BCN and pore size distributions (inset).

Table 2.2. Surface composition of each phase of molybdenum carbides determined by XPS

Sample	Mo [At. %]	C [At. %]	N [At. %]	B [At. %]	O [At. %]
o-α-Mo_2C@BCN	10.44	60.81	17.37	1.04	10.34
h-η-MoC@BCN	10.39	55.93	24.27	1.23	8.18
h-β-Mo_2C@BCN	11.03	59.09	21.17	1.60	7.11
c-α-Mo_2C@BCN	11.3	60.02	18.7	3.15	6.83
o-β-Mo_2C@BCN	13.50	60.49	12.84	4.05	9.12

2.4.2 Hydrogen evolution reaction performances of BCN-protected molybdenum carbides

The electrocatalytic HER activity of all phased are examined by using three electrode system in both acidic and alkaline aqueous electrolytes as shown in **Figure 2.5**. Surprisingly, the c-α-MoC_{1-x}@BCN displays best performance from the other molybdenum carbides especially in the small current density in 0.5M H_2SO_4 (Figure 1.5a). It requires small onset potential of ~ 20 mV and overpotential 133 mV for a current density of 10 mA cm^{-2}. The Hexagonal β-Mo_2C phase also needs much lower onset and overpotential of ~18 and 147 mV as compared to orthorhombic α and β phases of Mo_2C composites. The hexagonal η-MoC@BCN also needs slightly higher overpotentials to achieve the same current densities. Overall, the best performance was observed by h-β-Mo_2C@BCN especially at higher currents in acidic medium, which is higher than earlier reported molybdenum carbide-based catalysts in literature (**Table 2.3**). The higher HER activity of β-Mo_2C could be due to a slightly higher density of

states (DoS) around Fermi level than other Mo-carbide phases.[32, 37] The HER performance was also determined in 1.0M KOH (**Figure 2.5b**) and 1.0M NaOH (**Figure 2.5c**) aqueous solutions. The h-β-Mo_2C@BCN displays the current density of 1 and 10 mA cm^{-2} at the smallest overpotentials in 1.0M NaOH (45 and 92 mV) and 1.0M KOH (46 and 98 mV) aqueous solutions. The less active Cubic α-MoC_{1-x} also displayed better performance than previously reported one due to the BCN promotional effect.[32] Similarly, h-η-MoC@BCN composite also exhibits exceptional activity as compared to previous reports on η-MoC_x nano-octahedrons and η-MoC.[6, 32] It requires the low onset potential (~30 mV) and overpotentials (106 mV) to generate current of 10 mA cm^{-2}. Surprisingly, the all BCN encapsulated Mo-carbides catalysts show higher performance than Pt/C especially at higher current densities. The electrochemical properties in both acidic and alkaline media for all hybrid catalysts are summarized in **Table 2.3** and **2.4**.

The Tafel slopes and exchange current densities at zero overpotential (J_0) are calculated by using the Tafel equation $\eta = a + b \log (j)$ in all electrolytes (**Figure 2.5d-f**). The c-α-MoC_{1-x}@BCN displays the lowest Tafel slope (~47 mV dec^{-1}) and higher exchange currents (0.124 mA cm^{-2}) which confirm its exceptional HER performance in 0.5M H_2SO_4. Hexagonal β-Mo_2C@BCN and orthogonal β-Mo_2C@BCN show the similar Tafel slopes, but higher J_0 (0.392 mA cm^{-2}) of former than later (0.109 mA cm^{-2}) indicate of higher HER kinetic for h-β-Mo_2C@BCN. The low comparable J_0 values and Tafel slopes of both h-η-MoC and o-α-Mo_2C also indicate that they following same reaction route in acidic media. In alkaline media, all hybrid catalysts show the Tafel slope in the range of 52-60 mv dec^{-1} and relatively higher J_0 values. The cubic α-MoC_{1-x} also displays comparable or smaller Tafel slopes than other reported catalysts as enlisted in **Table 2.3 & 2.4**. Another important factor i.e. electrochemical active surface areas (ECSA) were also calculated by determining the specific double layer capacitance (C_{dl}) from linear slopes of the plots (**Figure 2.5g-h**) between ($\Delta J = J_a - J_c)/2$ and scan rates (10-100 mV s^{-1}).[28, 38] Interestedly, o-α-Mo_2C display the better specific capacitance and ECSA than other phase, but a little less HER activity in all electrolytes. Although c-α-MoC_{1-x}@BCN displays almost same ECSA in all conditions but it has better activity in 0.5M H_2SO_4 than other alkaline. This behavior indicates that ECSAs are not the crucial parameter in determining HER activity as reported previosly.[6]

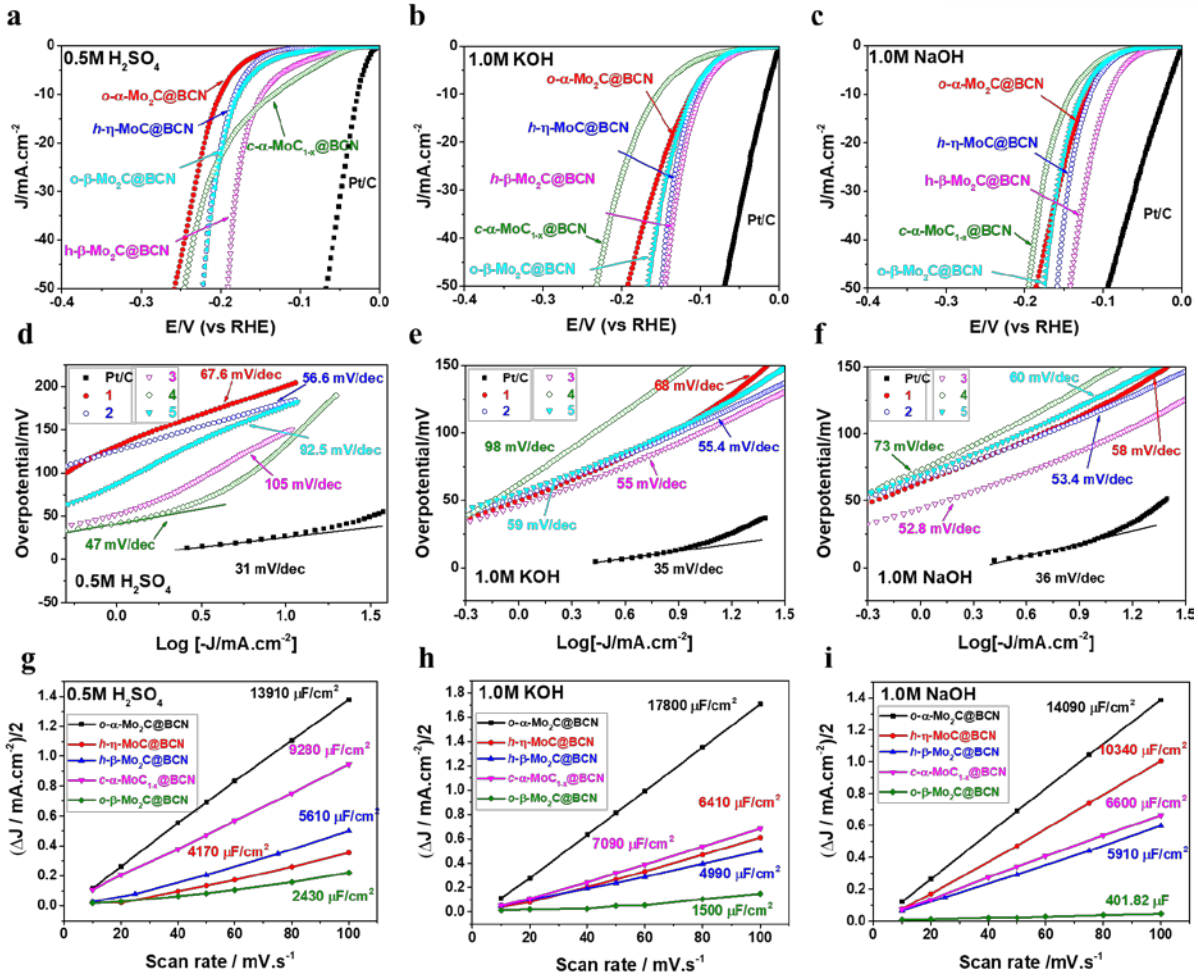

Figure 2.5. HER performance curves (a-c) of all hybrid catalysts at a scan rate of 5 mVs^{-1} and (d-f) corresponding Tafel plots in all electrolytes. Half of ($\Delta j = J_a - J_c$) plotted against scan rates in (g) 0.5M H_2SO_4, (h) 1.0M NaOH and (i) for orthorhombic α-Mo_2C@BCN (black), hexagonal η-MoC@BCN (red), hexagonal β-Mo_2C@BCN (blue), cubic α-MoC_{1-x}@BCN (pink) and orthorhombic β-Mo_2C@BCN (green).

Thus electrochemical impedance spectroscopy (EIS) analysis was also performed and compared in all electrolyte constant overpotentials 148 mV_{RHE} in 0.5M H_2SO_4 and at 90 mV_{RHE} in alkaline conditions (**Figure 2.6a-c**). The h-β-Mo_2C@BCN has relatively small charge transfer resistances (R_{ct}) than other composites in both acidic and basic solutions. The c-α-MoC_{1-x} hybrid displays a higher R_{ct} in alkaline solutions as compared to acidic electrolyte, which is in accordance it performance behavior in both electrolytes. The EIS results have consistency with the HER activities of all electrocatalysts, revealing that charge transfer is the most important factor effecting the HER performance. Electrochemical durability was also determined by performing the accelerated cyclic voltammetry (CV) continuously for 3000 cycles at a scan rate of 100 mVs^{-1} in both acidic as well as alkaline media as shown in **Figure 2.6d-e**. The h-β-Mo_2C and o-β-Mo_2C composites show the remarkable stable performance for HER without any significant increment in overpotential up to 3000 CV cycles. While c-α-MoC_{1-x} @BCN exhibits a minor but continuous loss of current density in both electrolyte, revealing a small corrosion

and instability of this phase than others.[32] The stability of h-η-MoC@BCN and o-α-Mo_2C@BCN were also improved after encapsulation of BCN network.

Table 2.3. Comparison of HER activity in acidic media with other reported electrocatalysts

Catalyst	*η1* [mV]	*η10* [mV]	Tafel Slope [mV/dec]	J_0 [mA/cm^2]	Reference
c-α-MoC_{1-x}@BCN	41	133	47 167	0.124 1.505	This Work
h-β-Mo_2C@BCN	52	147	105	0.392	
***o*-β-Mo_2C@BCN**	87	177	104	0.109	
***h*-η-Mo_2C@BCN**	125	182	56.6	0.006	
***o*-α-Mo_2C@BCN**	131	200	67.6	0.011	
Mo_2C-carbon nanocomposites	160	260	110		*J. Mater. Chem. A* **2014,** *2* (27), 10548-10556.
$Mo_{0.06}W_{1.94}C$/CB	150	220			*Angew. Chem. Int. Edit.* **2014,** *53* (20), 5131-5136.
Mo_2C/Graphitic Carbon Sheets	160	210	62.6	0.0125	*ACS Catal.* **2014,** *4* (8), 2658-2661.
Mo_2C	155	210	56	0.0013	*Angew. Chem.* **2012,** *124* (51), 12875-12878.
Mo_2C NWs	115	200	55.8		*Electrochim. Acta* **2014,** *134*, 182-186.
Mo_2C nanoparticles	150	198	56		*J. Mater. Chem. A* **2015,** *3* (16), 8361-8368.
MoS_2/Mo_2C embedded N-CNT		190	69		*J. Mater. Chem. A* **2014,** *2* (44), 18715-18719.
Mo1Soy(β-Mo_2C and γ-Mo_2N)	120	177	66.4	0.037	*Energy Environ. Sci.* **2013,** *6* (6), 1818-1826.
MoS_x@Mo_2C	130	170	52	0.131	*ACS Catal.* **2015,** *5* (11), 6956-6963.
Mo_2C on CNT	63	152	55.2	0.014	*Energy Environ. Sci.* **2013,** *6* (3), 943-951.
Ni-Mo_2C nano-rod	100	150	58	0.033	*Appl. Catal. B* **2014,** *154*, 232-237.
3D Mo_xC/Ni network	44	150	49		*ChemCatChem* **2014,** *6* (7), 2059-2064.
Mo_2C–NCNT	72	147	71	0.114	*J. Mater. Chem. A* **2015,** *3* (11), 5783-5788.
MoCN	55	145	46		*J. Am. Chem. Soc.* **2014,** *137* (1), 110-113.
Mesoporous η-MoC_x nano-octahedrons	87	142	53		*Nat. Commun.* **2015,** *6*, 6512-6520.
Mo_2C, CNT-Graphene composite	90	130	58	0.062	*ACS Nano* **2014,** *8* (5), 5164-5173.
Mo_2C on RGO	91	130	57.3		*Chem. Commun.* **2014,** *50* (86), 13135-13137.
Nanoporous Mo_2C nanowires	70	130	53		*Energy Environ. Sci.* **2014,** *7* (1), 387-392.
Mo_2C@NC	60	124	60	0.096	*Angew. Chem. Int. Edit.* **2015,** *54* (37), 10752-10757.
NS-doped Mo_2C	56	86	47	0.038	*Small* **2015,** *11* (47), 6278-6284.
Mo_xC-Ni@NCV	22	75	45		*J. Am. Chem. Soc.* **2015,** *137* (50), 15753-15759.
β- Mo_2C	205		120	0.01729	*Angew. Chem.* **2014,** *126* (25), 6525-6528.

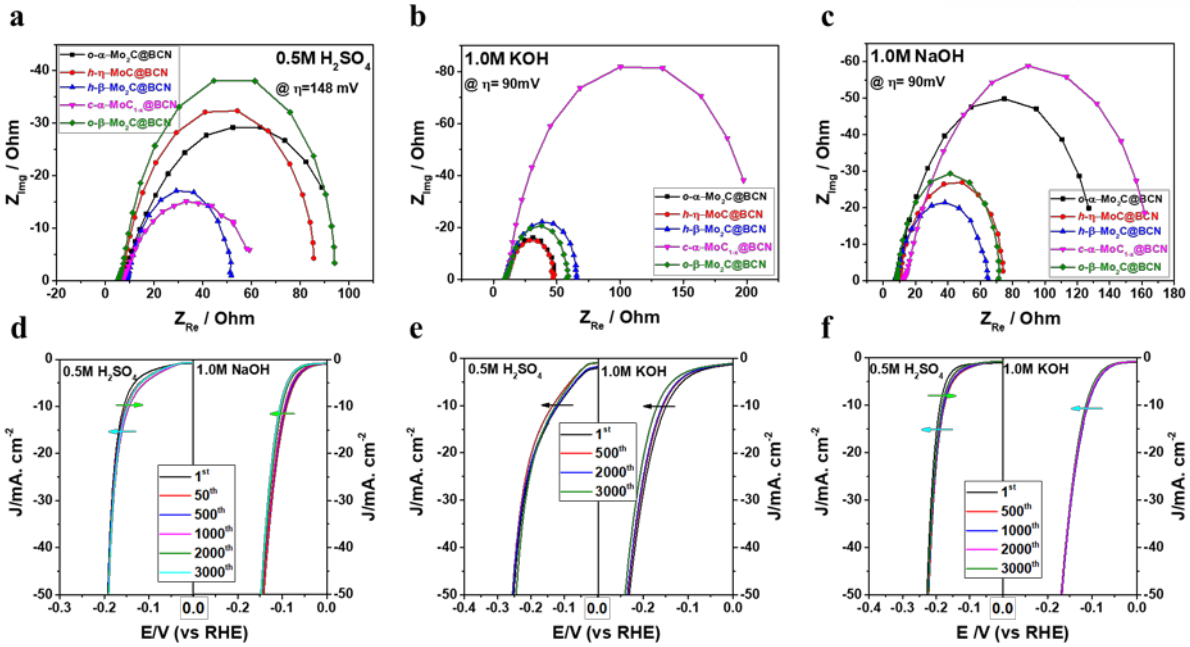

Figure 2.6. Comparison of EIS Nyquist plots at overpotentials of 148 mV in (a) 0.5M H_2SO_4; and at 90 mV in (b) 1.0M KOH and c) 1.0M NaOH. Polarization curves before and after continuous CV cycles at scan rate of 100 mVs^{-1} for (d) h-β-Mo_2C@BCN; (e) c-α-MoC_{1-x}@BCN and (f) o-β-Mo_2C@BCN in acidic and alkaline media.

Table 2.4. Comparison of HER activity of as-synthesized molybdenum carbides other Mo_2C-based electrocatalysts in alkaline media

Catalyst	*η1* [mV]	*η10* [mV]	Tafel Slope [mV/dec]	J_0 [mA/cm^2]	Reference
***h*-β-Mo_2C@BCN**	45	92	52.8	0.162	1.0M NaOH This work
***h*-η-Mo_2C@BCN**	65	116	53.4	0.063	
***o*-α-Mo_2C@BCN**	63	119	58.5	0.0861	
***o*-β-Mo_2C@BCN**	69	126	60	0.075	
***c*-α-MoC_{1-x}@BCN**	73	141	73	0.113	
***h*-β-Mo_2C@BCN**	46	98	55	0.162	1.0M KOH This work
***h*-η-Mo_2C@BCN**	52	106	55.4	0.120	
***o*-α-Mo_2C@BCN**	49	111	68	0.218	
***o*-β-Mo_2C@BCN**	56	110	59	0.127	
***c*-α-MoC_{1-x}@BCN**	62	154	98	0.225	
Dual-doped Co@BCN	70	183	73.2		*ACS Nano* **2015,** *10* (1), 684-694.
Mo_2C–NCNT	195	257			*J. Mater. Chem. A* **2015,** *3* (11), 5783-5788.
Mo_2C	130	190	54	0.0038	*Angew. Chem.* **2012,** *124* (51), 12875-12878.
Mo_2C nanoparticles	110	176	58		*J. Mater. Chem. A* **2015,** *3* (16), 8361-8368.
Mesoporous η-MoC_x nano-octahedrons	92	151	59		*Nat. Commun.* **2015,** *6*, 6512-6520.
Mo_2C nano-rod Ni impregnated Mo_2C nano-rod	48	130	49	0.27	*Appl. Catal. B* **2014,** *154*, 232-237.
Mo_2C@NC	10	60			*Angew. Chem. Int. Edit.* **2015,** *54* (37), 10752-10757.

2.4.3 The synergistic roles of BCN network to enhance HER activity

The N-doped molybdenum carbides NPs are also prepared by using Mo-imidazole complex as a precursor at the similar conditions. The XRD pattern of N-doped Mo_2C (without BCN) catalyst in **Figure 2.7a** clearly confirms the formation of β-Mo_2C with large crystal size (15-30 nm) and displays poor HER activity than BCN encapsulated molybdenum carbides and requires η10 values 355 and 256 mV in 0.5M H_2SO_4 and 1.0M KOH, respectively (**Figure 2.7b-c**). Thus it is another evidence of advantage of BCN-encapsulation to improve the HER activity. Firstly, it controls the agglomeration of molybdenum carbide NPs, secondly, it reduced the charge transfer resistance due to its excellent conductivity as confirmed by the EIS analysis and thirdly, it can provide protection to the carbide particle from chemical corrosion and increase the stability.

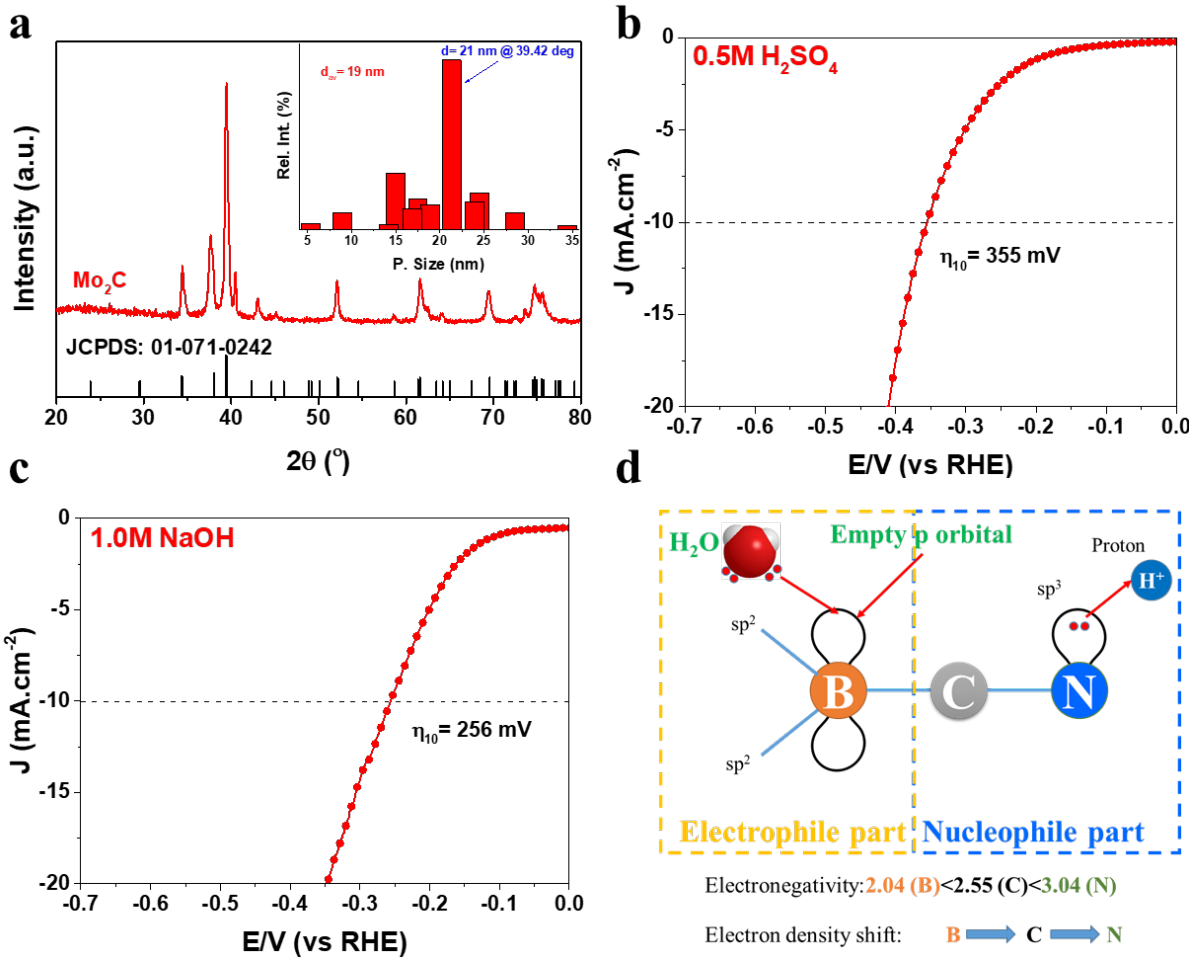

Figure 2.7. (a)XRD pattern, HER performance curves in (b) 0.5M H_2SO_4 and (c) 1.0M KOH aqueous solutions of N-doped Mo_2C. (d) The electrophilic and nucleophilic role of BCN layer to increase the HER activity.

Here let us discuss another unique electrophilic as well as nucleophilic characteristics of BCN shell differentiated it from other carbonaceous layers as shown in **Figure 2.7d**. Boron attached to C can act

electrophile (electron loving) and at other end N play a role of nucleophile (proton loving). Thus, B and N co-doped carbon could make sp3-C Stone-Wales defects in the carbon structure, which can also activate neighbor carbon atoms by increasing electron density which also act as nucleophile. Thus B and N co-doping in carbon could increase the proton (H^+) adsorption sites, enhances wetting property and thereby maximize the electrochemical active surface area (ECSA).[33-34, 39] As the C atom in BCN with an electronegativity (χ) of 2.55 is residing in between N (χ=3.04) and B (χ=2.04) atoms, being more electronegative, the N may withdraw electron density from adjacent C via 2p orbital which the again reduces the electron density at B, resulting more proton adsorption sites at N/C and water adsorption sites at B.[33] An electron deficient B atom is surrounded by only six valence electrons, and thus, it can coordinates with lone pairs of oxygen atom in water in order to complete a stable octet, hence enhances the wetting properties by weakening –O-H bond of water molecule (Figure 1.7d, left). From the above discussion, it can be concluded that BCN encapsulation of molybdenum carbides NPs may be responsible for enhancing the HER performance and stability by promoting electron/proton transfer in the molybdenum carbides-based catalysts.

2.5 Conclusion

The electrocatalytic HER performance of five different phases of molybdenum carbides are tuned by synthesizing BCN encapsulated carbides NPs via a unique organometallic complex-assisted approach. The multiple phases of molybdenum carbides are prepared by slight modification in the imidazole-borate ligands keeping the other conditions constant. This method prevents the carbide NPs from agglomeration during a confined *in-situ* carburization reaction between Mo atom and imidazole-borate monomer of MIB-complex structure. The BCN network protected multiple phases of mesoporous molybdenum carbide display high electrochemical active surface area, reduced charge transfer resistances and improved wetting properties. All phases of molybdenum carbides show a remarkable electrocatalytic HER performance and durability in both acidic and basic aqueous defeating the most of earlier reported molybdenum carbides based electrocatalyst in the literature. Especially, the hexagonal β-Mo_2C outstandingly performs well than other phases in all electrolytes. The improved HER performance of all phases is mainly due to synergistic role of the BCN network.

2.6 References

1. Levy, R.; Boudart, M., Platinum-like behavior of tungsten carbide in surface catalysis. *Science* **1973,** *181* (4099), 547-549.

2. Zhong, Y.; Xia, X.; Shi, F.; Zhan, J.; Tu, J.; Fan, H. J., Transition Metal Carbides and Nitrides in Energy Storage and Conversion. *Adv. Sci.* **2016,** *3* (5), 1500286.

3. Chen, W.-F.; Muckerman, J. T.; Fujita, E., Recent developments in transition metal carbides and nitrides as hydrogen evolution electrocatalysts. *Chem. Commun.* **2013,** *49* (79), 8896-8909.

4. Lengauer, W., Transition metal carbides, nitrides, and carbonitrides. *Handbook of ceramic hard materials* **2000**, 202-252.

5. Ang, H.; Tan, H. T.; Luo, Z. M.; Zhang, Y.; Guo, Y. Y.; Guo, G.; Zhang, H.; Yan, Q., Hydrophilic Nitrogen and Sulfur Co-Doped Molybdenum Carbide Nanosheets for Electrochemical Hydrogen Evolution. *Small* **2015,** *11* (47), 6278-6284.

6. Wu, H. B.; Xia, B. Y.; Yu, L.; Yu, X.-Y.; Lou, X. W. D., Porous molybdenum carbide nano-octahedrons synthesized via confined carburization in metal-organic frameworks for efficient hydrogen production. *Nat. Commun.* **2015,** *6*, 6512.

7. Xiao, P.; Ge, X.; Wang, H.; Liu, Z.; Fisher, A.; Wang, X., Novel molybdenum carbide–tungsten carbide composite nanowires and their electrochemical activation for efficient and stable hydrogen evolution. *Adv. Funct. Mater.* **2015,** *25* (10), 1520-1526.

8. Yan, H.; Tian, C.; Wang, L.; Wu, A.; Meng, M.; Zhao, L.; Fu, H., Phosphorus-Modified Tungsten Nitride/Reduced Graphene Oxide as a High-Performance, Non-Noble-Metal Electrocatalyst for the Hydrogen Evolution Reaction. *Angew. Chem.* **2015,** *127* (21), 6423-6427.

9. Zhao, Y.; Kamiya, K.; Hashimoto, K.; Nakanishi, S., In Situ CO2-Emission Assisted Synthesis of Molybdenum Carbonitride Nanomaterial as Hydrogen Evolution Electrocatalyst. *J. Am. Chem. Soc.* **2014,** *137* (1), 110-113.

10. Esposito, D. V.; Chen, J. G., Monolayer platinum supported on tungsten carbides as low-cost electrocatalysts: opportunities and limitations. *Energy Environ. Sci.* **2011,** *4* (10), 3900-3912.

11. Pang, M.; Li, C.; Ding, L.; Zhang, J.; Su, D.; Li, W.; Liang, C., Microwave-assisted preparation of Mo2C/CNTs nanocomposites as efficient electrocatalyst supports for oxygen reduction reaction. *Ind. Eng. Chem. Res.* **2010,** *49* (9), 4169-4174.

12. Schweitzer, N. M.; Schaidle, J. A.; Ezekoye, O. K.; Pan, X.; Linic, S.; Thompson, L. T., High activity carbide supported catalysts for water gas shift. *J. Am. Chem. Soc.* **2011,** *133* (8), 2378-2381.

13. Zhang, B.; Cui, G.; Zhang, K.; Zhang, L.; Han, P.; Dong, S., Molybdenum nitride/nitrogen-doped graphene hybrid material for lithium storage in lithium ion batteries. *Electrochim. Acta* **2014,** *150*, 15-22.

14. Zhu, J.; Sakaushi, K.; Clavel, G.; Shalom, M.; Antonietti, M.; Fellinger, T.-P., A general salt-templating method to fabricate vertically aligned graphitic carbon nanosheets and their metal carbide

hybrids for superior lithium ion batteries and water splitting. *J. Am. Chem. Soc.* **2015,** *137* (16), 5480-5485.

15. Yang, E.; Ji, H.; Kim, J.; Kim, H.; Jung, Y., Exploring the possibilities of two-dimensional transition metal carbides as anode materials for sodium batteries. *Phy. Chem. Chem. Phy.* **2015,** *17* (7), 5000-5005.

16. Pande, P.; Rasmussen, P. G.; Thompson, L. T., Charge storage on nanostructured early transition metal nitrides and carbides. *J. Power Sources* **2012,** *207*, 212-215.

17. Kitchin, J. R.; Nørskov, J. K.; Barteau, M. A.; Chen, J. G., Trends in the chemical properties of early transition metal carbide surfaces: A density functional study. *Catal. Today* **2005,** *105* (1), 66-73.

18. Chen, W. F.; Sasaki, K.; Ma, C.; Frenkel, A. I.; Marinkovic, N.; Muckerman, J. T.; Zhu, Y.; Adzic, R. R., Hydrogen-Evolution Catalysts Based on Non-Noble Metal Nickel–Molybdenum Nitride Nanosheets. *Angew. Chem. Int. Ed.* **2012,** *51* (25), 6131-6135.

19. Ham, D. J.; Lee, J. S., Transition metal carbides and nitrides as electrode materials for low temperature fuel cells. *Energies* **2009,** *2* (4), 873-899.

20. Zou, X.; Zhang, Y., Noble metal-free hydrogen evolution catalysts for water splitting. *Chem. Soc. Rev.* **2015,** *44* (15), 5148-5180.

21. Liu, Y.; Yu, G.; Li, G. D.; Sun, Y.; Asefa, T.; Chen, W.; Zou, X., Coupling Mo2C with Nitrogen-Rich Nanocarbon Leads to Efficient Hydrogen-Evolution Electrocatalytic Sites. *Angew. Chem. Int. Ed.* **2015,** *54* (37), 10752-10757.

22. Vrubel, H.; Hu, X., Molybdenum boride and carbide catalyze hydrogen evolution in both acidic and basic solutions. *Angew. Chem.* **2012,** *124* (51), 12875-12878.

23. Liao, L.; Wang, S.; Xiao, J.; Bian, X.; Zhang, Y.; Scanlon, M. D.; Hu, X.; Tang, Y.; Liu, B.; Girault, H. H., A nanoporous molybdenum carbide nanowire as an electrocatalyst for hydrogen evolution reaction. *Energy Environ. Sci.* **2014,** *7* (1), 387-392.

24. Ito, Y.; Cong, W.; Fujita, T.; Tang, Z.; Chen, M., High Catalytic Activity of Nitrogen and Sulfur Co-Doped Nanoporous Graphene in the Hydrogen Evolution Reaction. *Angew. Chem. Int. Ed.* **2015,** *54* (7), 2131-2136.

25. Zheng, Y.; Jiao, Y.; Ge, L.; Jaroniec, M.; Qiao, S. Z., Two-Step Boron and Nitrogen Doping in Graphene for Enhanced Synergistic Catalysis. *Angew. Chem.* **2013,** *125* (11), 3192-3198.

26. Zhao, J.; Lai, H.; Lyu, Z.; Jiang, Y.; Xie, K.; Wang, X.; Wu, Q.; Yang, L.; Jin, Z.; Ma, Y., Hydrophilic Hierarchical Nitrogen-Doped Carbon Nanocages for Ultrahigh Supercapacitive Performance. *Adv. Mater.* **2015,** *27* (23), 3541-3545.

27. Zhang, K.; Zhao, Y.; Fu, D.; Chen, Y., Molybdenum carbide nanocrystal embedded N-doped carbon nanotubes as electrocatalysts for hydrogen generation. *J. Mater. Chem. A* **2015,** *3* (11), 5783-5788.

28. Tang, C.; Wang, W.; Sun, A.; Qi, C.; Zhang, D.; Wu, Z.; Wang, D., Sulfur-decorated molybdenum carbide catalysts for enhanced hydrogen evolution. *ACS Catal.* **2015,** *5* (11), 6956-6963.

29. Jager, H.; Wegmuller, H., Boric acid/amine reaction products, their manufacture and use. *U. S. Patents.* **1979,** 4136039.

30. Sun, H.; Qu, Q., Preparation of boron crosslinking agents for fracturing fluids. *U.S. Patents* **2014,** 8921597.

31. Park, K. S.; Ni, Z.; Côté, A. P.; Choi, J. Y.; Huang, R.; Uribe-Romo, F. J.; Chae, H. K.; O'Keeffe, M.; Yaghi, O. M., Exceptional chemical and thermal stability of zeolitic imidazolate frameworks. *Proc. Natl. Acad. Sci.* **2006,** *103* (27), 10186-10191.

32. Wan, C.; Regmi, Y. N.; Leonard, B. M., Multiple phases of molybdenum carbide as electrocatalysts for the hydrogen evolution reaction. *Angew. Chem.* **2014,** *126* (25), 6525-6528.

33. Zhang, H.; Ma, Z.; Duan, J.; Liu, H.; Liu, G.; Wang, T.; Chang, K.; Li, M.; Shi, L.; Meng, X., Active sites implanted carbon cages in core–shell architecture: highly active and durable electrocatalyst for hydrogen evolution reaction. *ACS Nano* **2015,** *10* (1), 684-694.

34. Chhetri, M.; Maitra, S.; Chakraborty, H.; Waghmare, U. V.; Rao, C., Superior performance of borocarbonitrides, B x C y N z, as stable, low-cost metal-free electrocatalysts for the hydrogen evolution reaction. *Energy Environ. Sci.* **2016,** *9* (1), 95-101.

35. Sanjinés, R.; Wiemer, C.; Almeida, J.; Levy, F., Valence band photoemission study of the Ti □ Mo □ N system. *Thin Solid Films* **1996,** *290*, 334-338.

36. Li, R.; Wang, S.; Wang, W.; Cao, M., Ultrafine Mo 2 C nanoparticles encapsulated in N-doped carbon nanofibers with enhanced lithium storage performance. *Phy. Chem. Chem. Phy.* **2015,** *17* (38), 24803-24809.

37. Hugosson, H. W.; Eriksson, O.; Nordström, L.; Jansson, U.; Fast, L.; Delin, A.; Wills, J. M.; Johansson, B., Theory of phase stabilities and bonding mechanisms in stoichiometric and substoichiometric molybdenum carbide. *J. Appl. Phy.* **1999,** *86* (7), 3758-3767.

38. Kibsgaard, J.; Jaramillo, T. F., Molybdenum Phosphosulfide: An Active, Acid-Stable, Earth-Abundant Catalyst for the Hydrogen Evolution Reaction. *Angew. Chem. Int. Ed.* **2014,** *53* (52), 14433-14437.

39. Duan, J.; Chen, S.; Jaroniec, M.; Qiao, S. Z., Porous C3N4 nanolayers@ N-graphene films as catalyst electrodes for highly efficient hydrogen evolution. *ACS Nano* **2015,** *9* (1), 931-940.

3. Boron and Nitrogen Dual-Doped Molybdenum Carbide Nanoparticles as Hydrogen Evolution, Oxygen Evolution and Reduction Reactions catalysts

3.1 Abstract

Boron and nitrogen co-doped molybdenum carbides (B, N: Mo_2C@BCN) nanoparticles are synthesized as a noble metal-free hybrid electrocatalyst *via* a unique and eco-friendly organometallic complex of Mo-imidazole and boric acid. When used as a trifunctional electrocatalyst for the hydrogen (HER), oxygen evolution (OER) and oxygen reduction (ORR) reactions in an aqueous alkaline solution, the hybrid (B, N: Mo_2C@BCN) catalyst displays excellent activity and stability in basic electrolytes, outperforming the reported transition metal carbides-based electrocatalysts. The mechanistic study reveal that the excellent performance of the hybrid material is attributable to the improved charge and mass transfer characteristics of the Mo_2CBN nanoparticles owing to their modified electronic structure with B and N species. A B, N: Mo_2C@BCN cathode exhibits a stable HER performance in 1.0M aqueous solution without any current density loss per hour at approximately -0.16 V during long-term operation as compared to Pt/C cathode (1.5 $mA.cm^{-2}h^{-1}$). This hybrid structure performance also displays superior stability and activity towards OER as compared to an IrO_2 and N: Mo_2C@NC anode. The synthesis approach employed in this study could also be suitable for tuning properties of other transition metal carbides for use as electrocatalysts.

3.2 Introduction

The water electrolysis has attracted a great attention recently as a key technology for sustainable hydrogen and oxygen production.[1-3] The great challenge in practical water electrolysis is to replace the precious Pt based catalysts for hydrogen evolution reaction (HER), oxygen reduction reaction (ORR) and Ir/Ru-based catalysts for oxygen evolution reaction (OER) with non-precious metals having similar performance and stablity.[4] To achieve this target, much effort has been exercised to minimize overpotentials of HER kinetics using cheaper earth-abundant materials such as carbides, sulfides, borides, nitrides, and phosphides,[4-7] and for OER with phosphates, perovskites, chalcogenides, oxides/hydroxides and phosphides.[1, 8-10] Although commercially available alkaline electrolyzers offer higher system efficiency than acidic proton exchange membrane ones, the HER rate in alkaline solutions is 2-3 orders of magnitude lower than that in acidic solutions.[11-12] The development of efficient and durable non-precious metal HER and OER catalysts for alkaline electrolyzer has great significance.

Transition metal carbides have received a great research interest as active materials for electrochemical applications (e.g. HER,[13-15] OER[16] & ORR[17]) owning to their noble metal-like properties,[18] excellent electrical and thermal conductivities, better mechanical strength and hardness, and also their chemical stabilities in corrosive environment.[6] Among the transition metal carbides, the molybdenum carbides are extensively investigated especially for hydrogen evolution reaction in both acidic and basic solutions.[19-20] Many attempts have been exercised to tune the electrochemical properties for improved HER performance by i) making nanoporous structure,[13, 21-22] ii) doping with heteroatoms such as N,[23] S[24], P[25] or dual doping,[6, 26] iii) MoS_2/Mo_2C heterostructures[27-28] and iv) decorating with transition metals (Ni, Co, W or Pt).[29-32] All these efforts were made to enhance HER performance, unfortunately, molybdenum carbides did not receive much attention as oxygen evolution/reduction or bifunctional water splitting catalysts. Recently a few reports have demonstrated the possibility of Mo_2C as a potential bifunctional (HER/OER) electrocatalysts.[16, 33] Still, there is a big room to improve their OER activity by decreasing the overpotential required to generate benchmark current of 10 mA cm^{-2} as at Ru/Ir oxide surfaces. In the recent times, some reports have shown that coupling Mo_2C with other transition metals (Co or Ni)[34-35] or making bimetallic (Co, Mo) carbides-based nanocomposite,[36] significantly improves the OER performance. Infect, Mo_2C based catalysts convert to actual OER active Mo-oxides by in-situ electro-oxidation during OER,[34] which already have been demonstrated as a good OER catalyst.[37] The presence of heteroatoms (e.g. B and N) in Mo-oxides structure could increase its OER activity and stability after in-situ oxidation heteroatom-doped Mo_2C. The similar modification strategies could be applied to enhance the OER/ORR and HER performance by doping the molybdenum carbide nanostructure with heteroatoms such B and N, which can improve electron/mass transfer and wetting properties.

Herein, we report a simple strategy to synthesize B and N co-doped molybdenum carbide, which display excellent electrocatalytic HER and OER performances in alkaline media. These hybrids are prepared by annealing the mixture of Mo-imidazole complex with optimized amount of boric acid (H_3BO_4), which relies on the restrained in-situ carburization between Mo-imidazole complex and H_3BO_4, thus forming molybdenum carbides nanoparticles imbedded in a BCN network. A unique advantage of this hybrid structure shows excellent HER and especially OER activity at post *in-situ* oxidized B and N dual doped Mo-oxide in 1.0M KOH and good ORR performance in 0.1M KOH better than most of molybdenum carbides reported in the literature. These exceptional performances are related to tiny nanoparticles, less charge transfer resistances and enhanced wetting properties due to the presence of boron and nitrogen species in carbide's network.

3.3 Methods

3.3.1 Synthesis of B and N co-doped Mo_2C nanoparticles

All chemicals were used as purchased without further purification. Mo-imidazole complex was synthesized by slightly modifying of previously reported methods aspects.[6, 38] Typically, 15 ml aqueous solution molybdenum chloride ($MoCl_5$) (3.0 mmol, Sigma-Aldrich) was gradually poured in ethanoic solution (35 mL) of imidazole (10.0 mmol, Sigma-Aldrich) to form brownish Mo-imidazole complex precipitates in a three neck round bottom flask (250 mL) equipped with magnetic stirrer and nitrogen purging line. To control the grain size and reaction kinetics, 20 mL of glycerol (Sigma) was added to the above solution. The reaction mixture was heated to 80-90 ^{0}C until the removal of whole water and ethanol. After cooling the reactor, the brownish precipitates of $Mo(ImH)_{1-x}Cl_x$ were collected and washed with plenty of ethanol to remove glycerol and unreacted species. Then, this freshly prepared suspension of $Mo(ImH)_{1-x}Cl_x$ was dried at 60 ^{0}C to obtain the precursor powder for molybdenum carbide NPs.

The precursor $Mo(ImH)_{1-x}Cl_x$ powder was annealed under Ar gas with ramping temperatures (5 ^{0}C/min) to a pre-optimized temperature (900 ^{0}C), kept there for 4 h and then cooled down naturally to get N-doped Mo_2C NPs. For B and N co-doped molybdenum carbides (B, N: Mo_2C@BCN -X) NPs, the different molar ratio of boric acid (X= 1:4, 2:4, 3:4 and 4:4) to $Mo(ImH)_{1-x}Cl_x$ precursor was grinded and annealed at above conditions. For comparison, undoped Mo_2C NPs were also prepared by simply annealing in H_2 atmosphere.

3.3.2 Physical characterization.

Crystallographic structure of the electrocatalysts was investigated by powder X-ray diffraction (XRD, PANalytical pw 3040/60 X'pert) with Cu Kα radiation. The morphologies were probed with field-emission scanning electron microscope (FE-SEM, Hitachi, S-4800, 15 kV) and transmission electron microscope (TEM, JEOL, JEM-2100). The chemical compositions, elemental mapping and in-depth crystal information of samples were collected by high resolution transmission electron microscope (HR-TEM, JEOL, JEM-2100F). X-ray photoelectron spectroscopy (XPS, ThermoFisher, K-alpha) was used to identify the chemical states of the surface atoms.

3.3.3 Electrochemical characterization

The catalyst ink was prepared by dispersing electrocatalysts (5.0 mg/mL) in an equal volume mixture of deionized water and ethanol, and 10 μL of 5% Nafion solution. The working electrode for HER and ORR was prepared by drop casting of 10 μL sonicated ink onto a glassy carbon electrode (0.4-0.5 mg/cm^2 loading) and drying at room temperature. The as-prepared ink of nanoparticles was loaded on nickel foam (NF) to make the electrodes for oxygen evolution reaction (OER). Electrochemical HER,

OER/ORR activity and stability tests were carried out in a three electrode cell configuration using a rotating disc electrode (RDE, PAR Model 636 RDE) attached with a potentiostat (Ivium technologies). An Ag/AgCl (3.0M NaCl) electrode and a graphite rod were used as reference and counter electrodes, respectively. All potentials were iR corrected and referenced to the reversible hydrogen electrode (RHE) by the equation $E_{RHE}=E_{(Ag/AgCl)} + 0.059pH + 0.20$.

The HER performance was measured in aqueous 1.0 M KOH (pH 13.7) at a scan rate of 2 mV/ s after 20 cyclic voltammetry (CV) cycles in the range of 0.4 to -0.3 V_{RHE}. The electrochemical stability tests were conducted by performing chronoamperometry (CA) for 20 h. Electrochemical impedance spectroscopy (EIS) was conducted in the same setup in the frequency range of 100 kHz to 1 mHz with a modulation amplitude of 10 mV. To evaluate the electrochemical active surface area (ECSA), CV was conducted from -0.8 to -0.6 V in 1.0 M KOH *vs.* Ag/AgCl with different sweep rates between 20 to 100 mV s^{-1}.

3.4 Results and discussion

The molybdenum complexes with imidazole (ImH) and its substituted derivatives [MoL_3X_3, L: imidazole and X: Cl^-, Br^-, NCS^-], have been widely studied due to their several biologically important aspects.[38] It is proposed that the tertiary (-N=C-) nitrogen of imidazole binds metal (Mo, Co) ions rather than the secondary (-N-H) nitrogen.[38-39] These Mo-complexes could be used as precursors for molybdenum carbides. Therefore, a yellow colored molybdenum-imidazole complex [$Mo(ImH)_{1-x}Cl_x$] was synthesized by aging the imidazole monomer with molybdenum chloride ($MoCl_5$) at 80 ºC for 24 hours as described in (**Eqn. 3.1**). Then the as-prepared complex was used as a precursor along with boric acid (H_3BO_4) to synthesize B and N co-doped Mo_2C NPs (denoted as B, N: Mo_2C@BCN). For fair comparison, nitrogen doped (N: Mo_2C@NC) and without doping Mo_2C NPs were also synthesized by just annealing Mo-Imidazole complex in the presence of argon and hydrogen environment, respectively. The overall synthesis process is presented in **Figure 3.1**, and the experimental detail is described in Experimental Section.

$$MoCl_5 + x(C_3H_4N_2) \xrightarrow{pH\sim4,\ \frac{80^{\circ}C}{24h}} Mo(ImH)_{1-x}Cl_x + xHCl \quad (3.1)$$

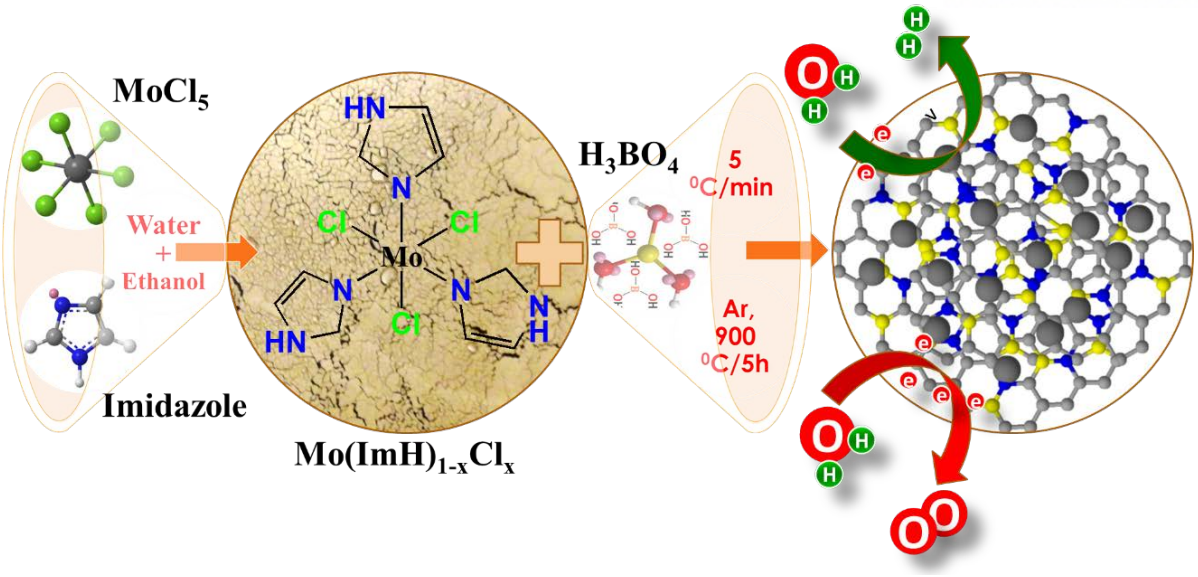

Figure 3.1. Schematic illustration of Mo–Imidazole complex assisted synthesis of B and N co-doped Mo_2C NPs (B,N:Mo_2C@BCN).

To identify chemical bonding between imidazole and molybdenum, the Fourier transform infrared (FTIR) spectra of $Mo(ImH)_{1-x}Cl_x$ is recorded in **Figure 3.2a**. The characteristic bands at 742, 968 and 1068 cm^{-1} are assigned to single and doubly bonded Mo with O and the signals at 1631 (–C=C), 3143 (–C–H) and 3415 (−N−H) are related to the imidazole functional groups. After the formation of Mo-Imidazole complex, the signal of C−N bond 1056 cm^{-1} is disappeared, indicating that the imidazole is bonded successfully to Mo atom through this tertiary nitrogen as reported in literature.[38-39] The nature of chemical bonding in $Mo(ImH)_{1-x}Cl_x$ is further studied by X-ray photoelectron spectroscopy (XPS). The XPS survey spectra (**Figure 3.2b**) confirms the presence of Mo, N, C and Cl species. A doublet at 231.4 & 234.6 eV in high resolution scan of Mo *3d* and two peaks at 198.1 & 199.7 in chlorine *2p* spectra indicate bonding between Mo-Cl as shown in **Figure 3.2c-d**. The other doublet at 232.5 & 235.5 eV in Mo *3d* are assigned to MoO_3. The signals at 284.7, 285.8 and 287.9 eV in C 1s (**Figure 3.2e**) are related to –C=C, –C=N and (–C–N–X) of imidazole. Similarly, in **Figure 3.2f**, the peaks at 395.9, 397.9, 400.3 and 402 eV are corresponded to Mo–N, pyridinic, pyrrolic and graphitic N. Thermogravimetric analysis (TGA) is conducted in air and N_2 to determine quantity of Mo and the carbonization temperature of $Mo(ImH)_{1-x}Cl_x$. As shown in **Figure 3.2f**, the whole quantity of imidazole is decomposed at ≈200 °C while the two decomposition steps are observed in $Mo(ImH)_{1-x}Cl_x$. The first degradation ranged from 250 to ≈700 °C, indicating the thermal decomposition of imidazole ligand to the carbon nitride matrix along with removal of H_2O and CO_2. The second-stage from 800 to 1000 °C can be attributed to the formation of nitrogen doped Mo-carbides through reaction between Mo species with the carbon nitride matrix and the graphitization of remaining carbon materials. Therefore, the

900 °C temperature is chosen to synthesize all catalysts in this study. The 4.1 wt. % of Mo element is confirmed by TGA in air.

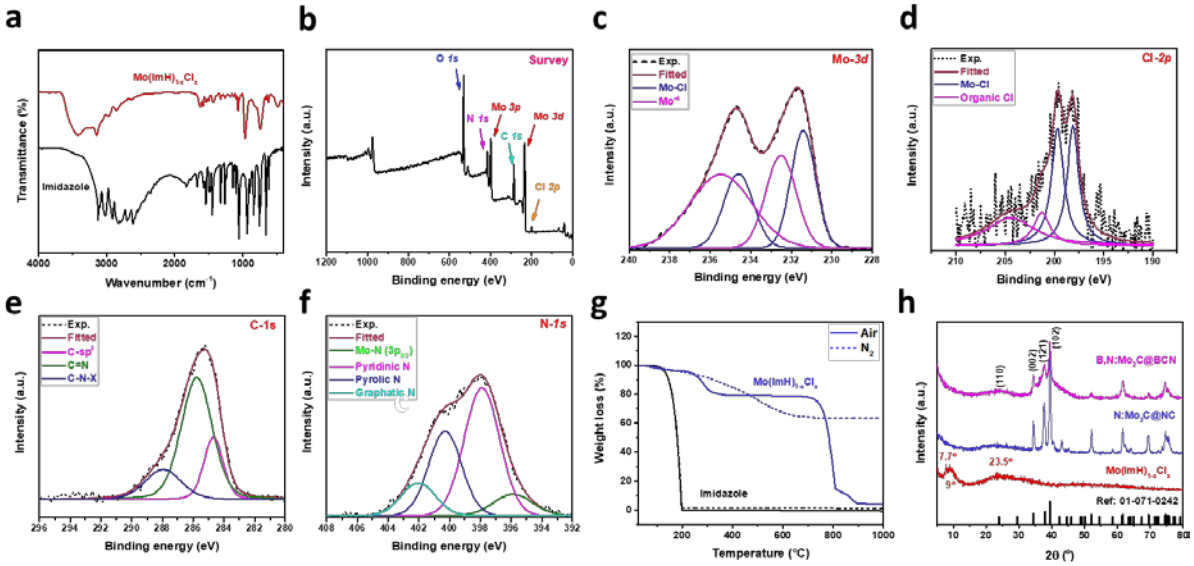

Figure 3.2. Fourier transform infrared (FTIR) spectra (a) X-ray photoelectron spectroscopy (XPS) survey (b) Mo 3d (c), Cl 2p (d), C 1s (e), N 1s (f) and Thermogravimetric (TGA) analysis (g) in N_2 and air of $Mo(ImH)_{1-x}Cl_x$. (h) X-ray diffraction (XRD) of Mo-imidazole complex (red), N-doped Mo_2C (blue) and B & N co-doped Mo_2C NPs (pink).

The crystal structure of $Mo(ImH)_{1-x}Cl_x$ was also determined by powder X-ray diffraction (XRD) in **Figure 3.2h**. The complex displays amorphous like structure with wide peaks at low angles 7.7, 9 and 23.5 indicated the organic-inorganic hybrids between imidazole and Mo. The orthorhombic β-phase of Mo_2C NPs (space group: Pbcn, ICDD No. 01-071-0242) in both N: Mo_2C@NC and B, N: Mo_2C@BCN catalysts, is confirmed by XRD patterns after thermal decomposition of $Mo(ImH)_{1-x}Cl_x$ at a pre-determined temperature of 900 °C by TGA as shown in **Figure 3.2g**. The B and N-doping does not significantly alter the bulk crystal structure of Mo_2C. Convincingly, B and N-doping was decreased the crystal size of Mo_2C NPs from 29.1 (pure Mo_2C@C) to 17.6 (N: Mo_2C@NC) and 8.6 nm for B, N: Mo_2C@BCN, was calculated by applying the Scherrer equation to X-ray line broadening. Conversely, the hydrogen treatment sintered the Mo_2C to bulk material by removal of nitrogen species as displayed in **Figure 3.3a**. Scanning electron microscopy (SEM) image of the as-synthesized B, N: Mo_2C@BCN catalyst (**Figure 3.3b**) display that particles with a grain size of ~50 nm form a closely interconnected porous B and N doped carbon network. Interestingly, the grain size increases without doping of B for N: Mo_2C@NC (70 nm) and pure Mo_2C@C (100 nm) as displayed in **Figure 3.3c**.

3.4.1 Structural evaluation of catalysts before and post HER/OER

The nature of chemical bonding and oxidation states of Mo_2CBN NPs were investigated after 20 h of HER or OER stability tests by XPS in **Figure 3.3d-f**. Two prominent Mo *3d* peaks at ≈228.2 and 232.4

eV (**Figure 3.3d**, bottom) can be assigned to ≈64 % of surface Mo_2C species along with 21 % MoO_2 (229.6, 233.6 eV) and 15% MoO_3 (232.7, 235.1 eV) due to surface oxidation.[40] The shift of Mo_2C $3d_{5/2}$ and $3d_{3/2}$ peaks towards lower binding energy near to elemental Mo (228 eV)[40] and less than pure β-Mo_2C (229.54; 232.59)[41] confirms the more electronic clouds around Mo atom because of the N and B doping into the structure, which can readily weaken the H–O–H bond of water by splitting it into adsorbed proton (H_{ad}) and hydroxyl ion (OH^-). The companionable role of B and N in Mo_2C structure to dissociate the water will be discussed later. The post HER Mo*3d* high scan spectra (**Figure 3.3d**, middle) confirms that there is no significant alteration at the surface of the catalyst during HER. The post-OER analysis of B, N: Mo_2C@BCN catalyst in **Figure 3.3** (top) suggest around 64% of Mo species are converted to Mo-oxides after the in-situ electro-oxidation of Mo_2C during OER which are actually responsible for OER as in a good agreement with the previous reports of MoO_2.[34, 37] The peak positions and catalyst composition calculated by integrating the area under the curves of XPS signals are summarized in **Table 3.1**.

Table 3.1. Chemical compositions of catalysts before and after HER/OER calculated Mo *3d* XPS spectra

Catalyst		Mo_2C	MoO_2	MoO_3
		$3d_{5/2}$+$3d_{3/2}$	**$3d_{5/2}$+$3d_{3/2}$**	**$3d_{5/2}$+$3d_{3/2}$**
Fresh B,N:Mo_2C@BCN	Peak position	228.2, 231.4	229.6, 233.6	232.7, 235
	Species %age	34.6+29.4 = **64.0**	17.3+3.7 = **21.0**	7.9+7.1 = **15.0**
After HER	Peak position	228.5, 231.6	229.5, 233.9	232.6, 235.8
	Species %age	31.2+26.8= **58.0**	13.9+7.1 = **21.0**	13.6+7.4 = **21.0**
After OER	Peak position	228.2, 231.5	229.5, 234.5	232.9, 236.4
	Species %age	25.8+8.2 = **34.0**	16.6+9.4= **26.0**	31.3+8.7 = **40.0**

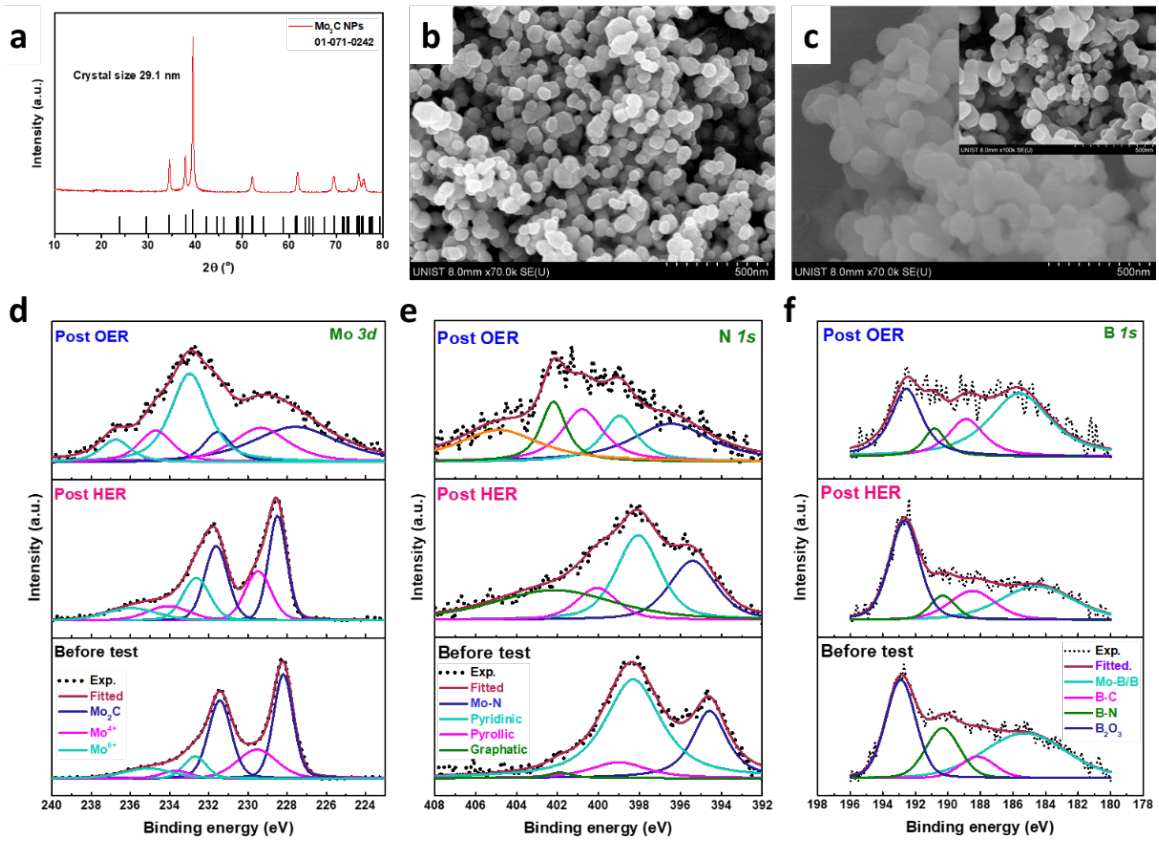

Figure 3.3. XRD pattern (a) of pure Mo_2C@C, SEM images of (b) B,N:Mo_2C@BCN, (c) N:Mo_2C@NC and (inset) pure Mo_2C@C. High-resolution XPS (d) Mo *3d*, (e) N 1s and (f) B 1s spectra of as-synthesized B,N:Mo_2C@BCN (bottom), post-HER (middle) and post-OER (top).

The elemental composition derived from XPS in **Table 3.2** shows an atomic ratio of N/B close to 1.6 for as-synthesized post-OER catalysts. However, post-OER catalyst displays a pronounced increment in O/Mo ratio from 1.7 (fresh) to 6.3 (after OER) due to dissociation of Mo-C bond and formation of OER active MoO_x species. The N1s XPS spectra (**Figure 3.3e**) give four peaks of Mo-N (396 eV), pyridinic N (398.2 eV), pyrrolic N (400 eV), graphitic N (402 eV) and one extra peak of N-O (404.2 eV) of post-OER catalyst. B1s spectra (**Figure 3.3f**) of the Mo_2CBN before (bottom), after HER (middle) and OER (top) confirms that these species are remained inside of the catalyst and strongly bonded to C, Mo, O and N playing active role in overall water splitting.

Table 3.2. Elemental compositions of catalysts before and after HER/OER test derived from XPS analysis

Catalyst	Elements derived from XPS data (At. %)						
	Mo	C	B	N	N:B	O	O:Mo
Fresh B,N:Mo_2C@BCN	10.8	58.9	4.7	7.6	1.62	18.0	1.7
After HER	7.2	63.3	4.1	4.2	1.02	21.2	2.9
After OER	4.5	58.3	3.4	5.6	1.65	28.2	6.3

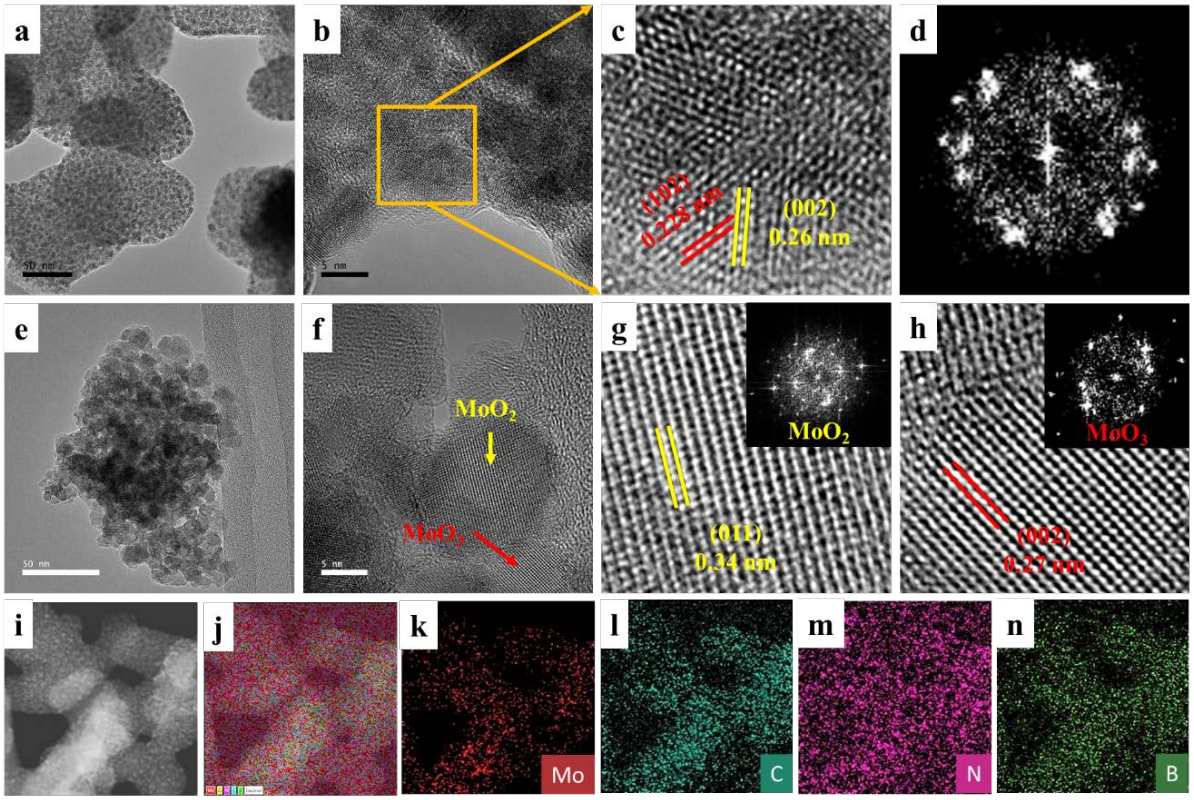

Figure 3.4. TEM image of (a) Mo_2C NPs imbedded in BCN network; average size of NPs is 5 nm, (b) HR-TEM image of B,N:Mo_2C@BCN NPs, (c) magnified HR-TEM images showing (102) and (002) planes and (d) corresponding FFT patterns . (e) TEM image, (f) HR-TEM image in-situ oxidized B,N:Mo_2C@BCN sample after 20-h OER durability test. Magnified HR-TEM images of (g) MoO_2 and (h) MoO_3 showing (011) and (002) planes and corresponding FFT patterns (inset). (i-m) EDS-STEM elemental maps for Mo (red), C (light green), N (purple) and B (dark green)

The Mo_2C NPs imbedded in B and N-doped carbon, are further characterized by high resolution transmission electron microscopy (HR-TEM) before and after OER long term stability test for 20 h. The Mo_2C NPs with an average size of ~5 nm (range: 3-10 nm) are embedded in B and N-doped carbon network as displayed in **Figure 3.4a**. The lattice fringes of 0.228 and 0.226 nm are assigned to the (102) and (002) facets of Mo_2C in HR-TEM image (**Figure 3.4b-c**) the corresponding fast Fourier transform (FFT) of orthorhombic β-phase of Mo_2C is also shown in **Figure 3.4d**. The electro-oxidation of B, N: Mo_2C@BCN NPs during OER is also observed by HR-TEM images in **Figure 3.4e-h**. The clear lattice fringes are observed with an interplaner distance from 0.34 nm for (011) plane of MoO_2 (PDF#: 01-086-0135, space group: P21/c) and 0.27 nm for (002) facet of MoO_3 (PDF#: 00-047-1081, space group: P21/c). Elemental mapping by energy-dispersive X-ray spectroscopy (EDS)-STEM of as-prepared B, N: Mo_2C@BCN NPs (**Figure 3.4i-n**) clearly display uniform distribution of Mo, C, B and N throughout the nanoparticles.

3.4.2 Mechanism of hydrogen and oxygen evolution reactions over Mo_2CBN NPs.

Before discussing the electrochemical HER/OER performance, it is desirable to see the synergistic effect of B and N doped carbon network. As it is already confirmed by XPS, the B and N elements directly/indirectly attached to the C atom which is then bonded to Mo atoms for B, N: Mo_2C@BCN catalyst. The nitrogen is more electronegative than C and B, therefore, it withdraws electron density from C–B bond through C–N bond and then donate its loan pair of electrons through sp^3 hybrid orbital to vacant *3d* orbital of Mo atom attached to adjacent C and hence causes in reducing the Mo oxidation state. As shown in **Figure 3.5** (HER upper part), the electron deficient B adsorbs water by coordinating with loan pair of electrons which then weakens O–H bond (**Eq.3.2**). The aqueous (H^+_{aq}) and adsorbed proton (H_{ad}) at MoCN site then combine to form hydrogen molecule (**Eq. 3.3**). The hydroxyl anion at B (OH^-_B) react with the nearby hydroxyl group (OH^-_{Mo}) of adsorb water molecule at adjacent Mo atom to form oxygen and hydrogen molecules as described in **Eq. 3.4** and in green square brackets of **Figure 3.5** (OER part).

$$H_2O + Mo_2CBN \longrightarrow H_{ad} - MoCN + OH_B - BCMo \qquad \text{(Eq. 3.2)}$$

$$H_{ad} - MoCN + H^+_{aq} + e^- \longrightarrow MoCN + H_2 \qquad \text{(Eq. 3.3)}$$

$$OH_B - BCMo + OH_{Mo} - MoCB \longrightarrow O_2 + H_2 + Mo_2CBN \qquad \text{(Eq. 3.4)}$$

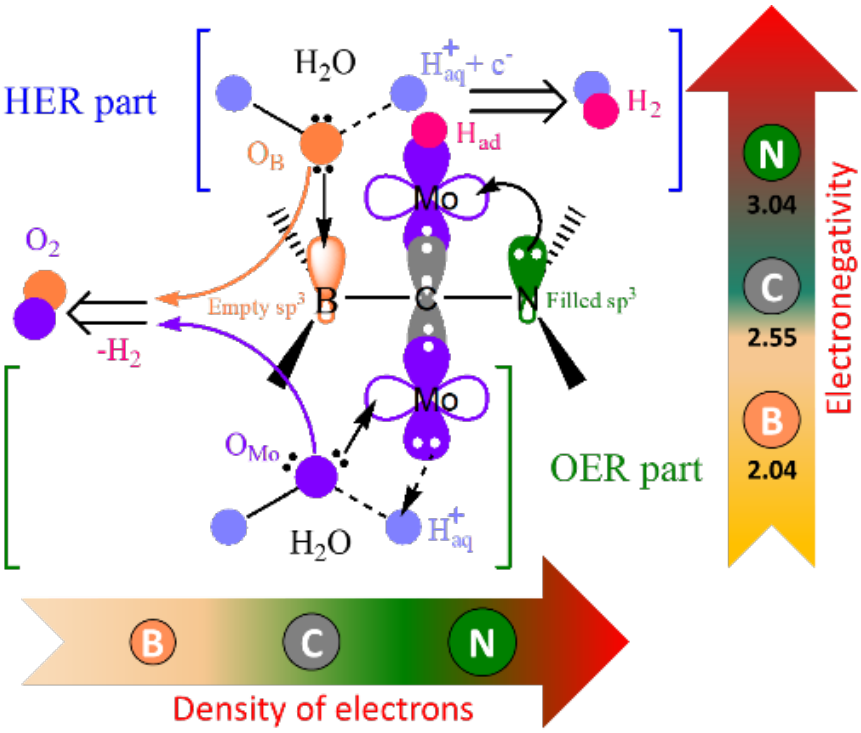

Figure 3.5. Mechanism of overall water splitting at B,N:Mo_2C@BCN nanoparticle showing the synergestics effect of B and N attached to C atom of Mo_2C for hydrogen evolution reaction in blue and oxygen evolution reaction in green square brackets.

3.4.3 Electrochemical HER and OER over Mo_2CBN catalysts

The HER performances of as-prepared Mo_2C-based electrocatalysts are measured in 1.0M KOH aqueous solution using a three-electrode electrochemical cell the iR-corrected polarization curves are displayed in **Figure 3.6a**. Undoped Mo_2C NPs give cathodic currents densities of 1 and 10 mA/cm^2 at overpotentials of η_1~115 mV and η_{10}~270 mV, respectively, similar to Mo_2C based catalysts reported in the literature.[23, 33] However, doping with nitrogen (N: Mo_2C@NC NPs) improves HER performance to η_1~35 mV and η_{10}~150 mV which is superior than most of the catalysts as shown in **Table 3.2**. Therefore, doping of a trace of N species into the structure of Mo_2C simply exerts a promotional effect on its HER performance in alkaline media. The HER activity of the Mo_2C NPs electrocatalyst is further increased when boron (B) species are introduced into the carbon network along with nitrogen. The polarization curve of B, N: Mo_2C@BCN in **Figure 3.6a** clearly display remarkable enhanced HER activity by lowering η_{10} value from 270 mV (Mo_2C NPs) to 94 mV. The inferior performance of B and N doped carbon (BCN) than Mo_2C NPs imbedded in it clear indication of Mo atoms are active sites. Surprisingly, the promotional effect remains effective when the N/B ratio is in between 1.5 to 1.8 as depicted in performance curves of different B, N: Mo_2C@BCN -X (X: 1 to 4) electrocatalysts of **Figure 3.6b**. The reduction in current density with increasing of B contents is due to the formation of boride species at high annealing temperature, which are considered as less active and not stable in alkaline media than Mo_2C as reported in literature.[20] As shown in **Figure 3.6c**, the B, N: Mo_2C@BCN-based catalysts needed much lower overpotentials (η_{10}) to generate current density of 10 mA cm^{-2} in 1.0M KOH as compared to other reported Mo_2C-based electrocatalysts in **Table 3.3**.

The Tafel analysis are conducted in **Figure 3.6d-e** gives the Tafel slopes; Mo_2C@C (144 mV/dec), N: Mo_2C@NC (97 mV/dec), B, N: Mo_2C@BCN-1 (119 mV/dec), B, N: Mo_2C@BCN-2 (91 mV/dec), B, N: Mo_2C@BCN-3 (62 mV/dec), B, N: Mo_2C@BCN-4 (111 mV/dec) and Pt/C (40 mV/dec). The results suggest that HER on these catalysts follows the Volmer−Heyrovsky mechanism on B, N: Mo_2C@BCN in alkaline media as described in **Figure 3.5** (HER part). The exchange current densities (J_0) at zero overpotential (**Figure 3.6f**, right) and overpotential for 100 mA cm^{-2} (**Figure 3.6f**, left) on different B, N: Mo_2C@BCN-X (X:1-4) are also compared with Pt/C, pure Mo_2C@C and N: Mo_2C@NC NPs. The comparable J_0 values of B, N: Mo_2C@BCN samples to the Pt/C confirm that the HER kinetics become faster due to electronic and chemical promotional effects of B and N-doping in carbide network.

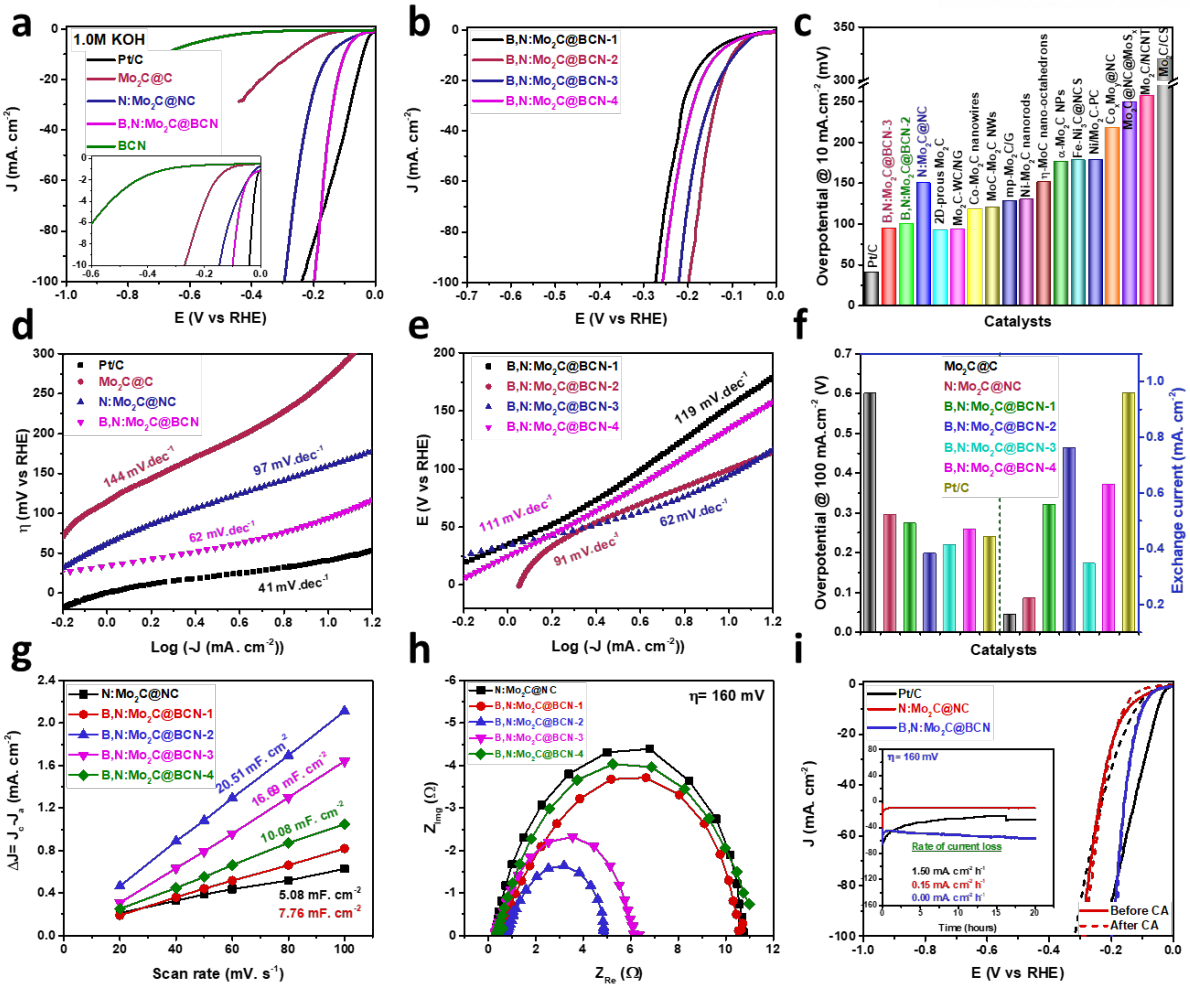

Figure 3.6. iR-corrected polarization curves during HER for (a) undoped Mo_2C@C NPs, N:Mo_2C@NC NPs, and B,N:Mo_2C@BCN NPs and (b) effect of B contents one HER performance curves. Comparison of overpotential at 10 mA cm-2 with other Mo_2C based electrocatalysts (c) and Tafel slopes in 1.0 M KOH (d-e). Comparison of exchange current densities (right) and η_{100} values (left) of all as-prepared catalysts (f), double layer capacitance (g) and EIS analysis (h). The polarization curves before and after 20h long chronoamperometry (CA) tests (inset) of Pt/C, N:Mo_2C@NC and B,N:Mo_2C@BCN (f).

In order to determine the promotional effect of B and N-doping on HER performance, the electrochemical surface area calculated from double layer capacitances (C_{dl}) and are measured at the electrolyte-electrode interface with cyclic voltammetry (CV) at different scan rates (20 to 100 mV s^{-1}). As shown in **Figure 3.6g**, C_{dl} and ECSA value of B, N: Mo_2C@BCN-2 (20.51 mF/cm^2, 512.8 cm^2) is higher than B, N: Mo_2C@BCN-3 (16.69 mF/cm^2, 427.3 cm^2), B, N: Mo_2C@BCN-4 (10.08 mF/cm^2, 252 cm^2), B, N: Mo_2C@BCN-1 (7.76 mF/cm^2, 194 cm^2) and N: Mo_2C@NC NPs (5.08 mF/cm^2, 127 cm^2). The higher C_{dl}, and electrochemical surface area (ECSA) are directly related to B and N co-doping in ultra-small carbide NPs as shown in HR-TEM images (**Figure 3.4a**). In order to find solution resistance (R_s) for iR correction and charge transfer resistance (R_{ct}), the electrochemical impedance spectroscopy (EIS) analysis was conducted for all electrocatalysts in 1.0M KOH at an overpotentials of 160 mV (**Figure 3.6h**). The relatively smaller R_{ct} values of B, N: Mo_2C@BCN-based catalysts than N-

doped Mo_2C NPs indicate improved charge transfer process at electrode-electrolyte interface due to duel B & N-doping.

Table 3.3. Comparison of HER performance of B and N co-doped molybdenum carbide (B,N:Mo_2C@BCN) catalysts with other Mo_2C-based electrocatalysts in alkaline media

Catalyst	η10 (mV)	Tafel slope (mV/dec)	References
B,N:Mo_2C@BCN NPs	**94**	**62**	**This work**
N:Mo_2C@NC NPs	**150**	**97**	
Pt/C	**41**	**40**	
Mo_2C–NCNT	257	--	*J. Mater. Chem. A* **2015,** *3* (11), 5783-5788.
Mo_2C/CS	320	82	*ChemSusChem* **2017,** *10*, 3540 –3546
Ni/Mo_2C-PC	179	101	*Chem. Sci.* **2017,** *8* (2), 968-973.
Mo_2C@NC@MoS_x	249	--	*Carbon* **2017,** *124*, 555-564.
Co_xMo_y@NC	218	31.5	*J. Mater. Chem. A* **2017,** *5* (32), 16929-16935.
2D porous Mo_2C	92	47	*Adv. Funct. Mater.* **2017,** *27* (45), 1703933
Co-Mo_2C nanowires	118	44	*Adv. Funct. Mater.* **2016,** *26* (31), 5590-5598.
MoC–Mo_2C NWs	120	42	*Chem. Sci.* **2016,** *7* (5), 3399-3405.
$(Mo_2C)_{0.34}$-$(WC)_{0.32}$/NG	93	53	*J. Mater. Chem. A* **2017,** *5* (35), 18494-18501.
mp Mo_2C/G	128	56	*ACS Appl. Mater. Inter.* **2016,** *8* (28), 18107-18118.
Ni-Mo_2C NRs	130	--	*Appl. Catal. B: Environ.* **2014,** *154*, 232-237.
η-MoC nano-octahedrons	151	59	*Nat. Commun.* **2015,** *6*, 6512.
α-Mo_2C NPs	176	58	*J. Mater. Chem. A* **2015,** *3* (16), 8361-8368.
Fe-Ni_3C-2%@NCS	178	36.5	*Angew. Chem.* **2017,** *129* (41), 12740-12744.

The another important factor, electrochemical stability was determined by the chronoamperometry (CA) test for up to 20 h at a static overpotential of 160 for B, N: Mo_2C@BCN, N: Mo_2C@NC NPs and Pt/C, respectively. As displayed in **Figure 3.6i** (inset), the B, N: Mo_2C@BCN electrode exhibits excellent stability without any current loss and negligible decrease in current densities per hour ($\Delta J/\Delta t$) of 0.15 $mA.cm^{-2}h^{-1}$ as compared to Pt/C (1.5 $mA.cm^{-2}h^{-1}$). The linear sweep voltammetry curves in **Figure 3.6i** show excellent stability for HER of B, N: Mo_2C@BCN catalyst even after a long period of 20 h operation than commercial Pt/C.

Now, the electrocatalytic OER performance of B, N: Mo_2C@BCN catalysts are compared in 1.0M KOH with pure Mo_2C@C, N: Mo_2C@NC NPs and a commercial IrO_2 electrode for the same mass loadings (~1.0 mg/cm^2) on 3D nickel foam (NF) substrate. As in **Figure 3.7a**, B, N: Mo_2C@BCN NPs electrode requires a lower overpotential (η_{10}~290 mV) to reach 10 mA/cm^2 as compared to N: Mo_2C@NC NPs (303 mV), Mo_2C@C NPs (366 mV) and commercial IrO_2 (337 mV). The OER performance is further

compared with different level of B and N-doping as shown in **Figure 3.7b**. The overpotential (η_{10}) values are also compared with other recently reported Mo_2C and Mo-based electrocatalysts as displayed in **Figure 3.7c**. The B and N doping in carbide skeleton significantly lowered the η_{10} values than other state of art Mo-based catalysts in 1.0M KOH as also enlisted in **Table 3.4**. As discussed before in **Figure 3.5**, the higher OER activity is attributed to the promotional effects of B and N species those remain inside of the catalyst (confirmed by XPS) even after *in-situ* oxidation of Mo during OER.

Table 3.4. Comparison of OER performance of B and N co-doped molybdenum carbide (B,N:Mo_2C@BCN) catalysts with other electrocatalysts in alkaline media.

Catalyst	η10 (mV)	Tafel slope (mV/dec)	References
B,N:Mo_2C@BCN NPs	**290**	**61**	**This work**
N:Mo_2C@NC NPs	**303**	**66**	
IrO_2 NPs	**337**	**82**	
Mo_2C/CS	380	98	*J. Mater. Chem. A* **2015,** *3* (11), 5783-5788.
Co_xMo_y@NC	330	46.1	*J. Mater. Chem. A* **2017,** *5* (32), 16929-16935.
Ni_3C/C	330	46	*Adv. Mater.* **2016,** *28* (17), 3326-3332.
$Co_6Mo_6C_2$/NCRGO	260	50	*ACS Appl. Mater. Inter.* **2017,** *9* (20), 16977-16985
Ni/Mo_2C-PC	386	--	*Chem. Sci.* **2017,** *8* (2), 968-973.
Mo–N/C@MoS_2	390	65	*Adv. Funct. Mater.* **2017,** *27* (44).
MoS_2@CoF	297	47	*Nanoscale* **2017,** *9* (8), 2711-2717.
a-MoS_x/$Co(OH)_2$ NSs	350	65.4	*J. Mater. Chem. A* **2017,** *5* (44), 23103-23114.
MoS2-Ni_3S_2 HNRs/NF	249	57	*ACS Catal.* **2017,** *7* (4), 2357-2366.
$Mo_{(1-x)}W_xS_2$@Ni_3S_2 heterostructure	285	90	*ACS Appl. Mater. Inter.* **2017,** *9* (31), 26066-26076.
MoP/Ni_2P/NF	≈300	77.6	*J. Mater. Chem. A* **2017,** *5* (30), 15940-15949.
γ-MoC/Ni@NC	310	62.7	*Nanoscale* **2017,** *9* (17), 5583-5588.
Fe/Co–N–C	380	61	*Adv. Funct. Mater.* **2017,** *27* (17), 1606497
Fe-Ni3C-2%@NCS	275	62	*Angew. Chem.* **2017,** *129* (41), 12740-12744.
Ti_3C_2@g-C_3N_4	420	74.6	*Angew. Chem. Int. Ed.* **2016,** *55* (3), 1138-1142.

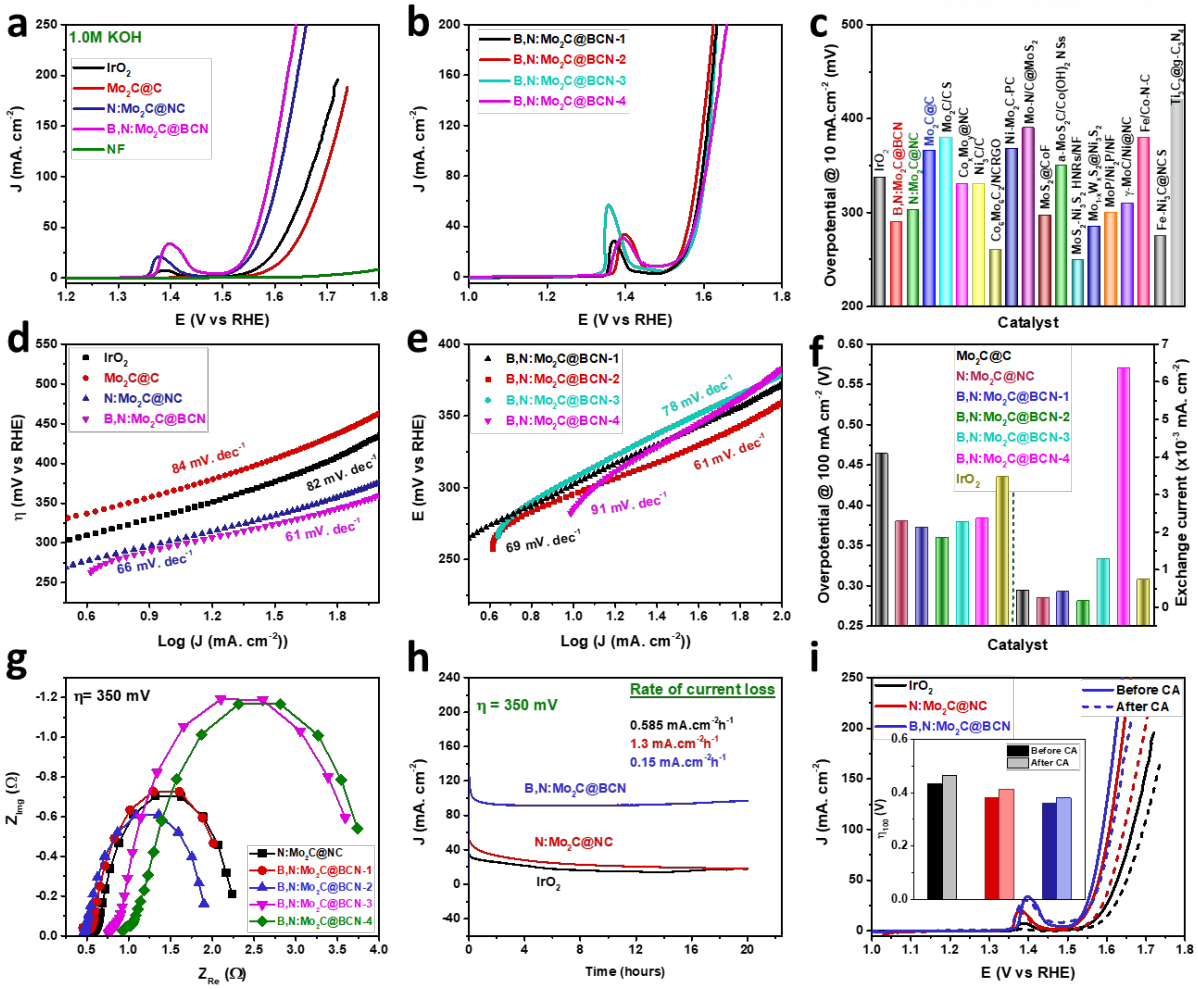

Figure 3.7. iR-corrected polarization curves of OER for (a, b) all catalysts loaded on NF electrode, (c) comparison of η_{10} value with other Mo-based electrocatalysts and corresponding (d, e) Tafel slopes in 1.0 M KOH. (f) Comparison of exchange current densities (right) and η_{100} values (left) of all as-prepared catalysts, (g) EIS analysis at overpotential of 350 mV, (h) OER durability as determined by CA, (i) LSV curves and comparison of overpotentials (inset) required for 100 mA cm^{-2} before and after 20-h CA durability test for IrO_2, N:Mo_2C@NC and B,N:Mo_2C@BCN in 1.0 M KOH.

The Tafel slopes of different Mo_2CBN based electrocatalysts (**Figure 3.7d-e**) lie in the range of 61-78 mV/dec. The Tafel slope of B, N: Mo_2C@BCN (61 mV/dec) is much lower than those Tafel slopes for IrO_2 electrode (82 mV/dec), pure Mo_2C@C (84 mV/dec) and N: Mo_2C@NC NPs (64 mV/dec). The exchange currents (J_0) and the overpotential required to generate current density of 50 mA cm^{-2} are also compared in **Figure 3.7f**. Interestingly, the J_0 values for B, N: Mo_2C@BCN catalysts is almost same or more than IrO_2, Mo_2C@C and N: Mo_2C@NC NPs, indicating a more rapid OER kinetics especially on B, N: Mo_2C@BCN electrode. The B, N: Mo_2C@BCN-2 requires (**Figure 3.7f**, left) the lowest overpotential (η50~336 mV) to produce current of 100 mA/cm^2 relative to B, N: Mo_2C@BCN-1 (350 mV), N: Mo_2C@NC (351 mV), B, N: Mo_2C@BCN-3 NPs (353 mV), B, N: Mo_2C@BCN-4 (358 mV) and commercial IrO_2@NF (397 mV). The EIS measurements are also conducted for B, N: Mo_2C@BCN catalysts at constant overpotential of 350 mV in **Figure 1.7g**. The low charge-transfer resistance R_{ct} of

B, N: Mo_2C@BCN-2 (~1.5 ohm) than those of N: Mo_2C@NC (1.9 ohm), B, N: Mo_2C@BCN-1 (1.81 ohm), B, N: Mo_2C@BCN-3 (3.7 ohm) and B, N: Mo_2C@BCN-4 CoP NPs (3.9 ohm) is related to the rapid faster ions/electrons transfer on the Mo_2CBN-2 electrode for water oxidation, confirming the promotional effect of dual B and N-doping for improved OER performance. Interestingly, either increasing the B contents or without B as in N: Mo_2C@NC increased the charge transfer resistance by lowering the HER/OER performance.

The current-time (*i-V*) test for 20 h long OER was also performed at a constant overpotential of ~350 mV to evaluate the stability of IrO_2, N: Mo_2C@NC and B, N: Mo_2C@BCN electrodes in **Figure 3.7h**. The initial decrease in current density in all CA curves of Mo_2C based catalyst is related to in-situ formation of Mo-oxides by dissolution of surface Mo-C species, after 30 minutes the B, N: Mo_2C@BCN gets the equilibrium state in contrast of IrO_2 electrode, i.e. continuous reduction in current. The overall rate of current loss of IrO_2 electrode (0.585 mA. $cm^{-2}h^{-1}$) is much higher than of Mo_2CBN B, N: Mo_2C@BCN. The degradation of N: Mo_2C@NC electrode also faster than B, N: Mo_2C@BCN) clearly indicate the significance of B and N co-doping. The polarization curves were also compared (**Figure 3.7i**) before and after chronoamperometry (CA) test for 20 h. The negligible reduction in overpotentials required at 100 mA.cm^{-2} for Mo_2CBN catalyst (**Figure 3.7i**, inset) displays excellent stability and higher conductivity for OER even after 20 h of OER operation due to presence of trace B and N elements. All above results have demonstrated that the B and N dual-doping has significantly improved HER and OER activities along with exceptional stability.

After usefully electrochemical water splitting over B, N: Mo_2C@BCN NPs, we tested them for oxygen reduction reactions (ORR). Linear sweep voltammetry (LSV) polarization curves were first performed for the B, N: Mo_2C@BCN catalyst in an O_2/N_2-saturated 0.1 M aqueous KOH solution. As displayed in **Figure 3.8**, the B, N: Mo_2C@BCN catalysts have more positive onset and half-wave potentials than of pure Mo_2C and N: Mo_2C@NC NPs. The onset and overpotential required to produce current density of 1 mA cm^{-2} of all B, N: Mo_2C@BCN catalysts lie in the range of 0.86-0.88 V and 0.78-0.79 V, respectively, which are much higher than of pure Mo_2C (0.78 & 0.66 V) and N: Mo_2C@NC NPs (0.83 & 0.73 V). Although, the ORR performance are not up to the mark as the state of art Pt/C catalyst, but more than other recently reported Mo_2C based electrocatalysts.[42-45] This basic study provides the opportunity to tune the electronic properties of other transition metal carbides/nitrides materials. Secondly, these NPs can be used as co-catalysts with other highly active ORR catalysts.

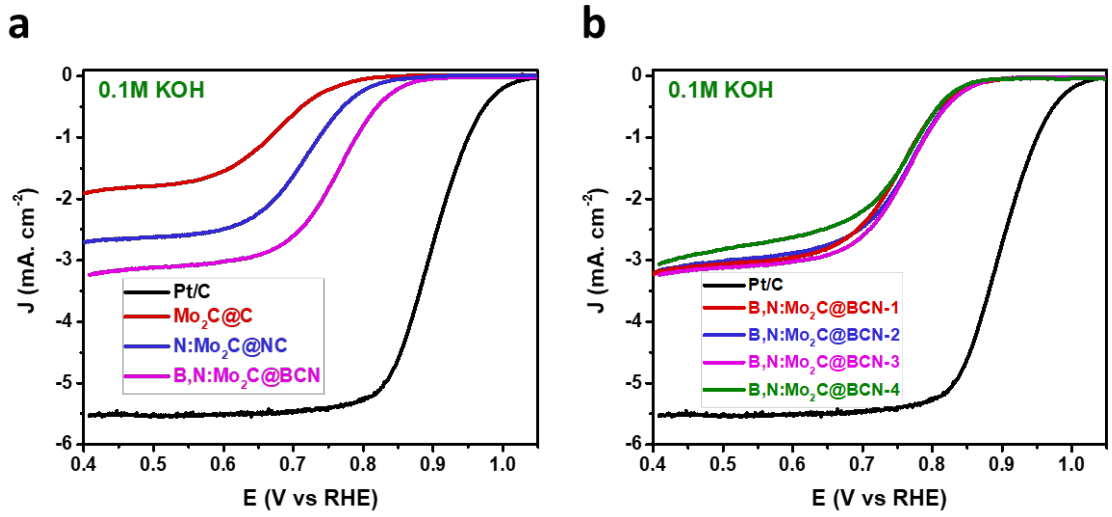

Figure 3.8. Polarization curves (without iR correction) of as-synthesized different Mo_2C based catalysts for ORR in O_2-saturated 0.1M KOH aqueous solution.

3.5 Conclusions

In summary, the electronic/chemical properties of Mo_2C were regulated by doping N and B into its structure through a novel Mo-imidazole complex route, in which a monomer, namely, imidazole, works as a source of graphitic C & N and controls the particle size of Mo_2C, while H_3BO_4 is the source of B. The as-synthesized trifunctional HER, OER and ORR B, N: Mo_2C@BCN NPs, display excellent electrocatalytic performance and remarkable stability especially during both the HER and the OER. Further, their performances exceed those of the other reported Mo_2C based electrocatalysts in the literature. The mechanistic study and role of B and N species as co-catalyst in Mo_2C structure for water electrolysis to generate hydrogen and oxygen is also conducted, which indicate that the excellent performance of Mo_2C is related to the improved charge/mass-transfer and wetting properties due to the modifications induced in their electronic structure with B and N co-doping. The present, unique and eco-friendly synthesis method could also become a general approach to tune the electrochemical characteristics of other transition metal carbides for use as water-splitting bifunctional or oxygen reduction catalysts.

3.6 References

1. Roger, I.; Shipman, M. A.; Symes, M. D., Earth-abundant catalysts for electrochemical and photoelectrochemical water splitting. *Nat. Rev. Chem.* **2017,** *1*, 0003.

2. Bashyam, R.; Zelenay, P., A class of non-precious metal composite catalysts for fuel cells. *Nature* **2006,** *443* (7107), 63-66.

3. Chu, S.; Cui, Y.; Liu, N., The path towards sustainable energy. *Nat. Mater.* **2017,** *16* (1), 16-22.

4. Zou, X.; Zhang, Y., Noble metal-free hydrogen evolution catalysts for water splitting. *Chem. Soc. Rev.* **2015,** *44* (15), 5148-5180.

5. Faber, M. S.; Jin, S., Earth-abundant inorganic electrocatalysts and their nanostructures for energy conversion applications. *Energy & Environmental Science* **2014,** *7* (11), 3519-3542.

6. Anjum, M. A. R.; Lee, M. H.; Lee, J. S., BCN Network-Encapsulated Multiple Phases of Molybdenum Carbide for Efficient Hydrogen Evolution Reaction in Acidic and Alkaline Media. *J. Mater. Chem. A* **2017,** *5* (25), 13122-13129

7. Anjum, M. A. R.; Lee, J. S., Sulfur and Nitrogen Dual-Doped Molybdenum Phosphide Nanocrystallites as an Active and Stable Hydrogen Evolution Reaction Electrocatalyst in Acidic and Alkaline Media. *ACS Catal.* **2017,** *7* (4), 3030-3038.

8. Anantharaj, S.; Ede, S. R.; Sakthikumar, K.; Karthick, K.; Mishra, S.; Kundu, S., Recent Trends and Perspectives in Electrochemical Water Splitting with an Emphasis on Sulfide, Selenide, and Phosphide Catalysts of Fe, Co, and Ni: A Review. *ACS Catal.* **2016,** *6* (12), 8069-8097.

9. Wang, J.; Cui, W.; Liu, Q.; Xing, Z.; Asiri, A. M.; Sun, X., Recent Progress in Cobalt-Based Heterogeneous Catalysts for Electrochemical Water Splitting. *Adv. Mater.* **2016,** *28* (2), 215-230.

10. Xie, L.; Zhang, R.; Cui, L.; Liu, D.; Hao, S.; Ma, Y.; Du, G.; Asiri, A. M.; Sun, X., High-Performance Electrolytic Oxygen Evolution in Neutral Media Catalyzed by a Cobalt Phosphate Nanoarray. *Angew. Chem.* **2017,** *129* (4), 1084-1088.

11. Zheng, Y.; Jiao, Y.; Zhu, Y.; Li, L. H.; Han, Y.; Chen, Y.; Jaroniec, M.; Qiao, S.-Z., High Electrocatalytic Hydrogen Evolution Activity of an Anomalous Ruthenium Catalyst. *J. Am. Chem. Soc.* **2016,** *138* (49), 16174-16181.

12. Rheinländer, P. J.; Herranz, J.; Durst, J.; Gasteiger, H. A., Kinetics of the hydrogen oxidation/evolution reaction on polycrystalline platinum in alkaline electrolyte reaction order with respect to hydrogen pressure. *J. Electrochem. Soc.* **2014,** *161* (14), F1448-F1457.

13. Wu, H. B.; Xia, B. Y.; Yu, L.; Yu, X.-Y.; Lou, X. W. D., Porous molybdenum carbide nano-octahedrons synthesized via confined carburization in metal-organic frameworks for efficient hydrogen production. *Nat. Commun.* **2015,** *6*, 6512.

14. Zhao, Y.; Kamiya, K.; Hashimoto, K.; Nakanishi, S., In Situ CO_2-Emission Assisted Synthesis of Molybdenum Carbonitride Nanomaterial as Hydrogen Evolution Electrocatalyst. *J. Am. Chem. Soc.* **2014,** *137* (1), 110-113.

15. Ma, T. Y.; Cao, J. L.; Jaroniec, M.; Qiao, S. Z., Interacting Carbon Nitride and Titanium Carbide Nanosheets for High-Performance Oxygen Evolution. *Angew. Chem. Int. Ed.* **2016,** *55* (3), 1138-1142.

16. Regmi, Y. N.; Wan, C.; Duffee, K. D.; Leonard, B. M., Nanocrystalline Mo2C as a bifunctional water splitting electrocatalyst. *ChemCatChem.* **2015,** *7* (23), 3911-3915.

17. Pang, M.; Li, C.; Ding, L.; Zhang, J.; Su, D.; Li, W.; Liang, C., Microwave-assisted preparation of Mo2C/CNTs nanocomposites as efficient electrocatalyst supports for oxygen reduction reaction. *Ind. Eng. Chem. Res.* **2010,** *49* (9), 4169-4174.

18. Levy, R.; Boudart, M., Platinum-like behavior of tungsten carbide in surface catalysis. *Science* **1973,** *181* (4099), 547-549.

19. Liu, Y.; Yu, G.; Li, G. D.; Sun, Y.; Asefa, T.; Chen, W.; Zou, X., Coupling Mo2C with Nitrogen-Rich Nanocarbon Leads to Efficient Hydrogen-Evolution Electrocatalytic Sites. *Angew. Chem. Int. Ed.* **2015,** *54* (37), 10752-10757.

20. Vrubel, H.; Hu, X., Molybdenum boride and carbide catalyze hydrogen evolution in both acidic and basic solutions. *Angew. Chem.* **2012,** *124* (51), 12875-12878.

21. Liao, L.; Wang, S.; Xiao, J.; Bian, X.; Zhang, Y.; Scanlon, M. D.; Hu, X.; Tang, Y.; Liu, B.; Girault, H. H., A nanoporous molybdenum carbide nanowire as an electrocatalyst for hydrogen evolution reaction. *Energy Environ. Sci.* **2014,** *7* (1), 387-392.

22. Wan, J.; Wu, J.; Gao, X.; Li, T.; Hu, Z.; Yu, H.; Huang, L., Structure Confined Porous Mo2C for Efficient Hydrogen Evolution. *Adv. Funct. Mater.* **2017,** *27* (45), 1703933.

23. Zhang, K.; Zhao, Y.; Fu, D.; Chen, Y., Molybdenum carbide nanocrystal embedded N-doped carbon nanotubes as electrocatalysts for hydrogen generation. *J. Mater. Chem. A* **2015,** *3* (11), 5783-5788.

24. Tang, C.; Wang, W.; Sun, A.; Qi, C.; Zhang, D.; Wu, Z.; Wang, D., Sulfur-decorated molybdenum carbide catalysts for enhanced hydrogen evolution. *ACS Catal.* **2015,** *5* (11), 6956-6963.

25. Shi, Z.; Nie, K.; Shao, Z.-J.; Gao, B.; Lin, H.; Zhang, H.; Liu, B.; Wang, Y.; Zhang, Y.; Sun, X., Phosphorus-Mo 2 C@ carbon nanowires toward efficient electrochemical hydrogen evolution: composition, structural and electronic regulation. *Energy Environ. Sci.* **2017,** *10* (5), 1262-1271.

26. Ito, Y.; Cong, W.; Fujita, T.; Tang, Z.; Chen, M., High Catalytic Activity of Nitrogen and Sulfur Co-Doped Nanoporous Graphene in the Hydrogen Evolution Reaction. *Angew. Chem. Int. Ed.* **2015,** *54* (7), 2131-2136.

27. Zhang, K.; Zhao, Y.; Zhang, S.; Yu, H.; Chen, Y.; Gao, P.; Zhu, C., MoS 2 nanosheet/Mo 2 C-embedded N-doped carbon nanotubes: synthesis and electrocatalytic hydrogen evolution performance. *J. Mater. Chem. A* **2014,** *2* (44), 18715-18719.

28. Zhao, Z.; Qin, F.; Kasiraju, S.; Xie, L.; Alam, M. K.; Chen, S.; Wang, D.; Ren, Z.; Wang, Z.; Grabow, L. C., Vertically Aligned MoS2/Mo2C hybrid Nanosheets Grown on Carbon Paper for Efficient Electrocatalytic Hydrogen Evolution. *ACS Catal.* **2017,** *7* (10), 7312-7318.

29. Xiao, P.; Yan, Y.; Ge, X.; Liu, Z.; Wang, J.-Y.; Wang, X., Investigation of molybdenum carbide nano-rod as an efficient and durable electrocatalyst for hydrogen evolution in acidic and alkaline media. *Appl. Catal. B: Environ.* **2014,** *154*, 232-237.

30. Lin, H.; Liu, N.; Shi, Z.; Guo, Y.; Tang, Y.; Gao, Q., Cobalt-Doping in Molybdenum-Carbide Nanowires Toward Efficient Electrocatalytic Hydrogen Evolution. *Adv. Funct. Mater.* **2016,** *26* (31), 5590-5598.

31. Hunt, S. T.; Nimmanwudipong, T.; Román-Leshkov, Y., Engineering Non-sintered, Metal-Terminated Tungsten Carbide Nanoparticles for Catalysis. *Angew. Chem. Int. Ed.* **2014,** *53* (20), 5131-5136.

32. Zhang, Q.; Tackett, B. M.; Wu, Q.; Chen, J. G., Trends in Hydrogen Evolution Activity of Metal-Modified Molybdenum Carbides in Alkaline and Acid Electrolytes. *ChemElectroChem.* **2016,** *3* (10), 1686-1693.

33. Wang, H.; Cao, Y.; Sun, C.; Zou, G.; Huang, J.; Kuai, X.; Zhao, J.; Gao, L., Strongly coupled molybdenum carbide@ carbon sheets as a bifunctional electrocatalyst for overall water splitting. ChemSusChem. **2017**.

34. Jiang, J.; Liu, Q.; Zeng, C.; Ai, L., Cobalt/molybdenum carbide@ N-doped carbon as a bifunctional electrocatalyst for hydrogen and oxygen evolution reactions. J. Mater. Chem. A **2017,** 5 (32), 16929-16935.

35. Yu, Z.-Y.; Duan, Y.; Gao, M.-R.; Lang, C.-C.; Zheng, Y.-R.; Yu, S.-H., A one-dimensional porous carbon-supported Ni/Mo 2 C dual catalyst for efficient water splitting. Chem. Sci. **2017,** 8 (2), 968-973.

36. Tang, Y.-J.; Liu, C.-H.; Huang, W.; Wang, X.-L.; Dong, L.-Z.; Li, S.-L.; Lan, Y.-Q., A Bimetallic Carbides-based Nanocomposite as Superior Electrocatalyst for Oxygen Evolution Reaction. ACS Appl. Mater. Interfaces **2017,** 9 (20), 16977-16985.

37. Jin, Y.; Wang, H.; Li, J.; Yue, X.; Han, Y.; Shen, P. K.; Cui, Y., Porous MoO2 Nanosheets as Non-noble Bifunctional Electrocatalysts for Overall Water Splitting. Adv. Mater. **2016,** 28 (19), 3785-3790.

38. Prasad, K.; Tripathy, A.; Thakur, N., Molybdenum (III) complexes with some imidazoles. Polyhedron **1991,** 10 (3), 323-324.

39. Park, K. S.; Ni, Z.; Côté, A. P.; Choi, J. Y.; Huang, R.; Uribe-Romo, F. J.; Chae, H. K.; O'Keeffe, M.; Yaghi, O. M., Exceptional chemical and thermal stability of zeolitic imidazolate frameworks. Proc. Natl. Acad. Sci. **2006,** 103 (27), 10186-10191.

40. Fleisch, T.; Mains, G., An XPS study of the UV reduction and photochromism of MoO3 and WO3. J. Chem. Phy. **1982,** 76 (2), 780-786.

41. Wan, C.; Regmi, Y. N.; Leonard, B. M., Multiple phases of molybdenum carbide as electrocatalysts for the hydrogen evolution reaction. Angew. Chem. **2014,** 126 (25), 6525-6528.

42. Wang, H.; Sun, C.; Cao, Y.; Zhu, J.; Chen, Y.; Guo, J.; Zhao, J.; Sun, Y.; Zou, G., Molybdenum carbide nanoparticles embedded in nitrogen-doped porous carbon nanofibers as a dual catalyst for hydrogen evolution and oxygen reduction reactions. Carbon **2017,** 114, 628-634.

43. Liao, L.; Bian, X.; Xiao, J.; Liu, B.; Scanlon, M. D.; Girault, H. H., Nanoporous molybdenum carbide wires as an active electrocatalyst towards the oxygen reduction reaction. Phy. Chem. Chem. Phy. **2014,** 16 (21), 10088-10094.

44. Luo, Y.; Wang, Z.; Fu, Y.; Jin, C.; Wei, Q.; Yang, R., In situ preparation of hollow Mo 2 C–C hybrid microspheres as bifunctional electrocatalysts for oxygen reduction and evolution reactions. J. Mater.s Chem. A **2016,** 4 (32), 12583-12590.

45. Huang, K.; Bi, K.; Liang, C.; Lin, S.; Wang, W.; Yang, T.; Liu, J.; Zhang, R.; Fan, D.; Wang, Y., Graphite carbon-supported Mo2C nanocomposites by a single-step solid state reaction for electrochemical oxygen reduction. PloS one **2015,** 10 (9), e0138330.

4. Sulfur and Nitrogen Dual-Doped Molybdenum Phosphide Nanoparticles for Catalyzing Hydrogen Evolution Reaction Efficiently

4.1 Abstract

The electrochemical properties of molybdenum phosphides nanocrystallite (MoP) are tuned by dual-doping of S and N via a unique and ecofriendly (thio)urea-phosphate-assisted rout. The S and N co-doped MoP/SN nanoparticles are synthesized by in-situ reductive phosphidation of locally generated hybrid composite of ammonium phosphate and P-doped MoS_x in the presence of hydrogen gas. The MoP nanoparticles are grown on self S and N-doped graphene to synthesize a hybrid catalyst (MoP/SNG). These hybrid electrocatalyst display remarkable and stable performance for electrochemical hydrogen evolution reaction in both 0.5M H_2SO_4 and 1.0M KOH aqueous solutions surpassing the most of MoP-based HER catalysts reported in the literature so far. The dual S and N doping in to the structure of MoP and graphene maximize electronic/protonic conductivity, help to stabilize ultrasmall MoP nanoparticles and causing to improve catalytic activity in both acidic and alkaline aqueous media.

4.2 Introduction

The electrochemical water splitting has captivated a massive attention recently to generate sustainable pure hydrogen gas with electricity produced from renewable energy-producing stations. A great challenge in electrochemical hydrogen evolution reaction (HER) from water is to replace expensive platinum with inexpensive non-precious metal.[1] The extensive efforts have be made in this direction by developing other transition metals alloys or their compounds like carbides, sulfides, borides, nitrides, and phosphides.[1-5] Because of the high conductivity, mechanical and chemical stability, the transition metal phosphides (TMPs) have extensively explored since last few years as an alternative of Pt.[4-6] They have been shown high HER activity, good stability, and almost ≈100% Faradic efficiency in all pH values.[6-11] According to previous findings the inserting P atoms into the lattice of transition metals (Fe, Co, Ni, Cu, Mo and W) plays an important role by acting as basic trap for protons (H^+) due to more electronegativity than other transition metals.[6, 12-14] The proper atomic ratio of TMs and P, commonly in metal-rich phosphides, provides superb electron/proton conductivity and behaves more noble metal-like comparative to individual transition metals.[15] However, there are still many challenges to enhance their catalytic properties and stability in alkaline and acidic solution. This could be achieved by modifying their electronic properties via doping with other heteroatoms and stabilizing P^{-3} in TMPs (less stable oxidation state of P) from dissolution in acidic and basic pH.

The more electronegative P atoms in TMPs withdraw electron density form the parent transition metals, causing in reduction of conductivity.[16] However, with an appropriate doping of other heteroatoms like S or N, the metal-rich phosphide can display more metallic properties or even superconductivity.[17] In recent years, similar approached have been adopted to improve the HER performance of MoP; i) making molybdenum phosphosulfide (MoP|S) structure by a post-sulfidation of MoP,[8] or post-phosphidation of MoS_2,[18] ii) growing nanoparticles on carbon materials like graphene,[19] or porous carbons,[20] and iii) doping other TMs (Co, Fe or W).[21-24] The TMPs are generally prepared via three common procedures: i) Solution-phase phosphidation of TMs by organic phosphine (e.g. tri-n-octylphosphine (TOP), tri-phenylphosphine (TPP) or tri-n-octylphosphine oxide (TOPO)) usually in high boiling point solvents like oleylamine,[17, 25] ii) reduction with highly dangerous and lethal PH_3 gas,[26] and iii) reduction of metal phosphates at high temperature to get the bulk TMPs.[17]

Herein, S and N co-doped MoP (MoP/SN) nanoparticles are synthesized by developing a unique, inexpensive and environmental-friendly (thio)urea-phosphate-assisted approach. The hybrid composites of MoP NPs with S and N doul-doped graphene (MoP/SNG) display excellent electrocatalytic activity and stability for HER compared to other non-noble metal electrocatalysts in both 0.5M H_2SO_4 and 1.0M KOH aqueous solutions. The present study relies on sulfidation of phosphomolybdic acid (PMo_{12}) by in-situ generated H_2S gas from thiourea in the presence phosphoric acid to generate a mixture of ammonium phosphate and P-doped MoS_x. Upon reduction of this hybrid in H_2 gas the MoP/SN NPs are formed. The doping level, phase and size of nanoparticles are controlled by manipulating the H_3PO_4 to thiourea in urea-phosphate system. Additionally, the carbon supports like graphene is also self-doped with N and S atoms by in-situ generated NH_3 and H_2S gas. These heteroatoms stabilize the P^{-3} state by making Mo/P-N and Mo/P-S bonds, enhances the electrical/protonic conductivity and increase proton adsorption sites via S and N. Because of simplicity, inexpensive and ecofriendly precursors, the other transition metal phosphides could be prepared by replacing or avoiding the use of costly, lethal and corrosive chemicals like PH_3, hypophosphite, organic phosphine and high boiling organic solvents.

4.3 Experimental section

4.3.1 Synthesis of S and N co-doped MoP NPs and their graphene composite

All chemicals were utilized as purchased without further purification. Thiourea-phosphate was synthesized by mixing thiourea with phosphoric acid. Typically, 85% phosphoric acid (5.5 mmol, 634.12 mg, Sigma-Aldrich) was dissolved in triply distilled water (20 mL) in a glass beaker (250 mL) equipped with a magnetic stirring bar and an aqueous solution thiourea (5.0 mmol, 380.60 mg, Sigma) was then added. The reaction mixture was heated to 60 ºC until the clear solution was obtained and was

maintained at this temperature for 1 h. A transparent yellow solution of phosphomolybdic acid (PMo_{12}, 0.5 mmol, 913 mg, Sigma-Aldrich) in water was poured slowly. The reaction mixture became bluish green at once, an indication of reduction of PMo_{12} from $[PMo_{12}O_{40}]^{3-}$ to $[PMo_{12}O_{40}]^{6-}$. For the synthesis of ammonium phosphate coated P-doped MoSx NPs, the as-prepared solution was hydrothermally treated at 180°C for 15 h. The reduced PMo_{12} is converted to P-doped MoSx (see XRD in Figure S1a) by internally produced H_2S gas, and the remaining phosphoric acid reacts with indigenously generated ammonia (NH_3) gas to form ammonium phosphate. Then, this freshly prepared suspension of pH 7 was dried at 60 ºC to be used for MoP synthesis.

The as-prepared ammonium phosphate coated P-doped MoSx was reduced in a tube furnace under H_2 gas with a ramping rate of 5 ºC/min, kept at a required temperature (550-700 ºC) for 3 h and then cooled down naturally to obtain diamond blackish powders, denoted as MoP/SN-X (X denotes reduction temperature). For comparison, N-doped MoP nanoparticles are also prepared by using urea instead of thiourea following the same procedure.

MoP NPs were grown on S and N co-doped graphene (MoP/SNG) by adding the required amount of exfoliated graphene oxide (GO) suspension directly into the hydrothermal step, and then reduced following the same conditions. For MoP-SN/G, the ammonium-phosphate coated P-MoS_x powder physically mixed with exfoliated GO suspension (20 wt.% G of MoP/SN-650), then dried at 60 °C before reduction in H_2 atmosphere.

4.3.2 Characterization

Crystallographic information of the as-synthesized electrocatalysts were investigated by powder X-ray diffraction (XRD, PANalytical pw 3040/60 X'pert) with Cu Kα radiations. The surface morphologies and structural information were recorded with field-emission scanning electron microscope (FE-SEM, Hitachi, S-4800, 15 kV) and transmission electron microscope (TEM, JEOL, JEM-2100). The chemical compositions, elemental mapping and in-depth crystal information of samples were collected by high resolution transmission electron microscope (HRTEM, JEOL, JEM-2100F). X-ray photoelectron spectroscopy (XPS, ThermoFisher, K-alpha) was used to identify the surface atomic composition and chemical states.

4.3.3 Electrochemical characterization

The catalyst ink was prepared by dispersing electrocatalysts (1.0 mg/mL) in a mixture of deionized water and 2-propanol (7:3) and 10 µL of 5% Nafion solution. The mixture was sonicated for 1 h in a water bath. The working electrode was prepared by drop casting of 10 µL ink onto a glassy carbon electrode (0.4-0.5 mg cm^{-2} loading) followed by dropping 5 µL Nafion solution in order to fix the

electrocatalyst. The electrode was dried at room temperature before electrochemical measurements. Electrochemical HER activity and stability tests were carried out in a three electrode cell configuration using a rotating disc electrode (RDE, PAR Model 636 RDE) attached with a potentiostat (Ivium technologies). An Ag/AgCl (3.0M NaCl) electrode and a Pt wire were used as reference and counter electrodes, respectively. All potentials were referenced to the reversible hydrogen electrode (RHE) by converting with the equation $E_{RHE}=E_{(Ag/AgCl)} + 0.059pH + 0.209$.

The HER performance was measured in aqueous 0.5 M H_2SO_4 (pH 0.3) and 1.0 M KOH (pH 14) at a scan rate of 5 mV s^{-1} with 1600 rpm after 20 cyclic voltammetry (CV) cycles in the range of 0.4 to -0.3 V_{RHE}. The electrochemical stability tests were conducted by performing up to 2000 CV cycles in the above potential ranges. Electrochemical impedance spectroscopy (EIS) was conducted in the same setup in the frequency range of 100 kHz to 1 mHz with a modulation amplitude of 10 mV. The EIS spectra were fitted by the Z-view software. To evaluate the electrochemical active surface area (ECSA), CV was conducted from 0.0 to 0.2 V (in 0.5 M H_2SO_4) and -0.8 to -0.6 V (in 1.0 M KOH or NaOH) *vs.* Ag/AgCl with different sweep rates between 10 to 100 mV s^{-1}.

4.4 Results and discussion

4.4.1 Urea-phosphate-assisted approach for preparation molybdenum phosphide nanoparticles

Phosphomolybdic acid (PMo_{12}) is polyatomic anionic cluster composed of twelve unit of molybdenum oxide (MoO_3) and a main group oxyanion (phosphate), and is an excellent oxidizing agent and versatile inorganic building blocks for the preparation of nanomaterials.[27-29] A weak reducing agent thiourea effectively reduces it to P-doped MoS_x by in-situ produced H_2S gas and ammonia-phosphate especially in the acidic solution (H_3PO_4 and PMo_{12})[29] via hydrothermal reduction as described in **Eq. 4.1-4.3**.[30] Then, a mixture of ammonium-phosphate and P-doped MoS_x is recovered after drying the above product and is used as a precursor to synthesize S and N co-doped MoP nanoparticles (MoP/SN) after thermal decomposition in hydrogen gas as illustrated in **Figure 4.1**, and discussed under Experimental Section. To grow the MoP NPs on S and N co-doped reduced graphene (MoP/SNG), the aqueous suspension of exfoliated graphene oxide (GO) is added directly into the hydrothermal reactor along with starting precursors and followed the same reductive decomposition as for MoP/SN NPs. The nitrogen doped MoP NPs (MoP/N) are also prepared by just replacing the thiourea with simple urea.

$$[PMo_{12}O_{40}]^{3-} + (NH_2)_2CS \xrightarrow{H^+} [PMo_{12}O_{40}]^{6-} + H_2S + (NH_2)_2CO \qquad (4.1)$$

$$[PMo_{12}O_{40}]^{6-} + xH_2S \xrightarrow{\Delta} P - MoS_x + yH_2O \qquad (4.2)$$

$$(NH_2)_2CO + H_3PO_4 \xrightarrow{\Delta} (NH_2)_2.HPO_4\ (Amm.phosphate) + gases \quad (4.3)$$

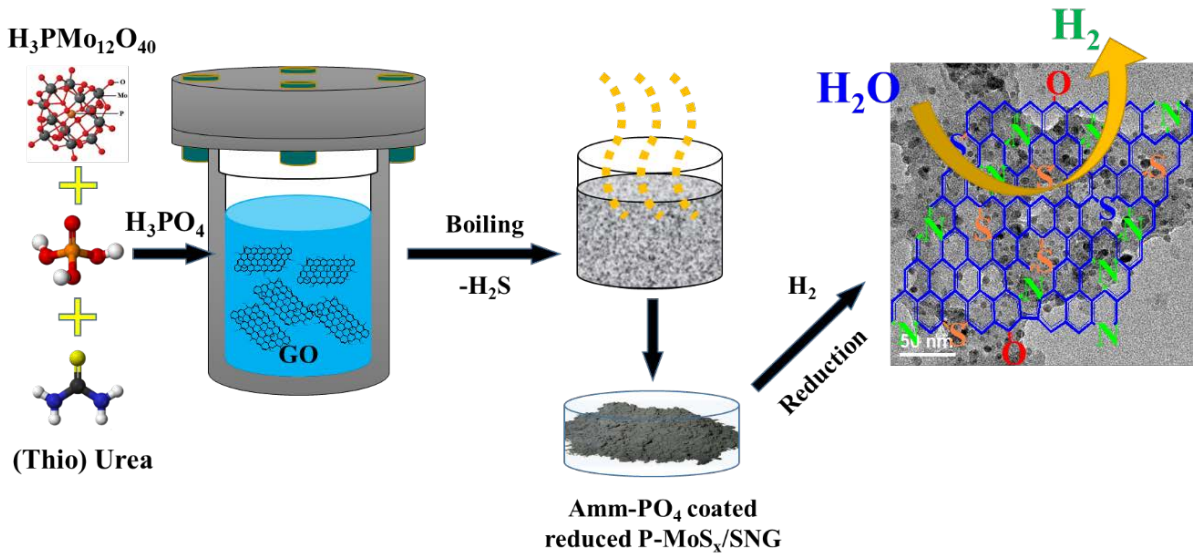

Figure 4.1. Schematic synthesis of MoP/SNG electrocatalysts via thiourea-phosphate route

The X-ray diffraction (XRD) pattern of P-doped MoS_x displays P-Mo_3S_4 as the main phase (**Figure S4.2a**) synthesize during the hydrothermal conditions (Eq., 1 to2) The phase identification during the reduction of precursors are confirmed by XRD of obtained MoP/SN powder at various annealing temperatures in H_2 gas as displayed in **Figure 4.2b**. A pure hexagonal phase of MoP (space group $P\bar{6}m2$) is formed above the reduction temperature 600 °C and minor fractions of molybdenum phosphate are still present in the samples annealed below this temperature. Interestingly, there is no change in bulk crystals of MoP even after doping of N and S as confirmed by XRD of sample above 600 °C. The average crystallite size of 12-14 nm was calculated by applying the Scherrer equation to X-ray line broadening, which increases with the annealing temperature (**Figure 4.2c**). The nitrogen doped MoP/N-650 NPs and hybrid catalysts with graphene (MoP/SNG) also display the alike XRD pattern MoP/SN catalysts (**Figure 4.2d-e**). Scanning electron microscopy (SEM) images of the as-prepared MoP/SN and MoP/SNG-20 (with 20 wt.% graphene) materials reveal that nanoparticles are closely interconnected with nonporous structure (**Figure 4.2f-g**). EDX-SEM spectrum (**Figure 4.2h**) and elemental mapping for MoP/SNG-20 (**Figure 4.2i**) clearly display the uniformly distribution of elements.

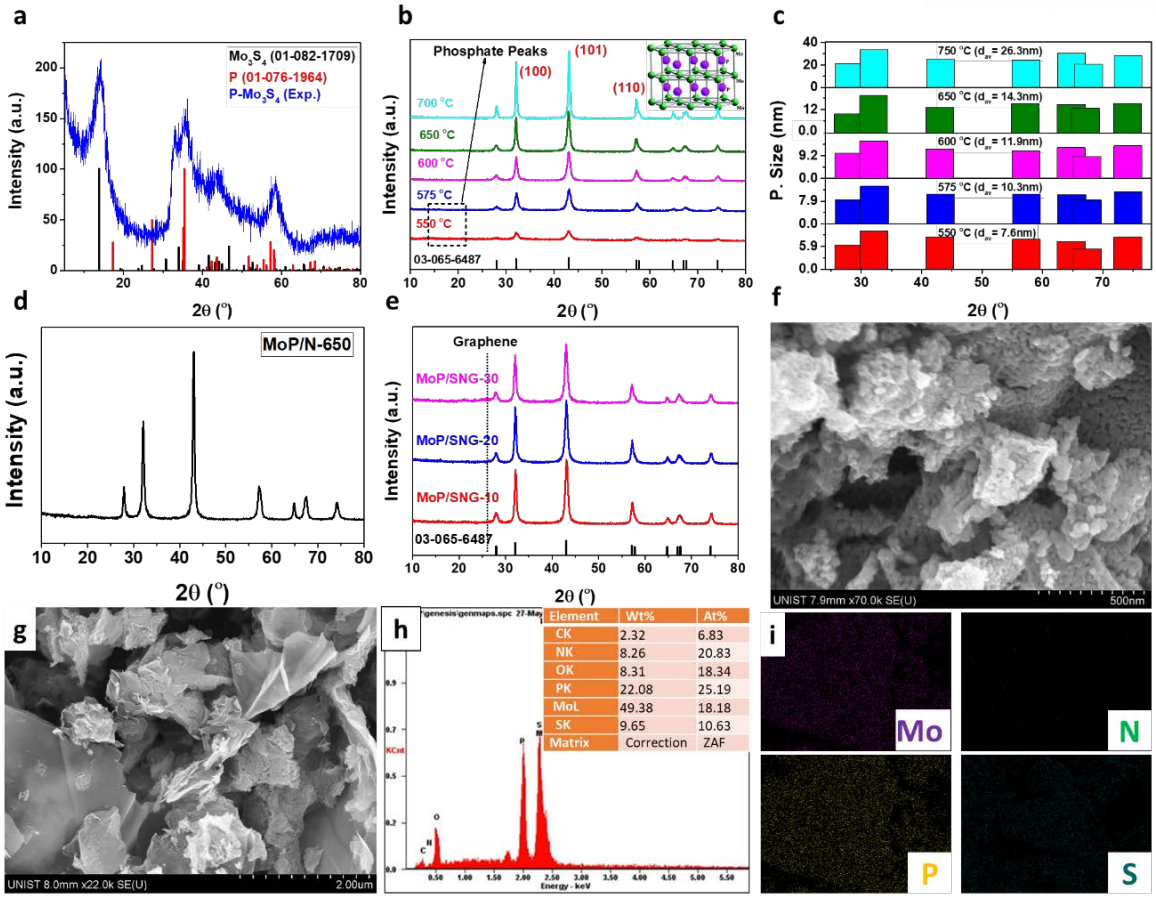

Figure 4.2. XRD pattern of (a) P-Mo_3S_4, (b) MoP/SN synthesized at different temperature and (c) corresponding particle size calculation against each XRD pattern. XRD of MoP/N-650 and MoP/SNG composites. SEM image of (a) MoP/SN-650, (g) MoP/SNG-20 and (h, i) EDS-SEM spectrum and elemental mapping for MoP/SNG-20.

The X-ray photoelectron spectroscopy (XPS) was also conducted to determine nature of chemical bonding and composition of in as-synthesized MoP/SN and MoP/SNG-20 electrocatalysts. A doublet at ≈228.2 eV and ≈231.3 eV of $Mo^{\delta+}$ ($0<\delta\leq4$) in high resolution XPS spectra of Mo3d (**Figure 4.3a**) for both MoP/SN and MoP/SNG catalysts can be ascribed to Mo in MoP.[6, 8, 18] Another doublet at ≈229.2 and ≈ 232.4 eV in Mo 3d confirms the successful doping of S atom into the structure of MoP[18] and maximum molybdenum sulfides are converted to S and N co-doped MoP NPS during reductive phosphidation in hydrogen. A poor signal at ≈235.8 eV/232.5eV[6] can also be seen due to surface oxidation of Mo to MoO_3. These surface oxides can easily be removed by chemical or electrochemical treatment during HER testing.[31-32] A XPS depth profiling (**Figure 4.1b**) further confirmed that the high concentration of oxygen is present only at the surface of the material and is significantly decreased with the etching level. Similarly, the signals at ≈129.4 eV and ≈130.2 eV in the P 2p (**Figure 4.3c**) and a doublet (≈161.8 eV, ≈163.0 eV) in S 2p (**Figure 4.3e-f**) spectra reveal the successful bonding between P, S and Mo atoms to form S-Mo-P type strucure.[8, 18] Four additional signals at ≈131.30, 132.8, 133.8 and 134.6 eV in P 2p are belongs to P-S, P-C, P-O and P-N/PON, respectively, confirming that a least

stable P^{3-} species in MoP are stabilized by sharing electron density with S, C, O and N atoms present in the material.[8, 20, 33-35] Similarly, a combined signal of -C-S/-C-SO at ≈164 eV and -C-SO_2 at ≈168.6 in in S 2p spectrum of MoP/SNG-20 (**Figure 4.3g-h**) further confirms the self-doping of S-species into the carbon structure,[36-37] which are directly provides the synergistic effect in promoting the electrode redox reactions.[37] A peak at 284.6 is belongs to sp^2 carbon while at 285.6 eV is designated to C-N and/or C=N in C1s spectra (Figure 2.1f). The XPS N 1s spectrum (**Figure 4.3i**) could be deconvoluted to Mo-N (≈394.0), MoS_2 (≈395.3), pyridinic (≈398.3 eV), pyrrolic (≈399.5 eV), graphitic (≈401.2 eV), and a broad peak of -SCN (≈397.8 eV).[38-40] From the above XPS analysis is justified the hypothesis that more electronegative atoms (S, N and C) withdraw electron density from the P^{3-} through P-S, P-N/PON and P-C bonds and back donated to empty d-orbitals of Mo, which stabilized the phosphide structure and maximized HER performance as discussed in electrochemical section.

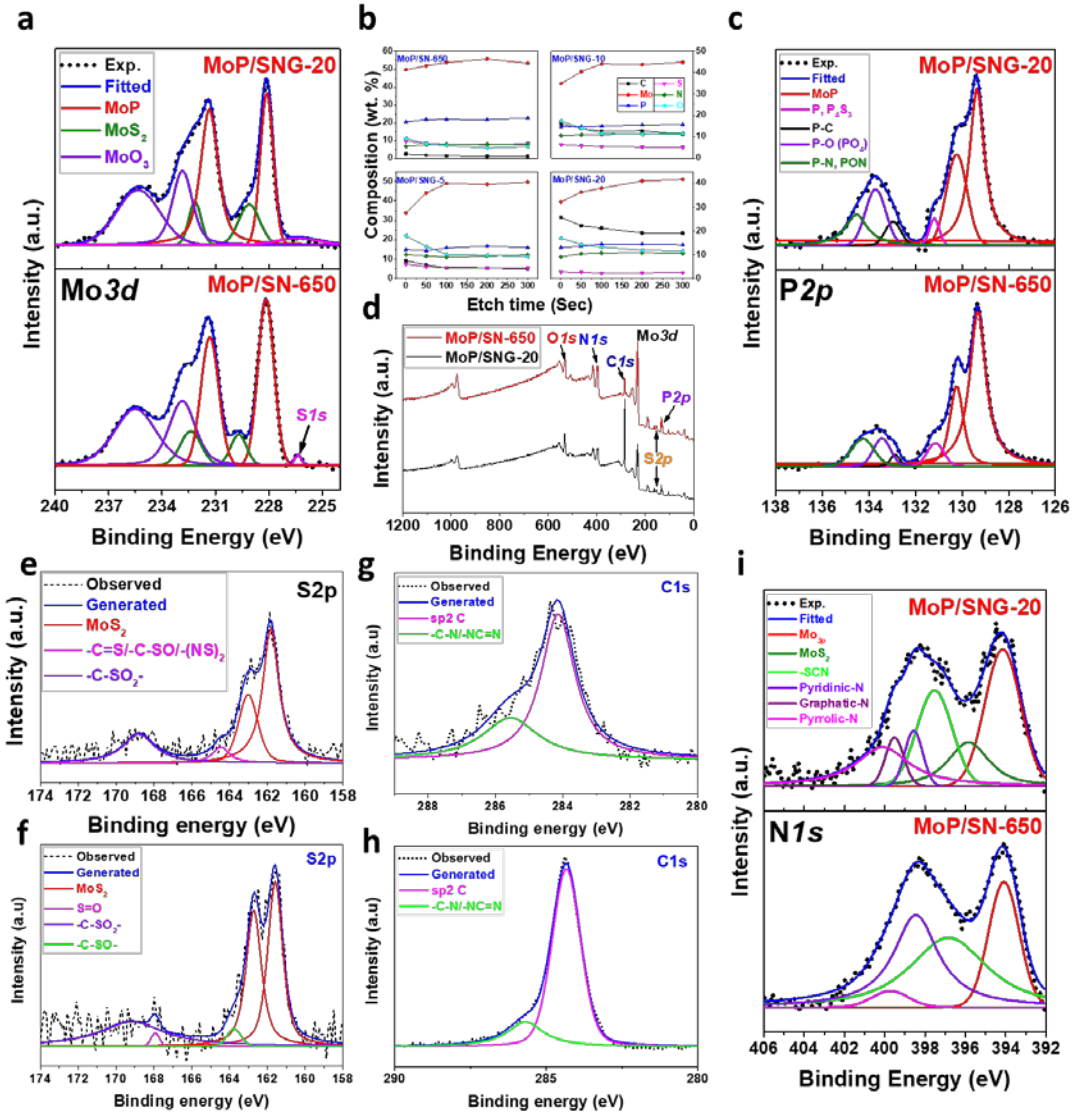

Figure 4.3. XPS spectra of (a) Mo 3d, (b) depth profiling analysis, (c) P 2p, (d) elemental survey, (e, f) S 2p, (g, h) C1s and (i) N1s for MoP/SN-650 and MoP/SNG-20.

The transmission electron microscopy (TEM) clearly display rod-shaped nanocrystallite in MoP/SN-650 catalyst (**Figure 4.4a**). These nanorods are changed to nanoparticles (3-7 nm) when sufficient amount (20%) of GO was added during hydrothermal reaction as shown in **Figure 4.4b**. The crystal (100) and (101) plane with lattice spacings of 0.27 and 0.21 nm are ascribed for hexagonal MoP in **Figure 4.4c-d**. Elemental spectrum and maps by energy-dispersive-X-ray-spectroscopy (EDS)-STEM of MoP/SNG-20 (**Figure 4.4e-l)** clearly confirm uniform distribution over graphene support.

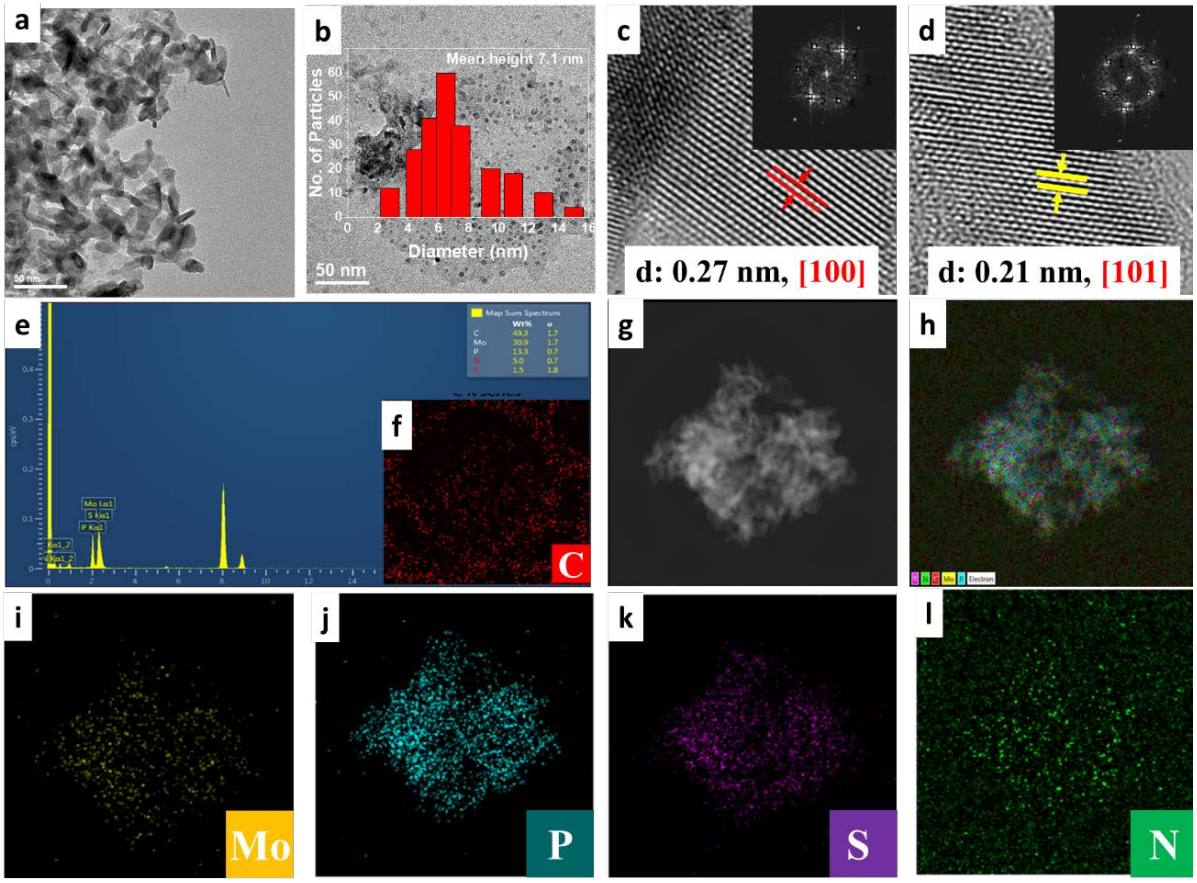

Figure 4.4. TEM image of (a) MoP/SN-650, (b) MoP/SNG-20 and particle size distribution (inset). HR-TEM images of MoP(a) (100) and (b) (101) planes and corresponding fast Fourier transformation (FFT) patterns (inset), (e) EDS-STEM spectrum and (f-l) elemental maps of MoP/SNG-20

4.4.2 Electrochemical hydrogen evolution reaction in acidic and alkaline solutions

The iR-corrected HER performance curves of MoP/SN catalysts synthesized at different reduction temperatures were compared in 0.5M H_2SO_4 and 1.0M KOH aqueous electrolyte (**Figure 4.5a, left**). Expectedly, the MoP/SN-650 catalyst displayed best performance due to the complete reduction of phosphates, whereas other catalysts give poor performance due to incomplete reduction at low temperature or more sintering along with removal of more S and N atoms into exhaust gases,[37] relatively at higher temperatures reduction. The MoP/SN-650 requires lowest onset potential (η_1) of ≈44 mV and overpotentials (η_{10}) of 57 and 104 mV to generate current densities of 1 and 10 mA/cm^2 in 0.5M H_2SO_4,

respectively. Surprisingly, the catalysts prepared at the reduction temperatures of 575-650 °C display almost similar HER activity in 1.0M KOH aqueous solution (**Figure 4.5a, right**). The 650 °C is found to be optimum reduction temperature to form phosphate and oxide free small MoP NPs.[31-32] The catalysts MoP/SN-575 to MoP/SN-650 demand overpotentials of η_1≈17-20 and η_{10}≈90-94 mV to generate current densities of 1 and 10 mA/cm^2 in alkaline solution. The MoP/SN-650 catalysts contains ≈7.9 wt.% N and ≈8.5 wt.% S atoms at the surface as determined by XPS in **Figure 4.3b**. These N and S species into the skeleton of phosphide stabilize least stable P^{3-} in MoP through coordinating bond with both P and Mo, which also results in higher HER activity through maximizing electrical conductivity and proton adsorption sites. The N-doped MoP (MoP/N-650) nanoparticles require more overpotentials (η_{10}=164 & η_{20}=164 mV) in 0.5M H_2SO_4 and (η_{10}=154 and η_{20}=182) in alkaline media than S, N co-doped MoP (**Figure 4.5b**). Similarly, the better HER activity of MoP/SN NPs in acidic solution than those of single N-doped and $MoS_{2(1-x)}$ Px (10 mA. cm^{-2} @ 150 mV) solid solution,[18] clearly signify the importance co-doping.

Table 4.1. Comparison of HER performance in acidic (0.5M H_2SO_4) media with other molybdenum phosphides-based electrocatalysts reported in literature.

Material	η_{10} (mV)	TS (mV/dec)	Source of P and reduction temperature	References
MoP/SN	**104**	**45.49**	**H_3PO_4, 650 °C**	**This work**
MoP/SNG-20	**99**	**54.41**	**H_3PO_4, 650 °C**	**This work**
MoP	117	50	$(NH_4)_2HPO_4$, 650 °C	*Angew. Chem. Int. Ed.* **2014,** *53*, 14433-14437.
MoP & Ni_2P	246	60	$(NH_4)_2HPO_4$, (500-700 °C)	*Chem. Commun.* **2014,** *50*, 11683-11685.
MoP, Mo, Mo_3P	140	54	$(NH_4)_2HPO_4$, 650-800 °C	*Energy Environ. Sci.* **2014,** *7*, 2624-2629.
Am. MoP NPs	90	45	Trioctylphosphine (320 °C)	*Chem.Mater.* **2014,** *26*, 4826-4831.
MoP NPs	125	54	$(NH_4)_2HPO_4$, (650 °C)	*Adv. Mater.* **2014,** *26*, 5702-5707.
MoP flakes	141	71.8	$NH_4H_2PO_4$, 800 °C	*Am.J. Anal. Chem.* **2014,** *5*, 1200.
MoP-G	234	63	MoP	*Appl.Catal. A* **2015,** *490*, 101-107.
MoP	150	50		*J. Mater. Chem. A* **2015,** *3*, 4368-4373.
MoP/CF	199	56.4	$NaH_2PO_4 \cdot 2H_2O$, 900 °C	*Appl. Catal. B* **2015,** *164*, 144-150.
$MoS_{2(1-x)}P_x$/CB	120		red phosphorus, 750 °C	*Adv. Mater.* **2015,** *28*, 1427–1432.
Mo-W-P/CC	90	52	NaH_2PO_2, 700 °C	*Energy Environ. Sci.* **2016,** *9*, 1468-1475.
MoP/CC	148	55	NaH_2PO_2 700 °C	*Energy Environ. Sci.* **2016,** *9*, 1468-1475.
3D-MoP	105	126	$(NH_4)_2HPO_4$, (500-700 °C)	*J. Mater. Chem. A* **2016,** *4*, 59-66.
Co-MoP NPs	210	50	$(NH_4)_2HPO_4$, 650 °C	*Catal. Sci. Technol.* **2016,** *6*, 1952-1956.
CoMoP	215	50	$(NH_4)_2HPO_4$, 650 °C	*Appl. Catal. A* **2016,** *511*, 11-15.

The HER performance of MoP/SNG electrocatalysts is further improved by growing MoP NPs on self-doped graphene substrate. The performance curve of MoP/SNG-20 (20% graphene) in **Figure 4.5c**

clearly displays the remarkable reduction in overpotentials and require η_{10} value of 99 and 52 mV in 0.5M H_2SO_4 and 1.0M KOH aqueous solution, respectively, which is significantly better than those of previously reported MoP-based catalysts as enlisted in **Table 4.1** and **4.2**. Comparison of η_{10}, η_{50} and η_{100} was also made in **Figure 4.5d-e** in both media. The above results reveal that the direct growth of MoP NPs on S and N co-doped graphene displays higher HER performance.

Table 4.2. Comparison of HER performance of S and N co-doped MoP with other MoP-based electrocatalysts in alkaline media.

Material	η_{10} (mV)	TS (mV/dec)	Source of P and reduction temperature	Reference
MoP/SN	94	59.7	H_3PO_4, 650 °C	This work
MoP/SNG-20	49	31.4	H_3PO_4, 650 °C	This work
MoP, Mo, Mo_3P	135	48	$(NH_4)_2HPO_4$, (650-800 °C)	*Energy Environ. Sci.* **2014,** *7*, 2624-2629.
MoP flakes	170	71.8	$NH_4H_2PO_4$, 800 °C	*Am.J. Anal. Chem.* **2014,** *5*, 1200.
MoP	190		MoP	*J. Mater. Chem. A* **2015,** *3*, 4368-4373.

The Tafel slopes of MoP/SN-650 and MoP/SNG (5 to 30) are 45, 51, 58, 54 and 54 mV/dec which suggest the Volmer−Heyrovsky mechanism in acidic media (**Figure 4.5f, left**). In 1.0M KOH, all samples display Tafel slopes in the range of 31-59 mV/dec (**Figure 4.5f, right**), suggesting similar mechanism as at Pt/C (31 mV/dec). The relatively lower activity and higher Tafel slopes of bare MoP/SN-650 NPs indicate that the hybrid MoP/SNG structure required less energy to activate HER reaction due to improved electron/proton conductivity by S, N-doping, strong bonding of MoP NPs through Mo-P-X-Mo (X = S, N and C). The higher exchange current densities (J_0) of all catalysts, indicate the fast kinetics and charge transfer at electrode-electrolyte interface. The MoP/SNG-20 catalysts more J_0 value (0.15 and 0.46 mA/cm^2) than pristine MoP/SN-650 (0.056 and 0.48 mA/cm^2) in acid and base, respectively.

Electrochemically active surface areas (ECSA) is calculated by measuring the double layer capacitance (C_{dl}) with cyclic voltammetry (CV) at various scan rates as shown in **Figure 4.5g**, the C_{dl} and ECSA values increase with loading of graphene. The MoP/SNG-20 (20.5 mF/cm^2, 512.5 cm^2) displayed more C_{dl} and ECSA values than bare MoP/SN NPs (3.96 mF/cm^2, 99 cm^2). The electrochemical impedance spectroscopy (EIS) was also compared at a same overpotential (η) of 120 mV_{RHE} in 0.5M H_2SO_4 and at 125 mV_{RHE} in 1.0M KOH electrolytes (**Figure 4.5h-i**). The Nyquist plot reveal that there are two time constants, one at high frequencies corresponds diffusion resistance (R_d) and second at low frequencies determines the charge transfer resistance (R_{ct}) offered at cathode. The MoP/SNG-X composites offer

small R_{ct} and R_d values of than bare MoP/SN-650 in all electrolytes because of improved electrical conductivity by S, N co-doping into the carbon skeleton. The EIS results are in accordance with the performances data, confirming that charge transfer resistance is the important factor in the HER.

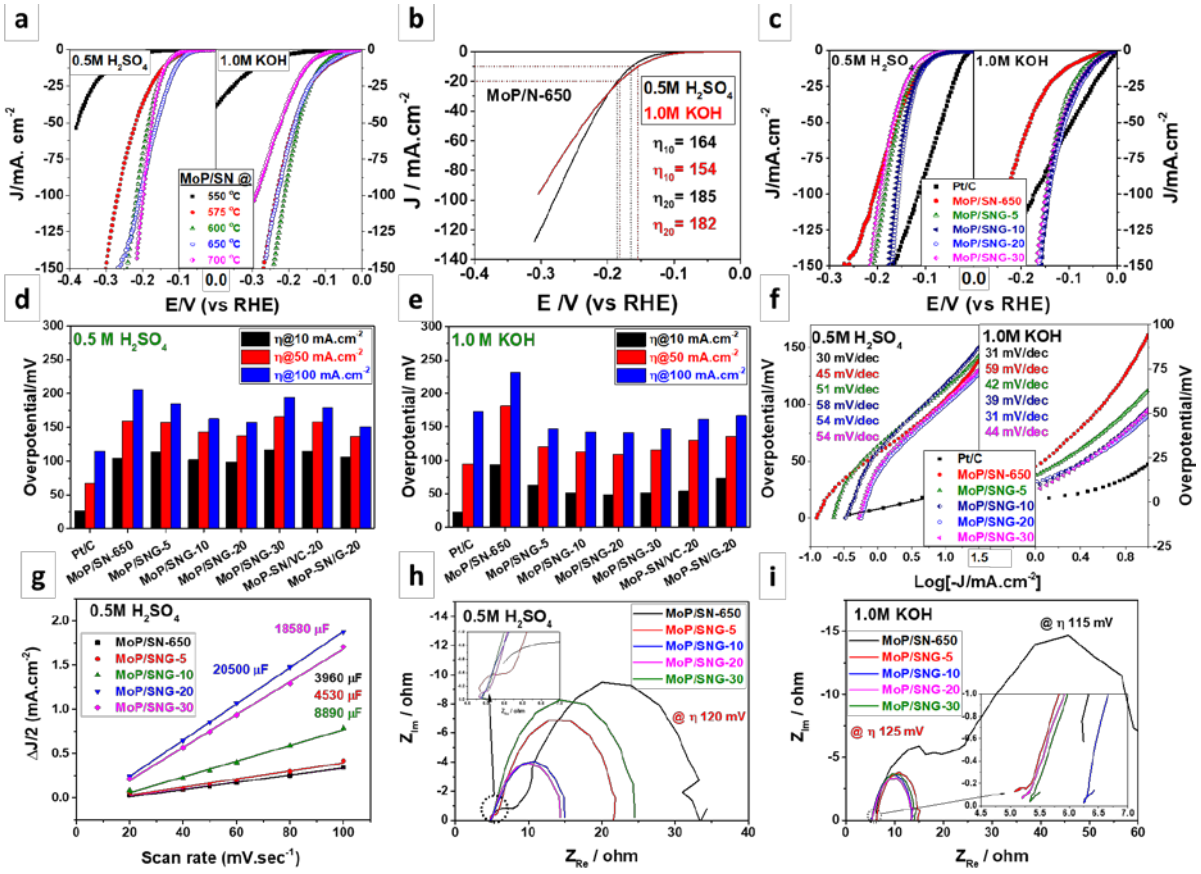

Figure 4.5. iR-corrected polarization curves of (a) MoP/SN synthesized at different reduction temperatures (i.e. 550-700 °C), (b) N-doped MoP NPs, and (c) MoP/SNG-X (X: 5,10, 20 and 30) hybrid catalysts in acidic and alkaline media. Comparison of η_{10}, η_{50} and η_{100} values in (d) 0.5M H_2SO_4 and (e) 1.0M KOH. (f) Tafel slopes in acid (left) and 1.0M KOH (right), (g) the plot between capacitive currents ($\Delta J/2$) and scan rates, EIS analysis in (h) acid and (i) alkaline aqueous solution.

The prime factor for commercial application i.e. electrochemical durability of electrocatalysts, determined by performing the accelerated cyclic voltammetry (CV) continuously for 2000 scans at a speed of 0.1 V/s in both 0.5M H_2SO_4 and 1.0M KOH solution as shown in **Figure 4.6a**. The MoP/SN nanoparticles display better stability in acidic electrolyte than in alkaline media. A continuous corrosion of the material in basic electrolyte, results in loss of HER performance. The activity and stability of the catalysts considerably improved in both electrolytes when the MoP NPs are grown on S and N co-doped graphene (MoP/SNG) as displayed in **Figure 4.6b-c**. Similarly, trend also observed in the 20 h long chronoamperometry (CA) durability test for MoP/SNG-20 at a constant overpotential in both aqueous solutions (**Figure 4.6c, inset**). The cyclic voltammograms (**Figure 4.6d-f**) are compared with Pt/C in the potential window −0.15 and 0.15 V represents similar behavior as of Pt/C. Since, most of transition

metals based electrocatalysts are unstable in acids, the present MoP/SNG could be a promising candidate for HER in acidic electrolyzers.

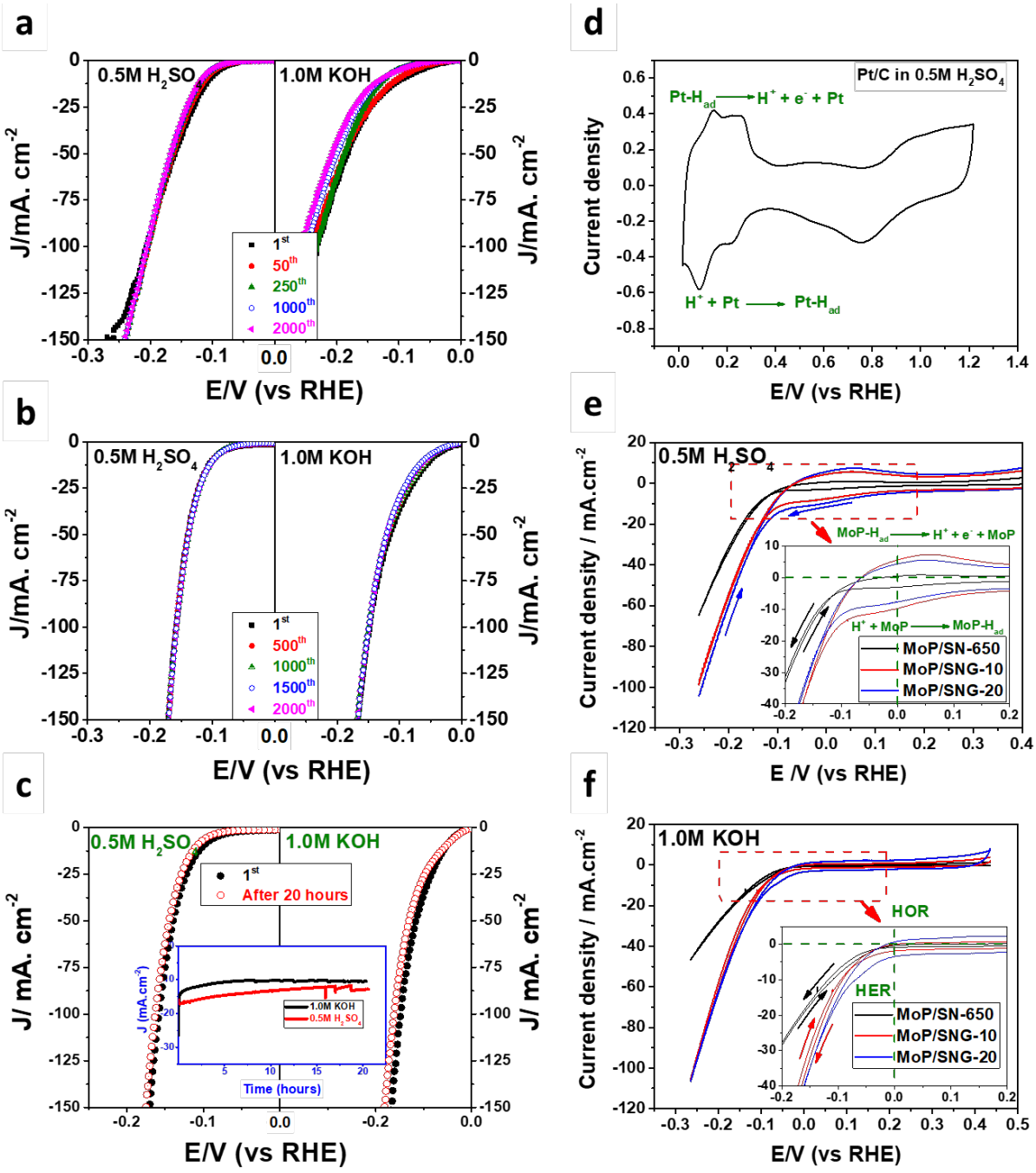

Figure 4.6. HER performance curves of MoP/SN-650 (a) and MoP/SNG-20 (b) after 2000th CV cycles in 0.5M H_2SO_4 and 1.0M KOH solutions. (c) LSV comparison after 20 h long chronoamperometry (CA) as inset for MoP/SNG-20 in acidic and alkaline aqueous solutions.

4.5 Conclusions

S and N co-doped MoP nanoparticles are prepared by developing a unique and ecofriendly (thio)urea-phosphate-assisted strategy, in which thiourea reduces the phosphomolybdic acid to P-doped MoS_x and provides the S and N elements and phosphoric acid (H_3PO_4) acts as a P source. The S and N co-doped MoP NPs are produced upon reduction of *in-situ* generated a mixture of ammonium phosphate and P-doped MoS_x in the hydrogen gas. The detailed spectroscopic investigations confirm that least stable P^{3-} state in MoP are stabilized by sharing its extra electron density with more electronegative dopants (S, N and C) through P-S, P-N/PON and P-C and increasing the electron density at Mo center by back donating to its empty d-orbitals. The high performance of MoP/SNG composites than bare nanoparticles in both acidic and basic aqueous solution is due to reduced particle size, higher electrochemical active surface area (ECSA) and enhanced conductivity. In precise, MoP NPs directly anchored on doped graphene (MoP/SNG) displays remarkable HER activity and durability, defeating the most of MoP-based electrocatalysts reported in the literature so far.

4.6 References

1. Zou, X.; Zhang, Y., Noble metal-free hydrogen evolution catalysts for water splitting. *Chem. Soc. Rev.* **2015,** *44* (15), 5148-5180.

2. Zhong, Y.; Xia, X.; Shi, F.; Zhan, J.; Tu, J.; Fan, H. J., Transition Metal Carbides and Nitrides in Energy Storage and Conversion. *Adv. Sci.* **2016,** *3* (5), 1500286.

3. Faber, M. S.; Jin, S., Earth-abundant inorganic electrocatalysts and their nanostructures for energy conversion applications. *Energy Environ. Sci.* **2014,** *7* (11), 3519-3542.

4. Wang, J.; Cui, W.; Liu, Q.; Xing, Z.; Asiri, A. M.; Sun, X., Recent Progress in Cobalt-Based Heterogeneous Catalysts for Electrochemical Water Splitting. *Adv. Mater.* **2016,** *28* (2), 215-230.

5. Cui, W.; Cheng, N.; Liu, Q.; Ge, C.; Asiri, A. M.; Sun, X., Mo2C nanoparticles decorated graphitic carbon sheets: biopolymer-derived solid-state synthesis and application as an efficient electrocatalyst for hydrogen generation. *ACS Catal.* **2014,** *4* (8), 2658-2661.

6. Xiao, P.; Sk, M. A.; Thia, L.; Ge, X.; Lim, R. J.; Wang, J.-Y.; Lim, K. H.; Wang, X., Molybdenum phosphide as an efficient electrocatalyst for the hydrogen evolution reaction. *Energy Environ. Sci.* **2014,** *7* (8), 2624-2629.

7. Tian, J.; Liu, Q.; Asiri, A. M.; Sun, X., Self-supported nanoporous cobalt phosphide nanowire arrays: an efficient 3D hydrogen-evolving cathode over the wide range of pH 0–14. *J. Am. Chem. Soc.* **2014,** *136* (21), 7587-7590.

8. Kibsgaard, J.; Jaramillo, T. F., Molybdenum Phosphosulfide: An Active, Acid-Stable, Earth-Abundant Catalyst for the Hydrogen Evolution Reaction. *Angew. Chem. Int. Ed.* **2014,** *53* (52), 14433-14437.

9. Chen, Z.; Lv, C.; Chen, Z.; Jin, L.; Wang, J.; Huang, Z., Molybdenum Phosphide Flakes Catalyze Hydrogen Generation in Acidic and Basic Solutions. *Am. J. Anal. Chem.* **2014,** *5* (17), 1200.

10. Zhu, W.; Tang, C.; Liu, D.; Wang, J.; Asiri, A. M.; Sun, X., A self-standing nanoporous MoP_2 nanosheet array: an advanced pH-universal catalytic electrode for the hydrogen evolution reaction. *J. Mater. Chem. A* **2016,** *4* (19), 7169-7173.

11. Jiang, P.; Liu, Q.; Liang, Y.; Tian, J.; Asiri, A. M.; Sun, X., A Cost-Effective 3D Hydrogen Evolution Cathode with High Catalytic Activity: FeP Nanowire Array as the Active Phase. *Angew. Chem. Int. Ed.* **2014,** *53* (47), 12855-12859.

12. Liu, P.; Rodriguez, J. A., Catalysts for hydrogen evolution from the [NiFe] hydrogenase to the Ni2P (001) surface: the importance of ensemble effect. *J. Amer. Chem. Soc.* **2005,** *127* (42), 14871-14878.

13. Pan, Y.; Liu, Y.; Zhao, J.; Yang, K.; Liang, J.; Liu, D.; Hu, W.; Liu, D.; Liu, Y.; Liu, C., Monodispersed nickel phosphide nanocrystals with different phases: synthesis, characterization and electrocatalytic properties for hydrogen evolution. *J. Mater. Chem. A* **2015,** *3* (4), 1656-1665.

14. Callejas, J. F.; Read, C. G.; Popczun, E. J.; McEnaney, J. M.; Schaak, R. E., Nanostructured Co2P Electrocatalyst for the Hydrogen Evolution Reaction and Direct Comparison with Morphologically Equivalent CoP. *Chem. Mater.* **2015,** *27* (10), 3769-3774.

15. Blanchard, P. E.; Grosvenor, A. P.; Cavell, R. G.; Mar, A., X-ray Photoelectron and Absorption Spectroscopy of Metal-Rich Phosphides M 2P and M 3P (M= Cr− Ni). *Chem. Mater.* **2008,** *20* (22), 7081-7088.

16. Carenco, S.; Portehault, D.; Boissiere, C.; Mezailles, N.; Sanchez, C., Nanoscaled metal borides and phosphides: recent developments and perspectives. *Chem. Rev.* **2013,** *113* (10), 7981-8065.

17. Shi, Y.; Zhang, B., Recent advances in transition metal phosphide nanomaterials: synthesis and applications in hydrogen evolution reaction. *Chem. Soc. Rev.* **2016,** *45* (6), 1529-1541.

18. Ye, R.; del Angel-Vicente, P.; Liu, Y.; Arellano-Jimenez, M. J.; Peng, Z.; Wang, T.; Li, Y.; Yakobson, B. I.; Wei, S. H.; Yacaman, M. J., High-Performance Hydrogen Evolution from MoS2 (1–x) P x Solid Solution. *Adv. Mater.* **2015,** *28* (7), 1427-1432.

19. Aravind, S. J.; Ramanujachary, K.; Mugweru, A.; Vaden, T. D., Molybdenum phosphide-graphite nanomaterials for efficient electrocatalytic hydrogen production. *Appl. Catal. A: General* **2015,** *490*, 101-107.

20. Han, S.; Feng, Y.; Zhang, F.; Yang, C.; Yao, Z.; Zhao, W.; Qiu, F.; Yang, L.; Yao, Y.; Zhuang, X., Metal-Phosphide-Containing Porous Carbons Derived from an Ionic-Polymer Framework and Applied as Highly Efficient Electrochemical Catalysts for Water Splitting. *Adv. Funct. Mater.* **2015,** *25* (25), 3899-3906.

21. Wang, D.; Zhang, D.; Tang, C.; Zhou, P.; Wu, Z.; Fang, B., Hydrogen evolution catalyzed by cobalt-promoted molybdenum phosphide nanoparticles. *Catal. Sci. Technol.* **2016,** *6* (6), 1952-1956.

22. Liang, X.; Zhang, D.; Wu, Z.; Wang, D., The Fe-promoted MoP catalyst with high activity for water splitting. *Appl. Catal. A: General* **2016,** *524*, 134-138.

23. Wang, X.-D.; Xu, Y.-F.; Rao, H.-S.; Xu, W.-J.; Chen, H.-Y.; Zhang, W.-X.; Kuang, D.-B.; Su, C.-Y., Novel porous molybdenum tungsten phosphide hybrid nanosheets on carbon cloth for efficient hydrogen evolution. *Energy Environ. Sci.* **2016,** *9* (4), 1468-1475.

24. Wang, D.; Zhang, X.; Zhang, D.; Shen, Y.; Wu, Z., Influence of Mo/P Ratio on CoMoP nanoparticles as highly efficient HER catalysts. *Appl. Catal. A: General* **2016,** *511*, 11-15.

25. McEnaney, J. M.; Crompton, J. C.; Callejas, J. F.; Popczun, E. J.; Biacchi, A. J.; Lewis, N. S.; Schaak, R. E., Amorphous molybdenum phosphide nanoparticles for electrocatalytic hydrogen evolution. *Chem. Mater.* **2014,** *26* (16), 4826-4831.

26. Xing, Z.; Liu, Q.; Asiri, A. M.; Sun, X., Closely interconnected network of molybdenum phosphide nanoparticles: a highly efficient electrocatalyst for generating hydrogen from water. *Adv. Mater.* **2014,** *26* (32), 5702-5707.

27. Zhou, D.; Han, B. H., Graphene-Based Nanoporous Materials Assembled by Mediation of Polyoxometalate Nanoparticles. *Adv. Funct. Mater.* **2010,** *20* (16), 2717-2722.

28. Chen, Y.-Y.; Zhang, Y.; Jiang, W.-J.; Zhang, X.; Dai, Z.; Wan, L.-J.; Hu, J.-S., Pomegranate-like N, P-Doped Mo2C@ C Nanospheres as Highly Active Electrocatalysts for Alkaline Hydrogen Evolution. *ACS Nano* **2016,** *10* (9), 8851-8860.

29. Shyla, B.; Nagendrappa, G., A simple spectrophotometric method for the determination of phosphate in soil, detergents, water, bone and food samples through the formation of phosphomolybdate complex followed by its reduction with thiourea. *Spectrochim. Acta Part A* **2011,** *78* (1), 497-502.

30. McCullough, J. F.; Sheridan, R. C.; Frederick, L. L., Pyrolysis of urea phosphate. *J. Agri. Food Chem.* **1978,** *26* (3), 670-675.

31. Wang, T.; Du, K.; Liu, W.; Zhu, Z.; Shao, Y.; Li, M., Enhanced electrocatalytic activity of MoP microparticles for hydrogen evolution by grinding and electrochemical activation. *J. Mater. Chem. A* **2015,** *3* (8), 4368-4373.

32. Cannon, P., The solubility of molybdenum trioxide in various mineral acids. *J. Inorg. Nuc. Chem.* **1959,** *11* (2), 124-127.

33. Pelavin, M.; Hendrickson, D.; Hollander, J.; Jolly, W., Phosphorus 2p electron binding energies. Correlation with extended Hueckel charges. *J. Phy. Chem.* **1970,** *74* (5), 1116-1121.

34. Jiang, H.; Zhu, Y.; Su, Y.; Yao, Y.; Liu, Y.; Yang, X.; Li, C., Highly dual-doped multilayer nanoporous graphene: efficient metal-free electrocatalysts for the hydrogen evolution reaction. *J. Mater. Chem. A* **2015,** *3* (24), 12642-12645.

35. Franke, R.; Chassé, T.; Streubel, P.; Meisel, A., Auger parameters and relaxation energies of phosphorus in solid compounds. *J. Electron Spectrosc. Relat. Phenom.* **1991,** *56* (4), 381-388.

36. Dong, H.; Liu, C.; Ye, H.; Hu, L.; Fugetsu, B.; Dai, W.; Cao, Y.; Qi, X.; Lu, H.; Zhang, X., Three-dimensional Nitrogen-Doped Graphene Supported Molybdenum Disulfide Nanoparticles as an Advanced Catalyst for Hydrogen Evolution Reaction. *Sci. Rep.* **2015,** *5*, 17542.

37. Ito, Y.; Cong, W.; Fujita, T.; Tang, Z.; Chen, M., High Catalytic Activity of Nitrogen and Sulfur Co-Doped Nanoporous Graphene in the Hydrogen Evolution Reaction. *Angew. Chem. Int. Ed.* **2015,** *54* (7), 2131-2136.

38. Sanjinés, R.; Wiemer, C.; Almeida, J.; Levy, F., Valence band photoemission study of the Ti □ Mo □ N system. *Thin Solid Films* **1996,** *290*, 334-338.

39. Patterson, T. A.; Carver, J. C.; Leyden, D. E.; Hercules, D. M., A surface study of cobalt-molybdena-alumina catalysts using X-ray photoelectron spectroscopy. *J. Phy. Chem.* **1976,** *80* (15), 1700-1708.

40. Duan, J.; Chen, S.; Jaroniec, M.; Qiao, S. Z., Porous C3N4 nanolayers@ N-graphene films as catalyst electrodes for highly efficient hydrogen evolution. *ACS Nano* **2015,** *9* (1), 931-940.

5. Sulfur-Doped Cobalt Phosphide Nanoparticles as a Highly Efficient Bifunctional Water Splitting Electrocatalyst

5.1 Abstract

Sulfur doping into cobalt phosphide lattice enhances greatly its electrocatalytic activity for the bifunctional water splitting of both hydrogen and oxygen evolution reactions through tuning its electronic structure. Thus sulfur doped-CoP (S: CoP) nanoparticles are directly grown on a highly porous and conductive nickel foam (S: CoP@NF) *via* unique and eco-friendly thiourea-phosphate-assisted solvothermal route to obtain a hybrid electrode. As a bifunctional electrocatalyst for water splitting, the electrode exhibits superb activity and stability in basic electrolytes outperforming commercial Pt/C and RuO_2, and other non-noble metal-based electrocatalysts reported so far in practical high current region. This excellent performance is related to the improved charge transfer characteristics of S:CoP nanoparticles due to the modified electronic structure, together with high electrochemical active surface area and the conductive NF supports of three-dimensionally interconnected structure. A S:CoP catalyst-based alkaline electrolyzer produces a stable current density of 100 mA/cm^2 at an overvoltage around 0.55 V in a long-term operation, better than the combination of Pt/C cathode and RuO_2 anode. The ingenious synthetic approach employed here could be readily extended to produce other transition metal phosphides electrocatalysts.

5.2 Introduction

The electrochemical hydrogen evolution reaction (HER) and oxygen evolution reaction (OER) from water splitting has attracted a great attention recently as a key technology for sustainable hydrogen production.[1-3] The most important challenge in practical water electrolysis is to replace the incumbent Pt for HER and Ir/Ru-based catalysts for OER with inexpensive, yet still efficient non-precious metals.[4] In particular, a great deal of efforts have been devoted over the last decade to replace the expensive noble metal-based electrocatalysts for HER with cheaper earth-abundant materials such as transition metal carbides, sulfides, borides, nitrides, selenides and phosphides[1, 4-6] and for OER with phosphates, perovskites, chalcogenides, oxides/hydroxides and phosphides.[1, 7-9] However, pairing HER and OER electrocatalysts in a practical electrolyzer is another challenge because of their mismatched stability and activity in widely different pH ranges. Therefore, developing a highly active and stable bifunctional electrocatalyst for both HER and OER in the same pH electrolyte is highly desirable.

Recently, nanostructured cobalt phosphides (CoP) have been extensively studied owing to their excellent bifunctional water splitting activity for both HER and OER in a wide pH range.[10-11] Yet, further improvement in activity and stability is needed to obtain performance comparable to that of the

noble metals. Experimental and theoretical investigations have revealed that introduction of more electronegative P atoms into transition metals may greatly restrict the electron delocalization in metal resulting in lower conductivity.[5, 12] However, doping of other heteroatoms or alloying with different metal atoms in the phosphides is known to enhance the metallic character to improve their intrinsic activity, especially for the metal-rich phosphides.[5] Similar approaches have been exercised to improve the HER/OER activity of CoP; i) making pyrite-type cobalt phosphosulfide (CoS|P) nanostructures on CNT/carbon fiber paper,[13-14] ii) hybridizing with highly conductive supports like graphene, carbon cloth (CC) and metallic Ni/Co foam,[15-19] and iii) promotion with a transition metal like Ni, Fe, Mn, Zn or Cu.[20-24] The metal phosphides nanostructures are commonly synthesized via three ways: i) Solution-phase synthesis by using tri-n-octylphosphine (TOP), tri-phenylphosphine (TPP) or tri-n-octylphosphine oxide (TOPO) as a P source in a high boiling solvent (e.g. oleylamine) in inert atmosphere.[5, 25] ii) Gas-solid reaction, in which hypophosphite or red phosphorus are used to produce extremely toxic and lethal PH_3 gas, and thus, post-treatment is mandatory with inert gas to remove the residual PH3.[25] iii)) High temperature reduction of metal phosphates to form bulk phosphides.[5, 25]

Here, we adopt a novel, inexpensive and eco-friendly thiourea-phosphate-assisted route to synthesize a highly active and stable bifunctional water splitting S-doped CoP electrocatalyst directly grown on a highly porous and conductive nickel foam (S:CoP@NF), which generates a current density of 100 mA/cm^2 at a low overpotential of ~0.55 V in an alkaline electrolyzer outperforming a commercial Pt/C - RuO_2 electrolyzer as well as CoP-based bifunctional electrocatalysts reported so far. This high performance originates from the improved charge transfer characteristics of S:CoP nanoparticles due to the modified electronic structure by S-doping, together with high electrochemical active surface area and the conductive NF supports of three-dimensionally interconnected structure. Refraining from the use of costly, poisonous and corrosive P-sources like PH_3, hypophosphite, organic phosphine and high boiling organic solvents is another advantage of this synthetic method, which could be applied to other transition metal phosphides.

5.3 Experimental section

5.3.1 Synthesis of S-doped CoP nanoparticles and their composites with substrates

All chemicals were used as purchased without further purification. Thiourea-phosphate complex was synthesized by mixing thiourea with phosphoric acid.[5] Typically, 85 % phosphoric acid (8.0 mmol, Sigma-Aldrich) and thiourea (8.0 mmol, Sigma) were mixed in triply distilled water (20 mL) to form an aqueous urea-phosphate solution in a stirred glass beaker (250 mL). The reaction mixture was heated to 60 ^{0}C until the transparent solution was obtained. A freshly prepared transparent aqueous solution (20 ml) of cobalt nitrate hexahydrate ($Co(NO_3)_2 \cdot 6H_2O$, 8.0 mmol, Sigma-Aldrich) was poured slowly.

The reaction mixture was hydrothermally treated at 160 °C for 24 h to convert the reactants to a S-doped Co-urea-phosphate complex by H_2S gas generated from internal decomposition of thiourea, and the remaining phosphoric acid reacts with indigenously generated urea/ammonia (NH_3) gas to form urea/ammonium phosphate. Then, this freshly prepared suspension of pH 7 was dried at 60 ^{0}C to obtain the precursor powder.

The precursor S-doped Co-urea-phosphate powder was reduced under H_2 gas with ramping temperatures (5 ^{0}C/min) to a pre-optimized temperature (600 ^{0}C), kept there for 3 h and then cooled down naturally to get S:CoP NPs. For comparison, undoped CoP NPs were also prepared by using simple urea following otherwise the same procedure. The S:CoP nanoparticles were also grown on N-doped graphene (S:CoP@NG), carbon cloth (S:CoP@CC) and nickel foam (S:CoP@NF) by loading the required amount of S-doped Co-urea-phosphate precursor onto the substrates, drying at 60 °C, and reduction in H_2 atmosphere.

5.3.2 Physical characterization.

Crystallographic structure of the electrocatalysts was investigated by powder X-ray diffraction (XRD, PANalytical pw 3040/60 X'pert) with Cu Kα radiation. The morphologies were probed with field-emission scanning electron microscope (FE-SEM, Hitachi, S-4800, 15 kV) and transmission electron microscope (TEM, JEOL, JEM-2100). The chemical compositions, elemental mapping and in-depth crystal information of samples were collected by high resolution transmission electron microscope (HRTEM, JEOL, JEM-2100F). X-ray photoelectron spectroscopy (XPS, ThermoFisher, K-alpha) was used to identify the chemical states of the surface atoms.

5.3.3 Electrochemical measurements.

The catalyst ink was prepared by dispersing S:CoP, S:CoP@NG and undoped CoP electrocatalysts (5.0 mg/mL) in an equal volume mixture of deionized water and ethanol, and 10 μL of 5% Nafion solution. The working electrode was prepared by drop casting of 10 μL sonicated ink onto a glassy carbon electrode (0.4-0.5 mg/cm^2 loading) and drying at room temperature. The S:CoP@CC and S:CoP@NF electrodes were used as-synthesized without adding any binder. Electrochemical HER/OER activity and stability tests were carried out in a three electrode cell configuration using a rotating disc electrode (RDE, PAR Model 636 RDE) attached with a potentiostat (Ivium technologies). An Ag/AgCl (3.0M NaCl) electrode and a Pt foil were used as reference and counter electrodes, respectively. In two electrode configuration, the cathode (HER electrode) is used a counter and reference electrode with anode (OER electrode) as working electrode. All potentials were iR corrected and referenced to the reversible hydrogen electrode (RHE) by the equation $E_{RHE}=E_{(Ag/AgCl)} + 0.059pH + 0.20$.

The HER performance was measured in aqueous 1.0 M KOH (pH 13.7) at a scan rate of 2 mV/ s after 20 cyclic voltammetry (CV) cycles in the range of 0.4 to -0.3 V_{RHE}. The electrochemical stability tests were conducted by performing chronoamperometry (CA) for 20 h. Electrochemical impedance spectroscopy (EIS) was conducted in the same setup in the frequency range of 100 kHz to 1 mHz with a modulation amplitude of 10 mV. To evaluate the electrochemical active surface area (ECSA), CV was conducted from -0.8 to -0.6 V in 1.0 M KOH *vs.* Ag/AgCl with different sweep rates between 20 to 100 mV s^{-1}.

5.4 Results and discussion

5.4.1 Urea-phosphate-assisted synthesis of cobalt phosphide nanoparticles

Thiourea [$(NH_2)_2CS$] is a weak reducing agent that forms H_2S gas and urea-phosphate in the presence of H_3PO_4 (**Eq. 5.1**).[5] The property led us to design a novel procedure to produce S-doped CoP nanoparticles (S:CoP NPs) illustrated in **Figure 5.1a** and described in Experimental Section; addition of $Co(NO_3)_2 \cdot 6H_2O$ to the urea-phosphate solution to form a S-doped Co-urea-phosphate precursor *via* a solvothermal reaction (**Eq. 5.2**), followed by H_2 reduction of the precursor. The precursor is also directly grown on exfoliated N-doped graphene (NG), oxidized carbon cloth (CC) or nickel foam (NF) to obtain S:CoP@NG, S:CoP@CC and S:CoP@NF electrocatalysts, respectively. For comparison, undoped CoP NPs were also prepared by using urea $(NH_2)_2CO$ instead of thiourea according to otherwise the same method.

$$H_3PO_4 + (NH_2)_2CS \xrightarrow{H^+} H_2S + (NH_2)CO(NH_2).H_3PO_4 \quad (5.1)$$

$$(NH_2)CO(NH_2).H_3PO_4 + xH_2S + Co^{2+} \xrightarrow{\Delta} \text{S} - \text{doped Co. urea. phosphate} \quad (5.2)$$

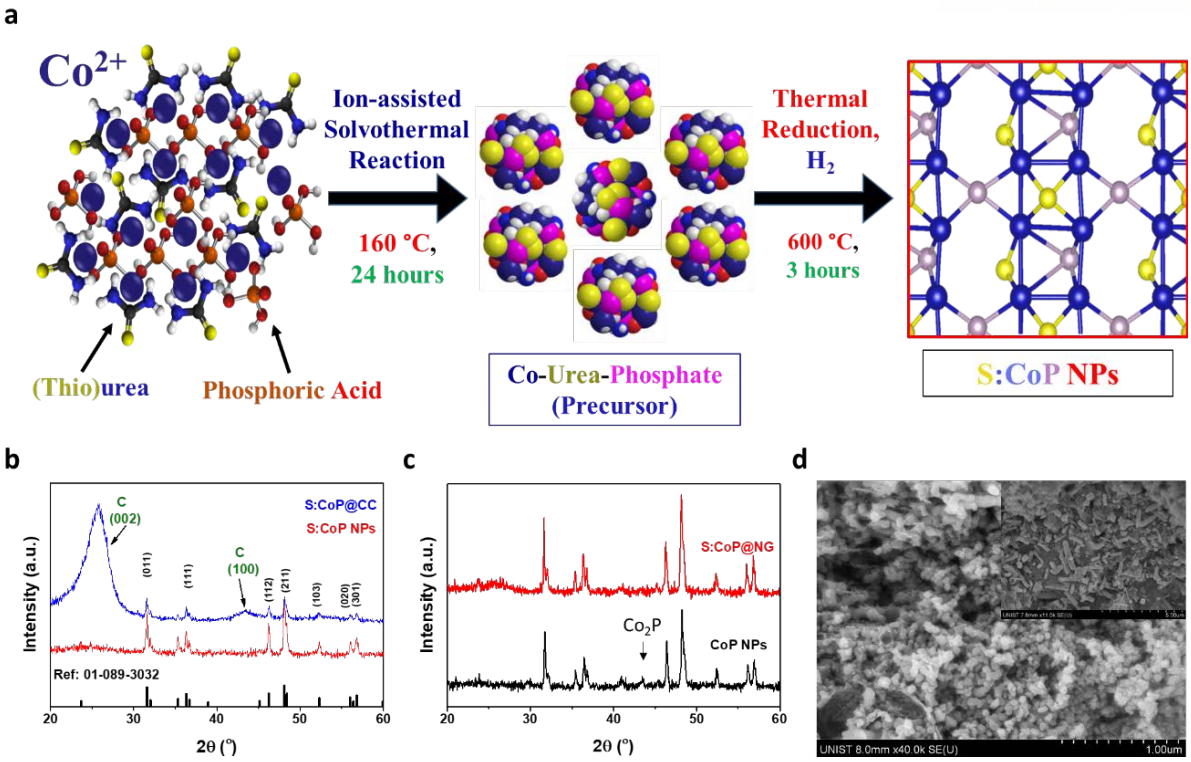

Figure 5.1. (a) Schematic illustration of thiourea-phosphate-assisted synthesis of S-doped CoP nanoparticles, (b) XRD patterns of S:CoP NPs and S:CoP@CC, (c) XRD of CoP NPs and S:CoP@NG synthesized at a reduction temperature of 600 °C. SEM image of (d) S:CoP NPs and (inset) CoP nanorods.

The pure crystal phase of orthorhombic CoP nanostructure (space group Pnma, ICDD No. 01-089-2747) is confirmed in S:CoP and CoP NPs by powder X-ray diffraction (XRD) patterns after H_2 reduction at a pre-optimized temperature of 600 °C as shown in **Figure 5.1b and 5.1c**. The S-doping does not significantly alter the bulk crystal structure of CoP, or form any side product like sulfide either. Additionally, S-doping decrease the crystalline size of CoP from 32 to 20nm as calculated by applying the Scherrer equation to X-ray line broadening. The XRD pattern of S:CoP/CC and S:CoP/NG show that the phase behavior is the same for both unsupported and supported materials as shown in **Figure 5.1b and 5.1c**. Scanning electron microscopy (SEM) image of the as-synthesized CoP (**Figure 5.1d**, inset) display nanorods and S:CoP spherical particles with a grain size of ~50 nm to form a closely interconnected porous network (**Figure 5.1d**). These nanoparticles are successfully grown on porous substrates of highly exfoliated N-doped graphene (NG), carbon cloth (CC) and nickel foam (NF) as shown in SEM images of Figure 4.2a-c.

5.4.2 Phase behavior of S:CoP during hydrogen and oxygen evolution reaction

The chemical states of S:CoP NPs after 20 h of HER or OER stability tests were investigated by X-ray photoelectron spectroscopy (XPS) in **Figure 5.2d-f**. The fresh and post-HER S:CoP catalysts exhibit

two prominent Co*2p* peaks at 778.7 eV and 793.2 eV (**Figure 5.2d**) and a doublet P*2p* peaks at 129.5 and 130.4 eV (**Figure 5.2e**), which can be assigned to Co^{3+} and P^{3-} in CoP.[11, 26] The undoped CoP NPs show the Co*2p* peak at 779.1 eV[11, 26], indicating that S-doping reduces the oxidation state of Co. The positive shift in binding energy (BE) from metallic Co*2p* (~778.1 eV) and negative shift in P*2p* from elemental P (~130.2 eV) are consistent with Co^{3+} and P^{3-}, and therefore, Co^{3+} can work as a hydride acceptor ($Co^{\delta+}$-$H^{\delta-}$) and P^{3-} as a proton acceptor ($P^{\delta-}$-$H^{\delta+}$), which would facilitate HER.[26]

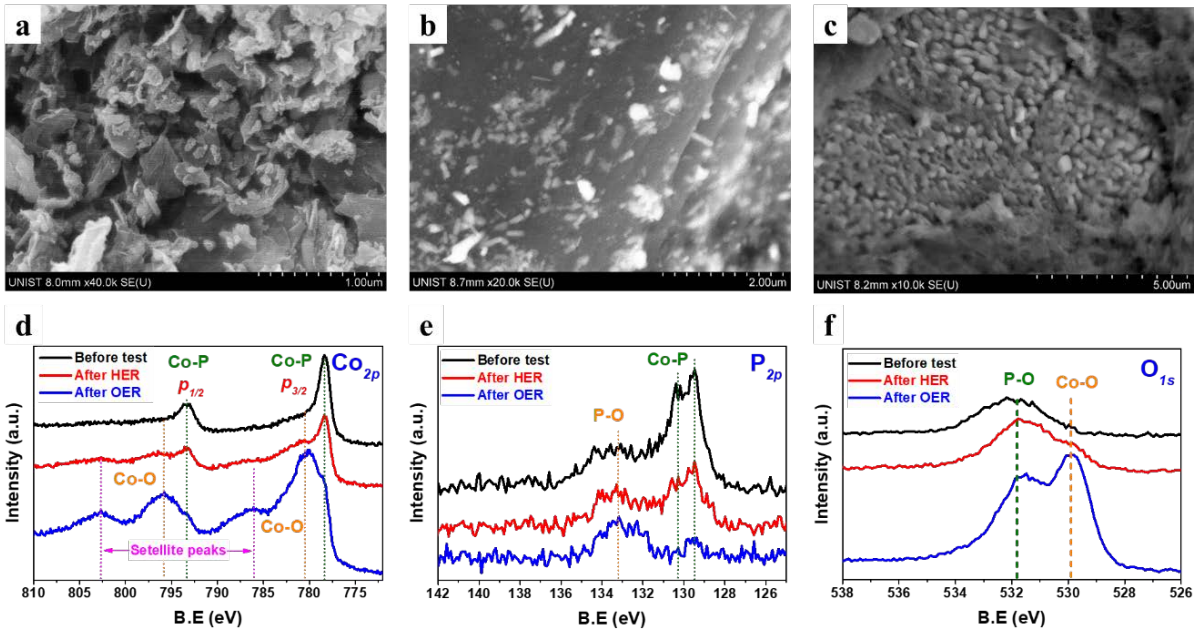

Figure 5.2. SEM images of S:CoP nanoparticles grown on substrates (a) NG, (b) carbon cloth and (c) nickel foam. High resolution XPS of S:CoP@CC; as-synthesized (black), after HER (red), and OER (blue): (d) Co*2p*, (e) P*2p* and (f) O*1s*.

An interesting observation was made in XPS of post-OER S:CoP NPs catalyst in **Figure 5.2d.** The two Co*2p* peaks at 780.2 and 795.8 eV along with satellites at 786.1 and 802.7 eV indicate the *in-situ* oxidation of CoP to a cobalt oxide (CoO).[11, 27] The satellite peaks can be assigned to reduction of the Co^{3+} ions of CoP to Co^{2+} and formation of oxygen vacancies in a good agreement with the previous reports of reducing Co_3O_4 to CoO.[27-28] This *in-situ* oxidation of CoP under OER conditions is further confirmed by the presence of an oxide peak 529.8 eV along with P-O at 531.4 eV in the O1s spectra (**Figure 5.2f**).[11, 29] The elemental composition derived from elemental analysis (EA) in **Table 5.1** shows an atomic ratio of P/Co close to 1 for as-synthesized and post-HER catalysts. However, post-OER catalyst shows a greatly reduced P/Co ratio due to dissolution of P-species into electrolyte. The increased oxygen content from 10.45 at% to 53.56 at% confirms that the most of the surface Co^{3+} ions derived from CoP are converted to a Co-oxide, while remaining 4.83 at% of P atoms indicate the presence CoP as a core in accordance with XPS data. As discussed later, the CoP core and CoO_x shell type structure provides the enhanced OER activity in alkaline media.[11] Interestingly, there is no

significant change in the content of S atoms even after HER and OER stability tests, which indicates that the promotional effect of sulfur remains effective throughout HER and OER.

Table 5.1. Elemental compositions of catalysts before and after HER/OER test derived from EA and ICP-OES.

Catalyst	Co	P	S	O
	Atomic %			
As-synthesized S:CoP	43.10	42.69	3.75	10.45
After HER	42.63	41.81	5.11	10.45
After OER	39.50	4.83	2.03	53.65

The S:CoP NPs were further characterized using high-resolution transmission electron microscopy (HR-TEM), which was conducted both before and after the 20-h HER/OER tests. The S:CoP NPs have an average size of ~5 nm (range of 3–15 nm) when grown directly on the NG or CC substrates, as shown in **Figure 5.3a**. In the HR-TEM images of S:CoP@CC (**Figure 5.3b-d**), the lattice fringes with spacings of 0.205 and 0.248 nm are assigned to the (112) and (111) facets, respectively, of orthorhombic CoP. The interplaner distances are larger because of S-doping. The (112), (211), and (103) crystallographic surfaces of CoP, which have interplaner distances of 0.203, 0.20, and 0.18 nm, respectively (**Figure 5.3e-h**) are well preserved even after the 20-h HER stability test. The elemental mapping of the as-prepared S:CoP NPs (**Figure 5.3i-m**), conducted using energy-dispersive X-ray spectroscopy (EDS)-scanning TEM, show clearly that Co, P, and S are distributed uniformly throughout the NPs.

The oxidation of S:CoP NPs during OER is also observed by HR-TEM images in **Figure 5.4a-d**. The clear lattice fringes are observed with an increased interplaner distance from 0.214 to 0.218 nm for (200) plane of CoO (PDF#: 01-078-0431, space group: Fm-3m) and from 0.243 to 0.257 nm for (311) facet of Co_3O_4 (PDF#: 01-074-1657, space group: Fd-3m).[30] This interplaner expansion is due to the presence S and P species even after OER stability test as shown in **Table 5.1**. The presence of a large amount of oxygen after OER in **Figure 5.4h** and **Table 5.1** is another evidence for the conversion of CoP to CoO_x during the reaction in agreement with the previous reports.[11, 27-28] However, as displayed in EDS-STEM mapping (**Figure 5.4e-j**), the remaining small quantities of homogeneously distributed P and S are enough to exert their promotional effects on its OER performance as discussed below.

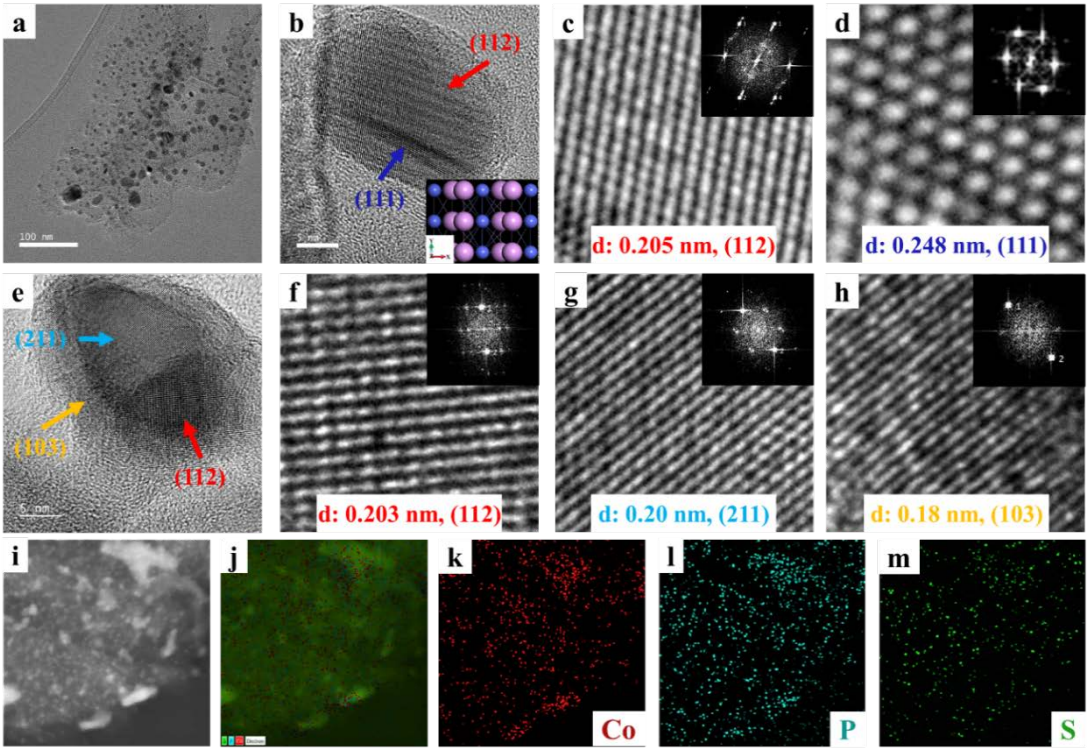

Figure 5.3. (a) TEM images of (a) S:CoP NPs grown on carbon cloth (CC) displaying NPs of 3-15 nm (scale bar: 100 nm). (b) HR-TEM image of S:CoP NPs/CC (scale bar: 5 nm). (c-d) Magnified HR-TEM images showing (112) and (111) planes and corresponding FFT patterns (inset). HR-TEM image (e) and magnified (112), (211) and (103) planes (f-h) and corresponding FFT (inset) after 20 h of HER stability test in 1.0M KOH. The EDS-STEM elemental maps of (i-m) as-synthesized S:CoP NPs.

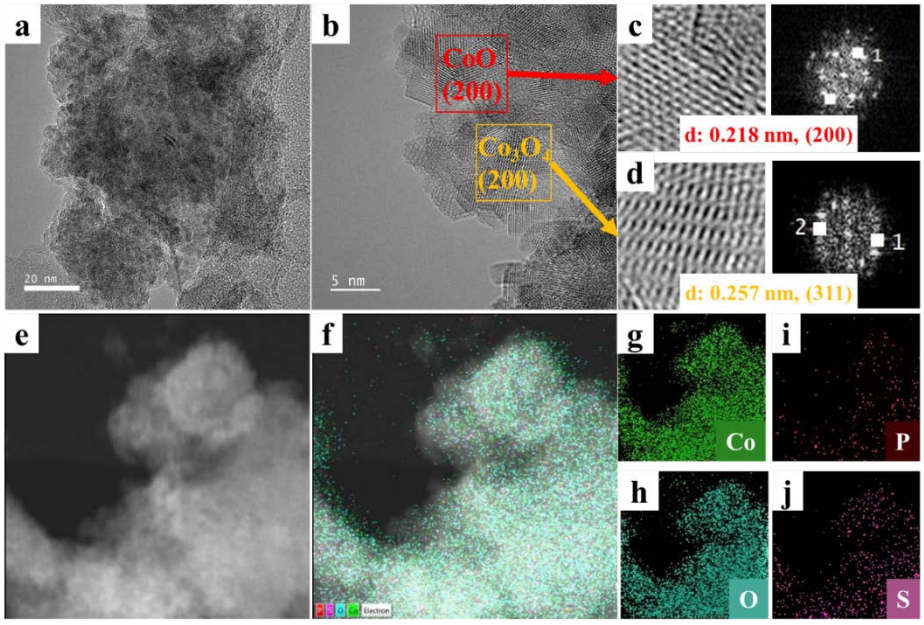

Figure 5.4. TEM images (a) and HR-TEM image (b) of oxidized S:CoP sample after a 20 h of OER durability test; scale bar 100 nm. Magnified HR-TEM image of CoO (c), Co_3O_4 (d) showing (200) and (311) planes and corresponding FFT patterns. EDS-STEM elemental mapping of (e-j) oxidized S-CoP.

5.4.3 Electrochemical HER performance

The HER activities of as-synthesized S:CoP-based electrocatalysts in 1.0M KOH aqueous solution using a three-electrode electrochemical cell are displayed with iR-corrected polarization curves in **Figure 5.5a**. Undoped CoP NPs produce cathodic currents densities of 1 and 10 mA/cm^2 at overpotentials of η_1~116 mV and η_{10}~216 mV, respectively. This HER performance is similar to those of rather active CoP catalysts reported in the literature.[26, 31] However, doping with sulfur (S:CoP NPs) improves HER performance to η_1~96 mV and η_{10}~175mV. Therefore, doping of a trace of S species into the structure of CoP exerts a profound promotional effect on its HER performance in alkaline media. The performance of the S:CoP electrocatalyst is further enhanced by directly growing S:CoP nanoparticles on a conductive substrate like NG, CC, and NF by controlled loading of the S-doped Co-urea-phosphate precursor on a pretreated substrate and subsequent H_2 reduction. The performance curves in **Figure 5.5a** clearly show markedly improved HER activity by lowering η_{10} value from 175 mV (S:CoP NPs) to 146 mV (S:CoP@NG), 121 mV (S:CoP@CC), and 109 mV (S:CoP@NF) with a mass loading of ~1.2 mg/cm^2. Surprisingly, the hybrid electrocatalysts exhibit superior HER performances relative to commercial Pt/C catalyst especially in practically important high current region with η_{100} values; 233 mV (Pt/C) > 228 mV (S:CoP/NG) > 200 mV (S:CoP@CC) > 185 mV (S:CoP@NF) (**Table 5.2**). In particular, the outstanding performance of S:CoP@NF is impressive.

The Tafel analysis was conducted in **Figure 5.5b** that gives the Tafel slopes and exchange current densities (J_0) at zero overpotential; CoP@NF (90 mV/dec, 0.04 mA/cm^2), S:CoP NPs (71 mV/dec, 0.052 mA/cm^2), S:CoP@NG (60 mV/dec, 0.04 mA/cm^2), S:CoP@CC (57 mV/dec, 0.074 mA/cm^2) and S:CoP@NF (54 mV/dec, 0.41 mA/cm^2). The results suggest that HER on these catalysts follows the Volmer−Heyrovsky mechanism in alkaline media. The higher J_0 values of S:CoP samples (0.05 - 0.41 mA/cm^2) than undoped CoP@NF (0.04 mA/cm^2) confirm that the HER kinetics become faster due to electronic and chemical promotional effects of S-doping. As shown in **Figure 5.5c**, double layer capacitance (C_{dl}) and electrochemically active surface areas (ECSA) of CoP@NF (2.78 mF/cm^2, 69.5 cm^2), S:CoP NPs (14.59 mF/cm^2, 364.75 cm^2), S:CoP@NG (43.09 mF/cm^2, 1077.25 cm^2), S:CoP@CC (186.27 mF/cm^2, 4656.75 cm^2) and S:CoP@NF (218.02 mF/cm^2, 5450.5 cm^2) also confirm that the HER activity of the electrocatalysts are directly related to their ECSA. The high ECSA of S:CoP NPs may be attributed to reduced grain sized interconnected 3-D porous network as compared to undoped bulk CoP NRs.

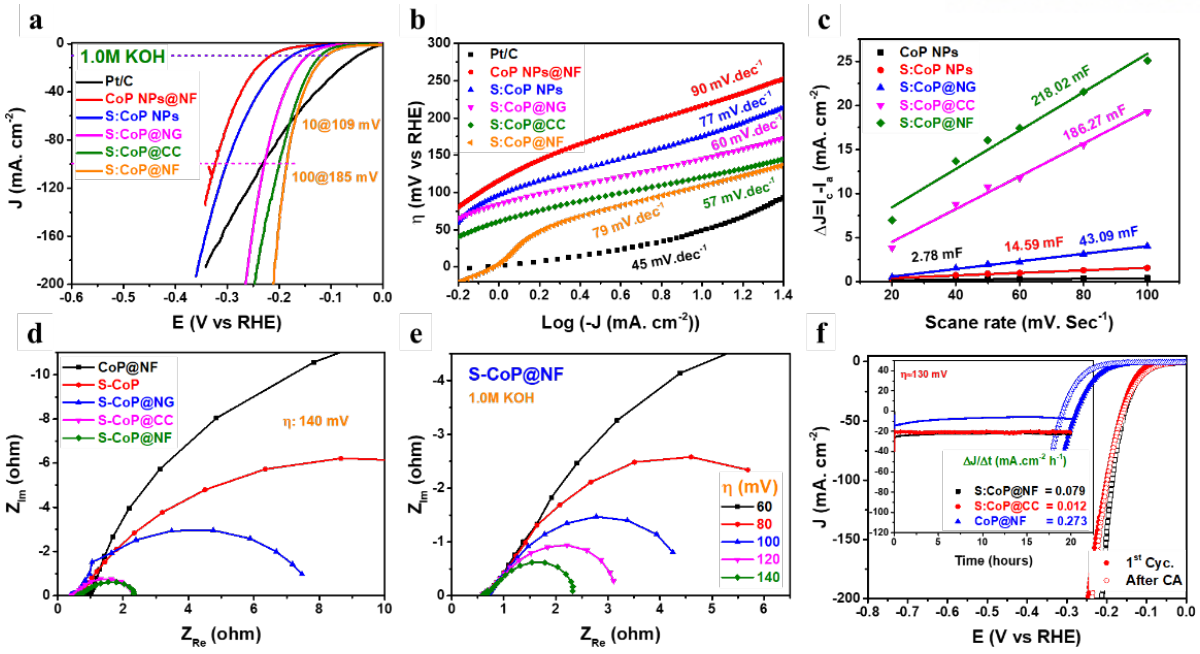

Figure 5.5. The iR-corrected LSV curves of HER for (a) undoped CoP NPs, S:CoP NPs and S:CoP grown on NG, CC and NF and corresponding (b) Tafel slopes. The measured double layer capacitance (C_{dl}) by plotting capacitive currents ($\Delta J=I_c-I_a$) as a function of scan rate (c). EIS comparison of (d) all catalysts at overpotential of 140 mV and (e) S:CoP@NF at various overpotentials. Stability comparison for HER (f) after 20 h durability test (by chronoamperometry as inset) for S:CoP@CC, S:CoP@NF and CoP@NF in 1.0M KOH.

Electrochemical impedance spectroscopy (EIS) was compared for all electrocatalysts in 1.0M KOH at an overpotentials of 140 mV (**Figure 5.5d**). The EIS Nyquist plots of S:CoP@NF (**Figure 5.5e**) at different overpotentials show that there are two time constants, one at high and second at low frequencies are corresponds to the diffusion (R_d) and charge transfer (R_{ct}) resistances at interface.[4] The relatively smaller R_{ct} and R_d values of S:CoP-based catalysts than those of undoped CoP indicate improved charge transfer characteristics by S-doping. The electrochemical stability is another important requirement for practical electrocatalysts. The chronoamperometry (CA) test was also performed for up to 20 h at a static overpotential of 130 for S:CoP@CC, S:CoP@NF and CoP@NF, respectively. As shown in **Figure 5.6f** (inset), the electrode exhibits excellent stability with negligible decrease in current densities per hour ($\Delta J/\Delta t$) of 0.012 and 0.079 $mA.cm^{-2}h^{-1}$ for S:CoP@CC and S:CoP@NF, respectively, as compared to undoped CoP@NF (0.273 $mA.cm^{-2}h^{-1}$). The linear sweep voltammetry curves in **Figure 5.6f** show excellent stability for HER of both electrodes even after a long period of 20 h operation.

Table 5.2. Comparison of HER performance of S-doped CoP with other CoP-based electrocatalysts in 1.0M KOH.

Material	η_{10} (mV)	η_{100} (mV)	TS (mV/Dec)	Electrolyte	References
S:CoP@NF	109	185	79	1.0M KOH	This work
S:CoP@CC	121	200	57	1.0M KOH	This work
S:CoP@NG	146	228	60	1.0M KOH	This work
S:CoP NPs	175	301	71	1.0M KOH	This work
CoP NPs	216	323	90	1.0M KOH	This work
Pt/C	49	233	45	1.0M KOH	This work
CoP/CC	209		129	1.0M KOH	*J. Am. Chem. Soc.* **2014,** *136* (21), 7587-7590.
CoP-MNA/Ni Foam	150		51	1.0M KOH	*Adv. Funct. Mater.* **2015,** *25* (47), 7337-7347.
Co-P/ N-doped carbon matrices	154		51	1.0M KOH	*Chem. Mater.* **2015,** *27* (22), 7636-7642.
Co-P Films/Cu Foil	94		42	1.0M KOH	*Angew. Chem.* **2015,** *127* (21), 6349-6352.
Co-phosphide/phosphate thin film	375			1.0M KOH	*Adv. Mater.* **2015,** *27* (20), 3175-3180.
CoP/RGO	150		38	1.0M KOH	*Chem. Sci.* **2016,** *7* (3), 1690-1695.
CoP NPs	170			1.0M KOH	*Nano Energy* **2016,** *29*, 37-45.
(CoxNi1-x)2P	180		63	1.0M KOH	*J. Mater. Chem. A* **2016,** *4* (20), 7549-7554.
CoP@BCN	215		52	1.0M KOH	*Adv. Energy Mater.* **2017,** *7* (9), 1601671.
h-CoP/NG	130		--	1.0 M KOH	*Nanoscale* **2016,** 8(21),10902-10907.
f-CoP/CoP_2/Al_2O_3	138		--	1.0 M KOH	*Nanoscale*, **2017,** 9, 5677
CoP@NPMG	151		--	1.0 M KOH	*Nanoscale*, **2018,** 10, 2603-2612

5.4.4 Effect S-doping band structure of CoP: A theoretical (DFT) study

Doping heteroatoms *e.g.* N, S or O into the structure of phosphides is known to play a crucial role for high HER and OER activities and.[5, 11, 13-14, 32] The total density of states (TDOS) of bulk, and low miller index stable (011) and (111) planes were calculated by using density functional theory (DFT) in order to see the effect of S-doping on electronic properties of CoP for the structures shown in **Figure 5.6a-b**. As displayed in **Figure 5.6c-d**, both CoP and S:CoP possesses non-zero DOS at Fermi level (E_0) revealing metallic band formation by overlapping Co*3d* and P*3p* orbitals. However, sulfur *3p* orbital enhances its metallic property by increasing the states deep into valance band and to the conduction band near Fermi level. In addition, S-doping makes the electron densities are more localized near Fermi level in Co*3d* of S:CoP as compared to bare CoP, which is responsible for the reduced oxidation state as indicated by Co XPS. This increased charge carrier density near Fermi level can facilitate the electrocatalytic water splitting into H_2 and O_2. The higher DOS of S:CoP at Fermi level (15.10 & 14.14) and integrated DOS 0.5eV above Fermi level (7.78 & 6.93) for (011) and (111) planes than clean CoP

confirms the increased number of electrons in conduction bands which are readily available for water absorption.

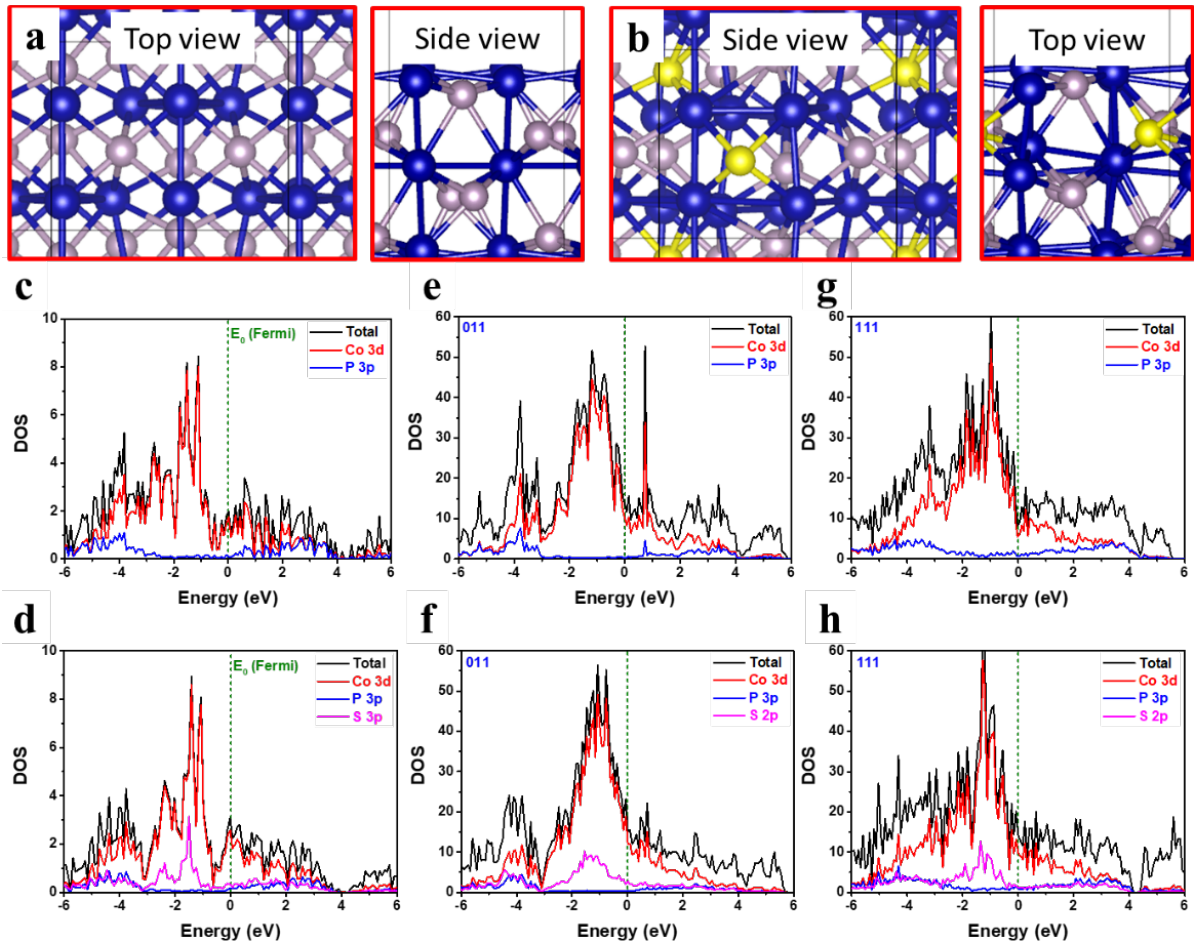

Figure 5.6. The optimized top and side view of (011) plane for (a) clean CoP and (b) S:CoP. Total density of states (TDOS) and projected density of states (PDOS) for bulk (c, d), 011 surface (e, f) and 111 surface (g, h) of undoped CoP and S:CoP, respectively.

5.4.5 Electrochemical oxygen evolution reaction

Now, the electrocatalytic OER performance in 1.0M KOH of S:CoP catalysts are compared with those of undoped CoP NPs and a commercial RuO_2 electrode for the same mass loadings (~1.2 mg/cm^2). As in **Figure 5.7a,** S:CoP NPs electrode requires a lower overpotential (η_{10}~300 mV) to reach 10 mA/cm^2 compared to CoP NPs (320 mV), and is comparable to commercial IrO_2 (337 mV). The overpotential is further lowered when these nanoparticles are directly grown on conductive substrates as shown in **Figure 5.7a**. Thus S:CoP@NF displays the lowest overpotential (η_{100}~360 mV) to produce current of 100 mA/cm^2 relative to S:CoP@CC (384 mV), S:CoP@NG (382 mV), S:CoP NPs (417 mV), CoP@NF (430 mV) and commercial IrO_2@NF (435 mV). As discussed already, the observed OER activity is attributed to an oxygen deficient surface cobalt oxide (CoO) species formed *in situ* during OER covering

S:CoP core. Thus the promotional effect of S-doping works well for OER just like HER with the *in-situ* modified active sites formed from S:CoP.

The Tafel slopes and current exchange densities of S:CoP electrodes in **Figure 5.7b** lie in the range of 82-108 mV/dec and 0.004-0.069 mA/cm^2, respectively. The Tafel slope and exchange currents of S:CoP@NF (82 mV/dec, 0.004 mA cm^{-2}) is much smaller than the Tafel slope for IrO_2@NF electrode (104 mV/dec, 0.007 mA cm^{-2}) indicating a more rapid OER reaction especially on the S:CoP@NF electrode. The EIS Nyquist plots in **Figure 5.7c** compare the electrode kinetics of all catalysts at an overpotential of 330 mV under OER conditions. The low charge-transfer resistance R_{ct} of S:CoP@NF (~1.05 ohm) than those of S:CoP@CC (1.94 ohm), S:CoP@NG (1.91 ohm), S:CoP NPs (2.43 ohm) and undoped CoP@NF (3.51 ohm) is related to the rapid electrocatalytic kinetics or faster reaction on the electrode for water oxidation. A chronoamperometry (CA) for 20 h OER was conducted at a constant overpotential of ~350 mV to evaluate the stability of IrO_2@NF, CoP@NF, S:CoP@CC and S:CoP@NF electrodes in **Figure 5.7d**. The initial increase in current density in all CA curves of CoP based catalyst may be due to *in-situ* formation of Co-oxides by dissolution of surface P species in contrast of IrO_2@NF electrode, i.e. continuous reduction in current. The LSV curves were also compared (**Figure 5.7e**) before and after chronoamperometry (CA) test for 20 h. The reduction in overpotentials required at 100 mA.cm^{-2} for all CoP catalyst (**Figure 5.7f**) show excellent stability and higher conductivity for OER even after 20 h of OER operation due to presence of trace P and S elements.

Another fundamental kinetic parameter "turnover frequency (TOF)" was calculated based on the surface active Co^{2+} sites determined from CV (**Figure 5.7g**) as reported in literatue. [33] The backward reduction peak was integrated to estimate the numbers of Co^{2+} sites per cm^{-2} for each catalyst, which were compared with current densties at overpotential of 0.35 V in **Figure 5.7h**. The TOF values of S:CoP NPs at 0.35 V_{RHE} is 0.23 s^{-1}, which is quite larger than CoP NPs (0.19 O_2 s^{-1}), S:CoP@NG(0.15 O_2 s^{-1}), S:CoP@CC(0.08 O_2 s^{-1}), CoP@NF (0.085 O_2 s^{-1}) and S:CoP@NF (0.12 O_2 s^{-1}). The overpotential η_{10} were further compared with other recently reported OER catalysts in **Figure 5.7i**, which demonstrated superiority of our S:CoP-based catalysts that needed much lower overpotentials.

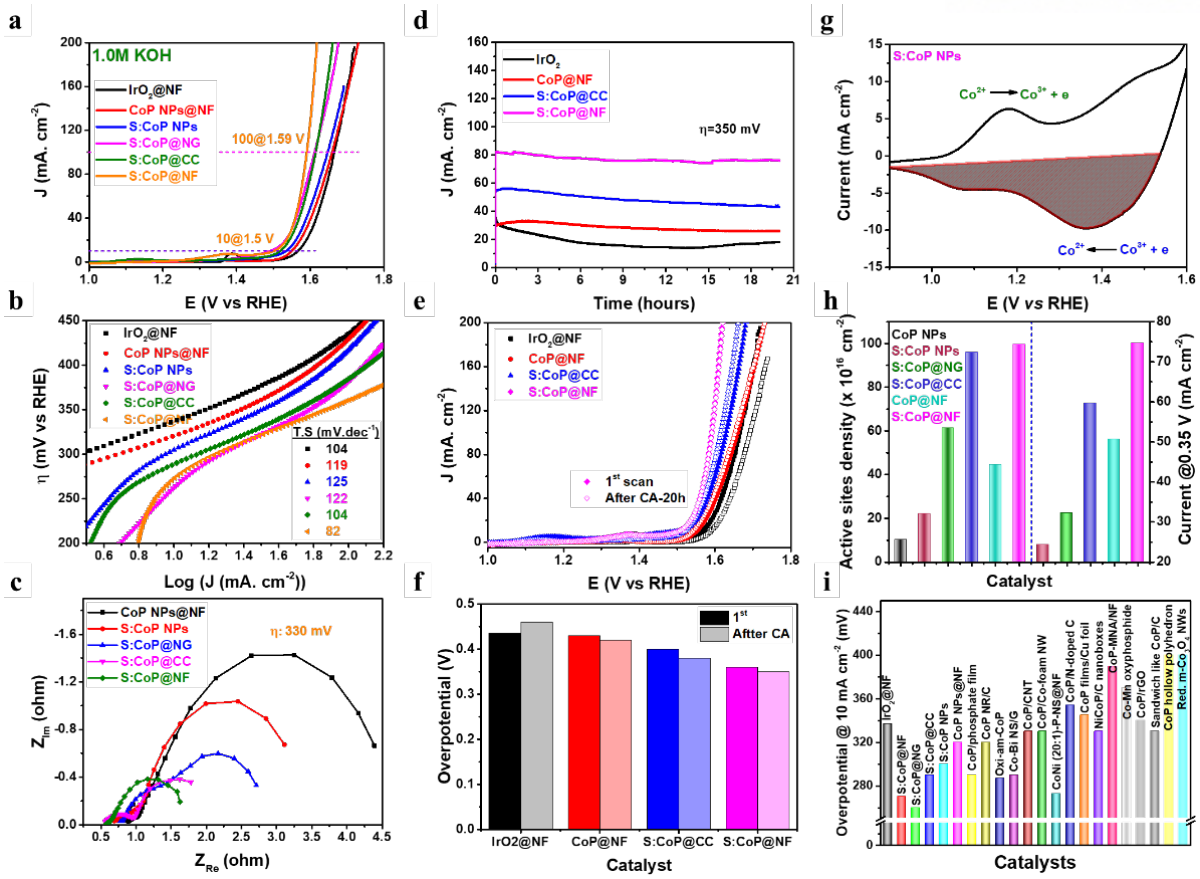

Figure 5.7. iR-corrected LSV curves of OER for (a) undoped CoP NPs, S:CoP NPs, and S:CoP grown on NG, CC, and NF substrates and corresponding (b) Tafel slopes. (c) EIS results for catalysts at overpotential of 330 mV. (d) Electrode durability by CA and (e) LSV after CA. (f) Overpotentials η_{100} before and after 20-h CA durability test. (g) CV of S:CoP NPs recorded at 100 mV s^{-1} in 1 M KOH to determine surface active Co^{2+} species. (h) Number of active sites (left), current density at an overpotential of 350 mV (right). (i) Comparison of η_{10} with other catalysts reported in literature.

5.4.6 Overall water splitting at S-doped CoP electrocatalyst

The superb HER and OER performances of S:CoP@NF electrode led us to design an alkaline electrolyzer cell using S:CoP@NF as both anode and cathode was tested in 1.0 M KOH. For comparison, cathode-anode combinations of CoP NPs - CoP@NF (no S-doping), S:CoP NPs - S:CoP@CC and Pt/C@NF - IrO_2@NF were also tested. As shown in **Figure 5.8a**, the S:CoP@NF electrolyzer displays an outstanding performance for overall water splitting with cell voltages of 1.61 V (η_{10}) and 1.78 V (η_{100}) to generate the current densities of 10 and 100 mA/cm^2. The bifunctional S:CoP@CC-based electrolyzer shows the similar performance of 1.63 V and 1.82 V, but other electrolyzers require significantly higher potentials (η_{10}, η_{100}); undoped CoP@NF (1.75 V and 1.97 V) and commercial Pt/C - IrO_2@NF (1.60 V and 1.82 V). The Tafel slope of S:CoP@NF electrolyzer is 162 mV/dec, which is much less than commercial Pt/C - IrO_2@NF (233 mV/dec) as in **Figure 5.8b.** The S:CoP@NF electrolyzer also shows excellent stability without any significant current density loss in LSV measured

after 20 h chronoamperometric stability test as shown in **Figure 5.8c** (inset). Interestingly, there is 9.1 % gain in the current density for S:CoP@NF electrolyzer after 20 h continuous operation in contrast to the Pt/C - RuO_2 electrolyzer (58.9 % loss) at cell voltage of 1.8V of the initial value as shown in **Figure 5.8d**. All the above results demonstrate that S-doped CoP electrodes exhibit excellent performance for HER, OER and overall water splitting as well as better durability than all other reported CoP-based electrocatalysts as summarized in **Table 5.3**. A representative photographs of the two-electrode configuration using S:CoP@NF as both anode and cathode are shown in **Figure 5.8e, f.** The **Figure 5.8f** clearly displays the H_2 (right) and O_2 (left) bubbles during overall water electrolysis.

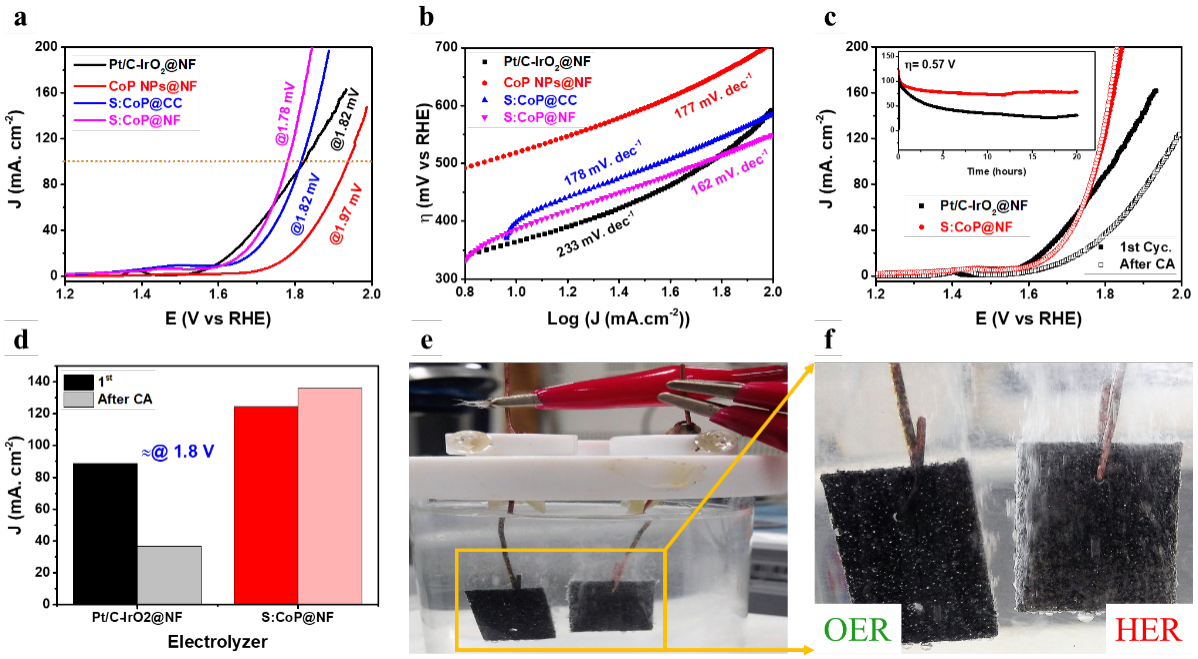

Figure 5.8. Polarization curves of a two-electrode electrolyzer (a) using CoP NPs- CoP@NF, S:CoP NPs -S:CoP@NF, S:CoP NPs – S:CoP@CC and Pt/C - RuO_2@NF at a sweeping rate of 2 mV/s and (b) Tafel plots (c) LSV curves of S:CoP NPs - S:CoP@NF and Pt/C - RuO_2@NF electrolyzer after a CA (inset) durability (20 h) test. The current density at a cell voltage of 1.8V before and after CA (e, f) and the representative photographs electrolyzer showing H_2 (right) and O_2 (left) bubbles during overall water electrolysis.

Table 5.3. Comparison with various electrocatalysts for overall water splitting

Material	η_{10} (mV)	η_{100} (mV)	References
S:CoP@NF	387	550	This work
S:CoP@CC	400	590	This work
S-CoP NPs	485	710	This work
CoP NPs@NF	520	740	This work
Pt/C - RuO_2	370	600	This work
CoP/TM	410	---	*Nanotechnol.* **2016,** *27* (23), 23LT01.
Co-P film	420	520	*Angew. Chem.* **2015,** *127* (21), 6349-6352.
Amorphous CoSe film/Ti	420	650	*Chem. Commun.* **2015,** *51* (93), 16683-16686.
CoP-MNA/Ni Foam	390	---	*Adv. Funct. Mater.* **2015,** *25* (47), 7337-7347.
Ni_2P nanoparticle	400	---	*Energy Environ. Sci.* **2015,** *8* (8), 2347-2351.
Hollow Co_3O_4 MTA	400	---	*Angew. Chem. Int. Ed.* **2017,** *56* (5), 1324-1328.
Ni_2S_3/NF	13 mA.cm^2 @530 mV	---	*J. Am. Chem. Soc.* **2015,** *137* (44), 14023-14026.
$NiCo_2S_4$ NA/CC	450	---	*Nanoscale* **2015,** *7* (37), 15122-15126.
Ni2.3%-CoS_2/CC	430	---	*Electrochem. Commun.* **2016,** *63*, 60-64.
Co_3O_4 NC/carbon fiber paper	680	---	*Chem. Commun.* **2015,** *51* (38), 8066-8069.
Co_1Mn_1CH/NF	450		*J. Am. Chem. Soc.* **2017,** 139, 8320−8328
CoB@CoO nanoarray/Ti	440 @50		*Small* **2017**, 13, 1700805
NiFe-OH-PO_4/NF	450		*ACS Appl. Mater. Interfaces*, 2017, 9 (41), pp 35837–35846
$(Ni_xFe_{1-x})4P_5$	390		*J. Mater. Chem. A*, **2018**, DOI: 10.1039/C8TA00622A.
Ni_xFe_{3-x}-O/NF	410		*Adv. Energy Mater.* **2017**, 1701347
NiFeOF holey film	600		*ACS Catal.* **2017,** 7, 8406−8412
3D $NiFeO_x$ & NiFe-P/IF	--	630	*Adv. Energy Mater.* **2017**, 7, 1700107
$NiCo_2Se_4$ holey nanosheets	450		*ACS Nano* **2017**, 11, 9550−9557

5.5 Conclusions

In summary, the electronic properties of CoP have been modulated by S-doping into its structure by adopting a unique and environmental friendly thiourea-phosphate route, in which a reductant thiourea controls the particle size of CoP and becomes a source of S, while H_3PO_4 provides P. The as-synthesized bifunctional water splitting S:CoP NPs, especially those grown directly on a conductive substrate like nickel foam display excellent performance and remarkable stability for both HER and OER exceeding commercial precious metal catalysts of Pt/C and RuO_2, respectively. An overall water splitting electrolyzer with S:CoP@NF as a bifunctional electrode generates current density of 10 and 100 mA/cm^2 at overpotentials of 0.387 and 0.55 V in 1.0 M KOH outperforming commercial Pt/C - IrO_2 electrolyzer and all CoP-based electrocatalysts reported so far. The low-cost and eco-friendly synthetic approach employed in this study could become a general synthetic method for other transition metal phosphides as OER, HER and overall water splitting bifunctional catalysts.

5.6 References

1. Roger, I.; Shipman, M. A.; Symes, M. D., Earth-abundant catalysts for electrochemical and photoelectrochemical water splitting. *Nat. Rev. Chem.* **2017,** *1*, 0003.

2. Bashyam, R.; Zelenay, P., A class of non-precious metal composite catalysts for fuel cells. *Nature* **2006,** *443* (7107), 63-66.

3. Chu, S.; Cui, Y.; Liu, N., The path towards sustainable energy. *Nat. Mater.* **2017,** *16* (1), 16-22.

4. Zou, X.; Zhang, Y., Noble metal-free hydrogen evolution catalysts for water splitting. *Chem. Soc. Rev.* **2015,** *44* (15), 5148-5180.

5. Anjum, M. A. R.; Lee, J. S., Sulfur and Nitrogen Dual-Doped Molybdenum Phosphide Nanocrystallites as an Active and Stable Hydrogen Evolution Reaction Electrocatalyst in Acidic and Alkaline Media. *ACS Catal.* **2017,** *7* (4), 3030-3038.

6. Anjum, M. A. R.; Lee, M. H.; Lee, J. S., BCN Network-Encapsulated Multiple Phases of Molybdenum Carbide for Efficient Hydrogen Evolution Reaction in Acidic and Alkaline Media. *J. Mater. Chem. A* **2017,** *5* (25), 13122-13129.

7. Anantharaj, S.; Ede, S. R.; Sakthikumar, K.; Karthick, K.; Mishra, S.; Kundu, S., Recent Trends and Perspectives in Electrochemical Water Splitting with an Emphasis on Sulfide, Selenide, and Phosphide Catalysts of Fe, Co, and Ni: A Review. *ACS Catal.* **2016,** *6* (12), 8069-8097.

8. Wang, J.; Cui, W.; Liu, Q.; Xing, Z.; Asiri, A. M.; Sun, X., Recent Progress in Cobalt-Based Heterogeneous Catalysts for Electrochemical Water Splitting. *Adv. Mater.* **2016,** *28* (2), 215-230.

9. Xie, L.; Zhang, R.; Cui, L.; Liu, D.; Hao, S.; Ma, Y.; Du, G.; Asiri, A. M.; Sun, X., High-Performance Electrolytic Oxygen Evolution in Neutral Media Catalyzed by a Cobalt Phosphate Nanoarray. *Angew. Chem.* **2017,** *129* (4), 1084-1088.

10. Yang, Y.; Fei, H.; Ruan, G.; Tour, J. M., Porous Cobalt-Based Thin Film as a Bifunctional Catalyst for Hydrogen Generation and Oxygen Generation. *Adv. Mater.* **2015,** *27* (20), 3175-3180.

11. Chang, J.; Xiao, Y.; Xiao, M.; Ge, J.; Liu, C.; Xing, W., Surface oxidized cobalt-phosphide nanorods as an advanced oxygen evolution catalyst in alkaline solution. *ACS Catal.* **2015,** *5* (11), 6874-6878.

12. Carenco, S.; Portehault, D.; Boissiere, C.; Mezailles, N.; Sanchez, C., Nanoscaled metal borides and phosphides: recent developments and perspectives. *Chem. Rev.* **2013,** *113* (10), 7981-8065.

13. Liu, W.; Hu, E.; Jiang, H.; Xiang, Y.; Weng, Z.; Li, M.; Fan, Q.; Yu, X.; Altman, E. I.; Wang, H., A highly active and stable hydrogen evolution catalyst based on pyrite-structured cobalt phosphosulfide. *Nature Commun.* **2016,** *7*, 10771.

14. Cabán-Acevedo, M.; Stone, M. L.; Schmidt, J.; Thomas, J. G.; Ding, Q.; Chang, H.-C.; Tsai, M.-L.; He, J.-H.; Jin, S., Efficient hydrogen evolution catalysis using ternary pyrite-type cobalt phosphosulphide. *Nat. Mater.* **2015,** *14* (12), 1245.

15. You, B.; Jiang, N.; Sheng, M.; Gul, S.; Yano, J.; Sun, Y., High-performance overall water splitting electrocatalysts derived from cobalt-based metal–organic frameworks. *Chem. Mater.* **2015,** *27* (22), 7636-7642.

16. Huang, H.; Yu, C.; Yang, J.; Zhao, C.; Han, X.; Liu, Z.; Qiu, J., Strongly Coupled Architectures of Cobalt Phosphide Nanoparticles Assembled on Graphene as Bifunctional Electrocatalysts for Water Splitting. *ChemElectroChem.* **2016,** *3* (5), 719-725.

17. Li, W.; Gao, X.; Xiong, D.; Xia, F.; Liu, J.; Song, W.-G.; Xu, J.; Thalluri, S. M.; Cerqueira, M.; Fu, X., Vapor–solid synthesis of monolithic single-crystalline CoP nanowire electrodes for efficient and robust water electrolysis. *Chem. Sci.* **2017,** *8* (4), 2952-2958.

18. Zhu, Y. P.; Liu, Y. P.; Ren, T. Z.; Yuan, Z. Y., Self-Supported Cobalt Phosphide Mesoporous Nanorod Arrays: A Flexible and Bifunctional Electrode for Highly Active Electrocatalytic Water Reduction and Oxidation. *Adv. Funct. Mater.* **2015,** *25* (47), 7337-7347.

19. Wang, P.; Song, F.; Amal, R.; Ng, Y. H.; Hu, X., Efficient Water Splitting Catalyzed by Cobalt Phosphide-Based Nanoneedle Arrays Supported on Carbon Cloth. *ChemSusChem.* **2016,** *9* (5), 472-477.

20. Yu, J.; Li, Q.; Li, Y.; Xu, C. Y.; Zhen, L.; Dravid, V. P.; Wu, J., Ternary Metal Phosphide with Triple-Layered Structure as a Low-Cost and Efficient Electrocatalyst for Bifunctional Water Splitting. *Adv. Funct. Mate.* **2016,** *26* (42), 7644-7651.

21. Xiao, X.; He, C.-T.; Zhao, S.; Li, J.; Lin, W.; Yuan, Z.; Zhang, Q.; Wang, S.; Dai, L.; Yu, D., A general approach to cobalt-based homobimetallic phosphide ultrathin nanosheets for highly efficient oxygen evolution in alkaline media. *Energy Environ. Sci.* **2017,** *10* (4), 893-899.

22. He, P.; Yu, X. Y.; Lou, X. W. D., Carbon-Incorporated Nickel–Cobalt Mixed Metal Phosphide Nanoboxes with Enhanced Electrocatalytic Activity for Oxygen Evolution. *Angew. Chem.* **2017,** *129* (14), 3955-3958.

23. Tang, C.; Zhang, R.; Lu, W.; He, L.; Jiang, X.; Asiri, A. M.; Sun, X., Fe-Doped CoP Nanoarray: A Monolithic Multifunctional Catalyst for Highly Efficient Hydrogen Generation. *Adv. Mater.* **2017,** *29* (2), 201602441.

24. Zhang, X.; Zhang, X.; Xu, H.; Wu, Z.; Wang, H.; Liang, Y., Iron-Doped Cobalt Monophosphide Nanosheet/Carbon Nanotube Hybrids as Active and Stable Electrocatalysts for Water Splitting. *Adv. Funct. Mater.* **2017,** *27* (24), 201606635.

25. Shi, Y.; Zhang, B., Recent advances in transition metal phosphide nanomaterials: synthesis and applications in hydrogen evolution reaction. *Chem. Soc. Rev.* **2016,** *45* (6), 1529-1541.

26. Tian, J.; Liu, Q.; Asiri, A. M.; Sun, X., Self-supported nanoporous cobalt phosphide nanowire arrays: an efficient 3D hydrogen-evolving cathode over the wide range of pH 0–14. *J. Am. Chem. Soc.* **2014,** *136* (21), 7587-7590.

27. Wang, Y.; Zhou, T.; Jiang, K.; Da, P.; Peng, Z.; Tang, J.; Kong, B.; Cai, W. B.; Yang, Z.; Zheng, G., Reduced mesoporous Co3O4 nanowires as efficient water oxidation electrocatalysts and supercapacitor electrodes. *Advanced Energy Materials* **2014,** *4* (16), 201400696.

28. Liao, L.; Zhang, Q.; Su, Z.; Zhao, Z.; Wang, Y.; Li, Y.; Lu, X.; Wei, D.; Feng, G.; Yu, Q., Efficient solar water-splitting using a nanocrystalline CoO photocatalyst. *Nat. Nanotechnol.* **2014,** *9* (1), 69-73.

29. Jeong, S.; Park, S.; Cho, J., High-Performance, Layered, 3D-LiCoO2 Cathodes with a Nanoscale Co3O4 Coating via Chemical Etching. *Adv. Energy Mater.* **2011,** *1* (3), 368-372.

30. Yang, X.; Li, H.; Lu, A.-Y.; Min, S.; Idriss, Z.; Hedhili, M. N.; Huang, K.-W.; Idriss, H.; Li, L.-J., Highly acid-durable carbon coated Co 3 O 4 nanoarrays as efficient oxygen evolution electrocatalysts. *Nano Energy* **2016,** *25*, 42-50.

31. Tabassum, H.; Guo, W.; Meng, W.; Mahmood, A.; Zhao, R.; Wang, Q.; Zou, R., Metal–Organic Frameworks Derived Cobalt Phosphide Architecture Encapsulated into B/N Co-Doped Graphene Nanotubes for All pH Value Electrochemical Hydrogen Evolution. *Adv. Energy Mater.* **2017,** *7* (9), 201601671.

32. Dutta, A.; Samantara, A. K.; Dutta, S. K.; Jena, B. K.; Pradhan, N., Surface-Oxidized Dicobalt Phosphide Nanoneedles as a Nonprecious, Durable, and Efficient OER Catalyst. *ACS Energy Lett.* **2016,** *1* (1), 169-174.

33. Karthick, K.; Anantharaj, S.; Karthik, P. E.; Subramanian, B.; Kundu, S., Self-Assembled Molecular Hybrids of CoS-DNA for Enhanced Water Oxidation with Low Cobalt Content. *Inorg. Chem.* **2017,** *56* (11), 6734-6745.

6. Promoting the Overall Water-Splitting Efficiency of Di-cobalt Phosphide by Incorporating Sulfur

6.1 Abstract

The electronic properties of metallic di-cobalt phosphide (Co_2P) are regulated by in cooperation of more electronegative sulfur into its structure by simply using economical and eco-friendly thiourea-phosphate assisted strategy. Density functional theory (DFT) in conjunction with XPS reveal that the S decreases the electron density (TDOS) near the Fermi level minimizing the metallic nature of Co_2P by inducing more positive charge on metallic Co, creates equilibrium between hydride ($Co^{\delta+}$–$H^{\delta-}$) and proton ($S/P^{\delta-}$–$H^{\delta+}$) acceptors just like in CoP, increases the number of Co^{2+} active sites and turnover frequency (TOF). The obtained both hybrid electrodes S:Co_2P@NCC and S:Co_2P@NF exhibit superb HER, OER and bifunctional performance with ≈100 % efficiency in basic electrolytes defeating commercial Pt/C and IrO_2 catalysts at high current regions and most of other state of the art bifunctional electrocatalysts reported so far. The S:Co_2P@NF alkaline electrolyzers produce a stable current density of 100 mA/cm^2 at overvoltage 0.567 V better than the commercial IrO_2-Pt/C electrolyzer (0.593 V). The unique synthetic approach employed here could be readily extended to produce and regulate the electrochemical properties of other transition metal phosphides.

6.2 Introduction

The electrolysis of water to generate hydrogen and oxygen in a sustainable way is one of the "holy desire" but remains deceptive target in electrocatalysis and renewable energy technology.[1-3] This elusive goal has been unachieved so for mainly because of unavailability of more efficient non-precious metals to replace the most common incumbent noble-metal-based materials (Pt and Ir/Ru) for the hydrogen evolution reaction (HER) and oxygen evolution reaction (OER) in electrochemical water slitting.[4-6] To improve the water slitting efficiency by reducing the overpotentials of two half-reactions, a lot of cheaper earth-abundant materials have been explored for HER[5, 7-8] and OER.[9-11] However, designing a practical electrolyzer by pairing HER and OER active catalysts, has been remained a big challenge because of their mismatched stability and activity in widely different pH ranges. Therefore, it is a dire need to develop a highly active, stable and inexpensive bifunctional electrocatalyst for both HER and OER in the same pH electrolyte. Currently, cobalt-based heterogeneous catalysts like phosphates, chalcogenides, oxides/hydroxides and phosphides have extensively explored due to their exceptional bifunctional water splitting capability and electrochemical stability in acidic and alkaline electrolytes.[7] Uniform grafting of Co-based nanomaterials onto stable electrode materials such as nickel foam (NF)

or carbon cloth (CC) to reduce large overpotentials and enhance stability is a laborious job in practical application.[9]

Nanostructured mono cobalt phosphides (CoP) have been prepared using various methods and extensively studied in last decade due to its high performance for both HER and OER in a wide pH range.[12-14] However, metallic di-cobalt phosphide (Co_2P) has not been explored for overall water slitting as extensively as CoP, because many of current methods suffer from generation of competing phase control between CoP and Co_2P.[15] Although, a few successful examples are reported over metallic cobalt phosphide (Co_2P) as HER and OER catalysts, but they are synthesized via solution-phase strategy by using highly toxic organic phosphines i.e. tri-phenylphosphine (TPP), tri-n-octylphosphine (TOP) or tri-n-octylphosphine oxide (TOPO) as a P source in a high boiling solvent (*e.g.* oleylamine) in inert atmosphere[16-19] or direct Ph_3 gas.[20-21] In often cases, a mixture of a few stoichiometries are formed with a major product and a few other byproducts.[15, 22] According to previous experimental and theoretical studies, the metal to P ratio in transition metal phosphides play a significant role in water splitting as P act as proton acceptor and metal act as hydride acceptor.[23-25] Increasing the P contents or metal-phosphorus bonds at the surface results in improving the HER activity.[17] Therefore, due to low Co-P or more metal (Co) densities at the surface, Co_2P requires more overpotential as compared to CoP to generate same current density.[17] However, doping of more electronegative heteroatoms (N, S or O) especially in the metal-rich phosphides can improve intrinsic HER/OER activity.[7, 20] Recently, similar approaches have been exercised to regulate the HER/OER kinetic of Co_2P by incorporation of oxygen or surface oxidation of metallic cobalt phosphide.[20-21] Due to lack of phase-control ability, high toxicity and expensive precursors of current methods for phosphides it is highly desirable to develop ecofriendly, economical phase/shape flexible strategy to grow and regulate the electronic properties of Co_2P nanocrystals for stable HER/OER electrodes.

Here, we report for the first time a unique, economic and environmentally friendly urea-phosphate-assisted strategy to synthesize a phase-pure metallic cobalt phosphide. The electronic properties of Co_2P are regulated by in cooperation of more electronegative sulfur into its structure by simply replacing urea with thiourea. The dopant S induces more positive charge on metallic cobalt by creating equilibrium between hydride ($Co^{\delta+}-H^{\delta-}$) and proton ($S/P^{\delta-}-H^{\delta+}$) acceptors at surface and weakening the O-H bond of water through more positively charged $Co^{\delta+}$ at surface of S-doped Co_2P by facilitating release of proton to P/S. It also increases the electrochemical surface area (ECSA), number of active sites ant intrinsic activity. Theoretically study (DFT) in conjunction with XPS further confirms the decrease in density of states near Fermi level due to sulfur incorporation which regulates its electronic/protonic properties by minimizing metallic character of Co_2P. The S-incorporated metallic phosphide (S:Co_2P) NPs grafted on carbon cloth (CC) and nickel foam (NF) provides a current density of 100 mA/cm^2 at low overpotential of ~0.567 V, in an alkaline electrolyzer better than commercial IrO_2-Pt/C electrolyzer

and most of state of art bifunctional electrocatalysts reported so far. The 3-D supports (CC and NF) also improve the mass transport property as well as provide high electrochemical active surface area (ECSA) towards this ultrastable electrocatalytic HER and OER activity toward. Avoiding from the use of expensive and toxic organic phosphine in high boiling organic solvents or PH_3 and controlling the phase/shape of transition metal phosphides is another beauty of this systematic economical approach.

6.3 Experimental section

6.3.1 Synthesis of S-doped Co_2P nanoparticles and its composites

All chemicals were utilized as purchased without further purification. Thiourea-phosphate complex was synthesized by following our previous procedure with slight modification.[7] Typically, 4.0 mmol 85 % phosphoric acid (Sigma-Aldrich) and 8 mmol thiourea (Sigma-Aldrich) were dissolved in a mixture of melamine (0.5 mmol) and triply distilled water (30 mL) with 1:3 in a stirred glass beaker. Then 20 ml transparent aqueous solution of cobalt nitrate hexahydrate ($Co(NO_3)_2 \cdot 6H_2O$, 8.0 mmol, Sigma-Aldrich) was gradually poured into above thiourea phosphate complex solution while keep stirring at 60°C. Then the reaction mixture was hydrothermally heated at 160 °C for 24 h to get S-incorporated Co-urea-phosphate complex by thermal decomposition of thiourea to H_2S gas and urea/ammonia-phosphate in the presence of Co^{2+} ions and phosphoric acid. Then, this suspension was dried at 60 ^{0}C to obtain the precursor powder for S:Co_2P NPs.

The S:Co_2P NPs were synthesized by thermal reduction of above precursor powder under H_2 gas with ramping temperatures (5 ^{0}C/min) to a pre-optimized temperature (600 ^{0}C), kept there for 3 h and then cooled down naturally. The undoped Co_2P NPs were also formed by using simple urea-phosphate and following otherwise the same procedure. To get grow the nanoparticles (NPs) on N-doped carbon clothe (S:Co_2P@NCC) or N-doped graphene (S:Co_2P@NG), the pre-oxidized carbon cloth (Oxi-CC) or graphene oxide (GO) was directly added to hydrothermal reactor and after followed the above procedure. The S:Co_2P NPs were also grown on nickel foam (S:Co_2P@NF) by loading the required amount of S-doped Co-urea-phosphate precursor onto the NF and annealed in H_2 at pre-optimized conditions.

6.3.2 Physical characterization.

Crystallographic structure of the electrocatalysts were determined by powder X-ray diffraction (XRD, PANalytical pw 3040/60 X'pert) with Cu Kα radiation. The morphologies were seen with field-emission scanning electron microscope (FE-SEM, Hitachi, S-4800, 15 kV) and transmission electron microscope (TEM, JEOL, JEM-2100). The chemical compositions, elemental mapping and in-depth crystal information of samples were collected by high resolution transmission electron microscope (HRTEM, JEOL, JEM-2100F). X-ray photoelectron spectroscopy (XPS, ThermoFisher, K-alpha) was used to identify the chemical states of the surface atoms.

6.3.3 Electrochemical measurements.

The catalyst ink was made by dispersing the unsupported electrocatalysts (5.0 mg/mL) in an equal volume mixture of deionized water and ethanol, and 10 μL of 5% Nafion solution. The working electrode was prepared by drop casting of 10 μL sonicated ink onto a glassy carbon electrode (0.4-0.5 mg/cm^2 loading) and drying at room temperature. The S:Co_2P@NCC and S:Co_2P@NF electrodes were used as-synthesized without adding any binder. Electrochemical HER/OER activity and stability tests were performed in a three electrode cell configuration using a rotating disc electrode (RDE, PAR Model 636 RDE) attached with a potentiostat (Ivium technologies). An Ag/AgCl (3.0M NaCl) electrode and a Pt foil were used as reference and counter electrodes, respectively. In two electrode configuration, the cathode (HER electrode) is used a counter and reference electrode with anode (OER electrode) as working electrode. All potentials were iR corrected and referenced to the reversible hydrogen electrode (RHE) by the equation $E_{RHE}=E_{(Ag/AgCl)} + 0.059pH + 0.209$.

The HER performance was measured in aqueous 1.0 M KOH (pH 13.7) at a scan rate of 2 mV/ s after 20 cyclic voltammetry (CV) cycles in the range of 0.4 to -0.3 V_{RHE}. The electrochemical stability tests were conducted by performing chronoamperometry (CA) for 20 h. Electrochemical impedance spectroscopy (EIS) was conducted in the same setup in the frequency range of 100 kHz to 1 mHz with a modulation amplitude of 10 mV. To evaluate the electrochemical active surface area (ECSA), CV was conducted from -0.8 to -0.6 V in 1.0 M KOH *vs.* Ag/AgCl with different sweep rates between 20 to 100 mV s^{-1}.

6.4 Results and discussion

6.4.1 Synthesis of sulfur-incorporated metallic cobalt phosphide nanoparticles

Ultrasmall-sized sulfur-doped metallic cobalt phosphide (S:Co_2P) nanoparticles were synthesized by using indigenously formulated thiourea-phosphate in which a weak reductant thiourea liberates H_2S gas and urea-phosphate as a byproduct in aqueous phosphoric acid (H_3PO_4) solution upon thermal decomposition.[7] When cobalt nitrate hexahydrate ($Co(NO_3)_2 \cdot 6H_2O$) salt was mixed with optimized amount of thiourea-phosphate, cobalt ions (Co^{2+}) react with byproducts (H_2S and urea-phosphate) via ion-assisted solvothermal reaction to form a reduced S-incorporated Co-phosphate precursor for S:Co_2P NPs. In order to graft these NPs onto N-doped graphene (NG) or N-doped carbon cloth (NCC), the GO or oxidized carbon cloth (Oxi-CC) was directly added into the reactor along with starting precursors then followed by thermal reduction of S-doped Co-phosphate loaded support in H_2 gas. The synthetic procedure is schematically illustrated in **Figure 6.1** (see Experimental Section for detail). To obtain S:Co_2P@NF electrode, the S:Co_2P precursor was also directly loaded at nickel foam (NF) and follow the same H_2 reduction treatments. Simple urea was used to prepare undoped Co_2P NPs according to otherwise the same method.

The powder X-ray diffraction (XRD reveal that a pure phase of orthorhombic Co_2P nanocrystals with average size of ~18 nm (space group Pnma, ICDD No.: 01-089-3032) have successfully formed after H_2 reduction at an optimized temperature of 600 °C as shown in **Figure 6.1b**. No significant change in bulk crystal structure of Co_2P was detected in XRD pattern even after S-doping. The similar XRD behavior with a specific (002) graphitic peak of S:Co_2P/NG and S:Co_2P/NCC was also observed as the unsupported S:Co_2P and undoped Co_2P nanoparticles in **Figure 6.1b** and **Figure 6.1c**. Scanning electron microscopy (SEM) images (**Figure 6.1d**) of the as-synthesized S:Co_2P and S:Co_2P/NCC reveal that closely interconnected 50-60 nm grain sized nanocrystals have successfully grown on N-doped carbon cloth.

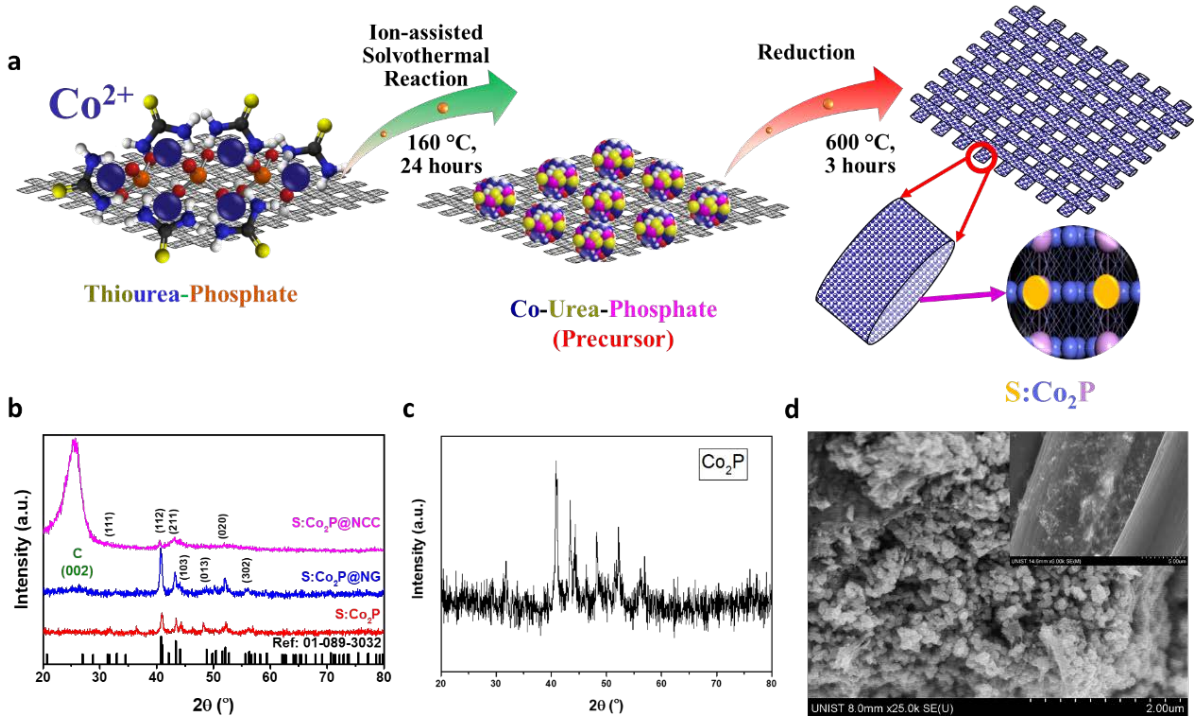

Figure 6.1. Schematic illustration of (a) S-incorporated Co_2P nanoparticles grafted onto a conductive support (S:Co_2P@NCC). XRD pattern of (b) S:Co_2P (red), S:Co_2P@NG (blue), S:Co_2P@NCC (pink) and (c) undoped Co_2P NPs. SEM image of (d) S:Co_2P NPs and S:Co_2P@NCC (inset).

X-ray photoelectron spectroscopy (XPS) was conducted in order to know the oxidation states change in as-prepared S:Co_2P/NCC electrode and after 20 h long HER or OER stability tests in **Figure 6.2a-d**. Due to higher electronegativity of S (2.44) than Co (1.70) and P (2.04), it induces more partial positive charge on $Co^{\delta+}$ ($0<\delta<2$) and share electron density with P and Co in Co_2P. The highly positively charged Co (δ+) could increase the water absorption and weaken the O-H bond, similarly the adjacent more negatively charged P (δ-) and S (δ-) could absorb more proton and hence create equilibrium between hydride ($Co^{\delta+}-H^{\delta-}$) and proton ($S/P^{\delta-}-H^{\delta+}$) acceptors at surface. The detailed water dissociation mechanism will be discussed later. Therefore, the characteristic $2p_{3/2}$ and $2p_{1/2}$ peaks of $Co^{\delta+}$ in metallic Co_2P are slightly shifted to higher binding energy of 778.3 eV and 793.4 eV than pure metallic Co ($2p_{3/2}$:

777.9 eV) or pristine Co_2P (778.1, 793.0).[16, 21] While Co (2+) $2p_{3/2}$ peak and its satellite is shifted from 781.7 & 785.6[16] to ≈779.5 & 782.8 eV and $2p_{1/2}$ from 797.2[21] to ≈797.0 eV due to back donation of electron from S to vacant *3d* orbital of Co.[7] No significant change in Co*2p* spectrum was observed after HER stability test as shown **Figure 6.2a**. A doublet P*2p* peaks at 129.4 and 130.3 eV (**Figure 6.2b**) can be assigned P^{3-} in Co_2P which is at a less binding energy than elemental P (~130-130.2 eV) or P in CoP (129.7).[16, 24] The positive shift in binding energy (BE) from metallic Co*2p* (~777.9 eV) and negative shift in P*2p* from elemental P (~130.2 eV) are suggesting that partial positively charged Co (δ^+) can work as a hydride acceptor ($Co^{\delta+}$-$H^{\delta-}$) while the partial negatively charged P/S (δ^-) as a proton acceptor ($P/S^{\delta-}$-$H^{\delta+}$), which would facilitate HER.[24] The Co $2p_{3/2}$ at 780.1 and $2p_{1/2}$ peak 795.9 eV along with their satellites at 786.7 and 802.6 eV indicate the *in-situ* formation of oxygen deficient cobalt oxide (CoO) from electrochemical oxidation of Co_2P after OER (**Figure 6.2a**).[13, 26] These $2p_{3/2}$ and $2p_{1/2}$ peaks are located at low binding energy than pure Co-oxides (782.1 & 798.1) due to presence of un-leached more electronegative S and P species and also confirm the formation of oxygen vacancies in consistent with the previous reports of reducing Co_3O_4 to CoO.[26-27] The presence of an oxide peak at 529.5 eV along with P-O at 531.2 eV in the O*1s* spectra (**Figure 6.2c**) confirms *in-situ* electro-oxidation of metallic Co in Co_2P. [13, 28] S2p and N1s spectra in **Figure 6.2d** confirm the presence of these species in Co_2P structure and sustained after HER and OER.

To see the effect of S-doping in electronic properties in Co_2P, the total density of states (TDOS) and projected density of states (PDOS) for Co, P and S, were also calculated by DFT method as shown in **Figure 6.2e-f**. The non-zero DOS at the Fermi level (E_0) confirms the metallic property of Co_2P sustained even after S-doping. The contraction of conduction/valance band near fermi level in S:Co_2P (**Figure 6.2f**) as compared to bare Co_2P **Figure 6.2e**, is signifying the reduction of density of states at metallic Co due to more electronegative S-doping which is confirmed in Co_2P XPS. The width and intensity of valance band of P and Co near fermi level seems to be enhanced due to overlapping of S*2p* orbitals with P*3p* and Co*3d* in S:Co_2P. As shown in **Figure 6.2e-f**, the DOS of S:Co_2P (2.42) at the Fermi level is lower than that the DOS for bare Co_2P (3.01) confirms that more hydride acceptor ($Co^{\delta+}$-$H^{\delta-}$) and proton acceptor ($P/S^{\delta-}$-$H^{\delta+}$) are available just like in CoP system. Conversely, the Co_2P could behave like CoP in overall water splitting after S-incorporation.

The more electronegative S (2.44) withdraws electron density from the less electronegative Co (1.70) and P (2.04), and induces more partial positive charge on $Co^{\delta+}$ ($0<\delta<2$) and then back donate by overlapping of p-orbitals with P*3p* and Co*3d* in Co_2P as shown in **Figure 6.2g**. The highly positively charged Co (δ+) could coordinate with the lone pair electrons of O in H_2O and facilitate the dissociation of –O-H bond by releasing proton (adsorbed H) to more electronegative atom P/S. Conversely, the S/P make hydrogen bonding with H of water by donating extra electron density and help the adjacent Co

(δ+) to extract hydrides (aqueous H) from water molecule. Then this hydride ($Co^{\delta+}-H^{\delta-}$) and proton ($S/P^{\delta-}-H^{\delta+}$) combine together to form H_2 molecule as displayed in **Figure 6.2h**.

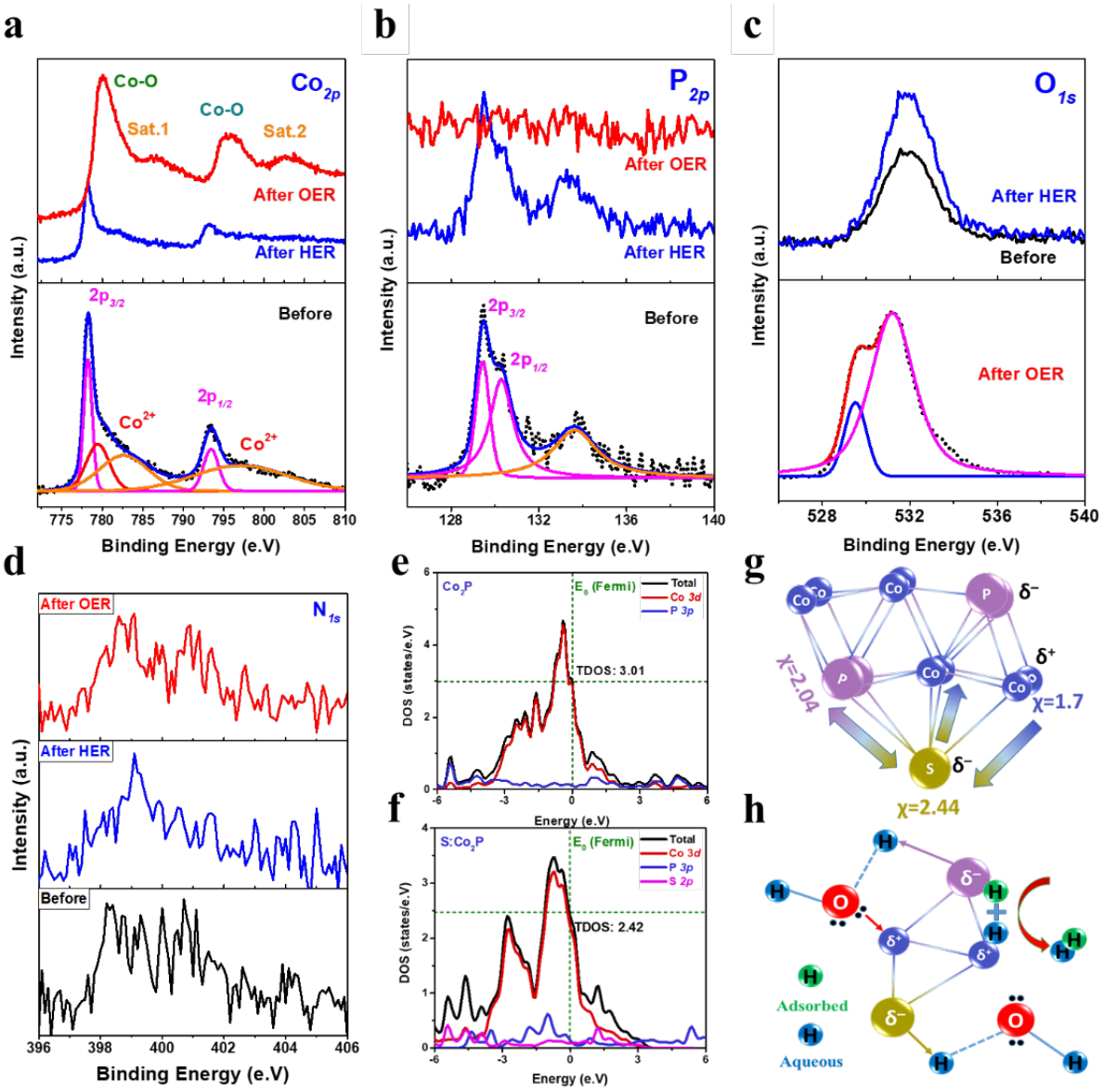

Figure 6.2. High resolution XPS of as-synthesized (black), after HER (blue), and OER (red) for S:Co_2P@NCC, (a) Co*2p* (b) P*2p*, (c) O*1s* and (d) N*1s*. Total-DOS and PDOS of (e) undoped and (f) S:Co_2P. (g) Electron density shift in S:Co_2P due to difference in electronegativity and (h) water dissociation mechanism. XPS spectra of

The transmission electron microscopy (TEM) images show that S:Co_2P NPs having an average size of ~5 nm (range: 3-10 nm) are successfully grown directly on N-doped carbon cloth (NCC) as shown in **Figure 6.3a**. The high-resolution TEM (HR-TEM) images and their closer look in **Figure 6.3b-c** display tiny nanoparticles with a well-resolved lattice fringes spacing of 0.23 and 0.228 nm of the (112) Co_2P plane of as-synthesized S:Co_2P@NCC and after HER, respectively. The larger interplaner distance than bare Co_2P (0.221 nm) is due to S-species in the structure. The corresponding Fast Fourier

transforms (FFT) are also shown in **Figure 6.3d**. The TEM image (**Figure 6.3e**) displays that the S:Co_2P NPs lose their morphology after electrochemical oxidation to Co-oxides after long term OER stability test which is also certified by XPS data. The HR-TEM images in **Figure 6.3f-h** reveal the clear lattice fringes with an enlarged interplaner distance of 0.249 nm for the (311) facet of Co_3O_4 (PDF#: 01-074-1657, d-space: 0.244 nm) and 0.22 nm correspond to (200) plane of CoO (PDF#: 01-078-0431, d-space: 0.212 nm).[29] The structural defects in CoO region (**Figure 6.3h**) are caused by the oxygen deficiency after oxidation of Co_2P to CoO_x as discussed in XPS section and in agreement with the previous reports.[13, 26-27] Uniform distribution of Co and traces of P, S and O was observed by Elemental mapping by energy-dispersive-X-ray-spectroscopy (EDS)-STEM in post OER sample (**Figure 6.3i-l)**. The presence of trace elements (P, S and N) and increased oxygen atomic % from 6.24 to 23.96 after OER (**Table 6.1**) confirms the *in situ* formation of an oxygen-deficient surface cobalt oxides (CoO_x) and the promotional effects of P, S on its OER performance. The surface-oxidized and oxygen incorporated cobalt phosphides can provide the enhanced OER performance in alkaline media.[13, 20-21]

Table 6.1. Elemental compositions of catalysts before and after HER/OER test derived from XPS analysis

Catalyst	Co	P	S	N	C	O
	Atomic %age					
As-synthesized S:Co_2P@NCC	3.59	1.81	0.5	5.72	82.14	6.24
After HER	3.18	1.61	0.6	5.24	82.58	6.79
After OER	10.93	0.5	0.7	4.05	59.86	23.96

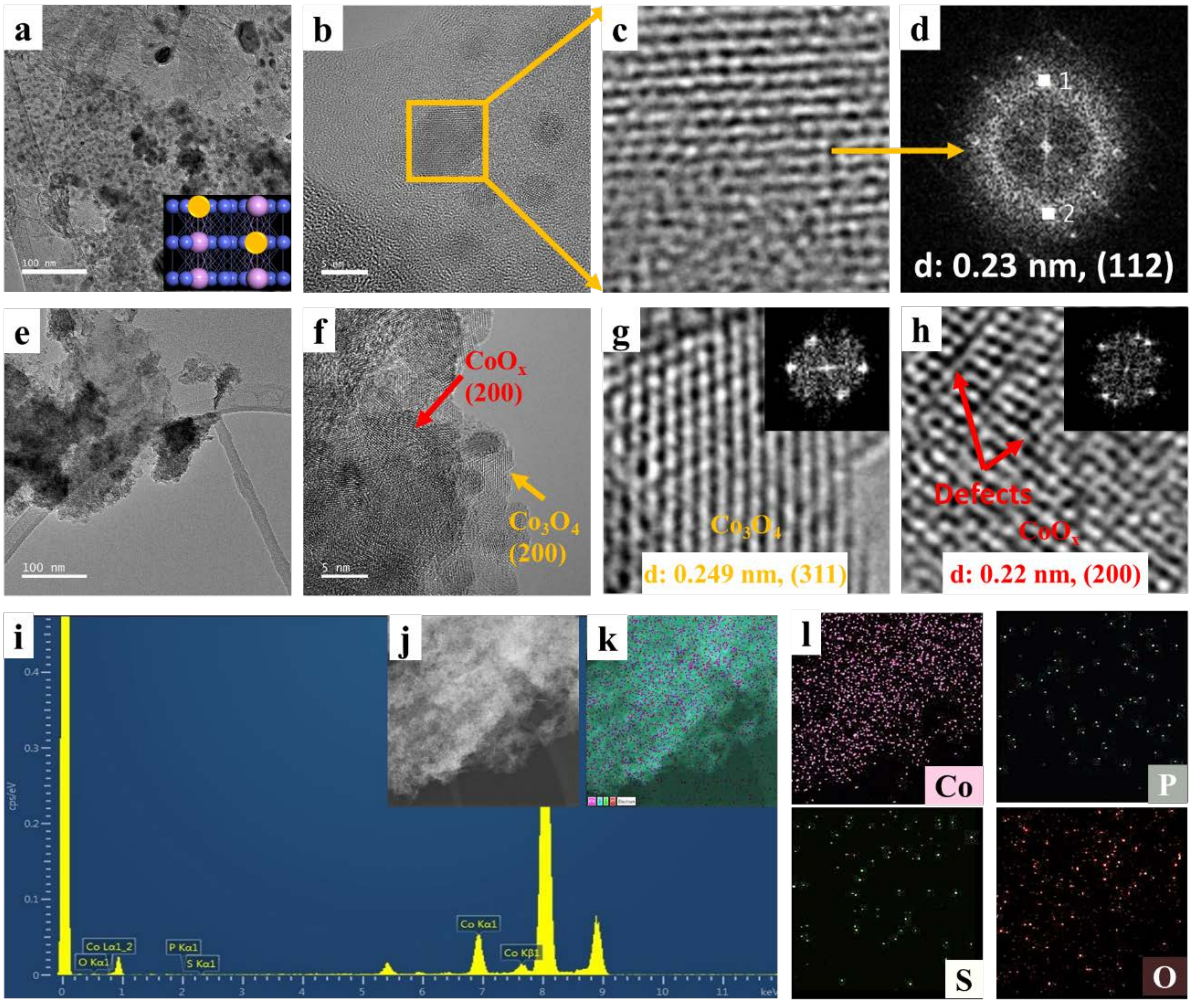

Figure 6.3. TEM images of as-synthesized S:Co_2P NPs (a); displaying nanoparticles in the range of 3-10 nm scale bar: 100 nm. (b) high resolution transmission electron microscopy (HR-TEM) image scale bar: 5 nm, (c-d) magnified HR-TEM image showing the prominent interlayer expanded (112) planes for Co_2P and corresponding fast Fourier transformation (FFT) patterns of as-prepared S:Co_2P. TEM (e); scale bar: 100 nm and HR-TEM (f); scale bar 5nm, and enlarged HR-TEM image of interlayer expanded (311) plane of Co_3O_4 (k), (200) plane of defective CoO (l) and corresponding FFT (inset) after OER.

6.4.2 Electrochemical hydrogen evolution reaction over S:Co_2P

The HER performance of all Co_2P-based electrocatalysts was evaluated by linear sweep voltammetry in 1.0M KOH aqueous solution using a three-electrode electrochemical cell (iR-corrected, **Figure 6.4a**). The unsupported S:Co_2P and S:Co_2P@NG NPs were loaded onto rotating disc electrode while Co_2P@NF, S:Co_2P@NCC and S:Co_2P@NF were used directly as a cathode/anode. The undoped Co_2P required overpotentials of ~102 and ~218 mV to generate cathodic currents densities of 1 and 10 mA/cm^2, which is equivalent to earlier reported CoP-based electrocatalysts.[21, 24, 30] However, the η_1 and η_{10} reduce to ~89 and ~184 after incorporation of trace amount of S into structure of Co_2P improves HER performance to η_1~96 mV and η_{10}~175mV. The S effectively reduces the energy barrier and provide the ample electrons in the conduction band to electrolyze the HER rapidly and is confirmed by

the total-DOS and PDOS in **Figure 6.2g-h**. This promotional effect is more pronounced when these (S:Co_2P) NPs are directly grown over conductive substrate like N-doped graphene (NG), N-doped carbon cloth (NCC) or nickel foam (NF). Especially, the S:Co_2P@NF and S:Co_2P@NCC trigger the HER reaction more efficiently with η_{10} value of 105 to 134 mV, respectively. Notably, the hybrid electrodes display remarkable HER activities compared to commercial Pt-catalyst and η_{100} values follow the order; 242 mV (S:Co_2P/NG)>233 mV (Pt plate) > 199 mV (S:Co_2P@NCC) > 192 mV (S:Co_2P@NF). The doping of heteroatoms *e.g.* N or S into the structure of phosphides could improve the electron/proton conductivity and ensure rapid electron/mass transfer inside the electrocatalyst which is favorably enhanced HER performance. These trace elements also coordinate with least stable P^{3-} and positively charged metal (M^{3+}) in phosphide by regulating its electronic properties, stabilizing its structure and generating more adsorption sites for proton.[7, 31-32]

Tafel slopes and exchange current densities (J_0) at zero overpotential are estimated in **Figure 6.4b**, for Pt-plate (56 mV/dec, 1.32 mA/cm^2), S:Co_2P@NF (89 mV/dec, 0.710 mA/cm^2), S:Co_2P@NCC (77 mV/dec, 0.168 mA/cm^2), S:Co_2P@NG (62 mV/dec, 0.033 mA/cm^2), S:Co_2P NPs (95 mV/dec, 0.115 mA/cm^2) and Co_2P@NF (113 mV/dec, 0.116 mA/cm^2). The small Tafel slopes and lower J_0 values for S-incorporated Co_2P than pristine one suggest that HER follows the Volmer−Heyrovsky mechanism and also establish chemical/electrical promotional effect of sulfur by improving the HER kinetics. This is further verified by performing the electrochemical impedance spectroscopy (EIS) for all electrocatalysts at a constant overpotentials of 140 mV (**Figure 6.4c**). The EIS Nyquist plots display the solution resistance (R_s) and two time constants, the first is related to the ions diffusion resistance (R_d) and the second one corresponds to the charge transfer resistance (R_{ct}) offered by material.[4] The comparative lower R_{ct} values of S:Co_2P-based electrocatalysts than bare Co_2P are further confirmed the promotional effect of S-doping.

6.4.3 Electrochemical oxygen evolution reaction over S:Co_2P

Besides the remarkable HER performance, the S-promotional effect was also profound in oxygen evolution reaction (OER) and S:Co_2P based electrocatalysts were also remarkably electrolyze OER in 1.0 M KOH as shown in **Figure 6.4d.** The S-doped Co_2P catalysts require lower η_{10} values (~288-310 mV) as compared to commercial IrO_2 (337 mV) and undoped Co_2P NPs (320 mV) electrodes with the same mass loadings (~1.2 mg/cm^2). Additionally, the S electronic and chemical promotional effect further lowered the overpotentials especially at higher current density region and thus S:Co_2P@NF requires the lowest overpotentials (~336 & ~360 mV) to generate current density of 50 and 100 mA/cm^2 as compared to S:Co_2P@CC (~348 & ~376 mV), S:Co_2P@NG (~356 & ~386 mV), S:Co_2P NPs (~370 & ~400 mV), Co_2P@NF (~390 & ~435 mV) and commercial IrO_2@NF (~397 & ~435 mV). As discussed in XPS and TEM section, the *in situ* formation of oxygen deficient surface oxides (CoO_x) through direct electrochemical oxidation of S:Co_2P NPs which can effectively catalyze the OER process.

Thus the promotional effect of trace elements P and S becomes stronger with the formation of abundant metal oxo-/hydroxide OER active sites on the surface by breaking the Co-Co metallic bonds in metallic Co_2P.[33]

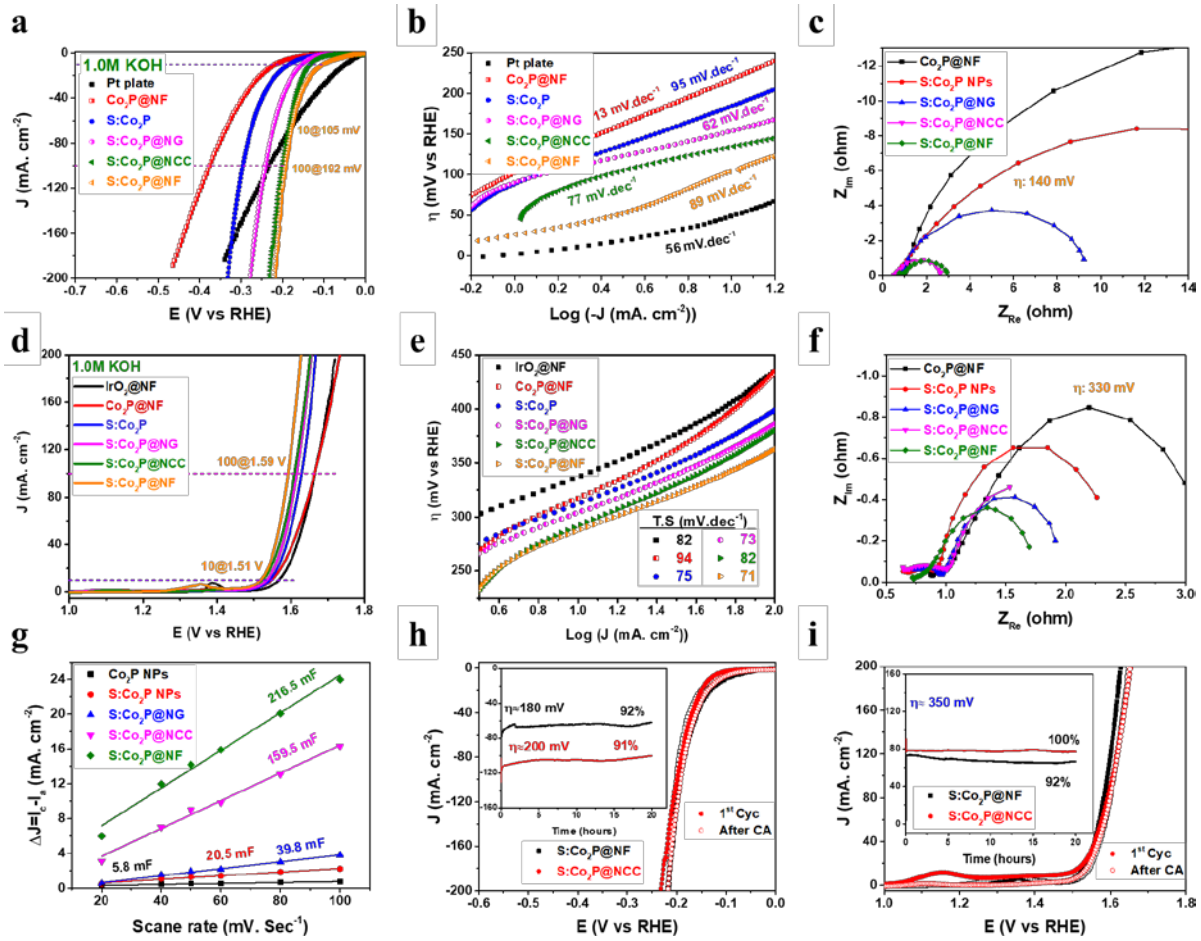

Figure 6.4. HER polarization (iR-corrected) curves of (a) undoped CoP NPs, S:CoP NPs and S:CoP grown on conductive substrates NG, CC and NF, corresponding (b) Tafel slopes and (c) Electrochemical impedance spectroscopy (EIS) analysis at overpotential of 140 mV in 1.0M KOH. iR-corrected LSV curves for OER (d), corresponding Tafel slopes (e) and EIS (f) of catalysts at an overpotential of 0.33 V in 1.0M KOH. The measured double layer capacitance (C_{dl}) by plotting capacitive currents ($\Delta J=I_c-I_a$) as a function of scan rate (g). polarization curves for HER (h) and OER (i) after 20 h durability tests (by chronoamperometry as inset) for S:Co_2P@CC and S:Co_2P@NF in 1.0M KOH.

The Tafel analysis was also conducted to estimate OER kinetic parameters i.e. Tafel slopes and current exchange densities (J_0) of all S:Co_2P based anodes in **Figure 6.4e**. The much smaller Tafel slopes and higher J_0 values for all S-Co_2P catalysts (71-82 mV/dec, 1-3 µA cm^{-2}) than undoped Co_2P@NF (94 mV/dec, 1.3 µA cm^{-2}) and commercial IrO_2@NF (82 mV/dec, 1.0 µA cm^{-2}) electrode, validating the promotional effect of S, P-doped oxygen deficient Co-oxide which accelerate OER reaction especially on the S-doped metallic Co_2P. As displayed in **Figure 6.4f**, The EIS Nyquist plots suggest that the charge transfer resistance at an overpotential of 330 mV of S:Co_2P@NF (0.969 **Ω**) is lower than those

of S:Co_2P@CC (1.38 Ω), S:Co_2P@NG (1.37 Ω), S:Co_2P NPs (1.88 Ω) and undoped Co_2P NPs (2.54 Ω), suggesting the rapid charge transfer process during OER. The smaller R_{ct} (~0.969 Ω) of S:Co_2P@NF than the undoped Co_2P@NF electrode clearly shows that S incorporation has an influential effect on the OER and as well as HER activity of Co_2P.

6.4.4 Electrochemical surface area and long-run stability for HER and OER

Electrochemically active surface areas (ECSA) were also estimated by calculating the double layer capacitance (C_{dl}) from the slope determined of the linear plot between current density difference ΔJ (J_a-J_c) and the increasing scan rates as shown in **Figure 6.4g**. The higher values of C_{dl} and ECSA for S:Co_2P@NF (216.5 mF/cm^2, 5412.3 cm^2) and S:Co_2P@NCC (159.5 mF/cm^2, 3988.5 cm^2) as compared to S:Co_2P@NG (39.8 mF/cm^2, 995.25 cm^2), S:Co_2P NPs (20.5 mF/cm^2, 511.75 cm^2) and Co_2P@NF (5.8 mF/cm^2, 139.75 cm^2) also indicating that the maximum HER/OER active sites are exposed over 3D supports (i.e.NF and NCC) which effectively improve electron/mass transport and largely enhance the HER and OER performance. The long term electrochemical stability for HER is confirmed by performing the chronoamperometric response (CA) test for up to 20 h at a static overpotential of 180 and 200 mV for S:Co_2P@NF and S:Co_2P@NCC, respectively. As displayed in **Figure 6.4h** (inset), the electrodes show super stable performance with insignificant current density degradation a long period of 20 h CA test. The similar overpotentials require to generate the current density 100 mA.cm^{-2} even after a long period of 20 h operation as determined by LSV curves (**Figure 6.4h**), conforming the outstanding stability of the catalysts. To evaluate the OER stability, the chronoamperometry (CA) tests for both electrodes were also at performed at same overpotential of ~350 mV in **Figure 6.4i** (inset). Again the S:Co_2P@NCC produces the 100% current efficiency until 20 hours long OER test in 1.0M KOH. The LSV curves before and after 20 h long CA tests display excellent stabilities for OER of both electrodes without any current density loss shown in **Figure 6.4i**. The high stabilities and activities for OER can be attributed to formation of more active cobalt oxo-/hydroxide species over the metallic Co_2P surface during OER in alkaline solution exactly according to Nernst equation[33] and are already confirmed by XPS and HR-TEM after 20h OER stability test. All above results have demonstrated the effectiveness of electronic/chemical promotional effect of S incorporation by providing the outstanding HER and OER activities along with great stabilities.

6.4.5 S:Co_2P catalysts based alkaline electrolyzer

The superb bifunctional performances of S:Co_2P@NF and S:Co_2P@NCC electrodes led us to design complete electrolyzer cells which could generate the current density of 100 mA at potentials (ΔV= V_c-V_a) 1.782 and 1.805 V, respectively as depicted in **Figure 6.5a**. Therefore, two alkaline electrolyzer cells S:Co_2P@NCC- S:Co_2P@NCC and S:Co_2P@NF- S:Co_2P@NF with similar cathode-anode were tested and compared with commercial IrO_2@NF- Pt/C@NF (anode-cathode) with same mass loading. As displayed in polarization curves (**Figure 6.5b**), the S:Co_2P@NF and S:Co_2P@NCC cells effectively

catalyze the overall water splitting with the similar cell voltages of 1.797 to 1.84 V to generate the current densities 100 mA/cm^2. Interestingly, the S:Co_2P@NF and S:Co_2P@NCC performed well when they were used as anode with Pt/C (cathode) and gives the higher performance even at low overpotentials. The η_{10} and η_{100} values for S:Co_2P@NF-Pt/C@NF (0.33 & 0.518 V) are much less than S:Co_2P@NCC-Pt/C@NF (0.332 & 0.57 V), S-Co_2P-S-Co2P@NF (0.4 & 0.567 V), S-Co_2P-S-Co2P@NCC (0.42 & 0.61 V) and IrO_2@NF-Pt/C@NF (0.37 & 0.593 V). A representative photographs of the S:Co_2P@NF electrolyzer producing hydrogen (right) and oxygen (left) is also shown in **Figure 6.5c**. The current densities at cell voltage 1.83 V are also compared in **Figure 6.5d**. Moreover, the S:Co_2P@NCC and S:Co_2P@NF electrolyzer also display superior stability with negligible current density loss (only ≈0.115-0.122 mA cm^{-2}h^{-1}) as compared to IrO_2-Pt/C@NF (≈1.2 mA cm^{-2}h^{-1}) as shown in **Figure 6.5e**. Almost same voltage required to produce the 100 mA cm^{-2} as determined by the LSV curves before and after stability test (**Figure 6.5f**) which confirm the excellent stability of both electrolyzer. The η_{10} values of S:Co_2P electrolyzers also compared with latest state of art electrolyzers reported in literature **Figure 6.5g**.

All the above results demonstrate that the electronic and chemical properties of metallic Co_2P could be regulated by incorporation of more electronegative S atom which induces more positive charge on metallic Co in Co_2P and create the balance between hydride ($Co^{\delta+}$–$H^{\delta-}$) and proton ($S/P^{\delta-}$–$H^{\delta+}$) acceptors which is critical factor for HER in TMPs. The S-doping also improves the water absorption ability of Co (δ^+) which weaken the O-H bond of water by coordinating with lone pair of O and facilitate the proton (H^+) release to P/S in S:Co_2P. On the other side S also shares its electron density to H of H_2O through hydrogen bonding by facilitating the hydride (H^-) release to adjacent Co (δ^+) in Co_2P, then both neighbors ($Co^{\delta+}$–$H^{\delta-}$) and ($S/P^{\delta-}$–$H^{\delta+}$) combine to form H_2. Lastly, the S also increase the electron density in overall material by overlapping its p-orbitals with P*3p* and Co*3d*, which is beneficial for overall water splitting.

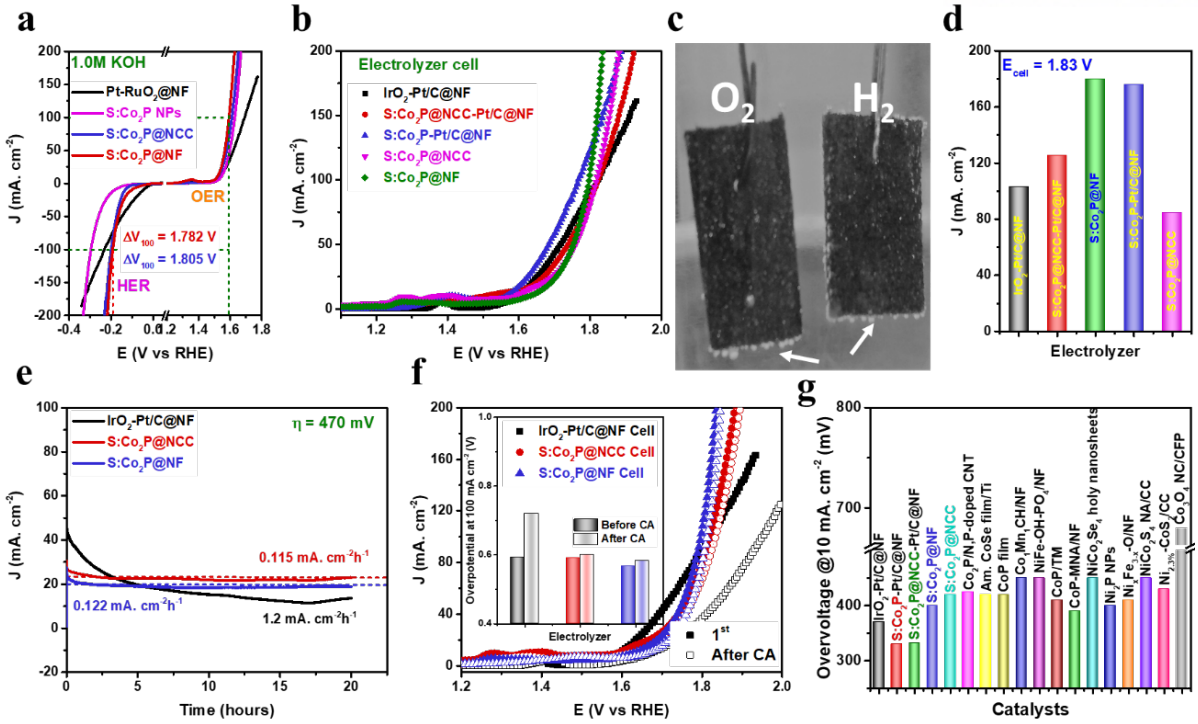

Figure 6.5. Polarization curves (a) for HER-cathode and OER-anode showing the potential difference between anode and cathode ($\Delta V = V_a - V_c$) at 100 mA/cm^2 in 1 M KOH, (b) LSV curves for electrolyzer cell at a sweeping rate of 2 mV/s and (c) the representative photograph of the electrolyzer showing H_2 (right) and O_2 (left) generation during overall water splitting. (d) comparison of current density at 1.83 cell voltage, (e) a chronoamperometry durability 20 h long test and (f) LSV curves; commercial IrO_2-Pt/C@NF (black); S:Co_2P@NF (red); S:Co_2P@NCC (blue) electrolyzer cell and η_{100} compare (inset) before and after 20h long CA test. (g) comparison of η_{10} values with other state of the art electrolyzers reported in literature.

6.5 Conclusion

In conclusion, the electronic and chemical properties of metallic Co_2P have been regulated by incorporation of trace amount of sulfur (S). We have demonstrated an economical and ecofriendly thiourea-phosphate strategy to synthesize and tune the electrochemical properties of TMPs with the ease of phase/morphology control. The as prepared S:Co_2P@NF and S:Co_2P@NCC give remarkable activities for HER/OER better than that of commercial Pt/C and RuO_2 especially in higher currents region. The S:Co_2P@NF electrolyzer produce current densities of 100 mA/cm^2 at overpotentials of 1.797 in 1.0 M KOH better that commercial IrO_2-Pt/C@NF electrolyzer and most of CoP-based electrocatalysts reported so far. Moreover, the η_{10} for S-Co_2P -Pt/C@NF (330 mV) and S-Co_2P@NCC -Pt/C@NF (332 mV) is much lower than IrO_2-Pt/C@NF (370 mV). This superior performance attributed to the following reason: (1) S decrease the electron density (TDOS) at the Fermi level by minimizing Co metallic nature; (2) being more electronegative S induces more positive charge on metallic Co balancing hydride and proton acceptor level by lowering free energy ΔG_{H^*} and ΔG_{H2O^*}; (3) S also increase the number of active sites and TOF, (4) 3D supports (NF and NCC) could provide high

electrochemical active surface area (ECSA), maximize the electron/proton conductivity and mass transfer. The low-cost and eco-friendly urea-phosphate methodology adopted here could also become a general method for producing other transition metal phosphides for use as water-splitting bifunctional catalysts.

6.6 References

1. Roger, I.; Shipman, M. A.; Symes, M. D., Earth-abundant catalysts for electrochemical and photoelectrochemical water splitting. *Nat. Rev. Chem.* **2017,** *1*, 0003.

2. Chu, S.; Cui, Y.; Liu, N., The path towards sustainable energy. *Nat. Mater.* **2017,** *16* (1), 16-22.

3. Anjum, M.; Jeong, H.; Lee, M.; Shin, H.; Lee, J., Efficient Hydrogen Evolution Reaction Catalysis in Alkaline Media by All-in-One MoS2 with Multifunctional Active Sites. *Adv. Mater.* **2018**, 1707105.

4. Suen, N. T.; Hung, S. F.; Quan, Q.; Zhang, N.; Xu, Y. J.; Chen, H. M., Electrocatalysis for the oxygen evolution reaction: recent development and future perspectives. *Chem. Soc. Rev.* **2017,** *46* (2), 337-365.

5. Zou, X.; Zhang, Y., Noble metal-free hydrogen evolution catalysts for water splitting. *Chem. Soc. Rev.* **2015,** *44* (15), 5148-5180.

6. Mahmood, J.; Li, F.; Jung, S.-M.; Okyay, M. S.; Ahmad, I.; Kim, S.-J.; Park, N.; Jeong, H. Y.; Baek, J.-B., An efficient and pH-universal ruthenium-based catalyst for the hydrogen evolution reaction. *Nature Nanotechnol.* **2017,** *12* (5), 441.

7. Anjum, M. A. R.; Lee, J. S., Sulfur and Nitrogen Dual-Doped Molybdenum Phosphide Nanocrystallites as an Active and Stable Hydrogen Evolution Reaction Electrocatalyst in Acidic and Alkaline Media. *ACS Catal.* **2017,** *7* (4), 3030-3038.

8. Anjum, M. A. R.; Lee, M. H.; Lee, J. S., BCN Network-Encapsulated Multiple Phases of Molybdenum Carbide for Efficient Hydrogen Evolution Reaction in Acidic and Alkaline Media. *J. Mater. Chem. A* **2017,** *5* (25), 13122-13129.

9. Anantharaj, S.; Ede, S. R.; Sakthikumar, K.; Karthick, K.; Mishra, S.; Kundu, S., Recent Trends and Perspectives in Electrochemical Water Splitting with an Emphasis on Sulfide, Selenide, and Phosphide Catalysts of Fe, Co, and Ni: A Review. *ACS Catal.* **2016,** *6* (12), 8069-8097.

10. Wang, J.; Cui, W.; Liu, Q.; Xing, Z.; Asiri, A. M.; Sun, X., Recent Progress in Cobalt-Based Heterogeneous Catalysts for Electrochemical Water Splitting. *Adv. Mater.* **2016,** *28* (2), 215-230.

11. Xie, L.; Zhang, R.; Cui, L.; Liu, D.; Hao, S.; Ma, Y.; Du, G.; Asiri, A. M.; Sun, X., High-Performance Electrolytic Oxygen Evolution in Neutral Media Catalyzed by a Cobalt Phosphate Nanoarray. *Angew. Chem.* **2017,** *129* (4), 1084-1088.

12. Yang, Y.; Fei, H.; Ruan, G.; Tour, J. M., Porous Cobalt-Based Thin Film as a Bifunctional Catalyst for Hydrogen Generation and Oxygen Generation. *Adv. Mater.* **2015,** *27* (20), 3175-3180.

13. Chang, J.; Xiao, Y.; Xiao, M.; Ge, J.; Liu, C.; Xing, W., Surface oxidized cobalt-phosphide nanorods as an advanced oxygen evolution catalyst in alkaline solution. *ACS Catal.* **2015,** *5* (11), 6874-6878.

14. Shi, Y.; Zhang, B., Recent advances in transition metal phosphide nanomaterials: synthesis and applications in hydrogen evolution reaction. *Chem. Soc. Rev.* **2016,** *45* (6), 1529-1541.

15. Li, W.; Zhang, S. L.; Fan, Q. N.; Zhang, F. Z.; Xu, S. L., Hierarchically scaffolded CoP/CoP2 nanoparticles: controllable synthesis and their application as a well-matched bifunctional electrocatalyst for overall water splitting. *Nanoscale* **2017,** *9* (17), 5677-5685.

16. Huang, Z. P.; Chen, Z. Z.; Chen, Z. B.; Lv, C. C.; Humphrey, M. G.; Zhang, C., Cobalt phosphide nanorods as an efficient electrocatalyst for the hydrogen evolution reaction. *Nano Energy* **2014,** *9*, 373-382.

17. Callejas, J. F.; Read, C. G.; Popczun, E. J.; McEnaney, J. M.; Schaak, R. E., Nanostructured Co2P Electrocatalyst for the Hydrogen Evolution Reaction and Direct Comparison with Morphologically Equivalent CoP. *Chem. Mater.* **2015,** *27* (10), 3769-3774.

18. Pan, Y.; Lin, Y.; Chen, Y. J.; Liu, Y. Q.; Liu, C. G., Cobalt phosphide-based electrocatalysts: synthesis and phase catalytic activity comparison for hydrogen evolution. *J. Mater. Chem. A* **2016,** *4* (13), 4745-4754.

19. Jin, Z. Y.; Li, P. P.; Xiao, D., Metallic Co2P ultrathin nanowires distinguished from CoP as robust electrocatalysts for overall water-splitting. *Green Chem.* **2016,** *18* (6), 1459-1464.

20. Dutta, A.; Samantara, A. K.; Dutta, S. K.; Jena, B. K.; Pradhan, N., Surface-Oxidized Dicobalt Phosphide Nanoneedles as a Nonprecious, Durable, and Efficient OER Catalyst. *ACS Energy Lett.* **2016,** *1* (1), 169-174.

21. Xu, K.; Ding, H.; Zhang, M. X.; Chen, M.; Hao, Z.; Zhang, L.; Wu, C. Z.; Xie, Y., Regulating Water-Reduction Kinetics in Cobalt Phosphide for Enhancing HER Catalytic Activity in Alkaline Solution. *Adv. Mater.* **2017,** *29* (28), 201606980.

22. Zhang, H. T.; Ha, D. H.; Hovden, R.; Kourkoutis, L. F.; Robinson, R. D., Controlled Synthesis of Uniform Cobalt Phosphide Hyperbranched Nanocrystals Using Tri-n-octylphosphine Oxide as a Phosphorus Source. *Nano Lett.* **2011,** *11* (1), 188-197.

23. Liu, P.; Rodriguez, J. A., Catalysts for hydrogen evolution from the [NiFe] hydrogenase to the Ni2P (001) surface: the importance of ensemble effect. *J. Am. Chem. Soc.* **2005,** *127* (42), 14871-14878.

24. Tian, J.; Liu, Q.; Asiri, A. M.; Sun, X., Self-supported nanoporous cobalt phosphide nanowire arrays: an efficient 3D hydrogen-evolving cathode over the wide range of pH 0–14. *J. Am. Chem. Soc.* **2014,** *136* (21), 7587-7590.

25. Carenco, S.; Portehault, D.; Boissiere, C.; Mezailles, N.; Sanchez, C., Nanoscaled metal borides and phosphides: recent developments and perspectives. *Chem. Rev.* **2013,** *113* (10), 7981-8065.

26. Wang, Y.; Zhou, T.; Jiang, K.; Da, P.; Peng, Z.; Tang, J.; Kong, B.; Cai, W. B.; Yang, Z.; Zheng, G., Reduced mesoporous Co3O4 nanowires as efficient water oxidation electrocatalysts and supercapacitor electrodes. *Adv. Energy Mater.* **2014,** *4* (16), 201400696..

27. Liao, L.; Zhang, Q.; Su, Z.; Zhao, Z.; Wang, Y.; Li, Y.; Lu, X.; Wei, D.; Feng, G.; Yu, Q., Efficient solar water-splitting using a nanocrystalline CoO photocatalyst. *Nat. Nanotechnol.* **2014,** *9* (1), 69-73.

28. Jeong, S.; Park, S.; Cho, J., High-Performance, Layered, 3D-LiCoO2 Cathodes with a Nanoscale Co3O4 Coating via Chemical Etching. *Adv. Energy Mater.* **2011,** *1* (3), 368-372.

29. Yang, X.; Li, H.; Lu, A.-Y.; Min, S.; Idriss, Z.; Hedhili, M. N.; Huang, K.-W.; Idriss, H.; Li, L.-J., Highly acid-durable carbon coated Co 3 O 4 nanoarrays as efficient oxygen evolution electrocatalysts. *Nano Energy* **2016,** *25*, 42-50.

30. Vigil, J. A.; Lambert, T. N.; Christensen, B. T., Cobalt phosphide-based nanoparticles as bifunctional electrocatalysts for alkaline water splitting. *J. Mater. Chem. A* **2016,** *4* (20), 7549-7554.

31. Liu, W.; Hu, E.; Jiang, H.; Xiang, Y.; Weng, Z.; Li, M.; Fan, Q.; Yu, X.; Altman, E. I.; Wang, H., A highly active and stable hydrogen evolution catalyst based on pyrite-structured cobalt phosphosulfide. *Nature Commun.* **2016,** *7*, 10771.

32. Cabán-Acevedo, M.; Stone, M. L.; Schmidt, J.; Thomas, J. G.; Ding, Q.; Chang, H.-C.; Tsai, M.-L.; He, J.-H.; Jin, S., Efficient hydrogen evolution catalysis using ternary pyrite-type cobalt phosphosulphide. *Nat. Mater.* **2015,** *14* (12), 1245.

33. Xu, K.; Cheng, H.; Liu, L.; Lv, H.; Wu, X.; Wu, C.; Xie, Y., Promoting active species generation by electrochemical activation in alkaline media for efficient electrocatalytic oxygen evolution in neutral media. *Nano Lett.* **2016,** *17* (1), 578-583.

7. All in one Molybdenum Sulfides for Efficient Hydrogen Evolution Reaction in Aqueous Alkaline Media

7.1 Abstract

Here, a simple strategy is developed to synthesize MoS_2 with multiple active sites such as defect, S-deficiency, Mo-exposed edge, and expanded interlayer spacing by hydrothermal reaction using supramolecular melamine-phosphomolybdate (MA-PMo_{12}) and thiourea as precursors. During the hydrothermal reaction, *in-situ* generated NH_3 molecules were intercalated into MoS_2 sheets with an interlayer spacing of 8.4 Å, and 1T phase MoS_2 (71%) was dominantly observed (A-MoS_2). The further defects and S-vacancies in A-MoS_2 (R-MoS_2) were generated by removing intercalated NH_3 and H_2S through thermal annealing in hydrogen gas at 500 °C. Edge-terminated and interlayer-expanded MoS_2 structures in R-MoS_2 after the thermal reduction remained, and the fraction of 1T phase was still considerable (33.7%). A-MoS_2, R-MoS_2, and hybrids of R-MoS_2 with reduced graphene oxide and nickel foam (R-MoS_2/NG and R-MoS_2/NF) were tested for electrocatalysts of hydrogen evolution reaction (HER) in basic media. R-MoS_2/NF exhibited superb stability and catalytic activity: the onset potential (5 mV) and exchange current density (2.27 mA/cm^2) are close to those (0 mV and 2.65 mA/cm^2) of commercial Pt/C and overpotential at 40 mA/cm^2 (105 mV) is lower than that (156 mV) of Pt/C. This work demonstrates that R-MoS_2 based materials afford a potential to replace a Pt catalyst used in the practical alkaline HER system.

7.2 Introduction

The sustainable generation of hydrogen gas through cost-effective electrochemical water splitting is highly desirable to overcome environmental problems and meet clean energy demand.[1] The most important challenge in hydrogen evolution reaction (HER) is to replace the most common incumbent Pt catalysts with readily available non-precious metals.[2] In order to achieve this goal, efficient, durable and economical non-Pt transition metal electrocatalysts (*e.g.,* carbides, sulfides, borides, nitrides and phosphides) have been extensively studied to accelerate hydrogen production by lowering kinetic overpotentials especially in alkaline solutions.[2-5] Although commercially available alkaline electrolyzers offer higher system efficiency than acidic proton exchange membrane electrolyzers, the rate of HER in alkaline solutions is 2−3 orders of magnitude lower than that in acidic solutions.[6-7] Therefore, the development of durable and efficient non-precious metal electrocatalysts for HER in alkaline solutions is crucial.

The molybdenum disulfide (MoS_2) has been intensively investigated for a catalyst in HER because of its nearly thermo-neutral hydrogen adsorption energy.[8] DFT studies reveal that the electrons localized

between Mo−H bond could be easily transferred to form dihydrogen with hydronium, as the hydronium protonation of the Mo-hydride is more promising than protonation of the hydrogen attached to S.[9-10] Therefore, it is highly desirable to synthesize Mo-exposed edges of MoS_2 which can reduce the free energy barrier between Mo-H and proton either from S-H on the edge site or from the hydronium in electrolyte. To this end, ample efforts have been made to enhance the catalytic performance of MoS_2 by converting 2H to 1T phase through chemical exfoliation,[11] multiplying the number of active sites through engineering its nanostructure such as vertically aligned nanofilms[12] and double-gyroid mesoporous films[13], creating sulfur vacancies and defects through thermal treatment,[14-17] introducing various chemical compositions such as amorphous MoS_x films,[18-19] dimeric $[Mo_3S_{13}]^{2-}$ clusters,[20] and metal-doped MoS_3,[21] compounding with conductive substrates (e.g. carbon nanotubes, Au, graphene, etc.)[22-25] and expanding the interlayer spacing through microwave-assisted solvothermal reduction of $(NH_4)_2MoS_4$[26-28] or trapping of foreign species into the MoS_2 sheets.[28-29] However, all these efforts have been made to enhance the HER activity in acidic solutions. The HER kinetics in alkaline media is sluggish due to high kinetic energy barrier of the first water dissociation (Volmer) step and the strong adsorption of hydroxyl anion (OH^-) on the surfaces of MoS_2. Recently, an attempt has been made to minimize this energy barrier by generating water dissociation sites in MoS_2 through doping of transition metals (Ni, Co and Fe) in alkaline media.[30] In addition, systematic investigations are required to understand critical factors such as phase, defects, high-density edges-oriented (EO), and interlayer-expanded (IE) geometry of both 2H and 1T phase MoS_2 and to enhance the HER performance especially in alkaline media.

Herein, we report a simple strategy to synthesize MoS_2 with multiple active sites, which may be required for high performance electrocatalysts in hydrogen evolution reaction, such as sulfur deficiency, defects, increased interlayer spacing, 1T phase, and Mo-exposed edge. Furthermore, hybrid materials of above all-in-one MoS_2 with N-doped graphene and nickel foam show superb electrocatalytic activity for HER in basic media. It outperforms all previously reported MoS_2 based materials.

7.3 Experimental section

7.3.1 Synthesis of S-deficient defective metallic molybdenum sulfide

All chemicals were utilized as purchased without further purification. Typically, melamine (2.0 mmol, 252.24 mg, Sigma-Aldrich) and HNO_3 (20µL) were dissolved in triply distilled hot water (20 mL) in a glass beaker (250 mL) equipped with a magnetic stirring bar. A transparent yellow solution of phosphomolybdic acid (PMo_{12}, 0.5 mmol, 913 mg, Sigma-Aldrich) in water was poured slowly into above solution to make a melamine-phosphomolybdate (P-Mo_{12}) supramolecular structure,[31] then the filter the precipitate to remove the unreacted species and disperse it again in water before adding an

aqueous solution of thiourea (20.0 mmol, 1522.4 mg, Sigma). The reaction mixture became bluish green at once, an indication of reduction of PMo_{12} from $[PMo_{12}O_{40}]^{3-}$ to $[PMo_{12}O_{40}]^{6-}$. It was heated to 60 ºC and maintained at this temperature for 1 h. For the synthesis of ammonia-intercalated A-MoS_2, the as-prepared solution was hydrothermally treated at 180°C for 20 h to convert the reduced PMo_{12} to A-MoS_2 by internally produced H_2S gas. This freshly prepared suspension of pH 7 was dried at 60 ºC to be used for R-MoS_2 synthesis.

The A-MoS_2 was reduced in a tube furnace under H_2 gas with a ramping rate of 5 °C/min, kept at a required temperature (400-600 ºC) for 3 h and then cooled down naturally to obtain brownish powders, denoted as R-MoS_2@X (X denotes reduction temperature). For comparison, MoS_2 without ammonia intercalated was also prepared by using thiourea only with PMo_{12} (no melamine) following the same procedure.

R-MoS_2 nanosheets were grown on N-doped graphene (R-MoS_2/NG) by adding the required amount of exfoliated graphene oxide (GO) suspension directly in the hydrothermal step, and then reduced following the same conditions. For R-MoS_2@NF, A-MoS_2 powder was dispersed in equal-ratio water/ethanol mixture along with Nafion binder, and this ink was then loaded (1 mg cm^{-2}) on pretreated nickel foam (NF), which was cleaned with 3M HCl then washed with distilled water followed by ethanol, by a drop casting method. The dried A-MoS_2/NF at 60 °C was reduced in H_2 atmosphere to get R-MoS_2/NF (0.8 mg cm^{-2}).

7.3.2 Characterization.

Crystallographic information of the as-synthesized electrocatalysts were investigated by powder X-ray diffraction (XRD, PANalytical pw 3040/60 X'pert) with Cu Kα radiations. The surface morphologies and structural information were recorded with field-emission scanning electron microscope (FE-SEM, Hitachi, S-4800, 15 kV) and transmission electron microscope (TEM, JEOL, JEM-2100F). HAADF STEM images and EDS analysis were taken using FEI Titan^3 G2 60-300 equipped with a probe-side spherical aberration (Cs) corrector operating at an accelerating voltage of 80 kV. HAADF STEM images were obtained at a probe current of approximately 30 pA with a convergence semi-angle of ~ 25mrad and an inner angle of ~ 80 mrad. X-ray photoelectron spectroscopy (XPS, ThermoFisher, K-alpha) was used to identify the surface atomic composition and chemical states. Raman spectra (AFM-Raman, WITec, alpha300S) was taken with 532 nm laser of 0.2mW. Absorptions (UV-Vis-NIR Spectrophotometer, Shimadzu, UV-3600 Plus) were measured in the range of 300-800 nm. Thermal (TGA, TA, Q500) analysis was done by ramping at10°C/min up to 900 °C in air. Elemental analysis was conducted with a Thermo Scientific Flash 2000 Analyzer and ICP-OES (Varian, 700-ES)

7.3.3 Electrochemical measurements.

The catalyst ink was prepared by dispersing electrocatalysts (1.0 mg/mL) in a mixture of deionized water and ethanol (1:1) and 10 μL of 5% Nafion solution. The mixture was sonicated for 1 h in a water bath. The working electrode was prepared by drop casting of 10 μL ink onto a glassy carbon electrode (0.4-0.5 mg cm^{-2} loading). The electrode was dried at room temperature before electrochemical measurements. Electrochemical HER activity and stability tests were carried out in a three electrode cell configuration using a rotating disc electrode (RDE, PAR Model 636 RDE) attached with a potentiostat (Ivium technologies). An Ag/AgCl (3.0M NaCl) electrode and a Pt wire were used as reference and counter electrodes, respectively. All potentials were referenced to the reversible hydrogen electrode (RHE) by the equation $E_{RHE}=E_{(Ag/AgCl)} + 0.059pH + 0.209$.[5]

The HER performance was measured in aqueous 1.0 M KOH (pH 13.7) at a scan rate of 5 mV s^{-1} with 1600 rpm after 20 cyclic voltammetry (CV) cycles in the range of 0.4 to -0.3 V_{RHE}. The electrochemical stability tests were conducted by performing up to 5000 CV cycles in the potential range. Electrochemical impedance spectroscopy (EIS) was conducted in the same setup in the frequency range of 100 kHz to 1 MHz with a modulation amplitude of 10 mV. The EIS spectra were fitted by the Z-view software. To evaluate the electrochemical surface area (ECSA), CV was conducted from -0.8 to -0.6 V in 1.0 M KOH *vs.* Ag/AgCl with different sweep rates between 10 to 100 mV s^{-1}.

7.4 Results and Discussion

7.4.1 Supramolecular-assisted hydrothermal synthesis

Supramolecular melamine-phosphomolybdate (MA-PMo_{12}) has been widely used in flame retardant composites and ion selective compounds for cesium (Cs).[31-32] MA-PMo_{12} supramolecular structure was synthesized by a slight modification of a known synthetic method.[31-32] The as-prepared MA-PMo_{12} used as a precursor to make the defective, edge-orientated (EO), and interlayer-expanded (IE) MoS_2 nanoflowers as aggregates of nanosheets by the hydrothermal reaction with thiourea at 180 ^oC for 20 h. During the hydrothermal reaction, it is expected that MA-PMo_{12} generates excess ammonia in an acidic solution, finally inducing ammonia intercalated molybdenum disulfide (A-MoS_2). At the same time, 1T phase in A-MoS_2 could be dominantly observed, which is possibly due to the octahedral MoO_3 units in PMo_{12} as a template for the 1T phase. The intercalation of ammonia and formation of 1T phase are features of using MA-PMo_{12} as a precursor in this study. Then, the further defects and S-vacancies are generated (R-MoS_2) by removing the ammonia and sulfur (as a form of H_2S) through thermal annealing at 500 ^oC in hydrogen gas for 3h. A schematic overview of the synthetic procedures is shown in **Figure 7.1a** and the details are described in the Experimental Section.

The X-ray diffraction (XRD) patterns of A-MoS_2 and R-MoS_2 are entirely different from bulk 2H-MoS_2 as shown in **Figure 7.1b**. The narrow and intense (002) peak for bulk 2H–MoS_2 indicates d-spacing of 6.15 Å. A broad (001) peak at 10.5^o corresponding to the interlayer spacing of 8.4 Å in A-MoS_2 suggests low crystallinity and random stacking of the nanosheets (**Figure 7.1b**).[33] The expanded interlayer spacing in the A-MoS_2 sample is likely due to the intercalation of in-situ generated ammonia (NH_3/NH_4^+) species between two S–Mo–S layers during the hydrothermal synthesis. Upon reduction, a sharper (002) peak in R-MoS_2 indicates the enhanced crystallinity retaining the interlayer spacing of 6.84 Å (**Figure 7.1b**), which is still larger than bulk 2H–MoS_2 (6.15 Å). High resolution TEM images (**Figure 7.1c** and **7.1d**) of both samples further confirm that a few layers of MoS_2 nanosheets are stacked with an interlayer spacing of 0.684 and 0.84 nm in R-MoS_2 and A-MoS_2, respectively, which is consistent with XRD data. Scanning electron microscopy (SEM) images of the as-synthesized R-MoS_2 (**Figure 7.1e**), A-MoS_2 (**Figure 7.1f**), show that nanosheets aggregated to well-defined nano-flowers with sharp edges like flower petals. The smaller grain size larger d-spacings of A-MoS_2 and R-MoS_2 nanoflowers than MoS_2 (synthesized with PMo_{12} only; 0.634 nm) as shown **Figure 7.1g-h** can provide the more edge-oriented geometry which contributes to high electrochemical active surface area (ECSA) and improved HER activity.

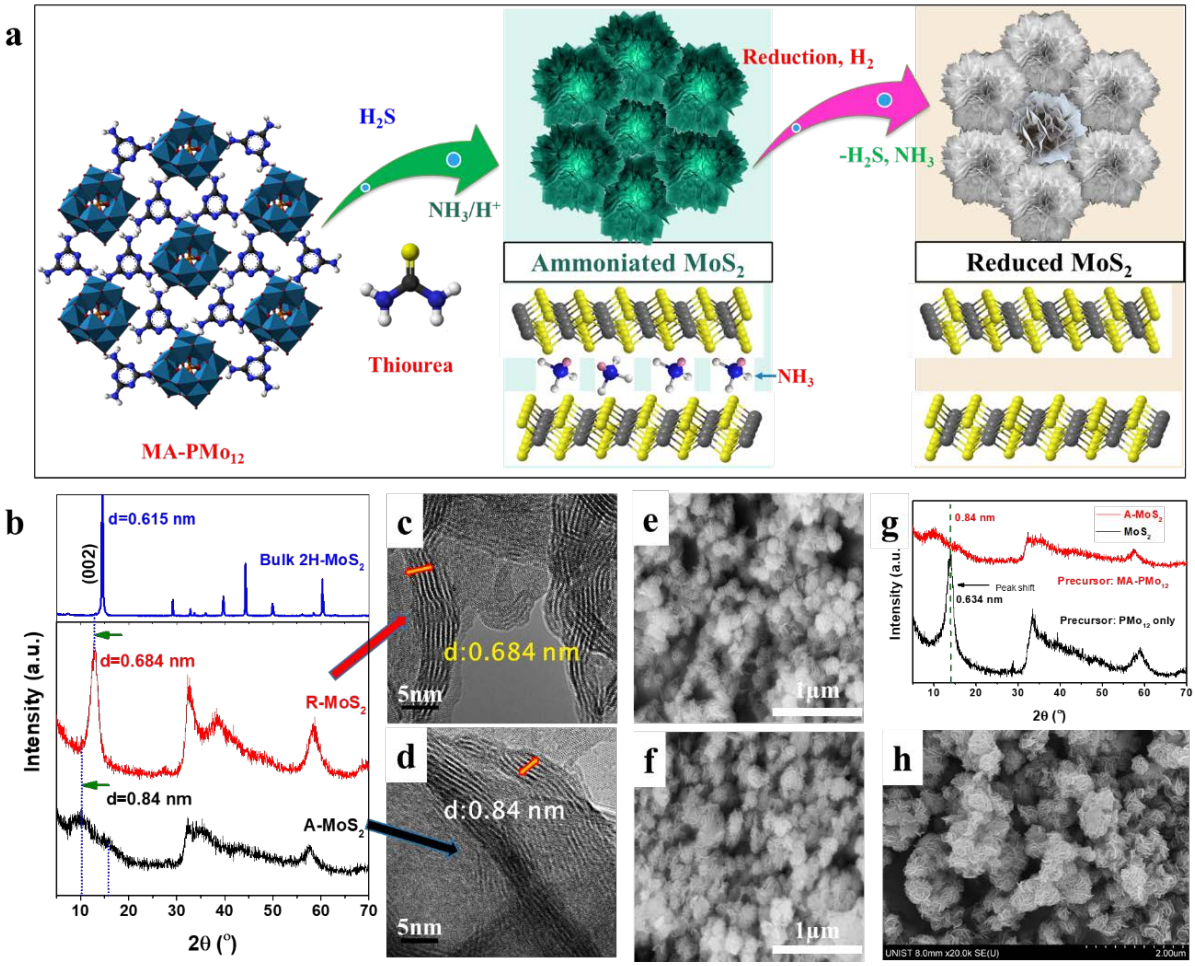

Figure 7.1. (a) Schematic illustration of MA-PMo_{12} structure-assisted synthesis of defective, Mo-exposed edges and S-deficient reduced molybdenum sulfide (R-MoS_2). XRD pattern of as-synthesized A-MoS_2, R-MoS_2 and bulk 2H-MoS_2 (b), High resolution TEM images indicating the d-spacing of 0.684 nm for (c) R-MoS_2 and (d) 0.84 nm for A-MoS_2. Scanning electron microscopy (SEM) images of (e) R-MoS_2 and (f) A-MoS_2. (g-h) XRD and SEM image for MoS_2 synthesized by using PMo_{12} as a precursor only.

The phase composition and elemental oxidation state for A-MoS_2 and R-MoS_2 were investigated by using X-ray photoelectron spectroscopy (XPS) in **Figure 7.2a-f**. In Mo *3d* XPS, A-MoS_2 shows Mo^{4+} peaks at 228.5 and 231.6 eV corresponding to the $3d_{5/2}$ and $3d_{3/2}$ components of 1T-MoS_2 phase[12, 34-35] and at 229.4 and 232.5 eV corresponding to those of 2H-MoS_2 phase (**Figure 7.2a-b**).[36] The fraction of 1T and 2H phases in A-MoS_2 is determined to be 71 and 29 %, respectively, by areas of Mo *3d* peaks. Larger fraction of 1T phase in as-synthesized A-MoS_2 can be attributed to octahedral MoO_3 units in PMo_{12} and the donation of lone pair electrons of intercalant NH_3 to Mo. Meanwhile, the XPS peak for R-MoS_2 after annealing at 500 °C in hydrogen gas showed that the fraction of 1T phase decreased to 33.7 % but was not marginal. Along with peaks for 1T and 2H phases, one more peak appeared, which corresponds to a lower oxidation state, $Mo^{0<\delta<4+}$ (14.9 %). The lower oxidation state is due to the thermal annealing in hydrogen gas that induced the release of H_2S from R-MoS_2. Atomic ratios of Mo to S in

A-MoS_2 and R-MoS_2 samples by elemental analysis and ICP-OES were 1: 2.06 and 1: 1.73, respectively, which supports the reduced oxidation state of Mo in R-MoS_2 by partially removed S through the release of H_2S during reduction. Similar results were obtained for S *2p* binding energies of A-MoS_2 and R-MoS_2 (**Figure 7.2c, d**). It is noted that high-resolution N1s spectrum (**Figure 7.2e-f**) reveals the existence of the of NH^{4+}/NH_3 (~398-400 eV) specie,[5, 37] which are responsible for interlayer expansion in A-MoS_2.

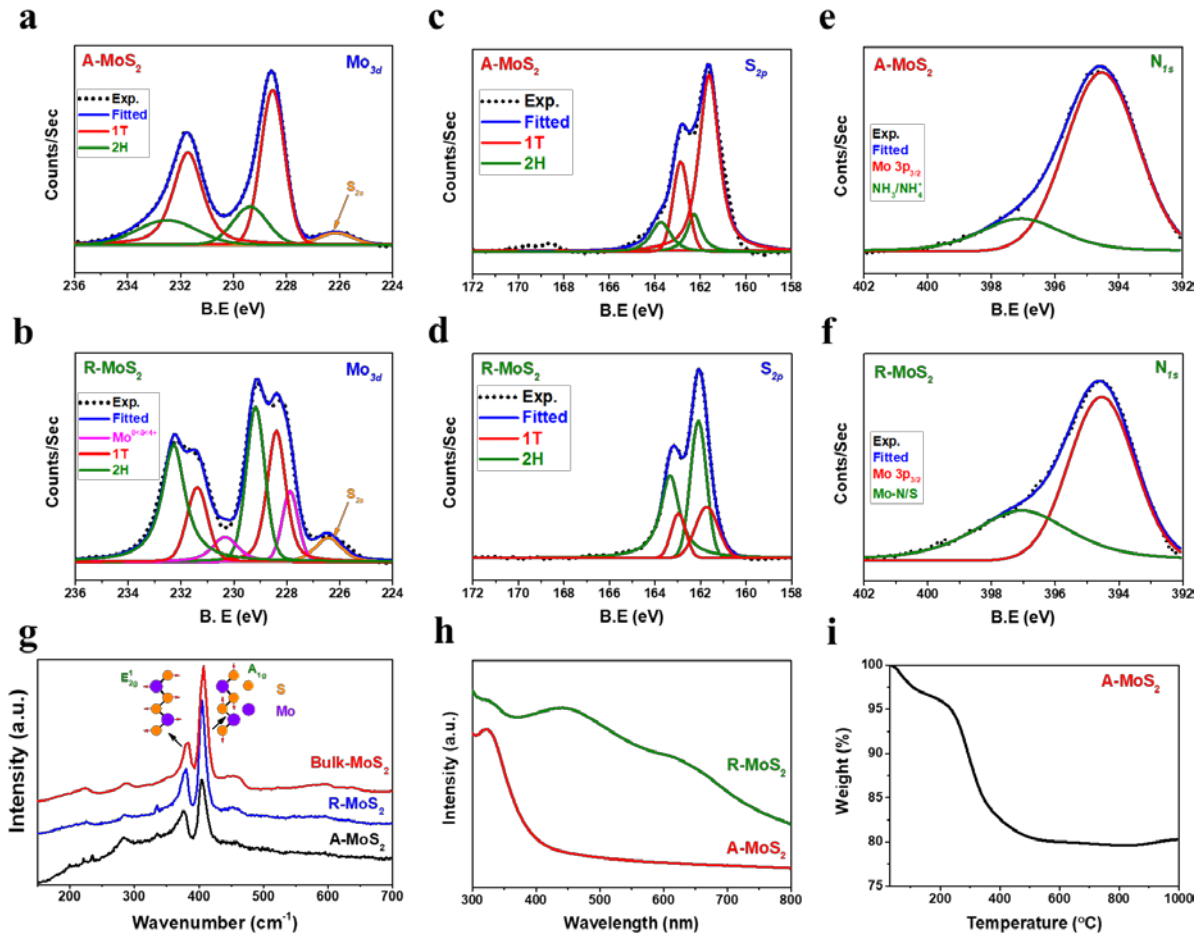

Figure 7.2. High resolution XPS Mo *3d* scan (a, b), S *2p* (c, d) and N *1s* (e, f) for A-MoS_2 and (b) R-MoS_2, Raman spectra (g), adsorption spectra (h) for both samples and thermal (TGA/DTA) analysis (i) of A-MoS_2.

Raman spectra in **Figure 7.2g** provide more information about the morphology and phase transition of MoS_2. The Raman peaks at 198, 222, 284 and 335 cm^{-1} in both samples, A-MoS_2 and R-MoS_2, are associated with the phonon modes in metallic 1T phase,[12, 36] while Raman peaks at ~379 and 404 cm^{-1} for E^1_{2g} and A_{1g} vibrational modes are typically for 2H phase.[36] Additionally, the larger intensity of A_{1g} peak compared to E^1_{2g} peak suggests the edge-rich features of the ultrathin MoS_2 nanosheets.[27, 37] Thus, it is speculated that R-MoS_2 shows more edge-terminated structures than A-MoS_2 from larger intensity ratio of A_{1g} and E^1_{2g} peaks in R-MoS_2. The ultraviolet–visible (UV-Vis) absorption spectra are shown

in **Figure 7.2h**. There is no salient absorption band for A-MoS_2, indicative of its metallic property.[36] R-MoS_2 showed similar absorption spectrum with three peaks at 446, 614, and 667 nm to 2H-MoS_2. The last two absorption peaks are due to the energy split from the valence band spin–orbital coupling in MoS_2 with enlarged lateral dimensions and the peak at 446 nm due to the quantum effect of smaller lateral-sized MoS_2 nanosheets.[36, 38] In thermal analysis (TGA) of A-MoS_2 as shown in **Figure 7.2i** , the first sharp weight loss (5%) up to 100 °C corresponds to release of water in the samples, followed by elimination of NH_3 and partial H_2S up to 200 °C and further removal of H_2S up to 460 °C, which is similar to thermal decomposition of $(NH_4)_2MoS_4$ in N_2.[39-40]

The structural features of A-MoS_2 and R-MoS_2 such as phase, defects and sulfur vacancies are further verified using transmission electron microscopy (TEM) in **Figure 7.3**. Bright-field transmission electron microscope (BFTEM) images (**Figure 7.3a and inset**) of both samples suggest that the flower like morphology of MoS_2 with sharp edges is retained even after thermal annealing of A-MoS_2 in hydrogen gas. The high crystallinity and sharp-edges of R-MoS_2 is also shown in high-resolution TEM (HRTEM) images and corresponding fast Fourier transforms (FFT) in **Figure 7.3a, b**.[41] High magnified STEM images of single layer A-MoS_2 and R-MoS_2 (**Figure 7.3d, and 7.3e**) show the coexistence of both 1T and 2H phases with defective regions. Interestingly, the R-MoS_2 layer with both 1T and 2H phases have smaller holes and well-defined sharp edges with Mo-atom termination, which can be active sites for the enhanced hydrogen evolution reaction.[9-10] The defective (porous) features and 1T and 2H phases in R-MoS_2 (**Figure 7.3e and 7.3f)** samples are marked by the red and yellow arrows in single layer region, which are very similar to earlier reported defective 1T-MoS_2 nanosheets exfoliated using n-butyl lithium,[11] three-step lithiation process,[17] and chemical vapor deposition (CVD) grown single layer MoS_2 with such defects.[42] The decrease in Mo to S ratio from 1.0:2.14 (A-MoS_2) to 1.0:1.73 (R-MoS_2) is another evidence of the presence of the sulfur vacancies after reduction of A-MoS_2 as confirmed by energy-dispersive X-ray spectroscopy (EDS) point analysis, which is also well matched with elemental analysis as mentioned above. These S-vacancies can strengthen the hydrogen adsorption by manipulating the hydrogen adsorption free energy (ΔG_H).[14] EDS elemental mappings spectrums of A-MoS_2 (**Figure 7.3g-j**) and R-MoS_2 (**Figure 7.3k-n**) clearly indicate uniform elemental (Mo, S, and N) distributions throughout the samples.

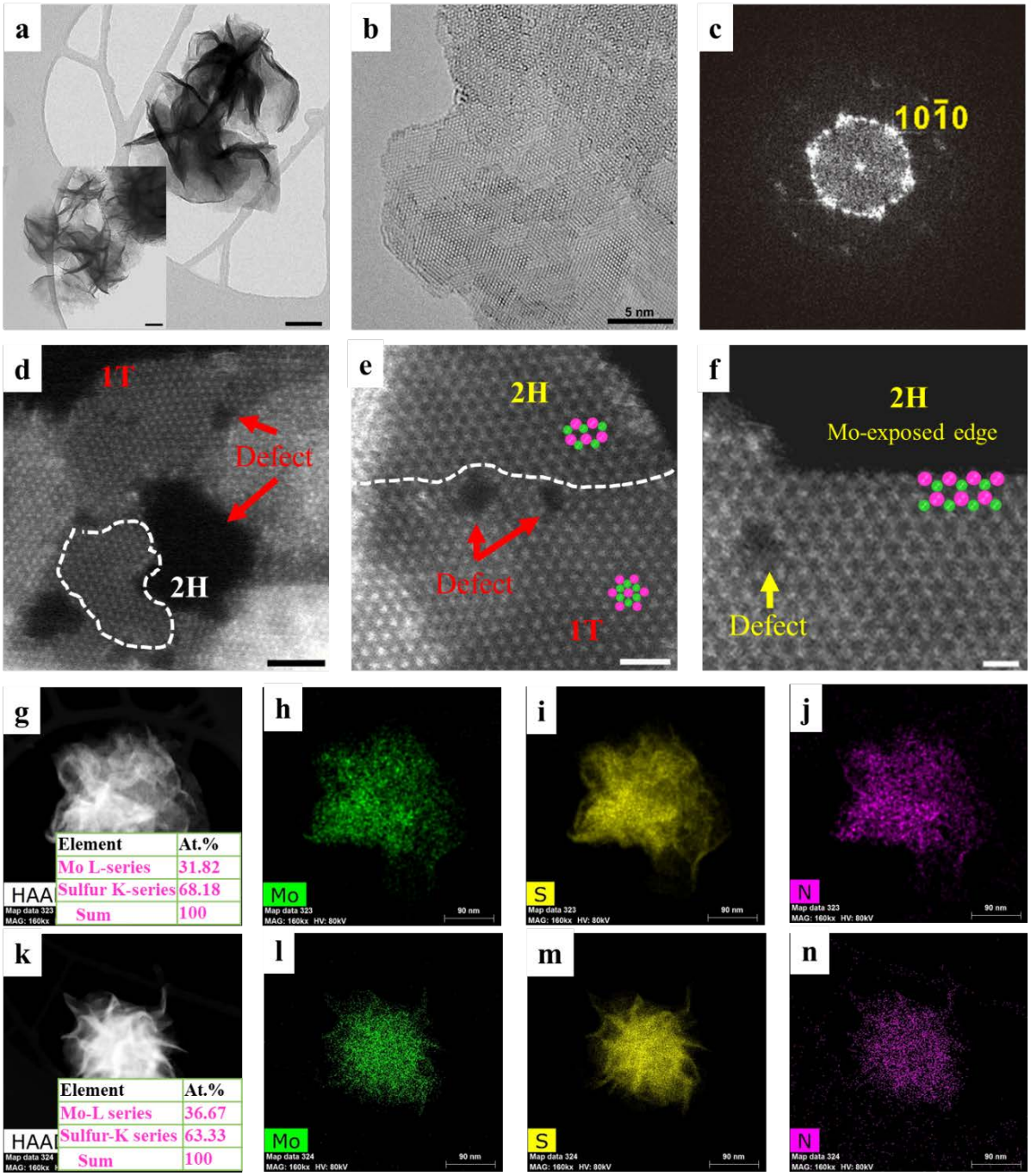

Figure 7.3. BFTEM images of (a) R-MoS_2 and (inset) A-MoS_2, scale bar, 50 nm. High resolution TEM image (b) R-MoS_2 and (c) corresponding FFT, scale bar, 5 nm. High-resolution HAADF STEM images (d) of A-MoS_2, scale bar, 2 nm and (e) R-MoS_2, showing the defects and coexistence of 1T and 2-H phase, scale bar, 1 nm. HAADF STEM images of 2-H (f), scale bar, 0.5 nm of R-MoS_2 monolayer sheet with Mo-edge termination and structural defects (pores), scale bar, 1 nm.

7.4.2 HER performance

The HER activities of A-MoS_2 and R-MoS_2 electrocatalysts were evaluated in 1.0M KOH aqueous solution using a three-electrode electrochemical cell (iR-corrected, **Figure 7.4a**). The HER activities of

commercial Pt/C and MoS_2 are provided for comparison. The HER activity of A-MoS_2 is worse than that of R-MoS_2 in terms of onset potential and overpotential (η_{10} or η_{40}) at current density of 10 or 40 mA/cm^2 normalized to geometric surface area of electrode. This is possibly due to low crystallinity and the detachment of A-MoS_2 samples from the electrode by reaction of NH_3/NH_4^+ species and OH^- to form NH_4OH. The R-MoS_2 sample reduced at 500 °C displayed optimized HER activity as compared to other samples annealed at temperature of 400 and 600 °C (**Figure 7.4b**). In order to scrutinize the effect of the structural defects formed in R-MoS_2, ammonia in A-MoS_2 was removed by reduction under a mild condition with $NaBH_4$ at 100 °C. As shown **Figure 7.4c,** the defect-free (DF) metallic (1T) MoS_2 electrode shows an improved HER performance than A-MoS_2, but significantly lower than that of R-MoS_2, demonstrating the contribution of the defects to the high performance of R-MoS_2. The cathodic currents normalized to loading mass in **Figure 7.4d** also show the similar behavior. The overpotentials (η_{10}) values to generate the mass activity of 10 A/g decreased in the following order 220, 167, 103 and 97 mV for A-MoS_2, DF-MoS_2, R-MoS_2 and R-MoS_2@NG, respectively.

The performance of the R-MoS_2 electrocatalyst can be further enhanced by combining with a conductive substrate like N-doped graphene (NG) and nickel foam (NF). For R-MoS_2/NG, A-MoS_2 nanoflowers were directly grown on graphene by adding an optimized amount (20 wt.%) of graphene oxide (GO) in the hydrothermal reactor, and then reduced at 500 °C in H_2. During the synthetic process, graphene was doped with N due to *in-situ* produced NH_3 from melamine and thiourea. The HER performance of R-MoS_2/NG was slightly improved compared to R-MoS_2, lowering η_{10} value from 111 mV (R-MoS_2) to 105 mV in 1.0 M KOH (**Figure 7.4a**). The R-MoS_2/NF exhibited superb HER performances: the onset potential is close to that of commercial Pt/C and η_{40} is better than that of Pt/C. Such high performance in R-MoS_2/NF can be attributed to the synergistic effect of highly conductive porous NF with large surface area (See the impedance data and electrochemical surface area later) and R-MoS_2 with multiple active sites such as defects, S-vacancies, Mo-exposed edges, and expanded interlayer spacing.

Tafel analysis provides information on intrinsic parameters to understand the HER mechanism, and it was conducted in a potential window of 20 to 225 mV. As shown in **Figure 7.4e-f**, the Tafel slopes of MoS_2 (119 mV/dec), A-MoS_2 (66 mV/dec), DF-MoS_2 (90 mV/dec), R-MoS_2 (105 mV/dec), R-MoS_2/NG (99 mV/dec) and R-MoS_2/NF (100 mV/dec) suggest that HER reactions are following the Volmer−Heyrovsky mechanism in 1.0 M KOH, similar to that for commercial Pt/C catalyst with Tafel slope ~70 mV/dec.[2, 30] The three possible reactions for HER in alkaline media are given in Equations 7.1 to 7.3.

Volmer Step: $H_2O + e^- + Mo^0.edges \longrightarrow H_{ads} - Mo^0.edges + OH^-$ (7.1)

Tafel Step: $2H_{ads} - Mo^0.edges \longrightarrow H_2 \uparrow$ (7.2)

Heyrovsky Step: $H_{ads} - Mo^0.edges + H_2O + e^- \longrightarrow H_2 \uparrow + OH^- + Mo^0.edges$ (7.3)

Next, exchange current densities (J_0) were determined by extrapolating Tafel plots to 0 mV. R-MoS_2, R-MoS_2@NG, and R-MoS_2@NF electrocatalysts display higher J_0 values (0.876, 0.877, and 2.27 mA/cm^2, respectively) than 2H-MoS_2 and A-MoS_2 (0.07 and 0.004 mA/cm^2, respectively). In particular, J_0 for R-MoS_2@NF almost approaches to J_0 value (2.65 mA/cm^2) for Pt/C. The J_0 value is proportional to the catalytic active surface area[5] and represents fast charge transfer kinetics over all electrodes due to EO and IE geometry, defects, S vacancies, and high conductivity. The η_{10} and J_0 value are compared in **Figure 7.4g**. Overall, HER activities of these R-MoS_2-based electrocatalysts are substantially higher than those of previously reported MoS_2-based catalysts as compared in **Figure 7.4h**.

Another fundamental kinetic parameter is turnover frequency ($TOF = \frac{J \times A}{2Fm}$), here, J is current density (C s^{-1} cm^{-2}) at a given overpotential, A is surface area of the electrode (cm^2), F is Faraday constant (96485.4 C/mol), the factor ½ is number of electrons required to make one hydrogen molecule and m is the molar mass of active metal components. The active sites in the material at pH=7 (phosphate buffer solution) are determined by CV cycle in the potential window from -0.2 to 0.6 V *vs*. RHE by following the previously reported methods.[43] The TOF values for each catalyst were calculated and compared with other catalysts in alkaline solutions in **Figure 7.4i**. The TOF values of MoS_2@NF at 0.1 V_{RHE} is 2.54 H_2 s^{-1}, which is quite larger than R-MoS_2(2.13 H_2 s^{-1}), R-MoS_2@NG (0.955 H_2 s^{-1}), DF-MoS_2 (0.103 H_2 s^{-1}) A-MoS_2 (0.038 H_2 s^{-1}), MoS_2 (0.071 H_2 s^{-1}) and other reported electrocatalysts such as Ni–Mo nanopowders,[44] Ni_2P,[45] α-Mo_2C,[46] Ni_5P_4[45] and γ-Mo_2N[46] (**Figure 7.4i**).

Electrochemical impedance spectroscopy (EIS) Nyquist plots (experimental and fitted) of R-MoS_2, R-MoS_2@NG and R-MoS_2@NF at a given overpotential (η) of 160 mV_{RHE} in 1.0M KOH solution are compared in **Figure 7.5a**. The EIS Nyquist plots show that there are two time constants. the first one at high frequencies is related to the surface defects (R_d) of the R-MoS_2 and the second one at low frequencies corresponds to the charge transfer (R_{ct}) process at the cathode/electrolyte interface. The diffusion (due to defects/pores) and charge transfer resistances were further decreased when R-MoS_2 was loaded on conductive substrates (*e.g.* NG and NF).

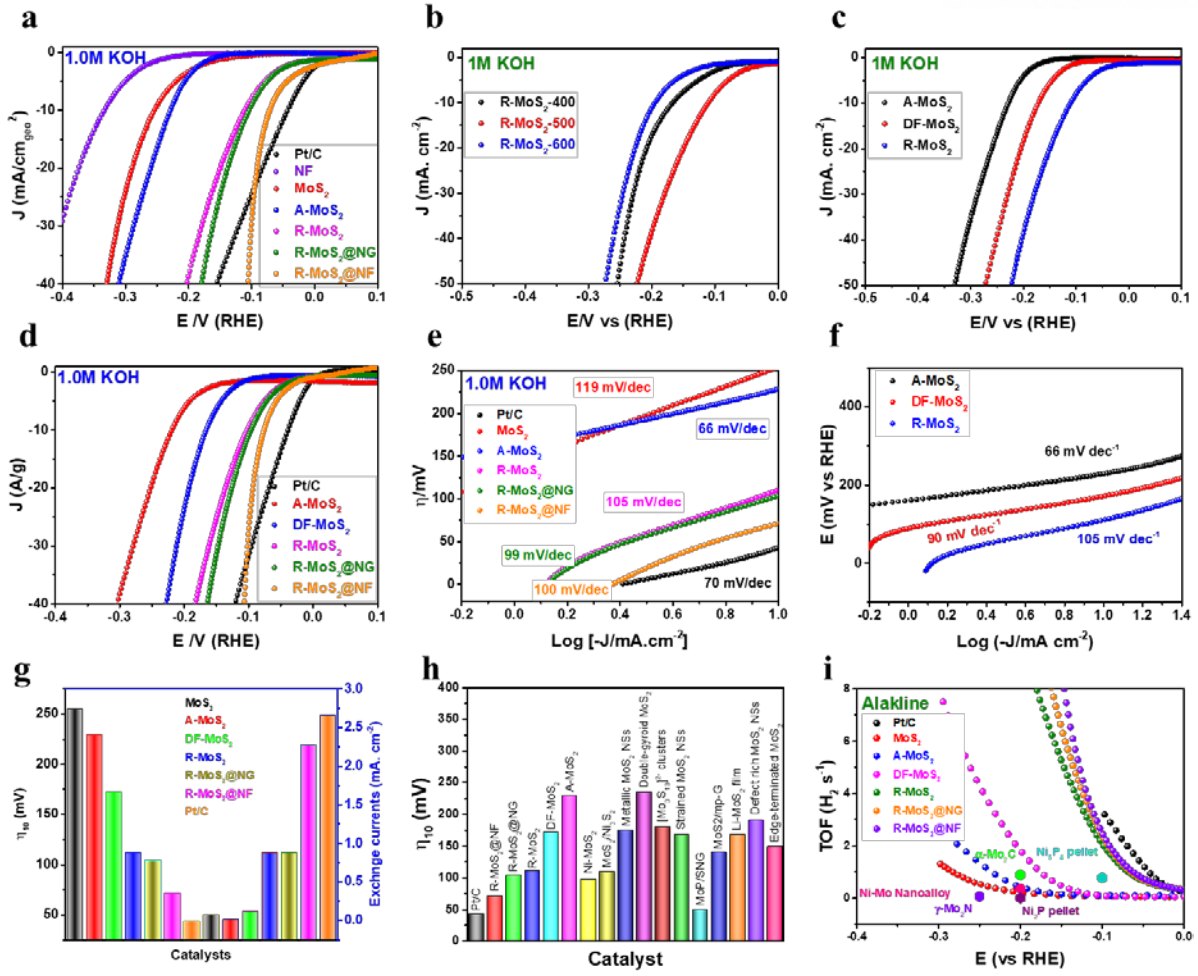

Figure 7.4. iR-corrected polarization curves normalized to (a-c) geometric surface area of the electrode and (d) normalized to loading mass of R-MoS_2, R-MoS_2/NG, and R-MoS_2/NF in 1.0 M KOH in and (e-f) corresponding Tafel plots. (g) Comparison between overpotential required for current density 10 mA cm-2 (left) and exchange currents (right), (h) comparison of η_{10} values with other MoS_2 based catalysts and (i) TOF plot, compared with other catalysts in alkaline media.

Electrochemical surface area (ECSA) is another parameter to effect the activity of the catalysts, and can be determined by measuring the double layer capacitance (C_{dl}) at the electrolyte/electrode interface with cyclic voltammetry (CV).[5] As shown in **Figure 7.5b**, the C_{dl} and ECSA values of R-MoS_2 (7.14 mF/cm^2, 178.5 cm^2), R-MoS_2@NG (18.22 mF/cm^2, 455.5 cm^2) and R-MoS_2@NF (173.01 mF/cm^2, 4325.25 cm^2) suggest a direct relationship between the exchange current density as a parameter of HER activity and ECSA. The electrocatalysts are also tested in 0.5 M aq. H_2SO_4 solution. As shown in **Figure 7.5c**, the HER overpotentials of 184 and 171 mV are measured for R-MoS_2 and R-MoS_2@NG catalysts at 10 mAcm^{-2}, which are far less than 111 and 104 mV in 1 M KOH, respectively. Thus, the initial acceleration of the water dissociation reaction at defective, and highly Mo-exposed edges of MoS_2 nanosheets is kinetically most favorable in aqueous 1.0M KOH rather than hydrogen adsorption in 0.5M H_2SO_4.[30]

The long-term electrochemical durability of R-MoS_2-based electrocatalysts was evaluated by continuous 5000 cycles of cyclic voltammetry (CV) at a scan rate of 100 mV/s in 1.0M KOH as displayed in **Figure 7.5d**. The R-MoS_2 electrocatalyst shows an extraordinary stability with a positive shift in overpotential from 127 mV to 111 mV after 5000 cycles. The performance remains even more stable for hybrid R-MoS_2/NG and R-MoS_2/NF with a negligible negative shift in overpotentials (1-5 mV) at current density of 10 $mAcm^{-2}$ as shown in **Figure 7.5e**. The time dependence of current density (chronoamperometry, CA) was also tested for up to 22 h at a static overpotential of ~100 mV for MoS_2@/NF (**Figure 7.5f**). There is a minor loss of current in R-MoS_2 and R-MoS_2@/NG due to detachment of catalyst from the speedy rotating disc electrode (RDE). In contrast, R-MoS_2@/NF displayed consistent current density because of strong attachment of catalyst to the NF electrode. Based on high activity and stability in alkaline media, the R-MoS_2-based electrocatalysts could be a promising candidate for practical HER in alkaline electrolytes.

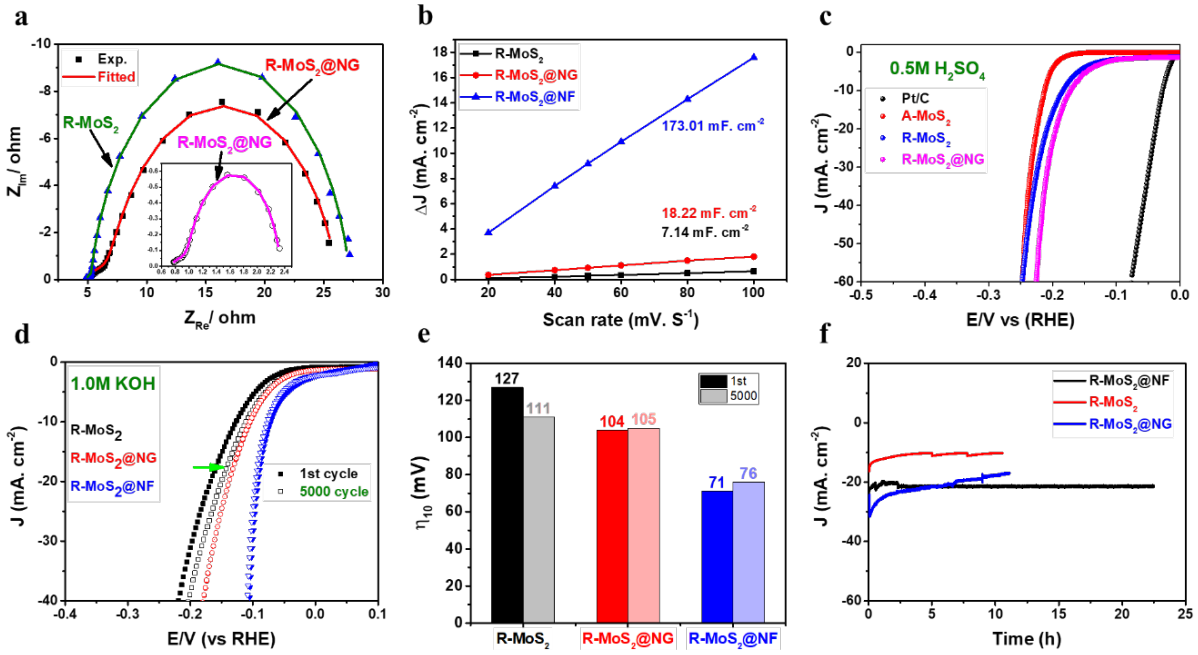

Figure 7.5. Electrochemical impedance spectroscopy (EIS) (a) Nyquist plots (solid line: fitted, symbol: experimental) of R-MoS_2, R-MoS_2@NG and R-MoS_2@NF (inset) in 1.0M KOH. (b) Measured capacitive currents (ΔJ) plotted as a function of scan rate and (c) HER performance in 0.5M H_2SO_4. (d) LSV curves of R-MoS_2, R-MoS_2/NG and R-MoS_2/NF for 1st and 5000th CV cycles. (e) η_{10} values for 1st and 5000th CV scans for HER. (f) A long-term durability test by chronoamperometry (CA) for 22 hours of R-MoS_2, R-MoS_2@NG and R-MoS_2@NF in alkaline solution.

7.5 Conclusions

Defect-rich, Mo-edge exposed, S-deficient and interlayer expanded metallic 1T-MoS_2 electrocatalysts have been synthesized successfully by adopting a unique melamine-phosphomolybdate (MA-PMo_{12}) supramolecular structure as a precursor. The interlayer spacing (8.4 Å) of A-MoS_2 was controlled by

in-situ generated ammonia gas from excess thiourea and melamine in a low pH environment. This ammonia along with H_2S gas was further removed by thermal reduction in hydrogen gas to generate S-vacancies and defects in R-MoS_2 The R-MoS_2 showed the superb HER activity in alkaline media due to intrinsic structural defects. In particular, the hybrid R-MoS_2/NF electrode showed HER performance very close to commercial Pt/C, and represents the best MoS_2-based electrocatalyst reported so far in alkaline media. The results suggest a great potential to replace expensive Pt catalyst in practical HER applications like water–alkali and chloro-alkali electrolyzers.

7.6 References

1. Gong, M.; Wang, D.-Y.; Chen, C.-C.; Hwang, B.-J.; Dai, H., A mini review on nickel-based electrocatalysts for alkaline hydrogen evolution reaction. *Nano Res.* **2016,** *9* (1), 28-46.

2. Zou, X.; Zhang, Y., Noble metal-free hydrogen evolution catalysts for water splitting. *Chem. Soc. Rev.* **2015,** *44* (15), 5148-5180.

3. Faber, M. S.; Jin, S., Earth-abundant inorganic electrocatalysts and their nanostructures for energy conversion applications. *Energy Environ. Sci.* **2014,** *7* (11), 3519-3542.

4. Anjum, M. A. R.; Lee, M. H.; Lee, J. S., BCN Network-Encapsulated Multiple Phases of Molybdenum Carbide for Efficient Hydrogen Evolution Reaction in Acidic and Alkaline Media. *J. Mater. Chem. A* **2017,** *5* (25), 13122-13129.

5. Anjum, M. A. R.; Lee, J. S., Sulfur and Nitrogen Dual-Doped Molybdenum Phosphide Nanocrystallites as an Active and Stable Hydrogen Evolution Reaction Electrocatalyst in Acidic and Alkaline Media. *ACS Catal.* **2017,** *7* (4), 3030-3038.

6. Zheng, Y.; Jiao, Y.; Zhu, Y.; Li, L. H.; Han, Y.; Chen, Y.; Jaroniec, M.; Qiao, S.-Z., High Electrocatalytic Hydrogen Evolution Activity of an Anomalous Ruthenium Catalyst. *J. Am. Chem. Soc.* **2016,** *138* (49), 16174-16181.

7. Rheinländer, P. J.; Herranz, J.; Durst, J.; Gasteiger, H. A., Kinetics of the hydrogen oxidation/evolution reaction on polycrystalline platinum in alkaline electrolyte reaction order with respect to hydrogen pressure. *J. Electrochem. Soc.* **2014,** *161* (14), F1448-F1457.

8. Hinnemann, B.; Moses, P. G.; Bonde, J.; Jørgensen, K. P.; Nielsen, J. H.; Horch, S.; Chorkendorff, I.; Nørskov, J. K., Biomimetic hydrogen evolution: MoS2 nanoparticles as catalyst for hydrogen evolution. *J. Am. Chem. Soc.* **2005,** *127* (15), 5308-5309.

9. Huang, Y.; Nielsen, R. J.; Goddard III, W. A.; Soriaga, M. P., The Reaction Mechanism with Free Energy Barriers for Electrochemical Dihydrogen Evolution on MoS2. *J. Am. Chem. Soc.* **2015,** *137* (20), 6692-6698.

10. Jaramillo, T. F.; Jørgensen, K. P.; Bonde, J.; Nielsen, J. H.; Horch, S.; Chorkendorff, I., Identification of active edge sites for electrochemical H2 evolution from MoS2 nanocatalysts. *Science* **2007,** *317* (5834), 100-102.

11. Lukowski, M. A.; Daniel, A. S.; Meng, F.; Forticaux, A.; Li, L.; Jin, S., Enhanced hydrogen evolution catalysis from chemically exfoliated metallic MoS2 nanosheets. *J. Am. Chem. Soc.* **2013,** *135* (28), 10274-10277.

12. Wang, H.; Lu, Z.; Xu, S.; Kong, D.; Cha, J. J.; Zheng, G.; Hsu, P.-C.; Yan, K.; Bradshaw, D.; Prinz, F. B., Electrochemical tuning of vertically aligned MoS2 nanofilms and its application in improving hydrogen evolution reaction. *Proc. Natl. Acad. Sci.* **2013,** *110* (49), 19701-19706.

13. Kibsgaard, J.; Chen, Z.; Reinecke, B. N.; Jaramillo, T. F., Engineering the surface structure of MoS2 to preferentially expose active edge sites for electrocatalysis. *Nature Mater.* **2012,** *11* (11), 963-969.

14. Wang, D.; Zhang, X.; Zhang, D.; Shen, Y.; Wu, Z., Influence of Mo/P Ratio on CoMoP nanoparticles as highly efficient HER catalysts. *Appl. Catal. A: General* **2016,** *511*, 11-15.

15. Ye, G.; Gong, Y.; Lin, J.; Li, B.; He, Y.; Pantelides, S. T.; Zhou, W.; Vajtai, R.; Ajayan, P. M., Defects Engineered Monolayer MoS2 for Improved Hydrogen Evolution Reaction. *Nano Lett.* **2016,** *16* (2), 1097-1103.

16. Xie, J.; Zhang, H.; Li, S.; Wang, R.; Sun, X.; Zhou, M.; Zhou, J.; Lou, X. W. D.; Xie, Y., Defect-rich MoS2 ultrathin nanosheets with additional active edge sites for enhanced electrocatalytic hydrogen evolution. *Adv. Mater.* **2013,** *25* (40), 5807-5813.

17. Yin, Y.; Han, J.; Zhang, Y.; Zhang, X.; Xu, P.; Yuan, Q.; Samad, L.; Wang, X.; Wang, Y.; Zhang, Z., Contributions of phase, sulfur vacancies, and edges to the hydrogen evolution reaction catalytic activity of porous molybdenum disulfide nanosheets. *J. Am. Chem. Soc.* **2016,** *138* (25), 7965-7972.

18. Tran, P. D.; Tran, T. V.; Orio, M.; Torelli, S.; Truong, Q. D.; Nayuki, K.; Sasaki, Y.; Chiam, S. Y.; Yi, R.; Honma, I., Coordination polymer structure and revisited hydrogen evolution catalytic mechanism for amorphous molybdenum sulfide. *Nat. Mater.* **2016,** *15* (6), 640.

19. Morales-Guio, C. G.; Hu, X., Amorphous molybdenum sulfides as hydrogen evolution catalysts. *Acc. Chem. Res.* **2014,** *47* (8), 2671-2681.

20. Kibsgaard, J.; Jaramillo, T. F.; Besenbacher, F., Building an appropriate active-site motif into a hydrogen-evolution catalyst with thiomolybdate [Mo3S13] 2− clusters. *Nat. Chem.* **2014,** *6* (3), 248-253.

21. Merki, D.; Vrubel, H.; Rovelli, L.; Fierro, S.; Hu, X., Fe, Co, and Ni ions promote the catalytic activity of amorphous molybdenum sulfide films for hydrogen evolution. *Chem. Sci.* **2012,** *3* (8), 2515-2525.

22. Shi, J.; Ma, D.; Han, G.-F.; Zhang, Y.; Ji, Q.; Gao, T.; Sun, J.; Song, X.; Li, C.; Zhang, Y., Controllable growth and transfer of monolayer MoS2 on Au foils and its potential application in hydrogen evolution reaction. *ACS Nano* **2014,** *8* (10), 10196-10204.

23. Voiry, D.; Fullon, R.; Yang, J.; e Silva, C. d. C. C.; Kappera, R.; Bozkurt, I.; Kaplan, D.; Lagos, M. J.; Batson, P. E.; Gupta, G., The role of electronic coupling between substrate and 2D MoS2 nanosheets in electrocatalytic production of hydrogen. *Nat. Mater.* **2016,** *15* (9), 1003.

24. Li, Y.; Wang, H.; Xie, L.; Liang, Y.; Hong, G.; Dai, H., MoS2 nanoparticles grown on graphene: an advanced catalyst for the hydrogen evolution reaction. *J. Am. Chem. Soc.* **2011,** *133* (19), 7296-7299.

25. Vrubel, H.; Merki, D.; Hu, X., Hydrogen evolution catalyzed by MoS 3 and MoS 2 particles. *Energy Environ. Sci.* **2012,** *5* (3), 6136-6144.

26. Sun, Y.; Alimohammadi, F.; Zhang, D.; Guo, G., Enabling Colloidal Synthesis of Edge-Oriented MoS2 with Expanded Interlayer Spacing for Enhanced HER Catalysis. *Nano Lett.* **2017,** *17* (3), 1963-1969.

27. Gao, M.-R.; Chan, M. K.; Sun, Y., Edge-terminated molybdenum disulfide with a 9.4-A interlayer spacing for electrochemical hydrogen production. *Nat. Commun.* **2015,** *6*, 7493.

28. Rasamani, K. D.; Alimohammadi, F.; Sun, Y., Interlayer-expanded MoS 2. *Mater. Today* **2017,** *20* (2), 83-91.

29. Tang, Y. J.; Wang, Y.; Wang, X. L.; Li, S. L.; Huang, W.; Dong, L. Z.; Liu, C. H.; Li, Y. F.; Lan, Y. Q., Molybdenum Disulfide/Nitrogen-Doped Reduced Graphene Oxide Nanocomposite with Enlarged Interlayer Spacing for Electrocatalytic Hydrogen Evolution. *Adv. Ener. Mater.* **2016,** *6* (12), 201600116.

30. Zhang, J.; Wang, T.; Liu, P.; Liu, S.; Dong, R.; Zhuang, X.; Chen, M.; Feng, X., Engineering water dissociation sites in MoS 2 nanosheets for accelerated electrocatalytic hydrogen production. *Energy Environ. Sci.* **2016,** *9* (9), 2789-2793.

31. BAXI, D., Melamine Phosphomolybdate—A New Ion Selective Compound for Caesium. *Radiochim. Acta* **1976,** *23* (2), 104-106.

32. Wang, C.; Li, J.; Ding, P., Roles of supermolecule structure of melamine phosphomolybdate in intumescent flame retardant polypropylene composites. *J. Anal. Appl. Pyrol.* **2016,** *119*, 139-146.

33. Acerce, M.; Voiry, D.; Chhowalla, M., Metallic 1T phase MoS2 nanosheets as supercapacitor electrode materials. *Nature Nanotechnol.* **2015,** *10* (4), 313-318.

34. Wang, H.; Lu, Z.; Kong, D.; Sun, J.; Hymel, T. M.; Cui, Y., Electrochemical tuning of MoS2 nanoparticles on three-dimensional substrate for efficient hydrogen evolution. *ACS Nano* **2014,** *8* (5), 4940-4947.

35. Chang, K.; Hai, X.; Pang, H.; Zhang, H.; Shi, L.; Liu, G.; Liu, H.; Zhao, G.; Li, M.; Ye, J., Targeted Synthesis of 2H-and 1T-Phase MoS2 Monolayers for Catalytic Hydrogen Evolution. *Adv. Mater.* **2016,** *28* (45), 10033-10041.

36. Geng, X.; Sun, W.; Wu, W.; Chen, B.; Al-Hilo, A.; Benamara, M.; Zhu, H.; Watanabe, F.; Cui, J.; Chen, T.-p., Pure and stable metallic phase molybdenum disulfide nanosheets for hydrogen evolution reaction. *Nat. Commun.* **2016,** *7*, 10672.

37. Wang, F.; Zheng, M.; Zhang, B.; Zhu, C.; Li, Q.; Ma, L.; Shen, W., Ammonia intercalated flower-like MoS2 nanosheet film as electrocatalyst for high efficient and stable hydrogen evolution. *Sci. Rep.* **2016,** *6*, 31092.

38. Mak, K. F.; Lee, C.; Hone, J.; Shan, J.; Heinz, T. F., Atomically thin MoS 2: a new direct-gap semiconductor. *Phy. Rev. Lett.* **2010,** *105* (13), 136805.

39. Lin, C.-H.; Tsai, C.-H.; Tseng, F.-G.; Yu, Y.-Y.; Wu, H.-C.; Hsieh, C.-K., Low-Temperature Thermally Reduced Molybdenum Disulfide as a Pt-Free Counter Electrode for Dye-Sensitized Solar Cells. *Nanoscale Res. Lett.* **2015,** *10* (1), 446.

40. Brito, J. L.; Ilija, M.; Hernández, P., Thermal and reductive decomposition of ammonium thiomolybdates. *Thermochim. Acta* **1995,** *256* (2), 325-338.

41. Gupta, A.; Rawal, T. B.; Neal, C. J.; Das, S.; Rahman, T. S.; Seal, S., Molybdenum disulfide for ultra-low detection of free radicals: electrochemical response and molecular modeling. *2D Mater.* **2017,** *4* (2), 025077.

42. Li, G.; Zhang, D.; Qiao, Q.; Yu, Y.; Peterson, D.; Zafar, A.; Kumar, R.; Curtarolo, S.; Hunte, F.; Shannon, S., All the catalytic active sites of MoS2 for hydrogen evolution. *J. Am. Chem. Soc.* **2016,** *138* (51), 16632-16638.

43. Merki, D.; Fierro, S.; Vrubel, H.; Hu, X., Amorphous molybdenum sulfide films as catalysts for electrochemical hydrogen production in water. *Chem. Sci.* **2011,** *2* (7), 1262-1267.

44. McKone, J. R.; Sadtler, B. F.; Werlang, C. A.; Lewis, N. S.; Gray, H. B., Ni–Mo nanopowders for efficient electrochemical hydrogen evolution. *ACS Catal.* **2013,** *3* (2), 166-169.

45. Laursen, A.; Patraju, K.; Whitaker, M.; Retuerto, M.; Sarkar, T.; Yao, N.; Ramanujachary, K.; Greenblatt, M.; Dismukes, G., Nanocrystalline Ni 5 P 4: a hydrogen evolution electrocatalyst of exceptional efficiency in both alkaline and acidic media. *Energy Environ. Sci.* **2015,** *8* (3), 1027-1034.

46. Ma, L.; Ting, L. R. L.; Molinari, V.; Giordano, C.; Yeo, B. S., Efficient hydrogen evolution reaction catalyzed by molybdenum carbide and molybdenum nitride nanocatalysts synthesized via the urea glass route. *J. Mater. Chem. A* **2015,** *3* (16), 8361-8368.

Acknowledgement

All thanks to Allah Almighty for blessing me the knowledge, strength, ability and opportunity to make this achievement. It is his blessings and mercy that would have made possible for me to write this success story. A huge respect offers to the beloved Holy Prophet Muhammad (ﷺ). Special gratitude and thanks to my lovely parents for their love, prayers and confidence have provided me to get this goal. It is their dreams for me have fulfilled in this accomplishment and without their loving upbringing and nurturing; I would not have been where and what I am today.

It is difficult to overstate my sincere gratitude to my Ph.D. advisor Prof. Jae Sung Lee (vice president of UNIST). With his inspiration, motivation, devotion, unconditional trust on my learning ability, his in-depth knowledge, continuous financial support for my Ph.D. study and his guidance during research and writing of this thesis, helped me to achieve this goal. A great appreciation to him for creating invaluable space for me, the freedom he has given to me to do this research and to develop myself as a researcher in the best possible way. It has been a great honor to be his first Pakistani Ph.D. student.

Besides my advisor, It's a great honor to say thank to Prof. Hyeon Suk Shin, Prof. Hu Young Jeong and Prof. Noejung Park for providing me technical and theoretical assistance to improve my results. It is mandatory to acknowledge Mr. Mahmut Sait Okyay and Dr. Mahesh Datt Bhatt for their efforts to conduct theoretical calculations for my projects. I would also like to thank my thesis committee members: Prof. Ja Hun Kwak, Prof. Sang Hoon Joo, Prof. Kwangjin An and Prof. Ji-Wook Jang, for their insightful comments and encouragement. Your valuable feedback incented and encouraged me to widen my research from various perspectives. I feel delighted and esteemed that you have accepted to be on my thesis committee.

I thank my ECOCAT colleagues for the stimulating discussions, for working hard together, and for all the fun we had enjoyed in monthly or annual lab gathering since last four years. Special thanks to Mr. Min Hee Lee for assisting in taking TEM images whenever I needed the most. Min Kyung Kim, I greatly admire your learning attitude and what you have recently achieved with the Ni_2P/MoS_2 project. It was a great experience to teach and guide you as your senior, you are always welcome for future collaboration. Also, I thank new and old lab secretaries, all lab committee in-charges who have run lab smoothly. Especially thank to Mr. Gyu-Sik Chae, Mr. Byeongjun Lee, Mr. Kwang Young Kim, Mr. Woo Jin Byun, Dr. Yo Han Choi and Mr. Dharmesh Parshottam Hansora for their nice and friendly company while staying in ECOCAT lab. Also to everyone in the ECOCAT, it was great sharing laboratory with all of you during last four years.

It is a great pleasure to thank my country fellows, Mr. Ishfaq Ahmad, Mr. Siraj Sultan, Mr. Imran Saeed, Dr. Toheed Akhter, Dr. Masood Yousaf, Dr. Sufyan Ali Memom and Mr. Muhammad Tufail at UNIST

whom cared for me beyond measures and cherished me in their hearts. It was a memorable time that I have spent with these lovely guys. My best wishes for all of their bright future and success in life. My eternal friend, Dr. Javeed Mahmood: I will miss our interesting and long-lasting chats during coffee breaks and get together. With his confidence, motivations, kindness and entrepreneurial spirit, he is one of the greatest examples. I thank him for all his feedback and encouragement and best wishes for his bright future ahead. It would be inappropriate if I omit to mention the friendly and motivational discussions on various political and scientific topics with our dearest friend Dr. Saqib Javaid either at Cow's trotters and Pakora/Samosa's parties or at coffee breaks. My gratitude to both of them, my formal UNIST colleagues, my PAEC fellows; Dr. Khaqan Shati, Dr. Muhammad Yousuf and Dr. M. Saleh, kept me going on my way to success, for assisting me as per their abilities, in whatever manner possible and for ensuring that good times keep flowing. The special thanks and gratitude to my all friend's families (my beloved bhabhies) for their best wishes and their delicious dishes served to me. They always considered and treated me like a real brother, because of them I never missed my family a lot.

I would like to thank my family: my parents, parents-in-law, in-laws and to my nephews, lovely brothers and their families for encouraging and supporting me spiritually throughout my study and my life in general.

In the end, it is a great contentment to thank and gratitude for my only love, my wife Shahnaz Ikram without her this thesis would never have been possible. Understanding me best, she has been proved herself as my best and great companion through her eternal love, support, encouragement and entertainment which helped me get through this agonizing time in the most positive way. I could understand her feelings, sacrificed a lot during my Ph.D. and her tough time that spent without me. I would thank her for holding my hands forever. My acknowledgment would be incomplete without mentioning the biggest source of my strength and blessings, my princesses, Laiba Mohsin, Aliha Mohsin and Manahil Mohsin. Their innocence smiles and little sweet gestures always made me fresh and motivated to accomplish this target well in time. I would like to dedicate this thesis to my parents, lovely wife and my sweet daughters.

Thanks for all your encouragement!

Mohsin Ali Raza Anjum

List of publications

1. **Anjum, M. A. R.**; Jeong, H. Y.; Lee, M. H.; Shin, H. S.; Lee, J. S., Efficient Hydrogen Evolution Reaction Catalysis in Alkaline Media by All-in-One MoS_2 with Multifunctional Active Sites. *Adv. Mater.* **2018**, *30* (20) 1707105.
2. **Anjum, M. A. R.**; Lee, J. S., Sulfur and Nitrogen Dual-Doped Molybdenum Phosphide Nanocrystallites as an Active and Stable Hydrogen Evolution Reaction Electrocatalyst in Acidic and Alkaline Media. *ACS Catal.* **2017,** *7* (4), 3030-3038.
3. **Anjum, M. A. R.**; Lee, M. H.; Lee, J. S., BCN network-encapsulated multiple phases of molybdenum carbide for efficient hydrogen evolution reactions in acidic and alkaline media. *J. Mater. Chem. A* **2017,** *5* (25), 13122-13129.
4. **Anjum, M. A. R.**; Okyay, M. S.; Lee, M. H.; Park, N.; Lee, J. S., Bifunctional sulfur-doped cobalt phosphide electrocatalyst outperforms all-noble-metal electrocatalysts in alkaline electrolyzer for overall water splitting. *Submitted*
5. **Anjum, M. A. R.**; Lee, M. H.; Lee, J. S., Boron and Nitrogen Co-doped Molybdenum Carbide Nanoparticles Imbedded in BCN Network as a Bifunctional Electrocatalyst for Hydrogen and Oxygen Evolution Reactions. *Submitted*.
6. Mahmood, J.[†]; **Anjum, M. A. R.**[†]; Shin, S. H.; Ahmad, I.; Noh, H. J., Jeong, H. Y.*; Lee, J. S.*; Baek, J. B.*, Encapsulating iridium nanoparticles inside 3D cage-like organic network as an efficient and durable catalyst for hydrogen evolution reaction. *Submitted*.
7. **Anjum, M. A. R.**; Lee, M. H.; Lee, J. S., Sulfur-doped di-cobalt phosphide outperforming precious metals as a bifunctional electrocatalyst for alkaline water electrolysis" has been received by journal Advanced Materials. *Submitted*.
8. Kim, M.;[†] **Anjum, M. A. R.;**[†] Lee, M. H.; Lee, B. J.; Lee, J. S., Trigging hydrogen evolution reaction by stimulating MoS_2 basal plane with Ni2P nanoparticles. *Will be submitted soon*.
9. **Anjum, M. A. R.;** Lee, M. H.; Lee, J. S. Efficient Catalysis of Hydrogen Evolution Reaction by Atomically produced Ni at surface of nickel sulfides. *Will be submitted soon*.

[†] contributed equally in these projects